

## **ABSTRACT**

INDEJE, MATAYO. Prediction and Numerical Simulation of the Regional Climate of Equatorial Eastern Africa. (Under the direction of Dr. Fredrick H. M. Semazzi.)

The objective in this investigation was to provide a better understanding of the mechanisms and physical processes responsible for climate variability over the equatorial eastern Africa, and explore potential for short-term climate prediction. Both statistical and numerical methods have been employed in this research. Application of cluster analysis yields 8 and 9 homogeneous climatic zones respectively for the variability of the annual and seasonal rainfall. Regions that are prone to drought or floods during the different phases of El Niño-Southern Oscillation (ENSO) are delineated. Positive rainfall anomalies occur in much of the region during March-May (MAM) and October-December (OND) of the ENSO(0) years and negative anomalies dominate during the following ENSO(+1) years. These rainfall patterns are useful for short-term climate monitoring over the region. The relationship between the Quasi-Biennial Oscillation (QBO) in the lower stratospheric zonal winds and the long-rains of MAM is more significant in lagged than in simultaneous, with the most distinct relationships occurring over the western parts of the region. The QBO-index explains about 36% of the seasonal rainfall variance. There is a 60/63 percent likelihood for the occurrence of above/below normal rainfall during the westerly/easterly phase of the QBO-index. The NCAR Regional Climate Model (RegCM2) simulations have demonstrated the added value of the nesting approach in improving regional climate simulations. The model reproduces the observed characteristics of the Turkana low-level jet. The study has shown the importance of orographic forcing, the large-scale background

monsoon flow and depth of the channel in the development and maintenance of the jet. Thermal and frictional forcing play equivalent roles as that of the large-scale winds in the formation of the jet. The identified regions of strong winds associated with the jet are important to the safety in the aviation industry and are also potential for alternative renewable energy resources in the form of wind energy. Large-scale orography is the most important factor. Divergence and anticyclonic vorticity partly explains the observed split in the jet cores. The dynamics of the flow in the channel and the dry conditions observed over the wider part of the valley is in partly explained by the Bernoulli theorem as applied to barotropic steady and non-viscous flows. Air-sea interaction phenomenon over the Indian Ocean, and the latitudinal location and intensity of the large-scale Walker and Hadley circulations are the main physical mechanisms responsible for the climate variability over the region during the wet and dry years. Abundant rainfall is associated with the presence of a midtropospheric cyclonic wind shear across the equator, and a negative vertical wind shear. Likewise, dry conditions are associated with the presence a strong westerly/southerly wind anomaly that occurs throughout the troposphere. Short-term climate prediction models developed in this study are capable of skillfully reproducing the space-time evolutions and distribution of the seasonal rainfall over the region, and specifically the observed floods that occurred during the 1997 ENSO year. Preliminary application of the RegCM2 in the prognostic mode successfully produces a 3-months projection of the extreme seasonal anomalies associated with the 1997 ENSO event. These models can be exploited further in operational short-term climate prediction over equatorial eastern Africa.

**PREDICTION AND NUMERICAL SIMULATION OF  
THE REGIONAL CLIMATE OF EQUATORIAL  
EASTERN AFRICA**

By

**MATAYO INDEJE**

A dissertation submitted to the Graduate Faculty of  
North Carolina State University  
in partial fulfillment of the  
requirements of the Degree of  
Doctor of Philosophy

**MARINE, EARTH AND ATMOSPHERIC SCIENCES**

Raleigh, North Carolina, USA.  
2000

**APPROVED BY:**

  
\_\_\_\_\_  
Dr. Adel Hanna

  
\_\_\_\_\_  
Dr. Sethu Raman

  
\_\_\_\_\_  
Dr. Lian Xie

  
\_\_\_\_\_  
Dr. Fredrick H. M. Semazzi  
Chair of Advisory Committee

## **DEDICATION**

The author dedicates this work to his family, wife Elizabeth, children; parents, mother Selinah Vilika Chevuneko (now deceased), father Reuben Indeje, brothers and sisters for their patience, support and encouragement through the years that he was away from home.

## **BIOGRAPHY**

Matayo Indeje was born on January 05, 1961 in Kenya. He attended Mombasa Polytechnic, Kenya where he graduated in 1980 with a high school diploma. He later joined University of Nairobi (UON) where he graduated with a Bachelor of Science degree with First Class Honors in 1985, majoring in Meteorology, Mathematics and Computer Science. He joined the National Weather Service (Kenya Meteorological Department) in October of 1985 where he worked for five years as a forecaster. Under the University of Nairobi scholarship, Indeje pursued graduate studies at UON between 1990-1993. He graduated with a Master of Science in 1994 in Atmospheric Science majoring in Numerical Weather Prediction in Meteorology. Between 1990 and 1996, Indeje worked at the World Meteorological Organization (WMO) regional Drought Monitoring Centre (DMC) for East, Central and Southern Africa, Nairobi (Kenya) as a research scientist. He also attended a 9 months graduate course in seasonal to inter-annual climate prediction, pilot project at the International Research Institute (IRI), Lamont-Doherty Earth Observatory of Columbia University, New York in 1994. Beginning fall season of 1996, Indeje started his doctoral studies in Atmospheric Science at North Carolina State University under the sponsorship of his advisors National Science Foundation (NSF) research grants. His research interests covers regional climate modeling and seasonal prediction. He was elected to the honor society of Phi Kappa Phi; the North Carolina State University Chapter in March 1999.

## ACKNOWLEDGMENTS

First of all I would like to express my sincerest thanks and highest appreciation to my advisor Dr. Fredrick H. M. Semazzi for his guidance and motivational support during the entire course of my study at North Carolina State University. I would also like to thank the other members of my advisory committee; Dr. Sethu Raman, Dr. Adel Hanna, and Dr. Lian Xie for their valuable advice and assistance, which greatly improved the research, and manuscripts of this dissertation.

The financial support provided by the National Science Foundation under grant ATM-9113511 for this graduate program is deeply appreciated. The computations were performed on the North Carolina Supercomputing Center (NCSC) Cray-T90, the *FOAM*<sup>V</sup> visualization and parallel computing facility at North Carolina State University, and on the NCAR Cray-J90 supercomputer. NCAR is sponsored by the National Science Foundation.

I also extend my gratitude to the Director of the Kenya Meteorological Department for granting me a study leave to pursue this advanced training. I would also like to thank the National Weather Service/NOAA for offering me a return air-ticket. I am indebted to the support I received from Prof. Laban J. Ogallo of the University of Nairobi, and my fellow staff members at the WMO/Drought Monitoring Centre for the East, Central and Southern Africa, Nairobi, Kenya. I further extend my deep appreciation to my fellow graduate students and particularly those in the climate research laboratory at North Carolina State University and at University of Nairobi, Kenya; (Song Yi, Sharon Baker, Gilbert Ouma and Richard Anyah) and to Drs. O. Roswintiarti, G. Pouliot, L. Sun and R. Nair, and Mr. Ray Burton for their general assistance. Last but not least, I would like to thank my wife, brothers and sisters for their endless love and support during the course of my study.

# TABLE OF CONTENTS

	Page
LIST OF TABLES .....	x
LIST OF FIGURES.....	xi
1 INTRODUCTION.....	1
1.1 Physical Features of Equatorial Eastern Africa .....	8
1.2 Climatology of Equatorial Eastern Africa .....	9
1.2.1 Forcing Mechanism on Climate Variability.....	15
1.2.1.1 Forcing due to Local Land Surface Characteristics.....	15
1.2.1.2 Radiative forcing and climate sensitivity .....	17
1.2.1.3 Global and Regional-Scale Teleconnections .....	20
1.2.1.3.1 Sea-surface Temperature and El Niño-Southern Oscillation.....	20
1.2.1.4 Quasi-biennial Oscillation in the Equatorial Zonal Wind .....	26
1.3 Objectives.....	28
1.3.1 Previous Related Research .....	30
2 ENSO SIGNALS IN EAST AFRICAN RAINFALL SEASONS .....	32
2.1 Background.....	32
2.2 Data Description and Methodology.....	35
2.2.1 Empirical Orthogonal Function (EOF) Analysis .....	37
2.2.2 Spatial Clustering of the Rainfall Observations Network.....	40
2.3 Results.....	43
2.3.1 Application of EOF Analysis on the East African Rainfall .....	43

2.3.2	Clustering East African Rainfall Stations into Homogeneous Regions .....	58
2.3.3	Composite Rainfall Map Patterns for the El Niño/La Niña (0) and Post-ENSO (+1) onset Years .....	60
2.3.4	Observed Shifts in the Seasonal Rainfall Cycle Induced by ENSO.....	82
3	RELATIONSHIPS BETWEEN QUASI-BIENNIAL OSCILLATION (QBO) IN THE LOWER EQUATORIAL STRATOSPHERIC ZONAL WINDS AND SEASONAL RAINFALL .....	93
3.1	Background .....	93
3.2	Data Description and Methodology.....	98
3.3	Results.....	102
3.3.1	Relationships between seasonal rainfall and the QBO-index .....	102
3.3.2	Predictability potentials of seasonal rainfall using the equatorial stratospheric QBO-Index .....	110
3.4	Discussion .....	121
4	SEASONAL PREDICTABILITY OF RAINFALL IN EQUATORIAL EASTERN AFRICA BASED ON TROPICAL PACIFIC OCEAN SEA-SURFACE TEMPERATURES.....	126
4.1	Background .....	126
4.2	Data and Methodology .....	130
4.2.1	Canonical Correlation Analysis (CCA).....	132
4.2.2	Model Validation Techniques .....	134
4.2.2.1	The Correlation Coefficient.....	135
4.2.2.2	Root Mean Square Error .....	135
4.2.2.3	Cross-Validation Techniques .....	136
4.2.2.4	Heidke Skill Score .....	137
4.3	CCA Model Results .....	138

4.3.1	Application of EOF analysis on the SST anomalies over the Tropical Pacific Ocean.....	138
4.3.2	Seasonal Predictability of East African Rainfall.....	143
4.3.2.1	The CCA Model.....	143
4.3.2.2	Model Validation.....	148
4.3.3	Application of the CCA model to the Prediction of the 1997 October-December Seasonal Rainfall.....	154
5	MECHANISTIC SIMULATIONS OF THE EAST AFRICAN CLIMATE USING NCAR REGIONAL CLIMATE MODEL: INFLUENCE OF LARGE-SCALE OROGRAPHY ON THE TURKANA LOW-LEVEL JET .....	157
5.1	Background.....	157
5.2	Observational studies .....	159
5.2.1	The Turkana Low-level Jet.....	164
5.2.2	Hypothesis of formation and maintenance of Turkana low-level Jet.....	166
5.3	Regional Climate Model Simulations.....	169
5.3.1	Description of the Numerical Model.....	169
5.3.2	Model Equations .....	174
5.3.3	Time Splitting.....	175
5.3.4	Horizontal Diffusion.....	176
5.3.5	Precipitation Physics.....	177
5.3.5.1	The Kuo-type Cumulus Cloud Parameterization Scheme.....	177
5.3.5.2	The Grell-type Cumulus Cloud Parameterization Scheme.....	178
5.3.6	Model physics .....	180
5.3.6.1	Surface Energy Formulation.....	181
5.3.6.2	Boundary Layer Physics.....	183
5.3.7	Boundary conditions.....	185

5.3.7.1	Surface boundary conditions .....	185
5.3.7.2	Lateral Boundary Conditions .....	186
5.3.8	Initial conditions.....	188
5.3.9	Design of numerical experiments .....	189
5.4	Model Simulations .....	190
5.4.1	Model Results of the Control Run .....	191
5.4.1.1	Circulation Features.....	191
5.4.1.2	Temperature and Humidity Fields .....	196
5.4.2	Simulation of the Turkana Low-level Jet.....	199
5.4.2.1	Dynamical Structure of the Jet .....	200
5.4.2.2	Thermal and Moisture Structure in the Jet Axis.....	212
5.4.3	Effects of Large-scale Orography on the Jet .....	217
5.4.4	Influence of the Large-scale Monsoon Flow on the Jet.....	217
5.4.5	Effects of the Channel depth on the Turkana Jet .....	218
6	DYNAMICS AND THERMODYNAMICS OF THE EL NIÑO AND NON-EL NIÑO ASSOCIATED CLIMATIC CONDITIONS OVER EASTERN AFRICA..	222
6.1	Background.....	222
6.2	Identification of the dry and wet years during the short rains season .....	226
6.3	Numerical Model Description and Experimental Detail.....	227
6.4	Results.....	228
6.4.1	Determining the Dry and Wet Rainfall Years .....	228
6.4.2	Kinematics associated with the wet and dry episodes over eastern Africa ..	230
6.4.2.1	Horizontal wind structure .....	230
6.4.2.2	Vertical wind structure.....	239
6.4.3	Thermodynamic Structure and Rainfall Distribution.....	243
6.4.3.1	Moisture Flux Convergence .....	243

6.4.3.2	Vertical Motion .....	246
6.4.3.3	Precipitation Distribution .....	255
6.5	Discussion .....	258
7	INVESTIGATING THE PRECTICTABILITY OF EQUATORIAL EASTERN AFRICAN CLIMATE USING NCAR REGIONAL CLIMATE MODEL. A CASE STUDY OF THE 1997 SEASON .....	263
7.1	Background .....	263
7.2	Numerical Model and Experimental Design.....	264
7.3	Model Results.....	266
7.3.1	Sensitivity of Model Horizontal spacing on Regional Climate Simulation ..	266
7.3.2	Simulation of the October - December 1997 Rainfall Season.....	275
7.3.2.1	Simulations of the Intraseasonal Rainfall Variability .....	277
8	SUMMARY AND CONCLUSIONS .....	286
9	SUGGESTED FUTURE WORK.....	302
10	REFERENCES.....	306
	APPENDIX A.....	323

## LIST OF TABLES

Table 2.1: Eigenvalues, variance and accumulated variance extracted by each mode of the normalized rainfall. ....	47
Table 3.1: Simultaneous and lag correlations [r], between the averaged equatorial stratospheric 30-mb zonal winds (QBO-Index) and MAM rainfall season over the eight homogeneous regions over East Africa. Bold and underlined values are above significant level of 10 percent based on a sample size of 14 years. ....	108
Table 3.2: Simultaneous and lag cross-correlation matrix for Rainfall, QBO and SOI indices. The sample size is 14 years (1979-92) and correlation coefficient [r] > 0.53 is significant at 5 percent level. Significant correlation values are bold and underlined. ....	109
Table 3.3: Contingency tables for zonal wind phases at 30-mb level and the MAM seasonal rainfall anomalies over three climatic regions of equatorial eastern Africa. ....	115
Table 4.1: Variance and accumulated variance extracted from the tropical Pacific SST anomalies. ....	140
Table 4.2: Correlation coefficient between the canonical vectors time series (u and v) between the predictor and predictand. ....	141
Table 4.3: Assessment of October-December seasonal rainfall using cross validation techniques (1961-1990). ....	152
Table 4.4: Assessment of March-May seasonal rainfall using cross validation techniques (1961-1990). ....	153
Table 4.5: Contingency table for cross-validated October-December seasonal rainfall for climatic Region 1. ....	153

# LIST OF FIGURES

Figure 1.1: Physical features of the equatorial eastern Africa. ....	6
Figure 1.2: Vegetation map of the equatorial eastern African region derived from the AVHRR-global area coverage (GAC) data set (extracted from: Laporte et al. 1998). ....	7
Figure 1.3: Long-term mean annual climatological rainfall over equatorial eastern Africa (1961-1990). Units are mm. ....	10
Figure 1.4: The spatial patterns of the mean seasonal rainfall (mm) over East Africa for (a) January-February, (b) March-May, (c) June-September, and (d) October-December. Contour interval is 100 mm. ....	12
Figure 1.5: Mean position of the ITCZ over Africa for (a) January, and (b) July/August (Nicholson 1986). Dotted and dashed lines show the location of the ITCZ...	14
Figure 1.6: The east-west Walker global circulation. ....	23
Figure 1.7: ENSO global precipitation deviations from average for November 1997 - April 1998 (Source: CPC/NCEP/NWS). ....	25
Figure 1.8: ENSO related global impacts (Source: CPC/NCEP/NWS). ....	26
Figure 1.9: Atypical evolution of Quasi-Biennial Oscillation (QBO) phases in the lower stratospheric zonal wind. ....	27
Figure 2.1: Network of rainfall stations. ....	36
Figure 2.2: The eight homogeneous climatic zones over East Africa obtained from combined EOF and simple correlation analyses using the annual rainfall series. ....	38

Figure 2.3: Examples of mean seasonal patterns of rainfall for some selected stations over East Africa. ....	42
Figure 2.4: Selection of the dominant EOF rainfall modes using the North et al. (1982) sampling techniques.....	45
Figure 2.5: The spatial patterns of the first rotated EOF modes for the March-May seasonal rainfall anomalies (loading $\times$ 100). Values less than -10 are shaded.	48
Figure 2.6: Same as in Figure 2.5, but for second EOF mode. ....	49
Figure 2.7: The spatial patterns of the first rotated EOF modes for the October-December seasonal rainfall anomalies (loading $\times$ 100). Values less than -10 are shaded.	50
Figure 2.8: Same as in Figure 2.7, but for second EOF mode. ....	51
Figure 2.9: The contour patterns of the first EOF rotated eigenvectors for annual rainfall anomalies (loading $\times$ 100). Values less than -5 are shaded. ....	53
Figure 2.10: Same as in Figure 2.9, but for second EOF mode. ....	54
Figure 2.11: The amplitude time series of the first two principal components for the MAM seasonal rainfall. ....	56
Figure 2.12: Same as in Figure 2.11, but for OND season. ....	57
Figure 2.13: The nine homogeneous climatic regions over East Africa obtained from seasonal rainfall series. ....	59
Figure 2.14: Time series of mean El Niño3 Pacific Ocean sea-surface temperature anomalies for November-December-January. The years with the sea-surface anomaly greater than +0.75 are classified warm ENSO and less than -0.75 classified cold ENSO. The years with sea-surface temperature anomalies within this range are classified as normal years.....	61

Figure 2.15: The composite map patterns for seasonal rainfall during the El Niño onset years (Loading $\times$ 100). The anomalies $\pm$ 20% of the long-term standard deviation are significant at 5% level. Negative significant anomalies are shaded.....	64
Figure 2.16: Same as in Figure 2.15 but for La Niña onset years. ....	65
Figure 2.17: The composite map patterns for monthly rainfall during the El Niño onset years for (a) March, (b) April, (c) May and (d) June (loading $\times$ 100). The anomalies $\pm$ 20% of the long-term standard deviation are significant at 5% level. Negative significant anomalies are shaded.....	67
Figure 2.18: Same as in Figure 2.17, but for La Niña onset years. ....	68
Figure 2.19: Same as in Figure 2.17, but for the months of (a) September, (b) October, (c) November and (d) December.....	71
Figure 2.20: Same as in Figure 2.19, but for La Niña onset years. ....	72
Figure 2.21: Same as in Figure 2.15 but for post-ENSO (+1) years. ....	75
Figure 2.22: Same as in Figure 2.21, but for post-La Niña (+1) years. ....	76
Figure 2.23: The composite map patterns for monthly rainfall during the post-ENSO (+1) years for (a) March, (b) April, (c) May and (d) June (loading $\times$ 100). The anomalies $\pm$ 20% of the long-term standard deviation are significant at 5% level. Negative significant anomalies are shaded.....	77
Figure 2.24: Same as in Figure 2.23 but for post-La Niña (+1) years. ....	78
Figure 2.25: Same as in Figure 2.23, but for the months of (a) September, (b) October, (c) November and (d) December.....	80
Figure 2.26: Same as in Figure 2.25 but for post-La Niña (+1) years. ....	81

Figure 2.27: The mean monthly precipitation by ENSO phase for the homogeneous rainfall regions 1 over East Africa. The error-bar on the mean climatological annual rainfall cycle represents $\pm 20\%$ of the climatological monthly mean. Values outside $\pm 20\%$ of the long-term mean are significant at 5% level.....	84
Figure 2.28: Same as in Figure 2.27. ....	86
Figure 2.29: Same as in Figure 2.27. ....	88
Figure 2.30: Same as in Figure 2.27. ....	91
Figure 3.1: The eight homogeneous rainfall groupings over East Africa obtained from combined EOF and simple correlation analyses (Indeje et al. 2000).....	101
Figure 3.2: A power spectrum of annual rainfall time series for the eight homogeneous regions over eastern Africa. Values $\geq 0.1$ on the y-axis are above confidence level of 95 percent.....	104
Figure 3.3: The mean correlation patterns of three seasons lag, two seasons lag, one season lag and zero lag between the QBO-Index and March-May (long-rains) season over East Africa. Correlation values above 5% significant levels are also indicated. ....	105
Figure 3.4: Time series of March-May (long rain) seasonal rainfall over central and western highlands of Kenya (Region 3), and March QBO-Index, and March SOI index (top) and, previous year July QBO-Index, and previous year July SOI index (bottom). ....	107
Figure 3.5: Annual mean time series for QBO-Index (top) and SOI index (bottom). Standardized values $\geq 0.1$ and $\leq -0.1$ are shaded. ....	112
Figure 3.6: Time series of standardized rainfall for three homogeneous regions: Region 3; central Kenya (top), Region 4; northwestern Kenya and northern Uganda (middle), and, Region 8; western Uganda (bottom). Shading information is similar to that in Figure 3.5.....	113

Figure 3.7: Time series of rainfall over central and western highlands of Kenya (Region 3) and the QBO-Index. ....	117
Figure 3.8: Composite plot for the QBO-Index corresponding to high- and low-March to May seasonal rainfall years. ....	117
Figure 3.9: Scatter diagram between MAM seasonal rainfall anomaly over central and western highlands of Kenya and the July 30-mb equatorial zonal wind (top), and the October to December minus June to August trend in the QBO-Index (bottom).....	120
Figure 3.10: Conceptual model representing the west phase of QBO and tropical convection over eastern Africa. DMI is the climate mode dipole index over the Indian Ocean (Webster et al. 1999, and Saji et al. 1999). ....	123
Figure 4.1: The contour patterns of the first EOF modes (loading $\times$ 100) for the July and December tropical Pacific Ocean SST anomalies. ....	142
Figure 4.2: The PC time series of the first EOF mode for December tropical Pacific Ocean SST anomalies. ....	143
Figure 4.3: The first spatial pattern pair for the canonical correlation between July Pacific SST and October-December rainfall over eastern Africa. (a) correlation between the predictor (SST) and the canonical vector (u), (b) correlation between the predictand (rainfall) and canonical vector (v) and, (c) normalized temporal functions (u and v) of the first CCA patterns for rainfall and SST. ....	146
Figure 4.4: The first spatial canonical pattern pair for the canonical correlation between December Pacific SST and the following March-May rainfall over eastern Africa. (a) correlation between the predictor (SST) and the canonical vector (u), (b) correlation between the predictand (rainfall) and canonical vector (v) and, (c) normalized temporal functions (u and v) of the first CCA patterns for rainfall and SST.....	147
Figure 4.5: Root mean square error and correlation forecast model skill for the prediction of OND rains over the nine climatic regions of eastern Africa. ....	149

Figure 4.6: Time evolutions of the forecast (cross-validated) and the observed OND standardized rainfall anomalies for the climatic homogeneous region 1 of eastern Africa. ....	149
Figure 4.7: Root mean square error and correlation forecast model skill for the prediction of MAM rains over the nine climatic regions of eastern Africa. ....	150
Figure 4.8: Time evolutions of the forecast (cross-validated) and the observed MAM standardized rainfall anomalies for the climatic homogeneous region 8 of eastern Africa. ....	150
Figure 4.9: CCA model performance for the 1997 October-December seasonal rainfall over eastern Africa using the July Pacific SST. (a) Predicted and (b) observed standardized rainfall anomaly. ....	155
Figure 5.1: Topography over the Turkana Channel. Terrain height values greater than 1000 m are shaded. ....	160
Figure 5.2: A simplified model showing the cross-equatorial monsoon flow diverting into the Turkana channel during (a) northern summer, and (b) northern winter. ....	163
Figure 5.3: RegCM2 model domain. ....	171
Figure 5.4: Topography of study area. Shaded are areas of elevation above 1250 m AMSL. Contour interval is 250m. ....	172
Figure 5.5: Land-use patterns over eastern Africa. Land cover type: 7 – water, 8 – semi-arid land, 9 – desert, 12 – tropical and subtropical forest, 13 – Savannah. ..	173
Figure 5.6: Simulated November mean horizontal wind vectors at a) 850-hPa and b) 700-hPa levels. Surface terrain above 1500 m is indicated as shaded. ....	193
Figure 5.7: Mean November NCAR/NCEP reanalysis (left panel) and RegCM2 (right panel) simulated zonal (upper panels) and meridional (lower panels) wind speed ( $\text{m s}^{-1}$ ) at 850-hPa level. Regions of strong easterly and southerly wind flow are shaded. ....	194

Figure 5.8: Longitude-height cross section of horizontal wind speed ( $\text{m s}^{-1}$ ) along a) $1^\circ\text{S}$ and b) $33^\circ\text{E}$ .....	195
Figure 5.9: November temperature ( $^\circ\text{C}$ ) at 850-hPa level for (a) RegCM2 model simulation, and b) NCAR/NCEP reanalysis.....	197
Figure 5.10: Simulated November surface temperature ( $^\circ\text{C}$ ) for a) RegCM2 and b) NCAR/NCEP GCM. ....	198
Figure 5.11: November specific humidity ( $\text{g kg}^{-1}$ ) at 850-hPa level for (a) RegCM2 model simulation, and b) NCAR/NCEP reanalysis.....	199
Figure 5.12: Streamlines of the simulated November mean conditions at a) 950-hPa, b) 850-hPa and c) 750-hPa levels over the Turkana channel in the control run. The mean configuration of the surface orography is indicated in dark shaded. ....	202
Figure 5.13: Simulated mean horizontal wind speed for a) October, b) November and c) December at lat. $3.5^\circ\text{N}$ along the Turkana Channel in the control run. Shaded are values with wind stronger than $8 \text{ m s}^{-1}$ and vectors indicate the wind direction.....	204
Figure 5.14: Simulated November mean zonal wind component a) at lat. $3.5^\circ\text{N}$ along the Turkana Channel, and b) at lon. $37.5^\circ\text{E}$ across the entrance of the Turkana Channel, for and control run. Shaded are values with wind speed stronger than $8 \text{ m s}^{-1}$ . ....	205
Figure 5.15: Simulated November mean horizontal divergence at a) the channel entrance near Marsabit, b) middle of the channel around Lake Turkana and c) at the exit of the channel near Logichoggio, for the control model run. These locations are shown in Figure 5.1. ....	207
Figure 5.16: Longitude-height cross section of vertical velocity at lat. $3.5^\circ\text{N}$ along the Turkana channel. Shaded are areas of upward vertical velocity. The bottom orography, which is almost flat in the channel, is also shown.....	209

Figure 5.17: Simulated November mean vorticity at a) the channel entrance near Marsabit, b) middle of the channel around Lake Turkana and c) at the exit of the channel near Logichoggio, for the control model run..... 211

Figure 5.18: Simulated November a) mean temperature ( $^{\circ}\text{C}$ ) at 850-hPa, and b) mean surface pressure (hPa) over the Turkana channel in the control model run.. 214

Figure 5.19: Simulated November mean moisture flux divergence ( $\text{kg kg}^{-1} \text{s}^{-1}$ ) along the Turkana channel in the control model run. Positive values indicate divergence and negative convergence of moisture flux. .... 215

Figure 5.20: Simulated November mean temperature flux divergence ( $\text{K s}^{-1}$ ) along the Turkana channel in the control model run. .... 216

Figure 5.21: Simulated November a) mean wind flow at 850-hPa over the Turkana channel, and b) mean wind speed along the Turkana channel, for the NOTOPO experiment..... 219

Figure 5.22: Simulated November a) mean wind flow at 850-hPa over the Turkana channel, and b) mean wind speed along the Turkana channel, for the zero large-scale ambient wind experiment..... 220

Figure 5.23: Simulated November a) mean wind flow at 850-hPa over the Turkana channel, and b) mean wind speed along the Turkana channel, for the channel depth experiment..... 221

Figure 6.1: The domain of study and the nine homogeneous climatic regions based on cluster analysis. The nine regions are as follows: CK - Central Kenya, EH - Eastern highlands of Kenya, CS - Coastal strip of Kenya and Tanzania, NEK - Northeastern Kenya, STZ - Southern Tanzania, WTZ - Western Tanzania, LV - Lake Victoria basin, WUG - Western and central Uganda, and NWK - Northwestern Kenya and parts of northeastern Uganda..... 224

Figure 6.2: Time series of area-averaged October-December seasonal rainfall indices over eastern Africa. .... 229

Figure 6.3: Simulated November mean horizontal wind flow at a) 850-, b) 700- and c) 500-hPa levels for the control model run. Shaded are areas with wind speed

greater than $4 \text{ m s}^{-1}$ . Convergence zones are shown with thick hatched lines. .....	232
Figure 6.4: Same as in Figure 6.1, but for the wet year 1982. ....	235
Figure 6.5: Same as in Figure 6.1, but for the dry year 1987.....	236
Figure 6.6: Simulated November mean horizontal wind anomaly vectors at 700-hPa level for a) wet year minus control (1988-1982), and b) Dry year minus control (1988-1987). A are areas of anticyclogenesis. ....	237
Figure 6.7: Latitude-height cross section of horizontal wind speed ( $\text{m s}^{-1}$ ) averaged over longitudes $25^\circ$ to $45^\circ\text{E}$ for a) wet year minus control model run, b) dry year minus control model run. ....	240
Figure 6.8: Longitude-height cross section of the RegCM2 simulated horizontal wind speed ( $\text{m s}^{-1}$ ) along latitude $1^\circ\text{S}$ for a) wet year minus control model run (1982-1988), b) dry year minus control model run (1987-1988).....	241
Figure 6.9: Same as in Figure 6.8, but for NCAR/NCEP reanalysis for (a) wet year (1982) minus control (1988), and (b) dry year (1987) minus control. ....	242
Figure 6.10: November mean horizontal moisture flux divergence field for (a) wet year, and (b) dry year. Negative values indicate convergence of moisture flux and positive divergence of moisture flux. Contour interval is $0.2 \times 10^{-06} (\text{kg kg}^{-1} \text{s}^{-1})$ . Wind vectors are also indicated.....	244
Figure 6.11: Mean Vertical Velocity ( $\times 10^{-2} \text{ m s}^{-1}$ ) for November at 620-hPa level in the a) control model run, b) wet year minus control, and c) dry year minus control. Shaded are areas of upward motion and sinking motion is shown by hatched contours.....	248
Figure 6.12: Longitude-height cross section of vertical velocity ( $\times 10^{-2} \text{ m s}^{-1}$ at latitude $1^\circ\text{S}$ during the month of November for a) control model simulation, b) wet (1982) year, and c) dry (1987) year. Bottom orography is also indicated....	252

Figure 6.13: Same as in Figure 6.12, but for a) wet year minus control (1982-1988), and c) dry year minus control (1987-1982).....	253
Figure 6.14: Contributions of the convective and non-convective seasonal rainfall to the months of October, November and December over nine homogeneous climatic regions of eastern Africa for the wet and dry simulations. ....	257
Figure 6.15: Schematic diagram showing the low-level water vapor advection (arrows) and, convergence and divergence (circles) associated with the wet and dry episodes during the October-December rainfall season over eastern Africa.	261
Figure 7.1: Observed seasonal rainfall distribution for 1988; a) October, b) November, and c) December.....	268
Figure 7.2: Simulated spatial distribution of seasonal rainfall in the control run (1988) for a) October, b) November, and c) December.....	269
Figure 7.3: CCM3 simulated precipitation for a) October, b) November, and c) December (1988).....	270
Figure 7.4: (a) Observed and (b) RegCM2 simulated precipitation in the control run (1988) for the nine climatic regions. ....	272
Figure 7.5: Percentage standardized rainfall deviations for the eight homogeneous climatic regions over East Africa at 60 and 30-km horizontal grid spacing. ....	274
Figure 7.6: RegCM2 simulated rainfall for October-December. (a) Control run (1988), (b) simulation for 1997, and (c) percent normalized rainfall index for the 1997 minus control (normalized by the control run).....	276
Figure 7.7: Daily evolution of model rainfall simulation for the control and 1997 anomaly run for some selected climatic regions of equatorial eastern Africa. The arrow indicates the approximate rainfall withdrawal dates.....	278
Figure 7.8: Model simulated and observed dekadal rainfall for some selected rainfall regions. ....	285



## LIST OF ABBREVIATIONS

LST	Local Standard Time
GCM	General Circulation Model
NCAR	National Centers for Atmospheric Research (USA)
NCEP	National Center for Environmental Prediction (USA)
RegCM2	NCAR - Regional Climate Model Version 2
NOAA	National Oceanographic and Atmospheric Administration (USA)
WMO	World Meteorological Organization
DMC	Drought Monitoring Centre – WMO project for East, Central and Southern Africa
KMD	Kenya meteorological Organization
CCM3	NCAR - Community Climate Model Version 3
ECMWF	European Centre for Medium and long-range Weather Forecasting (United Kingdom)
SST	Sea-Surface Temperature
CFL	Courant-Friedrichs-Lewy stability constraint
NCSC	North Carolina Supercomputing Center
NCSU	North Carolina State University
CPC	Climate Prediction Center – NOAA (USA)
NWS	National Weather Service – NOAA (USA)
RMSE/rmse	Root-Mean-Square-Error
HSS	Heidke Skill Score
PC	Principal Component time series
CCA	Canonical Correlation Analysis
DMI	Dipole Mode Index
EOF	Empirical Orthogonal Analysis
ENSO	El Niño – Southern Oscillation
QBO	Quasi-Biennial Oscillation
MAM	March-April-May
OND	October-November-December
ITCZ	Inter-Tropical Convergence Zone
GHGs	Green House Gases
IPCC	Inter-Governmental on Climate Change
SOI	Southern Oscillation Index
MLR	Multiple Linear Regression
LLJ	Low Level Jet
EALLJ	East African Low Level Jet

## LIST OF SYMBOLS

$c_v$	Specific heat of air at constant volume
$c_p$	Specific at of air at constant pressure
$c_{pm}$	Specific heat at constant pressure for moist air
$u$	Component of wind velocity in the eastward direction ( $m\ s^{-1}$ )
$v$	Component of wind in the northward direction ( $m\ s^{-1}$ )
$T$	Temperature (K)
$RH$	Relative humidity
$F_H\alpha$	Term representing contribution of horizontal diffusion of a variable $\alpha$ to the temporal rate of change of $\alpha$
$K_H$	Horizontal eddy diffusion ( $m^2\ s^{-1}$ )
$K'_H$	Coefficient used in the fourth-order diffusion ( $s^{-1}$ )
$F_v$	Water vapor flux
$P_s$	Surface pressure (cb)
$P_t$	Pressure (cb) at the model top
$P^*$	$P_s - P_t$
$\sigma$	Terrain-following nondimensional vertical co-ordinate of the model
$\dot{\sigma}$	Vertical velocity in $\sigma$ -coordinates ( $s^{-1}$ )
$\sigma'$	Dummy variable of integration
$\beta$	Precipitation efficiency parameter (used in Grell cumulus scheme)
$\omega$	Vertical velocity in pressure coordinates ( $cb\ s^{-1}$ )
$t$	Time (s)
$m$	Map scale factor
$\phi$	Geopotential; also latitude
$\Omega$	Angular velocity of the earth ( $7.2722 \times 10^{-5}\ s^{-1}$ )
$f$	Coriolis parameter ( $2\Omega\sin\phi$ )
$g$	Acceleration of gravity ( $9.8\ m\ s^{-1}$ )
$q_v$	Mixing ratio of water vapor
$q_{vs}, q_{va}$	Mixing ratio of water vapor at the ground and the lowest model layer
$\mathbf{V}$	Horizontal wind vector
$I1, I2$	Normalized condensate and evaporate in updraft
$m_b$	Cloud base mass flux
$L_v$	Latent heat of condensation ( $2.5 \times 10^6\ J\ kg^{-1}$ )
$\rho, \rho_a$	Density of air ( $kg\ m^{-3}$ )
$C_\theta, C_u$	Surface exchange coefficient for heat and momentum
$\theta_s, \theta_a$	Potential temperature (K) at the lowest model layer and at the ground surface
$F$	Large-scale forcing; also function of distance from the lateral boundary

# Chapter 1

## 1 INTRODUCTION

During El Niño climate events and in particular the 1997/1998 El Niño, equatorial eastern Africa experiences near record rainfall conditions. This observation prompted a surge of demand for information, ranging from assessment of the state of the event and its evolution, to actions that can be taken to help mitigate or even exploit the abnormal conditions. Understanding the causes of these climatic extremes and the prospects of their predictability is a matter of high research both for the eastern Africa and also the global climate because of the vast amounts of anomalous latent heat energy liberated during the El Niños.

Droughts and floods have become common features in the African climate in recent years. This climatic variability has been associated with many natural disasters in which the inhabitants of the African countries have only marginally been able to cope with. The economies of these African countries largely depend on agriculture, which is highly vulnerable to the amounts and distribution of precipitation. The efforts to achieve food security in most parts of the African continent including eastern Africa have long been hampered by civil wars, political volatility, worsening conditions of international trade, rapid population growth, floods and drought. Floods and droughts are natural events, which cannot be controlled. However, in East Africa, like some other parts of the World

including India and South Africa (Dyer 1982), there are prospects for out-of-season rainfall compensation of the deficit conditions. Accurate seasonal to inter-annual climate monitoring and forecasting is therefore crucial for proper planning and management of all climate sensitive social economic activities such as electricity production, transportation, tourism, forest resource management, and wildlife management which are dependent on precipitation distribution. There are other factors such as fires, spread of diseases etc., which are linked to climate variability, some of which have been discussed by Glantz (1984).

Long-range weather forecasting is a complex area of environmental science. However, recent improved understanding of atmospheric dynamics and better observations indicate that useful progress, rooted in scientifically sound ideas, may be possible with long-range forecasting in the tropics (Folland et al. 1991). Although day-to-day changes in atmospheric conditions cannot be predicted in detail beyond approximately two weeks, there is substantial evidence that conditions averaged over the seasonal time-scales of several weeks can be predicted in a probabilistic sense particularly in the tropics (Shukla 1981; Farmer 1988; Hastenrath 1991; Ward and Folland 1991; Smith 1994; Rowel et al. 1994). Statistical and numerical modeling methods are often used in long-range climate forecasting. Statistical forecast methods provide an estimate, based on past experience, of the atmospheric seasonal climatic anomaly that is likely to occur. Using statistical methods, the relation between regional atmospheric anomalies and pre-season global climate anomaly patterns can be studied using historical data. Where significant links are

found, current climate anomaly patterns can be used to predict future atmospheric anomalies. Some aspects of the capabilities of seasonal predictions using statistical models are summarized in Barnston et al. (1994).

Investigations to explore the prospects for seasonal climate prediction using statistical methods to the African climate variability have been encouraging. Folland et al. (1991) employed the stepwise multiple regression and the stepwise linear discriminant methods to predict the seasonal rainfall over the Sahel region. Cane et al. (1994) demonstrated remarkable skill in predicting the seasonal climate over Zimbabwe (southern Africa). The forecast system in this case consisted of two components. A simple atmosphere-ocean coupled model was used to predict the February to March sea-surface temperature (SST)-index over the Pacific Nino3 region up to 12 months in advance. Then a statistical model was used to infer the predicted February-March rainfall or the maize crop yield during the same months using the SST index time series as input data. Their results indicated that the SST index exhibited stronger connection with the maize yield, than the rainfall thus suggesting that it is important to go beyond the use of meteorological data in the development of regression models by including other parameters closer to the food supply. Farmer (1988) undertook a study to develop a prediction scheme for the short-rains over the Kenyan Coast. His results showed the existence of simultaneous and lagged relationships between seasonal rainfall and the Southern Oscillation Index (SOI), which could be used to produce skillful seasonal forecasts for the Kenyan Coast.

Numerical models are computer simulations of the earth's circulation system(s). The success of numerical modeling depends on the quality of the initial and boundary data and the assimilation system, the representation of processes that occur below the level of the discretization, and the accuracy of discrete approximations to the continuous equations. General Circulation numerical Models (GCMs) are used to simulate the evolution of the atmosphere through time from some initial state. The attractiveness of GCMs for climate studies is their ability to model the evolution of the atmosphere in response to external forcing mechanisms - for example, a doubling of carbon dioxide, increase in soil moisture, and increase in SST. These numerical models have been employed in climate studies over parts of Africa with encouraging results (Folland et al. 1991; Rowell et al. 1994; Ward et al. 1993; Mason et al. 1994; Rocha and Simmonds 1997; Landman and Mason 1999).

GCMs have however difficulties with the regional climate, which is influenced by local factors such as, steep orography that may not be represented by the relative coarse resolution. The possible solution to this model deficiency is to combine a GCM with a high-resolution limited-area regional climate model. In case of regional climate models, the initial conditions become less important though still relevant, and the simulated climate is largely determined by the internal dynamics of the region of interest. The regional climate modeling approach is however dependent on lateral boundary forcing, which is either supplied by the GCMs or observational data. The GCM/regional climate model nesting approach has been implemented in short-range weather and climate forecasts (Giorgi and Bates 1989; Giorgi et al. 1993ab; Kida et al. 1991; Giorgi and Marinucci 1991; Liu et al.

1994; Sun, Semazzi, Ogallo and Giorgi 1999ab, hereafter SSOG99). The one way nesting technique that has been used in many previous studies consists of using the output of GCM global climate simulations to provide driving initial and time-dependent lateral boundary conditions for high-resolution regional climate model simulations over areas of interest. With this methodology the regional climatic effects of the sub-GCM grid-scale forcings, for example, due to complex topographical features, coastlines, and large lakes, are represented in a physically based way (Giorgi and Mearns 1991). SSOG99 demonstrated how a high-resolution GCM/regional scale nested model could be used to resolve the detailed regional features associated with the East African climate variability. Using the observed SSTs and the European Centre for Medium Range Weather Forecasting (ECMWF) re-analysis data, they showed the ability of the NCAR Regional Climate Model version 2 (RegCM2) in realistically simulating the intra-seasonal and interannual climate variability over eastern Africa. Such information obtained from this downscaling technique is much more valuable for policy makers than the simple area-average climate advisories based on contemporary GCMs.



Figure 1.1: Physical features of the equatorial eastern Africa.

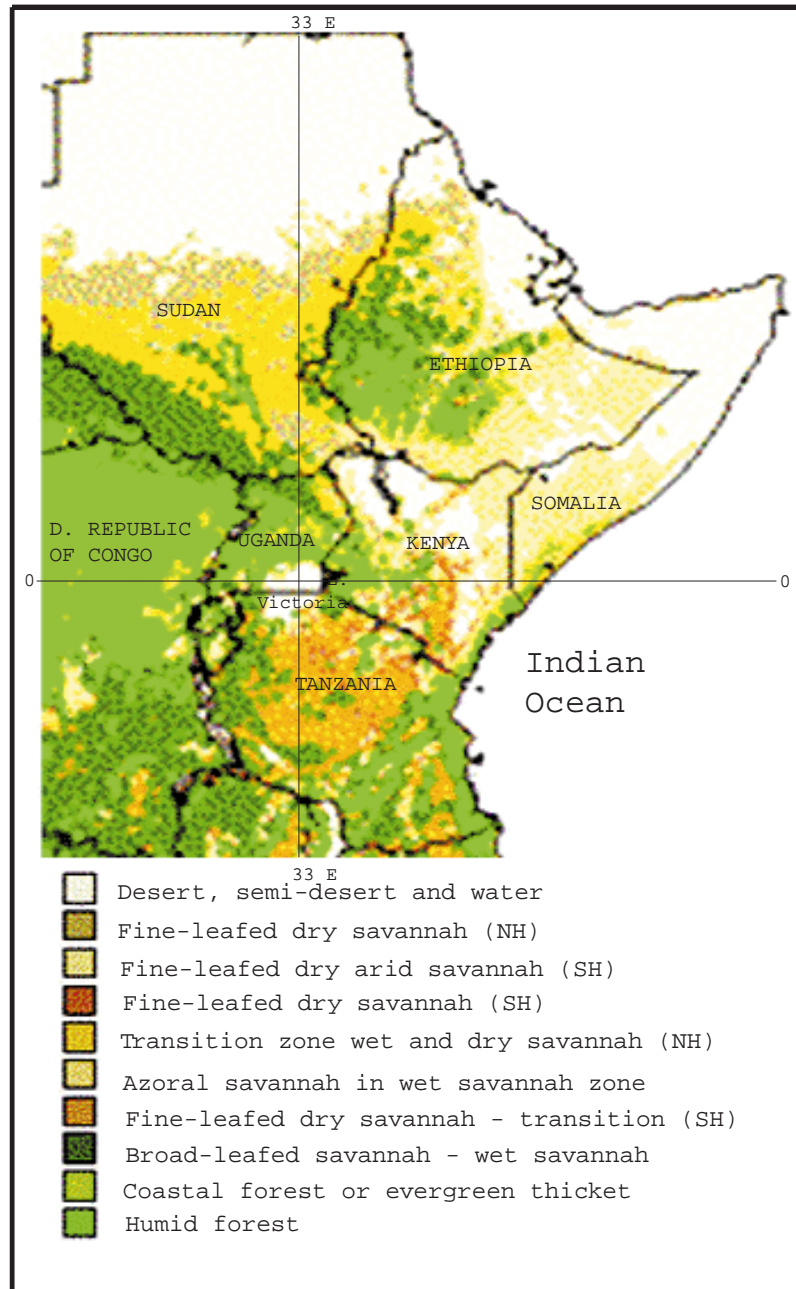


Figure 1.2: Vegetation map of the equatorial eastern African region derived from the AVHRR-global area coverage (GAC) data set (extracted from: Laporte et al. 1998).

### **1.1 *Physical Features of Equatorial Eastern Africa***

The geographical area of equatorial eastern Africa covers five countries (Kenya, Uganda and Tanzania, Rwanda, Burundi and the neighboring Ethiopia, Sudan, Somalia, Djibouti and Eiretria), the countries that form the Great Horn of Africa (GHA) sub-region. Latitudes - 10°N to 12°S and longitudes 26°E to 45°E (Figure 1.1) enclose this region. The region has complex topographical features, which include the Ethiopian highlands to the northeast and East African highlands to the southwest that include high mountains; Kenya (5199 m), Kilimanjaro (5895 m), Elgon (4321 m), Aberdare Ranges (3999 m) and the Mau escarpment (3098 m). Some of these mountains like Kenya and Kilimanjaro have permanent glaciers at their top throughout the year which makes them very special as potential indicators of regional and/or large-scale together with long-term climate fluctuations. The complex mountains are also the source watersheds for some of the major rivers of the region (Krishnamurti and Ogallo 1989). They therefore form an integral component of the regional hydrological cycle.

The other unique physical characteristics of the region include the water masses of Lake Victoria and Indian Ocean, the Western and Eastern Highlands, which decline, to a plain towards the Indian Ocean. In between these highlands lie the Great Rift Valley that is oriented north/south across central Kenya and Tanzania. This configuration generates land/sea and land/lake breezes, as a result of the water and land temperature contrasts, due to differential solar heating and radiative cooling. Lake Victoria, for instance, has a strong circulation of its own with a semi-permanent trough, which migrates from land to lake and

lake to land during the night and day respectively. The lake has an areal extent of about 60, 000 km<sup>2</sup> (Indeje 1994; Mukabana and Pielke 1996; Indeje and Anyamba 1998). Lake Victoria is also the source of river Nile (the longest rivers in the world). The major climates of equatorial eastern Africa ranges from cold polar type on top of some of the high mountains like the Kilimanjaro and Kenya, humid equatorial and tropical climate, savannah grasslands, hot dry semi-desert among many others (Figure 1.2). The savannah climate that has one distinct dry/wet season is the home of most of the African wildlife and livestock. Tourism and wide range of agricultural activities are extensive in this region. Most of the locations with equatorial climate are concentrated largely near the large water bodies and over the highlands. The semi-desert region covers the northeast and east. A relatively moist zone covers the coastal belt of the Indian Ocean. Agriculture and utilisation of forest resources are the major socio-economic activities in this region. Soil erosion arising from such activities is however a major environmental problems in many of these areas. The mean climate over eastern Africa is discussed in the next subsection.

## **1.2      *Climatology of Equatorial Eastern Africa***

The climate of equatorial eastern Africa has strong annual and seasonal cycle components, with precipitation being the parameter with highest space-time variability. Figure 1.3 shows long-term mean annual rainfall over region based on 1961-90 climatology.

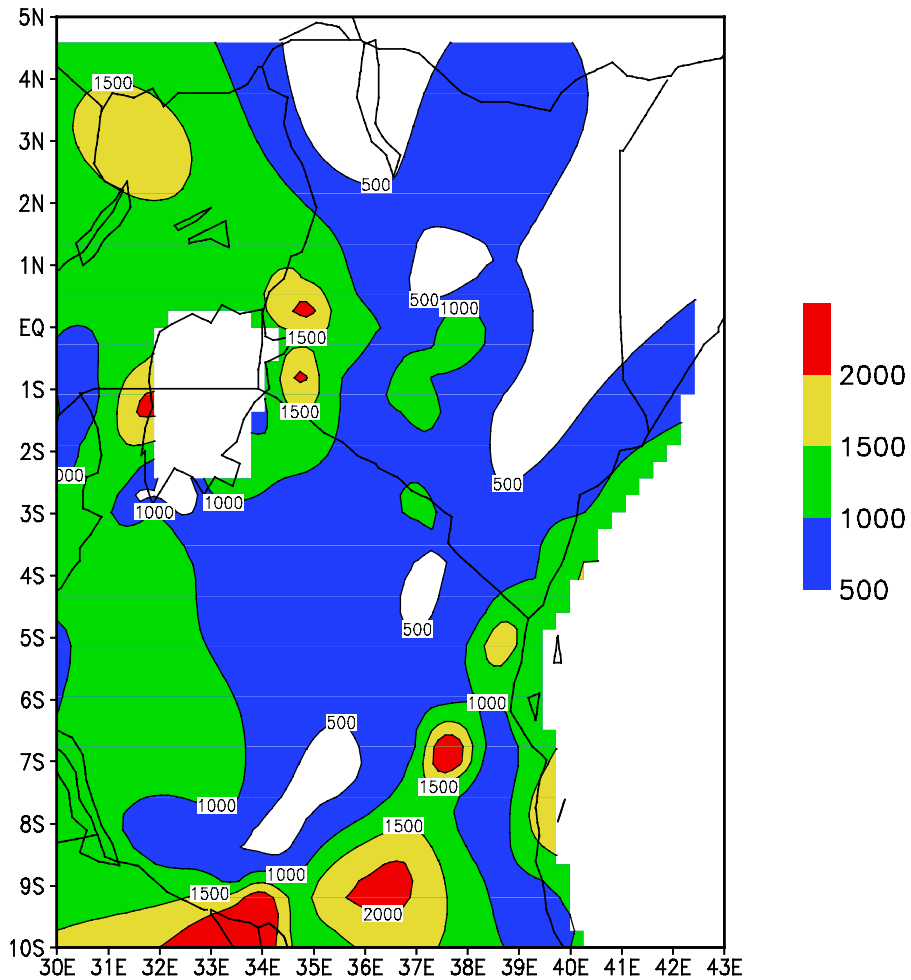


Figure 1.3: Long-term mean annual climatological rainfall over equatorial eastern Africa (1961-1990). Units are mm.

On average more than 800 mm of annual rainfall are observed over areas bordering Lake Victoria to the west, and the Indian Ocean to the east. The highlands of central Kenya and southern Tanzania, much of Uganda and western Tanzania also receive rainfall of more than 800 mm, with the northern and eastern parts of Kenya and, east and central Tanzania, which are semi-arid, receiving less.

Four rainfall seasons are experienced over the region; January-February (JF), 'long rains' of March-May (MAM), June-September (JJAS) and, 'short rains' of October-December (OND). Figure 1.4 displays the spatial patterns of the mean seasonal rainfall over East Africa based on the four rainfall seasons. These rainfall patterns are controlled by the seasonal migration of the Inter-Tropical Convergence Zone (ITCZ). The ITCZ forms a quasi-continuous belt of unsettled, often rainy weather around the tropics, sandwiched between generally fine weather to the north and south of the subtropical highs (Folland et al. 1991). It is associated with the convergence of air-streams from the subtropical highs. Where these flows meet, strong upward motion occurs that causes rainfall if the air contains sufficient moisture. It is therefore a region of large-scale convergence of the interhemispheric tropical monsoonal wind systems that generally move meridionally with the overhead sun. Figure 1.5 shows the mean position of the ITCZ for January and July/August respectively over the African continent. The other climatic factors known to influence precipitation over region are complex including tropical storms, easterly waves, jet streams, the continental low level trough, extra-tropical weather systems (Ogallo 1989); interactions between mesoscale flows and the large-scale monsoonal flows (Mukabana and Pielke 1996), teleconnections with global-scale climatic anomalies like those associated with SST, the Quasi-biennial Oscillation in the equatorial lower stratospheric zonal wind (QBO), solar and lunar forcing (Ogallo 1988; Indeje and Semazzi 2000), and inter-seasonal 30-60 day Madden-Julian wave (Anyamba 1992).

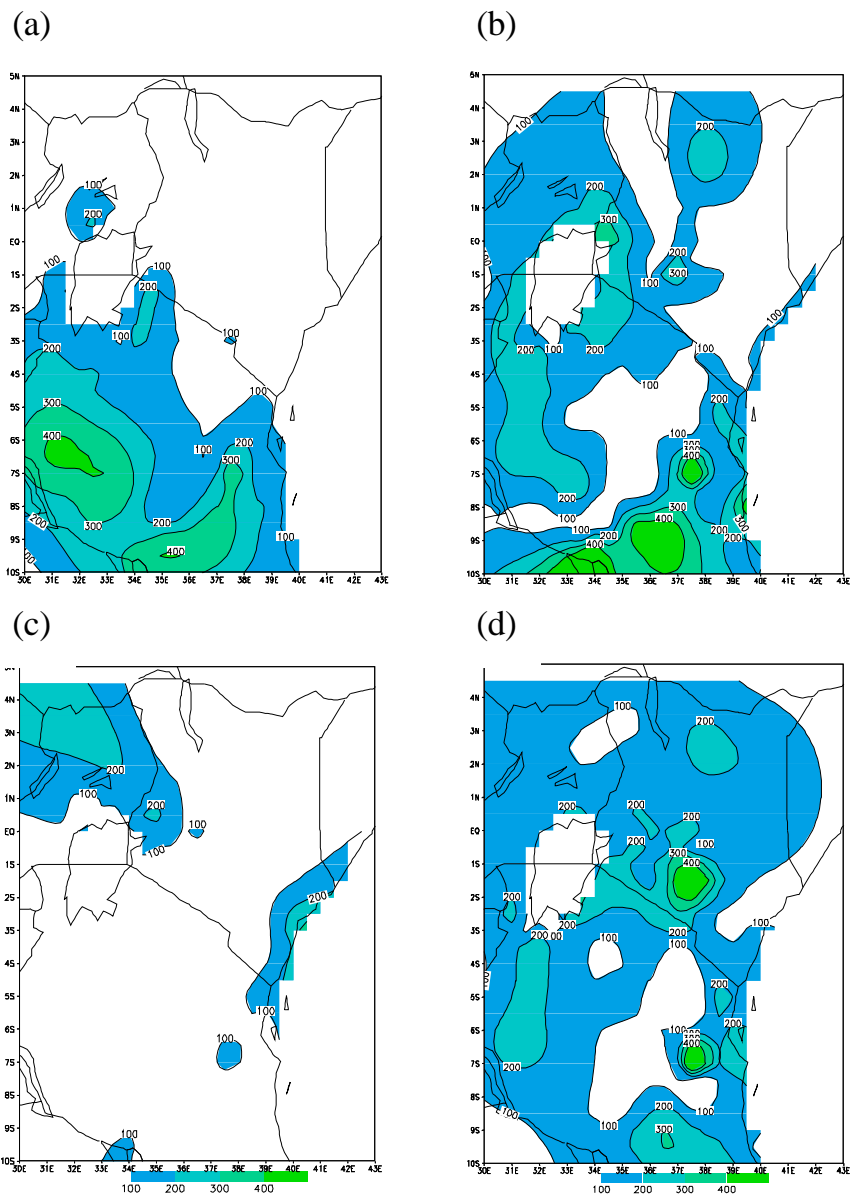


Figure 1.4: The spatial patterns of the mean seasonal rainfall (mm) over East Africa for (a) January-February, (b) March-May, (c) June-September, and (d) October-December. Contour interval is 100 mm.

In the JF season (Figure 1.4a), the rainfall is concentrated over the lake regions and most parts of Tanzania. This seasonal rainfall is associated with the extreme southward location of the ITCZ and partly with moisture influx from the Indian Ocean. About 42 per cent of the total regional annual rainfall is observed during MAM rainfall season, with the highest intensity observed near the water bodies of the Indian Ocean, Lake Victoria and the East African highlands. During this season only weak correlation has been found between rainfall time series at different stations (Ogallo 1980, 1983; Nyenzi 1992; Beltrando 1990) because of the large spatial rainfall variability. The high rainfall variability suggests dominance of local factors rather than large-scale factors in the modulation of rainfall patterns during this season. The JJAS rainfall season which accounts for about 15 per cent of the total regional annual rainfall is confined to the western highlands of Kenya, the coastal areas and most parts of Uganda. The OND rainfall season contributes about 25 per cent of the total regional annual rainfall and is well distributed in the whole of East African region. Earlier researchers (Ogallo 1983; Nyenzi 1992; Beltrando 1990; Nicholson 1996) have found significant station to station correlation and seasonal rainfall to annual rainfall correlations during this season. The dominance of large-scale weather systems may be responsible for the spatial homogeneity of rainfall during this season. The evidence for substantial influences of some large-scale global forcing factors on the East African climate is discussed in the next subsection.

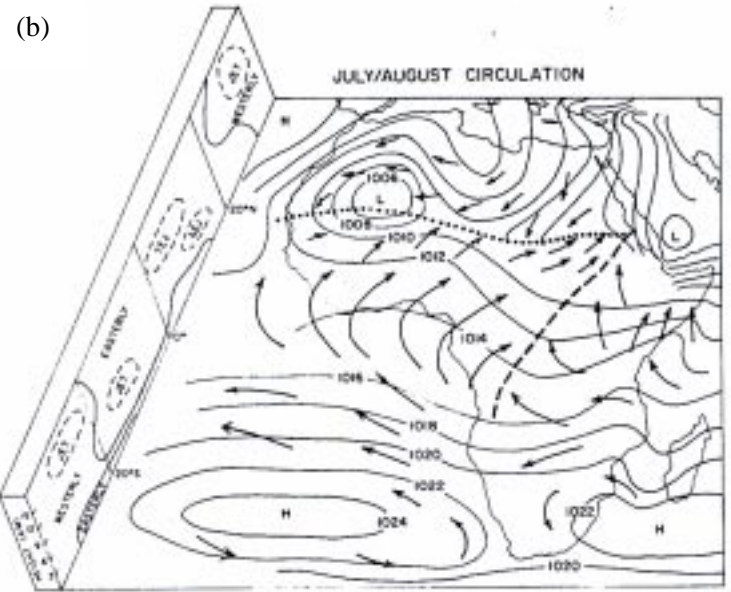
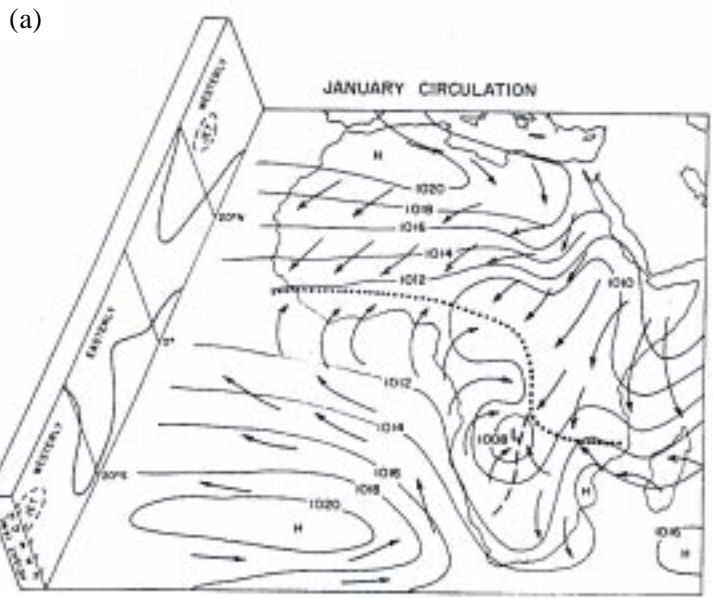


Figure 1.5: Mean position of the ITCZ over Africa for (a) January, and (b) July/August (Nicholson 1986). Dotted and dashed lines show the location of the ITCZ.

### **1.2.1 Forcing Mechanism on Climate Variability**

Several mechanisms have been advanced as being responsible for climate variability over equatorial eastern Africa, some of which are briefly reviewed below.

#### ***1.2.1.1 Forcing due to Local Land Surface Characteristics***

The land surface characteristics that include the surface roughness, albedo, moisture availability, among others control the land-atmosphere interactions, two components, which form part of the global climate dynamics. These surface conditions play a major role in the turbulence transfer of mass, momentum and heat in the Planetary Boundary Layer (PBL). This layer provides a vital physical link between the atmosphere and the surface of the earth for the exchanges of heat, moisture and momentum fluxes. Hence, the primary source of energy for driving the atmospheric circulations is at the surface of the earth. A realistic estimate of these fluxes is central to the satisfactory performance of numerical weather and climate models (Sud and Smith 1984; Huang and Raman 1991; Alapaty et al. 1996).

A number of studies have been undertaken to investigate the impacts of tropical deforestation on climate (e.g., Henderson-sellers and Gornitz 1984, Shukla et al. 1990; Mylne and Bowntree 1992; and Zhang et al. 1996a,b). SSOG99a showed that the removal of the Congo rainforest modified the local climate, namely, hydrological processes, surface energy budget, and the dynamic structure of the troposphere significantly. Changes in the surface energy budget following deforestation includes significant reduction in net solar radiation absorbed by the surface and latent heat flux, reduction in evapotranspiration and

hence reduction in total precipitation. The strong convective processes over the Congo Basin play a critical role in sustaining the meridional (Hadley) and the zonal (Walker) circulations. The strong upward motion associated with these circulations, induce strong water vapor convergence, which control the climate over eastern Africa (Semazzi and Indeje 1999; SSOG99). There is however, no sufficiently strong evidence to show whether changes in land surface conditions over equatorial eastern Africa and the surrounding Congo forest have been significant to affect the climate variability/change over the region. However, the existing land surface characteristics have to be specified accurately as the lower boundary conditions in the regional climate models applied over, since the model results are sensitive to these specifications (Giorgi et al. 1993a; SSOG99a).

Orography is one of the lower boundary factors that control the global climate dynamics. Whereas, the land/sea thermal contrast affects climate through thermal forcing, the effect of large-scale orography is mainly dynamical in nature (Kasahara 1966). Its main effect on the mean flow is through form drag that is associated with differences in tangential pressure across a mountain. Orographic forcing on regional weather and climate has been the subject of several major investigations ever since the pioneering work by Kasahara (1966). In chapter 4, we review the literature on orographic forcing on regional climate and discuss our findings on the investigation of the role of orography on the eastern African climate.

### *1.2.1.2 Radiative forcing and climate sensitivity*

The earth's energy balance requires that the influx of incoming energy from the sun, most of which is in visible part of the spectrum, must be balanced by an equal outgoing influx of infrared radiation. Any deviation on either side of the balance derives the earth's climate to a warmer or cooler equilibrium state so that the energy balance is again balanced. The sun's output of energy varies by small amounts over the 11-year cycle associated with the sunspots. A change in the solar energy reaching the earth is the main external forcing mechanism on climate. In the troposphere, dynamics driven by the direct solar surface warming and the hydrological cycle actively mix the air on timescales shorter than that of energy transport by radiative processes. Climate forcing may also be viewed as a change imposed on the planetary energy balance that has the potential to alter global temperature, while climate response is the meteorological result of these forcing, such as global temperature change, rainfall changes, sea level changes.

Green house gases (GHGs) intercept some of the outgoing radiation and thereby act to force the earth's surface to come to a higher equilibrium temperature. In contrast, aerosol particles influences the energy balance through scattering, reflection of the incoming solar radiation back to space thereby reducing the amount of energy reaching the ground and consequently cooling the earth. Over industrialized parts of the world, sulfate particles comprise much of the light scattering aerosols. Likewise, in the tropics, biomass burning of forests and savannas is a dominant source of airborne particles, which consists mainly of organic matter and soot. Mineral dust from wind acting on soils is always present in the

atmosphere to some degree, although human activities, such as disruption of soils by changing use of land in arid and sub-arid regions, can increase the loading of dust in the atmosphere. Mineral dust may act in two ways to the climate forcing; as a scattering and cooling effect in the visible part of the spectrum and in the infrared region, mineral dust acts as an absorber and hence has similar effects as a greenhouse gas.

The global-average cancellation between the GHGs warming and aerosol cooling may be misleading when considering the nature and climatic effects of the two opposite forcings. GHGs are virtually uniform globally; aerosol concentrations are highly variable in space and time. With lifetimes of about a week, sulfate aerosols are most abundant close to their sources. Biomass aerosols are emitted predominantly during the dry seasons in the tropical areas. Mineral dust appears downwind of large arid regions. Moreover, GHGs forcing operates day and night; aerosols forcing operate only during daytime. When superimposed to each other, the spatial distribution of GHGs warming and aerosol cooling are so uneven that, even if the global-average forcings are of equal and opposite sign, the pattern of climate change predicted by GCMs differs markedly when aerosol forcing is added GHGs forcing (IPCC 1995). When aerosol forcing is added to GHGs, patterns of near-surface temperature change become generally consistent with those observed.

The direct cooling effect of sulfate aerosol produced by industrial activity has recently been recognized and is estimated to have a negative global average radiative forcing in the range of  $-0.3$  to  $-0.9 \text{ W m}^{-2}$  (Kiehl and Briegleb 1993; IPCC 1995). Aerosol produced by

tropical biomass burning could lead to negative global average radiative forcing between -0.05 and  $-0.6 \text{ W m}^{-2}$ . Indirect effects of aerosol on tropospheric clouds could further enhance this negative forcing, but are highly uncertain (IPCC 1995). In localized areas the negative radiative forcing due to aerosols has the potential to offset the positive forcing of the primary greenhouse gases (Kiehl and Briegleb 1993). Increase in tropospheric ozone leads to a positive radiative forcing which is mainly regional in nature. The regional patterns in radiative forcing from ozone and aerosols are to warming. The ozone in the upper troposphere over several tropical sites close to the source of the burning region reveals a small seasonal variation, while that in the middle and lower troposphere varies in a manner consistent with the known seasonality of the burning (IPCC 1995). The decreased seasonal cycle in the upper troposphere argues against its stratospheric origin. Studies have shown that radiative forcing of tropospheric ozone is strongly dependent upon its vertical distribution (Lacis et al. 1990). Portman and Solomon (1997) indicated a widespread radiative forcing of at least  $0.5$  to  $1 \text{ W m}^{-2}$  over the large areas of the tropics much of the year, which were comparable in magnitude, but opposite in sign of the aerosol forcing from tropical biomass burning.

Evidence of an emerging pattern of climate response to forcings by GHGs and sulfate aerosols has emerged. The evidence comes from the geographical, seasonal, and vertical patterns of temperature change. Taken together, these results point towards a human influence on global climate (IPCC 1995). However, uncertainties of forcing by key factors, including long-term natural variability, and fine-evolving patterns of forcing by GHGs and

aerosols limit our ability at present to quantify the human effect on climate. Most of the GCMs and regional climate numerical models are currently using sophisticated radiation packages that takes care of the complex interactions and effects of GHGs and aerosols to the energy balance. The NCAR RegCM2 and Community Climate Model version 3 (CCM3) used in this study have complex radiation package that require specification for carbon dioxide and takes care of the indirect effects of aerosols on the radiative energy balance.

### ***1.2.1.3 Global and Regional-Scale Teleconnections***

#### **1.2.1.3.1 Sea-surface Temperature and El Niño-Southern Oscillation**

Although the land surface processes could be playing an important role in modifying the climate conditions globally and regionally, a large body of results based on numerical and statistical modeling have firmly established that SST anomaly forcing, is the major climate forcing because of its high memory. The climate predictability in the tropics is largely due to this slow evolving nature of SST and the land surface conditions. It has been postulated that air-sea interaction over the Indian Ocean influences the monsoon rainfall over India and eastern Africa (Saha 1974; Shukla 1974; Shukla and Misra 1977; Nicholson and Entekhabi 1986; Ogallo et al. 1988; Raverdin et al. 1986; Ininda, 1998). Recent papers by Webster et al. (1999) and Saji et al. (1999) have furnished evidence of some large-scale interactions between the Indian Ocean and the overlying atmosphere and indications of climatic consequences. They indicate unusual events in the tropical Indian Ocean that clearly point to the existence of a major ‘mode’ of interaction between the ocean and the

atmosphere lasting many months. They pointed out that the anomalies in the SST that developed in the Indian Ocean (cold in the east and warm in the west) during the second half of 1997, constitutes the Indian Ocean dipole (Anderson 1999). They also related this Indian Ocean temperature distribution to increase/decrease in rainfall over East Africa/Indonesia respectively. They argued that the Kelvin waves (equatorial eastward propagating at about 3 m/s) and the Rossby waves (off-equatorial westward slowly propagating) that take a few months to travel around the Indian Ocean, were associated with the intensification, duration and demise of the temperature anomaly in the spring of 1998. Similar large amplitudes of the dipole over the Indian Ocean occurred in the years 1961, 1967, 1972, and 1994. Webster et al. further indicate that there is little statistical relationship between Indian Ocean dipole and El Niño, as the dipole has been observed to occur in both El Niño and non El Niño years. The Indian Ocean dipole exhibits a biennial character, which may imply certain predictability from one year to the next. The relationship between the dipole and the Indian monsoon was found to be very weak, but of the two biggest dipole events, that of 1961 was associated with the heaviest monsoon in 150 years, whereas in 1997 rainfall over India was normal.

The advancement made in monitoring and analyzing in near real time of the global SST Sea level anomalies provides useful index that reflect the combined effects of barometric and wind forcing on the seasonal time-scale especially that associated with El Niño/Southern Oscillation (ENSO) events (Smith 1994). ENSO is the dominant air-sea interaction phenomenon in the tropical ocean system at the interannual time scale that is

known to be important to tropical and extra-tropical climatic variations (Barnett 1981; Ropelewski and Halpert 1987, 1989; Kiladis and Diaz 1989; Fraedrich and Muller 1992; Hutchinson 1992; Barnston and Smith 1996). The internal dynamics of the coupled ocean-atmosphere system is what determine the onset and termination of El Niño events. The physical processes are complicated they involve unstable air-sea interaction and planetary scale equatorial long eastward propagating Kelvin and short westward propagating Rossby ocean waves. The great width of the Pacific Ocean favors the formation of ENSO events in that ocean as compared to the Atlantic and Indian Oceans. The narrower width of the Atlantic and Indian Oceans means the waves can cross those basins in less time, so that ocean adjusts more quickly to wind variations. Conversely, wind variations in the Pacific Ocean excites waves that take a long time to cross the basin, so that the Pacific Ocean adjusts to wind variations more slowly. This slower adjustment time allows the ocean-atmosphere system to drift further from equilibrium than in the narrower Atlantic or Indian Ocean. Also, in the narrower Atlantic and Indian Oceans, bordering landmasses influence seasonal climate more significantly than in the broader Pacific. The Indian Ocean in particular is governed by monsoon variations, under the strong influence of the Asian landmass. Heating of the land in the summer and cooling of the land in the winter sets up land-sea temperature contrasts that affect the atmospheric circulation over the neighboring ocean. This land influence competes with ocean and atmosphere interactions, which are essential for generating ENSO.

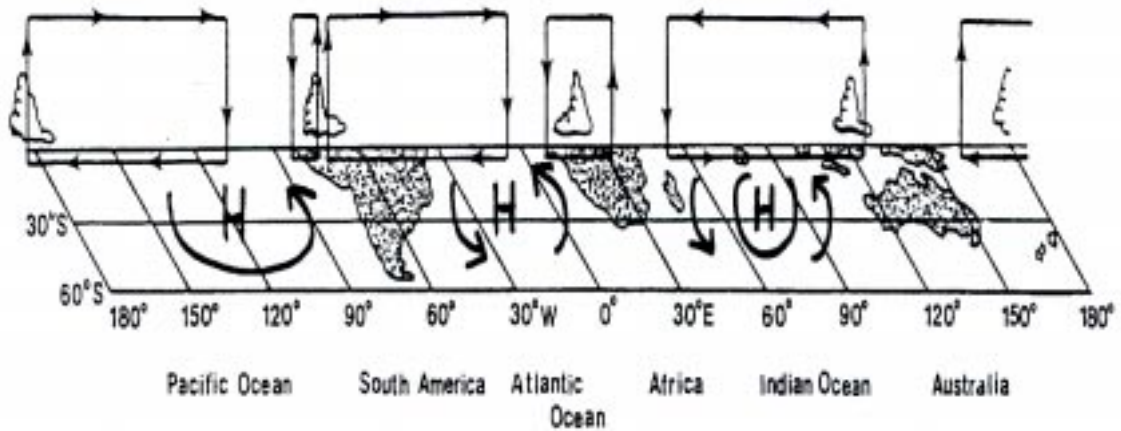


Figure 1.6: The east-west Walker global circulation.

Based on ocean wave solution, only long-waves can be unstable leading to ENSO. Thus, only Pacific Ocean is long enough to have long waves that can be unstable leading to ENSO phenomenon. The time it takes these waves to cross the Pacific Ocean is one of the factors that sets the time scale and amplitude of ENSO climate anomaly (also referred to as the delayed oscillator). The periodic oscillations between warm (El Niño) to neutral (or cold) condition ranges from seasonal to about eight years (Rasmusson and Carpenter 1983; Halpert and Ropelewski 1992). The eastward displacement of the atmospheric heat source overlaying the warmest water associated with ENSO results in large changes in the global atmospheric circulation, which in turn force changes in weather in regions far removed from the tropical Pacific through the Walker and Hadley circulations of the global teleconnections (Figure 1.6). Details of the various teleconnections that have been observed with the African climate can be obtained from Ogallo et al. (1988); Druyan and Koster (1989); Ropelewski and Halpert (1987, 1989); Nicholson (1996); Indeje et al. (2000) among others.

Some of the global impacts associated with ENSO are increased rainfall across the southern tier of the US and in Peru causing destructive flooding, and drought in the west Pacific, sometimes associated with devastating bush fires in Australia and the maritime continent of Indonesia. The 1982/83 ENSO, the strongest recorded event before the most recent 1997/98 event, was responsible for widespread incidence of drought, flooding and severe storms around the World, resulting in several hundred deaths and damages. Losses incurred over eastern and southern Africa during the 1982/83 ENSO was estimated at well over US \$ 3 billion dollars (about one-third of the total global estimate). The losses associated with the 1997/98 ENSO (see Figure 1.7) surpassed that of 1982/83 and 1991/92 and inflicted debilitating disruption of the social economic structures in many countries around the world including equatorial eastern Africa.

Ropelewski and Halpert (1987) showed an ENSO/rainfall dipole pattern over eastern and southern Africa (Figure 1.8). Wetter than normal conditions were indicated over eastern Africa and drier conditions over southern Africa during ENSO years. Chu (1995) observed that, at the height of warm ENSO episodes, warm pools of seawater and attendant convection shift eastward to the equatorial central Pacific, leading to stronger subsidence on the sinking branch of the local Hadley cell in the subtropical regions.

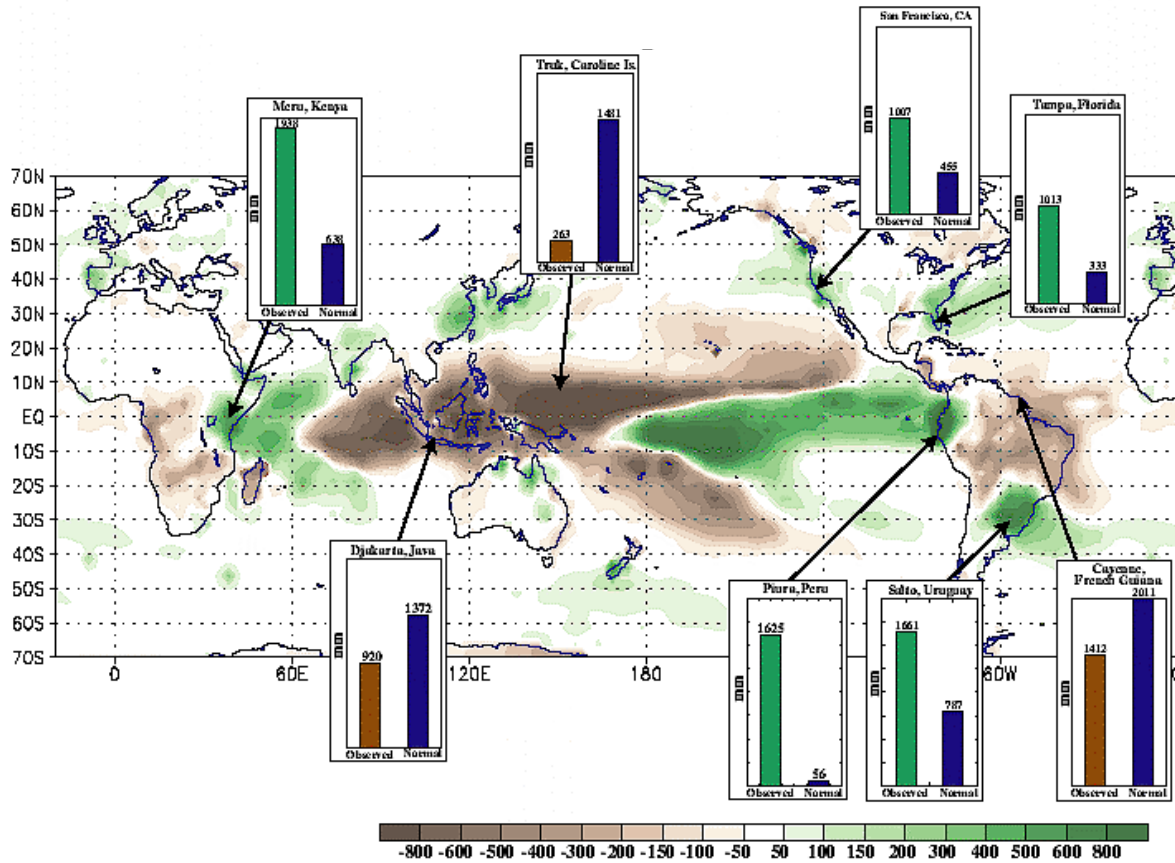


Figure 1.7: ENSO global precipitation deviations from average for November 1997 - April 1998 (Source: CPC/NCEP/NWS).

The simultaneous shift in the convection over the African continent associated with the Walker and Hadley circulations may partly explain the observed wet (dry) conditions over the eastern (southern) Africa respectively during the warm ENSO events. Although, eastern Africa exhibits very pronounced coupling with SST (Cadet and Diehl 1985; Ropelewski and Halpert 1987, 1989; Ogallo et al. 1988; Nyenzi 1992; Semazzi and Indeje 1999), there has been much less research effort to exploit these relationships for the purpose of improving seasonal climate forecasting over the region. In chapter 2, we

discuss our findings on the ENSO/rainfall evolution climate anomaly patterns over equatorial eastern Africa and the prediction potential for seasonal climate using information of the ENSO cycles.

**WARM EPISODE RELATIONSHIPS DECEMBER - FEBRUARY**

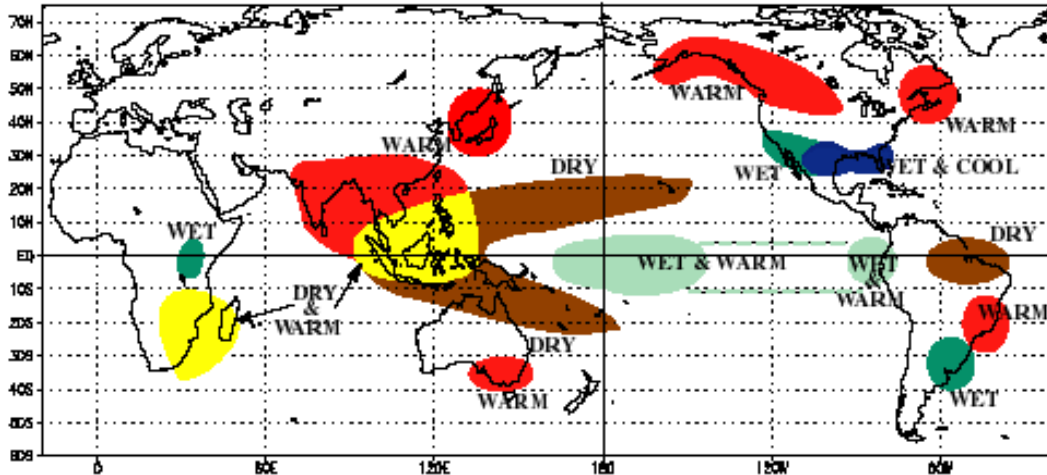


Figure 1.8: ENSO related global impacts (Source: CPC/NCEP/NWS).

**1.2.1.4 Quasi-biennial Oscillation in the Equatorial Zonal Wind**

Another interannual signal of interest on the tropical climate is the Quasi-biennial oscillations (QBO), which involves the fluctuation between westerly and easterly wind regimes in the lower stratosphere with a period of about 28 months (Figure 1.9). Studies by Holton and Lindzen (1972), Plumb (1977) and, Holton and Tan (1980) have indicated that the stratospheric QBO is forced locally by alternating downward propagating patterns of westerly and easterly mean zonal winds which repeat with somewhat irregular period averaging about 26 months. The stratospheric QBO plays a role in modulating rainfall

over parts of Africa (Mason and Tyson 1992; Jury et al. 1994). The Walker circulation cell connecting Africa and the Indian Ocean interacts with the QBO, and during its westerly phase, rising tropospheric motion occurs over Africa (Indeje and Semazzi 2000).

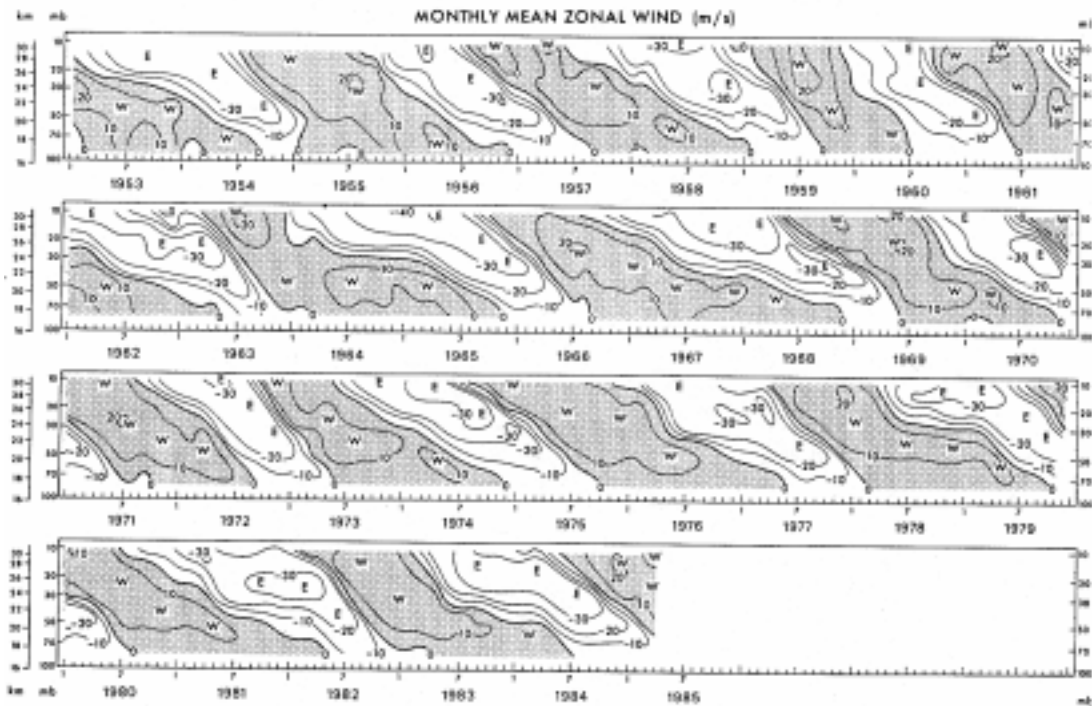


Figure 1.9: Atypical evolution of Quasi-Biennial Oscillation (QBO) phases in the lower stratospheric zonal wind.

During the QBO easterly phase, tropical cyclones are more frequent in the Indian Ocean and convection increases significantly over Madagascar (Jury et al. 1994). Increased cyclones over the western Indian Ocean drains most of the moisture from the neighboring African continent leaving the land relatively dry (Anyamba 1984; Ogallo et al. 1988; Shanko and Camberlin 1998). Shanko and Camberlin (1998) showed that years showing

the consecutive occurrence of several tropical depressions/cyclones over the southwest Indian Ocean coincided with the drought years in Ethiopia. Since the QBO is a “well behaved” regular oscillation feature of the tropical atmosphere with a 2-year cycle and because it is usually uniform over the equatorial zone, it is feasible to monitor and utilise it in improving long-range forecasting over equatorial eastern African region. However the mechanisms involved in the QBO-rainfall relationship over this region have not been fully understood. In chapter 3, we review the literature of the QBO kinematics forcing on climate and discuss our findings of the analysis of QBO/rainfall variability and the prediction potential for the long-rains over equatorial eastern Africa.

### **1.3 Objectives**

The primary objective of this investigation is to provide a better understanding of the mechanisms and physical processes responsible for the observed variability in the climate system over equatorial eastern Africa, and also explore the potential for seasonal prediction of this equatorial climate using statistical and numerical methods. The study involves the development of a seasonal climate prediction system for the region, for downscaling global climate model forecasts and therefore provides climate information at spatial scales that are more consistent with the requirements of the end-user. This thesis is organized as follows: In chapter 2, we identify aspects of rainfall variability in sub-regions of equatorial eastern Africa associated with ENSO signal to support operational activities of seasonal climate advisories for the region based on the knowledge of ENSO phases. First we perform cluster analysis on the rainfall stations network to group them into homogeneous region using both the Empirical Orthogonal Analysis (EOF) and simple correlation analysis. Then the

teleconnections between seasonal rainfall and ENSO to classify seasons and regions that are wet/dry during the El Niño onset and post El Niño years are investigated. This analysis is based on performing composite rainfall map patterns for ENSO onset and post-ENSO years to delineate regions that are wet/dry during these episodes. These analyses provide geographically detailed information about the climatic risks that should be expected when an ENSO phenomenon occurs. In chapter 3, we explore the prospects of incorporating the equatorial lower stratospheric (30-mb) zonal wind component (which for convenience, is merely referred to as QBO) as a predictor for the seasonal rainfall. We first investigate the relationships between the different phases of QBO phases and the long-rains season and also explore the predictive potential of the long rainy season using information about the phases of the QBO. Both simultaneous and lag correlation are investigated in the search for optimal predictive potential. This analysis represents an ongoing search for predictor variables, which modulate rainfall over equatorial eastern Africa with a hope of incorporating the field variables, which demonstrate sufficient cross-correlation in the region into an objective forecast following multi-variate analysis. We attempt to also explain the physical mechanisms underlying the relationships between QBO and seasonal rainfall. In chapter 4 and 5, we conduct research, based on systematic application and enhancement of a high resolution nested RegCM2 to investigate (i) the dynamics and thermodynamics of the Turkana low-level jet which is observed between the Ethiopian and East African highlands, (ii) the physical mechanisms responsible for the dry/wet climatic conditions observed over the region during the ENSO/non-ENSO years, and (iii) the predictive potential of the regional climate. RegCM2 is a modified version of NCAR's Community Regional Climate

Model (RegCM2 Giorgi et al, 1993). In chapter 6, we delineate the best SST predictor regions in the global oceans for seasonal rainfall. The SST/rainfall are subjected to the Canonical Correlation Analysis (CCA) procedure with a view to establishing (through the temporal amplitude functions) a connection between SST prior to the forecast time cutoff and rainfall in the specific parts of eastern Africa. Observed lagged relationships are then exploited to develop regression statistical prediction models for each of the homogeneous climatological zones delineated in the cluster analysis. Finally, in chapter 7, we employ the RegCM2 to investigate the role of horizontal grid spacing to the simulated regional climate. We also explore the performance RegCM2 in a predictive mode using a case study of the 1997 season. The atmospheric fields generated by the NCAR Community Climate Model version 3 (CCM3) are used to supply the lateral forcing to the RegCM2. A summary of the study is presented in chapter 8.

### **1.3.1 Previous Related Research**

The current research work is a continuation of the previous accomplishments through a collaborative effort among North Carolina State University, NCAR, Drought Monitoring Center (Nairobi, Kenya), and University of Nairobi (Kenya). This research is a follow up of the recent work in the customization of the RegCM2 to tropical eastern Africa SSOG99. SSOG99 have recently demonstrated how a high-resolution (60 x 60 km) GCM/regional scale nested model could be used to resolve the detailed regional features associated with the East African climate. In part the model validation in SSOG99 was incomplete because of lack of observation data. We have addressed some of the shortcomings in the modeling study by SSOG99, in order to answer various scientific

questions concerning the climate variability over equatorial eastern Africa. Beyond the expected improvements in the prediction of seasonal rains, we have tailored the forecast products to attend to the special geographical forecast needs to aid decision-makers in the formulation of policy for sustainable development. Thus, the seasonal rain forecasts are spatially averaged on climatological zones to assist the end users on the expected rainfall performance in each zone. We have also adopted the strategy based on the regional climate outlook forums organized by World Meteorological Organization (WMO)/Climate Information and Predictions (CLIPS), to clarify the model prediction products. Successful development of predictive capability for the equatorial eastern Africa seasonal rainfall anomalies is beneficial to planners and policy makers in making more constructive socio-economic decisions, particularly with regards to food, agricultural, and hydro-electric industries, by taking into account the detailed spatial and temporal climate variations.

## Chapter 2

### 2 ENSO SIGNALS IN EAST AFRICAN RAINFALL SEASONS

The evolutions of ENSO modes in the seasonal rainfall patterns over equatorial eastern Africa are examined in this study. The study covers the period 1961-1990. Both Rotated Empirical Orthogonal Function (EOF) and simple correlation analyses are used to delineate a network of 136 stations over the region into homogeneous rainfall regions in order to derive rainfall indices. Time series generated from the delineated regions are later used in the rainfall/ENSO analyses. Such analyses involve the development of composite rainfall map patterns for El Niño/La Niña and post-ENSO/post-La Niña (+1) years in order to investigate the associations between seasonal evolution of ENSO signals and the space-time evolution of rainfall anomalies over the region.

#### 2.1 *Background*

Several attempts have been made to study the spatial and temporal variability of rainfall in East Africa (Rodhe and Virji 1976; Ogallo 1983,1988; Barring 1988; Nyenzi 1992; Beltrando 1990; Nicholson 1996). Rodhe and Virji (1976) analyzed the trends and periodicity for annual rainfall over East Africa. Spectral analysis of the time series revealed major peaks centered on 2-2.5, 3.5 and 5.6 years. Ogallo (1980) and Ogallo et al. (1994) have shown the existence of three major peaks, centered on the QBO of 2.5-3.7 years, ENSO of 4.8-6 years and the sunspot cycle of 10-12.5 years. Nicholson and Nyenzi

(1990) and Nicholson (1996), observed a strong quasi-periodic fluctuation in the East African rainfall with a time scale of 5 to 6 years corresponding to the ENSO and SST fluctuations in the equatorial Indian and Atlantic Oceans.

Several studies have used principal component analysis techniques to examine the temporal and spatial variability of rainfall in East Africa (Atwoki 1975; Barring 1988; Ogallo 1980, 1983, 1988, 1989; Nyenzi 1992; Semazzi et al. 1996). Ogallo (1989) investigated rainfall variability using the Rotated Principal Component Analysis (RPCA) method, to characterize the seasonal rainfall over East Africa for the period 1922-1983. The results showed seasonal shifts in the patterns of the dominant RPCA modes that were similar to the seasonal migration of the rainfall patterns associated with the Inter-Tropical Convergence Zone (ITCZ). The first two eigenvectors, which generally represent the dominant wet and dry episodes, accounted for a maximum of 58 per cent of the variance. Recent Singular Value Decomposition (SVD) work by Semazzi and Indeje (1999) has identified the bipolar nature of rainfall over southern and eastern Africa. There is at least the implication of a pattern with wave-like features that travel northwards from southern Africa to eastern Africa and the migration of the ENSO-related rainfall anomalies across the entire continent of Africa during the annual cycle.

Some extreme rainfall anomalies in East Africa have been associated with ENSO (Ropelewski and Halpert 1987; Janowiak 1988; Ogallo 1988, among others). Ropelewski and Halpert (1987), in their study of the relationship between global rainfall and the

Southern Oscillation Index (SOI), concluded that, although the statistical association between rainfall over East Africa and the SOI was weak, there was a high probability of abnormally wet conditions in the region during El Niño Years. The 1997/98 ENSO event associated with catastrophic disruption of socio-economic infrastructure and loss of life in East Africa appears to give further support to this notion. Ogallo (1988) observed significant teleconnections between the SOI and seasonal rainfall over parts of East Africa, especially during the northern hemisphere autumn and summer seasons, with the strongest relationships being observed along the Kenyan coast in autumn. Janowiak (1988) showed evidence of association between rainfall anomalies during the austral summer over eastern and southeastern Africa and both the warm (El Niño) and cold (La Niña) phases of ENSO events. The high skill in predicting ENSO phases up to a year in advance (Cane et al. 1986) suggests high prospects of successful applications of ENSO forecasts to seasonal climate prediction in East Africa. ENSO explains about 50 per cent of the East African rainfall variance (Ogallo 1988), with other factors explaining the remaining variance. Sustainable development in East Africa could benefit significantly from these recent advances in the prediction of short-term climate variability.

Considerable amount of research work has been done in the East African region to explore rainfall/ENSO relationships. Relatively less attention has been directed to the investigation of the effects of ENSO on rainfall in different sub-regions of East Africa. The objective of this study is to identify for the sub-regions of East Africa aspects of rainfall variability, which are associated with ENSO. First, we perform cluster analysis on

data for the East African rainfall stations network, using both the EOF and simple correlation analysis to identify homogeneous regions of climate variability. Then we investigate the teleconnections between East African seasonal rainfall and ENSO to find seasons and regions that are wet/dry during the El Niño/La Niña onset and post-ENSO (+1) years. The analysis is based on performing composite rainfall map patterns corresponding to the timing of the ENSO onset and post-ENSO (+1) years to delineate regions that are wet/dry during these episodes, thus providing geographically detailed information on the climatic risks to be expected when ENSO phenomena occur.

## **2.2 Data Description and Methodology**

The data used in this study consisted of rainfall records for 136 stations scattered over East Africa (Figure 2.1). Figure 2.2 shows the delineated homogeneous rainfall regions over East Africa described in section 2.2.2. The initial data consisted of monthly rainfall totals for the period 1961-90. The rainfall monthly anomalies were computed by subtracting the monthly climatological means based on the 1961-90 climatology from the values, and normalized by dividing each record by the corresponding monthly standard deviation. The rainfall data were initially subjected to statistical quality control. Using both the Empirical Orthogonal Functional (EOF) analysis method and simple correlation analysis, the 136 rainfall stations were grouped into homogeneous regions. EOF and simple correlation analyses were further used to identify stations most representative of each region.

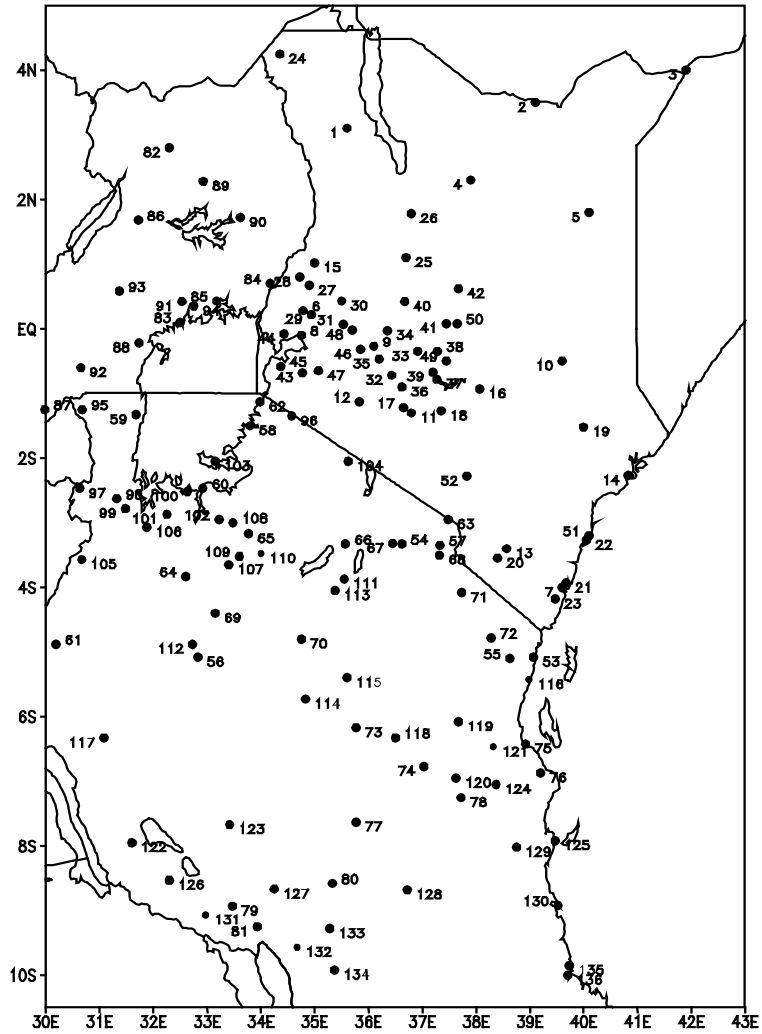


Figure 2.1: Network of rainfall stations.

These were then averaged to give a rainfall index representative of each of the delineated regions. Linkages between the observed rainfall anomalies in East Africa and different phases of ENSO were investigated, and seasonal rainfall patterns associated with the various ENSO evolution cycles identified. Analysis of the composite map patterns for

monthly and seasonal rainfall for both El Niño/La Niña onset and post-El Niño/post-La Niña (+1) years were based on the delineated homogeneous rainfall regions. Composite rainfall map patterns for El Niño/La Niña onset and post-El Niño/post-La Niña (+1) years were generated to delineate regions within East Africa that are wet/dry during these episodes. The November-December-January Niño3 Central Pacific Ocean SST anomaly index was employed to identify the years coinciding/following warm ENSO events during the period 1961-90. Further analyses were carried out to determine possible shifts in the rainfall seasons in each of the homogeneous rainfall sub-regions of East Africa.

### **2.2.1 Empirical Orthogonal Function (EOF) Analysis**

EOF analysis is the most efficient way of compressing geophysical data both in space and time, as well as separating noise from meaningful data. It enables fields of highly correlated data to be represented adequately by a small number of orthogonal functions and the corresponding orthogonal time coefficients, which account for much of the variance in their spatial and temporal variability. EOF techniques are used to extract from a covariance matrix, robust structures that explain the largest variance of the original matrix and at the same time are uncorrelated. The original data is split into orthogonal spatial patterns (eigenvectors) and corresponding time series coefficients (principal components). An eigenvector pattern that accounts for a large fraction of the variance (eigenvalues) is considered to be physically meaningful. Kutzbach (1967), and Storch and Zwiers (1999) have provided a lucid outline of the mathematical procedure necessary to define the functions and their time coefficients.

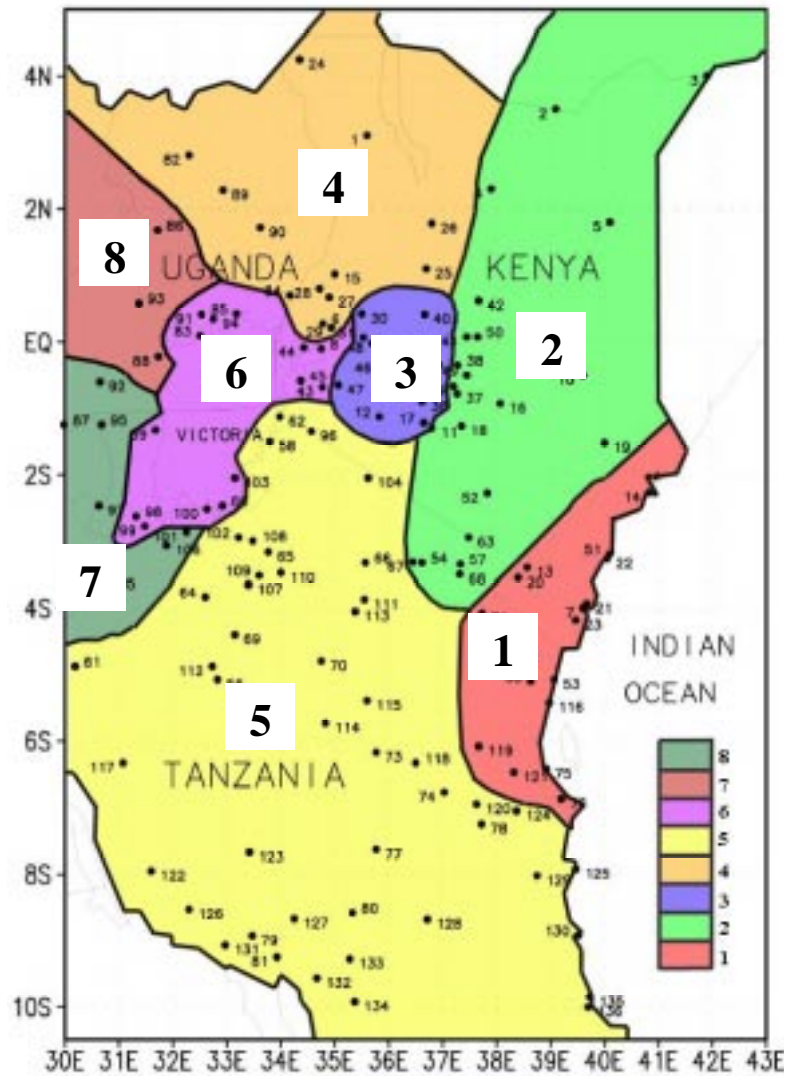


Figure 2.2: The eight homogeneous climatic zones over East Africa obtained from combined EOF and simple correlation analyses using the annual rainfall series.

In this study, the EOF method was applied on seasonal rainfall anomaly using the mathematical formulation described in Peixoto and Oort (1992). The following steps are followed in this procedure:

(a) Define a geophysical fluid matrix,  $F_{M \times N}$  whose elements ( $f_{mn}$ ) are standardized values, where  $m=1,2,\dots,M$ , (stations) and  $n=1,2,\dots,N$ , (time i.e. months, years, seasons etc.).

(b) Compute the covariance matrix  $R_{M \times M}$ ,

$$R = \frac{1}{N} FF^T. \quad 2.1$$

(c) Determine the eigenvectors  $E=[e_1, e_2, \dots, e_M]$  and the eigenvalues  $l=[l_1, l_2, \dots, l_M]$  from the characteristic equation of  $R$ , where

$$(R - \lambda I) = 0, \quad 2.2$$

and  $I$  is a unit matrix.

(d) Compute the principal component time series,  $C$  such that its elements  $C_{MN}$  are the projection of  $f_N$  on  $e_M$  given by

$$C = E^T F. \quad 2.3$$

There are a number of examples of applications of EOF analysis to meteorological fields (Trenberth 1974; Weare et al. 1975; Barnett and Davis 1975; Dyer 1977; Richman 1981; Semazzi et al. 1996; Storch and Zwiers 1999). Rotation of EOF has the effect of redistributing the variance within the eigenvectors and therefore removing the ambiguities while conserving the variance extracted by the selected subset of non-rotated eigenvectors. Various methods of determining the number of significant EOF modes to retain for rotation have been discussed (Anderson 1963; Overland and Preisendorfer 1982; North et al. 1982; Kraiser 1959). North et al. (1982) have suggested the use of sampling

errors in determining the number of significant eigenvectors. The sampling error test is based on comparison of sampling errors for the eigenvalues and the amount of separation from the neighboring eigenvectors. If the sampling errors in the eigenvalues are comparable to the distance from the nearby eigenvalue, then the sampling errors in the EOF will be comparable to the nearby EOF. In this study the criteria of North et al. (1982) and Kraiser (1959) were used in determining the number of dominant EOF modes to be retained and rotated.

### **2.2.2 Spatial Clustering of the Rainfall Observations Network**

Seasonal rainfall patterns over East Africa are very complex due to the existence of complex topography and large inland water bodies. Examples of seasonal rainfall variations for selected regions are shown in Figure 2.3, for Mubende (central Uganda), Mondo (southwestern Tanzania), Majimazuri (central Kenya) and Mombasa (coastal Kenya). Significant geographical variations have also been observed in ENSO signals over East Africa (Ogallo 1988), which suggest the need to adopt different empirical models for seasonal climate predictions over different parts of East Africa.

The use of normalized regionally averaged series reduces two problems inherent in the analysis of rainfall in sub-humid, tropical areas namely the highly diverse means and variabilities and the randomness of the convective process reflected in individual station totals. The problem becomes acute in sub-humid regions where a few disturbances produce most of the season's rainfall. Spatial averages are more representatives of the large-scale conditions than are data for individual stations (Nicholson 1986). Reduction of

regional data and delineation of homogeneous regions is therefore necessary for future development of empirical rainfall forecasting models for the region. Regionalization and averaging of rainfall over large but homogeneous regions have the advantages of reducing meteorological noise in the data as well as minimizing the number of variables, which describe the regional climate variability. The homogeneous rainfall regions could also be used in the verification of the numerical climate model runs over the East African region (SSOG99).

EOF analysis and simple correlation were used to delineate homogeneous climate regions in East Africa using annual and seasonal rainfall data. The method used in this analysis is a modified version of the technique employed by Ogallo (1988) and similar to the one adopted by Dyer (1977). Delineation of a homogeneous area was accomplished by identifying the stations with the largest correlation with the Principle Component (PC) time series associated with the first eigenvector of the annual rainfall anomaly. Each PC time series obtained from EOF analysis was correlated with the stations' rainfall data and areas that correlated significantly exceeding 0.6 correlation coefficient (at 5% level) were identified.

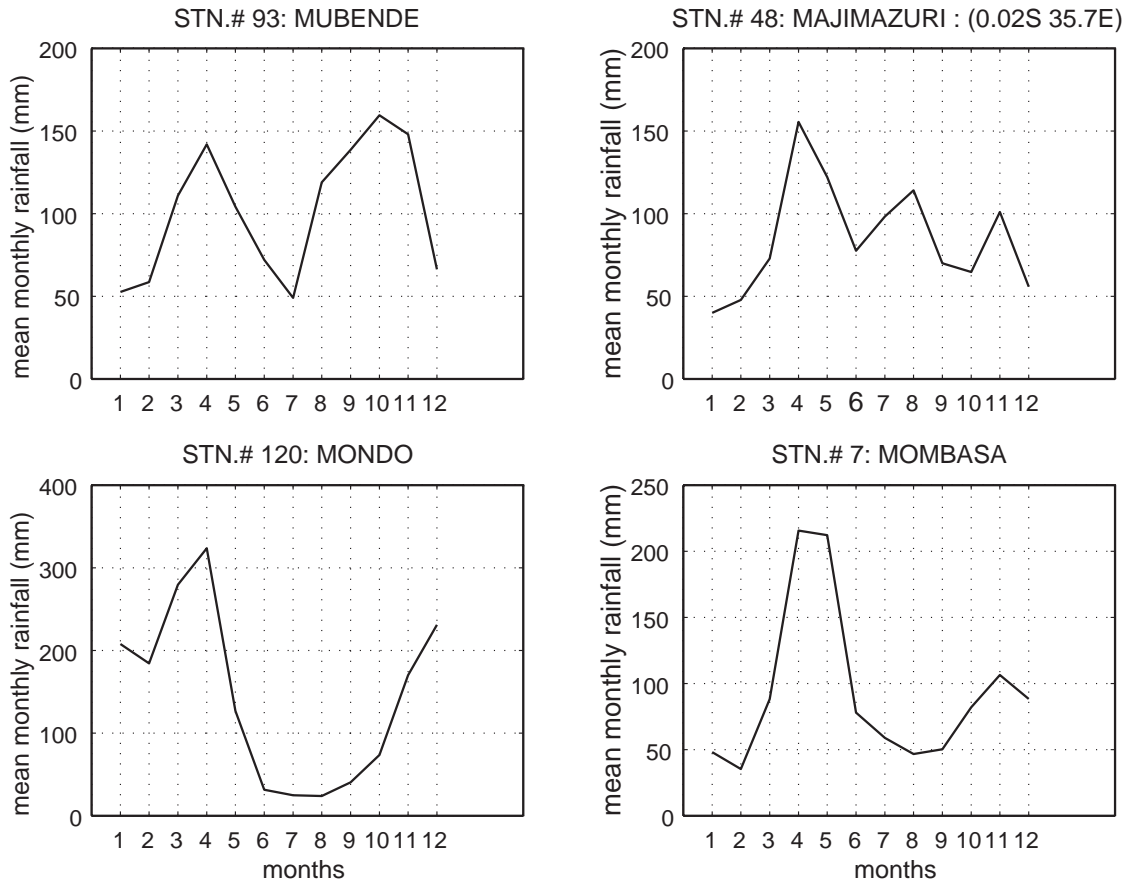


Figure 2.3: Examples of mean seasonal patterns of rainfall for some selected stations over East Africa.

These stations were retained and used to delineate the corresponding region. Stations were then annotated on the map according to the eigenvectors to which they were most strongly related. The procedure was repeated for the remaining stations until all the rainfall stations were assigned to a region. The stations retained through this process in each sub-region were re-subjected to EOF analysis and the important PC time series were correlated with the stations within that region. The stations with correlation coefficients

less than 0.6 with the dominant PC were rejected in this iterative process. This procedure was repeated until all the stations in each sub-region had a correlation of 0.6 or more with the first PC at the last iteration. The remaining stations were then averaged to obtain a regionally representative rainfall time series for use in the ENSO/rainfall analysis (section 2.3.4). This method has proved to be satisfactory with precipitation, which is a difficult weather parameter to estimate and should therefore be of value when analyzing another parameter like wind (Dyer 1977). The statistical techniques employed in this study could be extended beyond delineating homogeneous rainfall regions to identifying stations most representative of each sub-region, which may assist in identifying stations that need regular maintenance in each of the climatic region.

The results obtained from this study are discussed in the following sub-sections. In sub-sections 2.3.1 and 2.3.2, we discuss the results obtained from the EOF analysis and clustering of East African rainfall into homogeneous regions. In sub-sections 2.3.3 and 2.3.4, we present the results obtained from the composite rainfall map patterns for El Niño/La Niña onset and post-El Niño/post-La Niña (+1) years, and the ENSO modulated seasonal shifts in the regional rainfall, respectively.

## **2.3 Results**

### **2.3.1 Application of EOF Analysis on the East African Rainfall**

Based on the criteria used by North et al. (1982), a maximum of three and two EOF modes were found to be distinctly above the noise level for the MAM and OND rainfall

seasons respectively (Figure 2.4). The Monte Carlo significance test described by Overland and Preisendorfer (1982) suggested that two of the three modes are significant at the 5% level. Hence, the third mode may not be statistically significant. However, using Kaiser (1959) sampling techniques, up to nine and five EOF modes had eigenvalues greater than unity for the MAM and OND seasonal rains respectively (Table 2.1) and could hence be retained for rotation. The significant EOF rainfall modes identified by Kaiser's method explain about 70% of the total variance and are more representative of the regional seasonal rainfall than those modes identified using North et al. criteria. Up-to a maximum of twelve modes were above the noise level for the annual rainfall and accounted for about 70% of the total rainfall variance.

Figure 2.5 & Figure 2.6, and Figure 2.7 & Figure 2.8 display the contour patterns of the first and second rotated eigenvectors for the seasonal rainfall anomalies for the MAM and OND seasons respectively. Figure 2.9 & Figure 2.10 shows the corresponding rotated EOF modes for annual rainfall. The spatial patterns of the first component of the rotated EOF modes for the MAM and OND rainfall seasons are shown in Figure 2.5 and Figure 2.7.

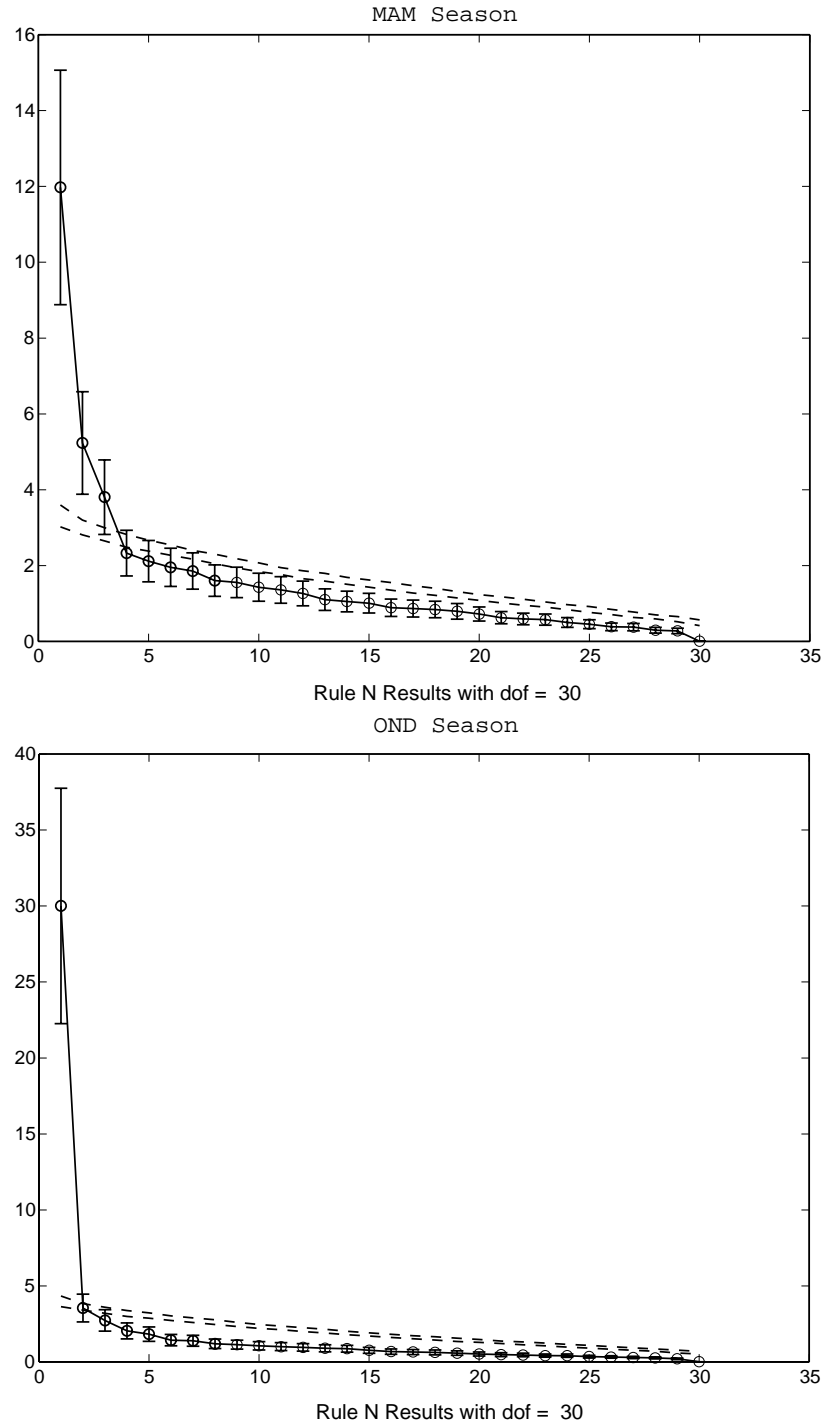


Figure 2.4: Selection of the dominant EOF rainfall modes using the North et al. (1982) sampling techniques.

This pattern accounts for 25 and 55 per cent of the total variance for the two rainfall seasons respectively. The first EOF mode is in phase throughout the analysis and most of the eigenvector coefficients are negative for the MAM season (Figure 2.5) and positive for the OND season (Figure 2.7). The highest values are concentrated over the East African highlands extending to the east to cover the coastal areas of the Indian Ocean. The principal mode (in phase everywhere) is comparable to the flow patterns over the region (Ogallo 1989). The dominant mode is related to the migration of the ITCZ, which is mainly responsible for seasonal rainfall in the region. The low variance explained by the first EOF mode for the MAM rainfall as compared to that of OND rainfall season suggests that factors other than global teleconnections play an important role in modulating the ITCZ.

The first EOF mode of the OND rainfall season (Figure 2.7) display an east/west dipole pattern with more weight centered over the East African highlands extending south to cover parts of Tanzania and the East African coast. The spatial pattern of the first EOF rainfall mode is well distributed over the domain and since this mode explains more than 50% of the rainfall variance, confirms the fact that rainfall during this season is spatially well correlated over East Africa. The east/west orientation of the first EOF mode during this rainfall season also suggests that the short rains are more influenced by the east/west oscillating meridional component of the ITCZ.

Table 2.1: Eigenvalues, variance and accumulated variance extracted by each mode of the normalized rainfall.

PERIOD	FACTOR	EIGENVALUE	VARIANCE EXTRACTED (%)	CUMMULATIVE VARIANCE (%)
MARCH-MAY	1	12	25	25
	2	5	11	36
	3	4	8	44
	4	2	5	49
	5	2	4	53
	6	2	4	57
OCTOBER- DECEMBER	1	30	53	53
	2	4	6	59
	3	3	5	64
	4	2	4	67
	5	2	3	70
	6	1	3	73
ANNUAL RAINFALL	1	4	30	30
	2	1	11	41
	3	1	7	48
	4	1	5	53
	5	1	4	57
	6	1	4	61

Similarly, the long-rains (MAM) are more influenced by the north/south movement of the zonal arm of the ITCZ in the region and other weather systems such as the meso-scale

systems, interactions between extra-tropical and tropical weather systems among others (Ogallo 1989; Beltrando 1990; Ininda 1998).

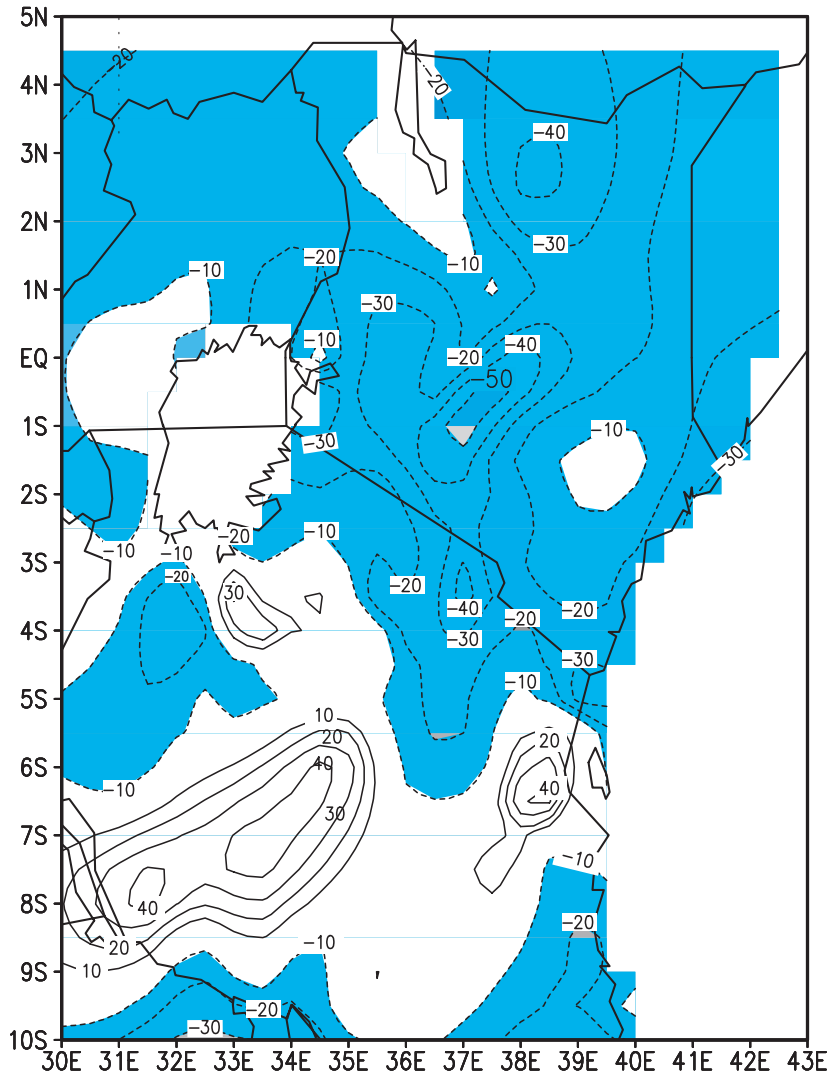


Figure 2.5: The spatial patterns of the first rotated EOF modes for the March-May seasonal rainfall anomalies (loading  $\times$  100). Values less than -10 are shaded.

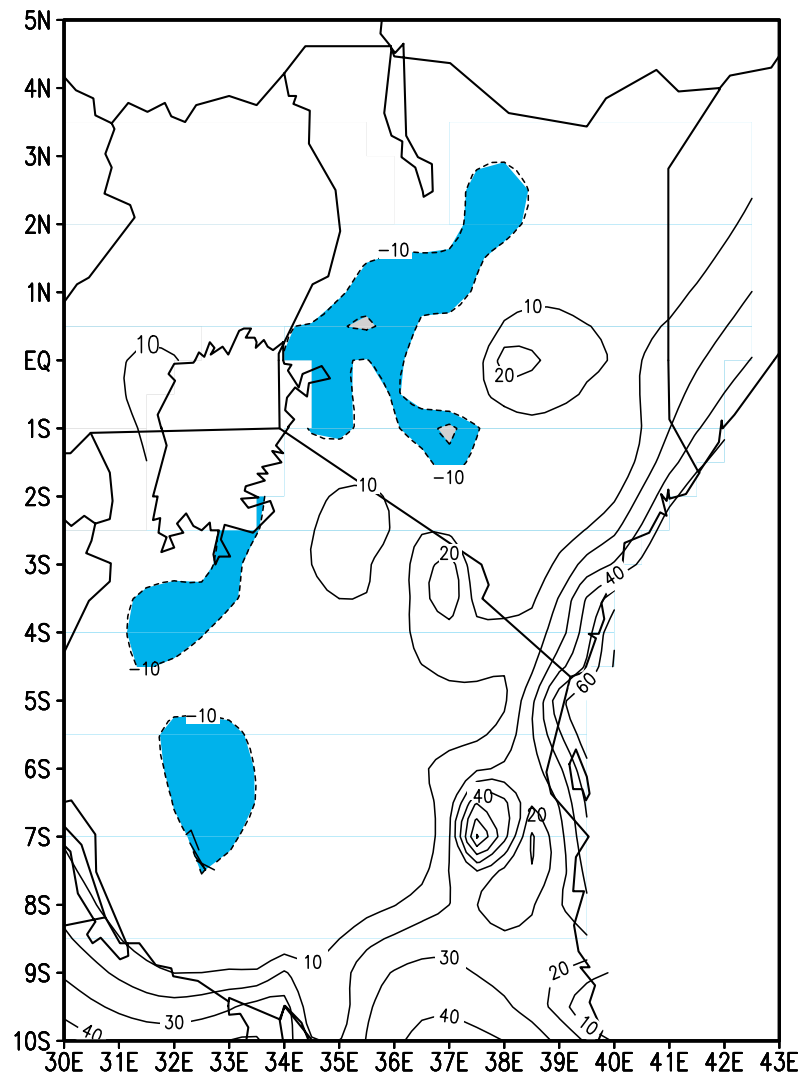


Figure 2.6: Same as in Figure 2.5, but for second EOF mode.



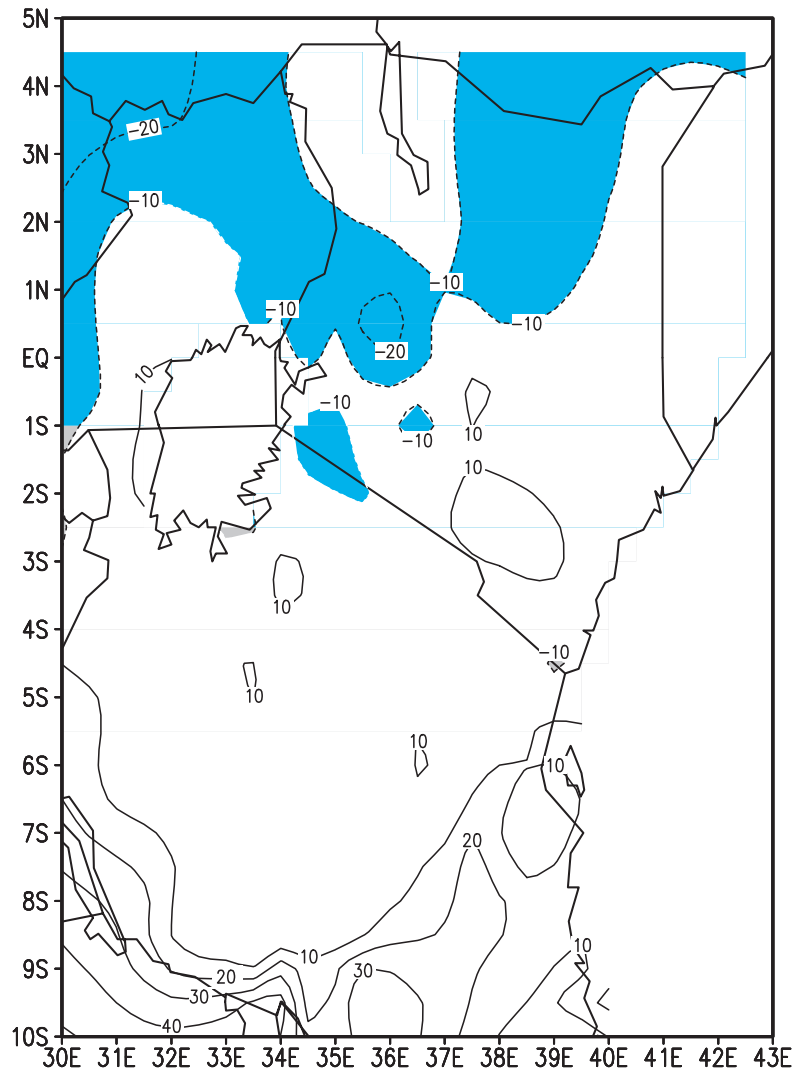


Figure 2.8: Same as in Figure 2.7, but for second EOF mode.

The spatial patterns of the second EOF rainfall components are given in Figure 2.6 and Figure 2.8. They are associated with the intra-seasonal rainfall variability. These patterns account for 11% and 6% of the rainfall variance for MAM and OND rainfall seasons, respectively. The MAM coefficients over the eastern parts of the East African highlands and western parts of the Lake Victoria regions, and those of the western parts of the East African highlands, are of opposite signs (Figure 2.6). This component represents a compensatory system. In those years where the intra-seasonal rainfall exhibits large positive anomalies over the western highlands, below normal rainfall anomalies are observed over the Eastern Highlands and the western parts of the Lake Victoria basin. The converse is also true since the reference for signs of the coefficients are arbitrary. These conditions may be linked to the intra-seasonal variability of rainfall over the region which is controlled by the interactions between the large-scale easterly flow and the coupling between the Lake Victoria land/lake breeze and the eastern Africa highlands-induced upslope/downslope diurnal meso-scale circulation systems. Both observational studies (Alusa 1976; Asnani and Kinuthia 1979) and numerical studies (Okeyo 1986; Mukabana and Pielke 1996; Indeje and Anyamba 1998) have associated the observed afternoon hail and thunderstorm activities over the western parts of the Kenya highlands to the interactions between the prevailing easterly flow and the diurnal meso-scale circulations in the region. The eastern parts of the Kenya highlands and the western parts of the Lake Victoria basin are observed to receive most of the rainfall during the morning hours. The influence of a westerly moist unstable airmass is also responsible for the intense convection over the Kenya highlands (Vincent et al. 1979).

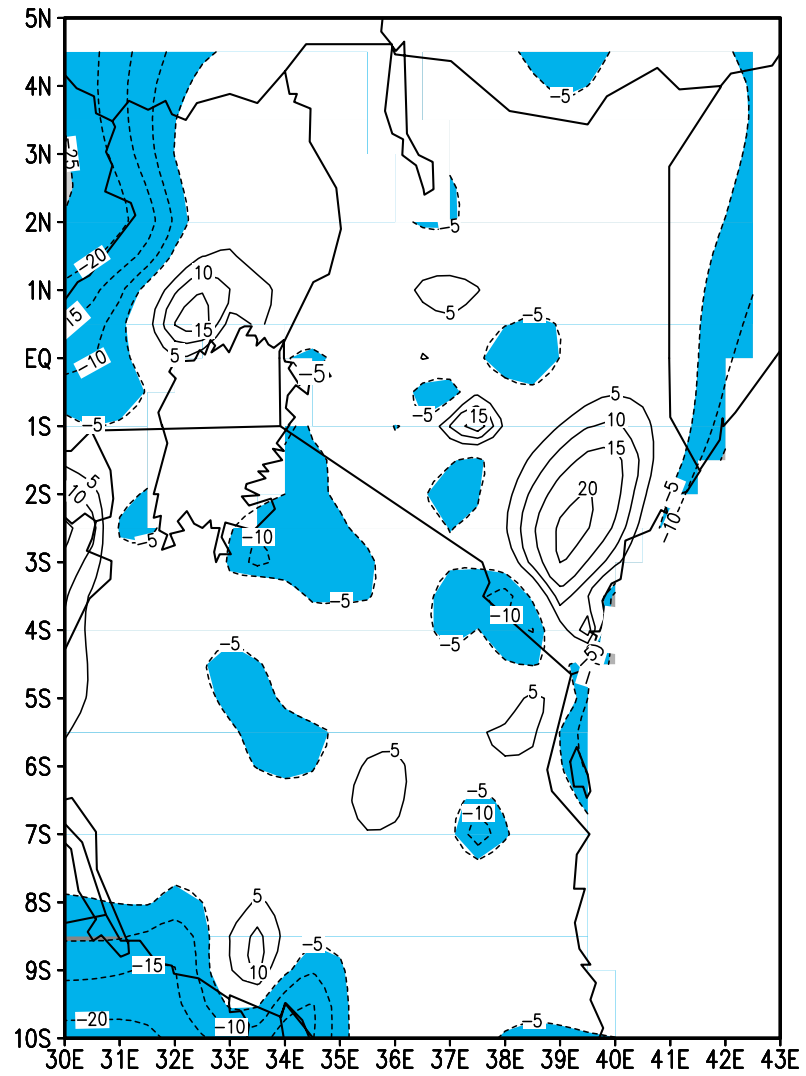


Figure 2.9: The contour patterns of the first EOF rotated eigenvectors for annual rainfall anomalies (loading  $\times 100$ ). Values less than -5 are shaded.

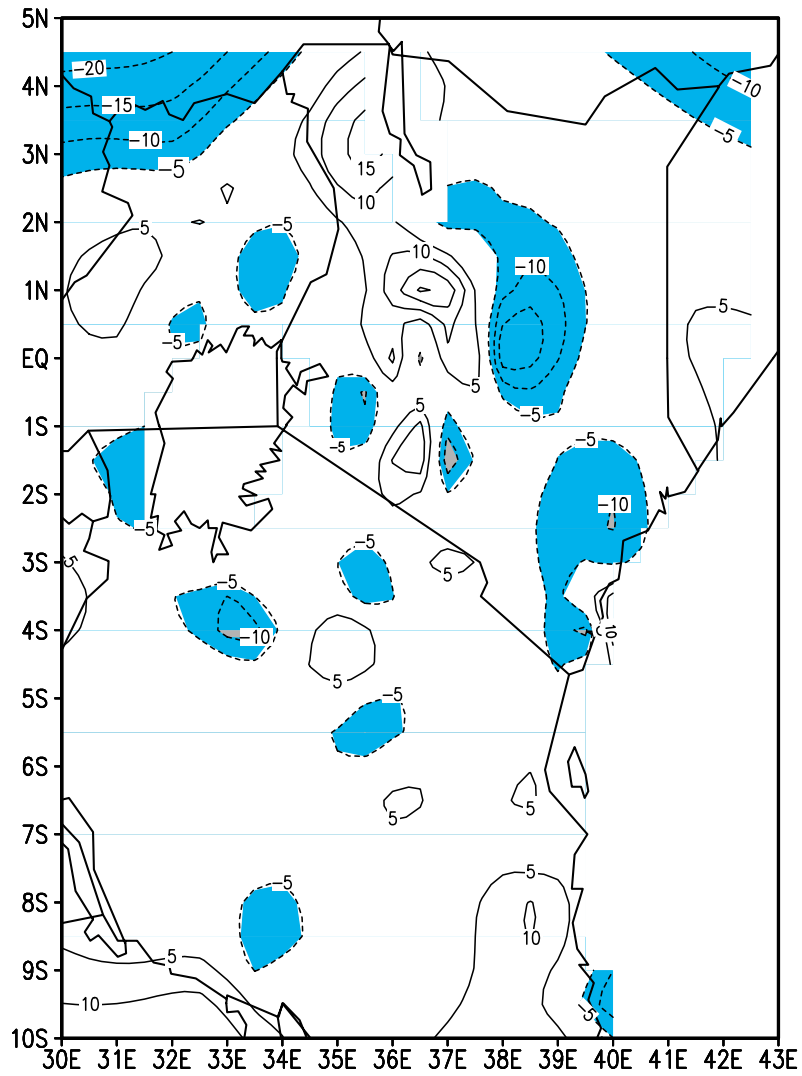


Figure 2.10: Same as in Figure 2.9, but for second EOF mode.

During the OND rainfall season, the second rainfall EOF mode displays a north/south dipole pattern (Figure 2.8). This pattern shows that whenever negative rainfall anomalies occur over the southern parts of East Africa, positive rainfall anomalies are experienced over the northern parts the region and vice versa. This configuration may be linked to an ENSO/rainfall dipole pattern (Semazzi and Indeje 1999) which is highly significant during the OND rainfall season. The spatial patterns of the first rotated EOF mode for annual rainfall (Figure 2.9) indicate some concentration of high positive scores over the coastal hinterland of Kenya. The second mode (Figure 2.10) shows a shift in the high positive scores from the coastal region to the central areas of Kenya. These patterns indicate some likelihood of homogeneous rainfall regions over the coastal areas of East Africa and central Kenya.

The principle component score time series provide insight concerning the strength of the EOF patterns over time. Strong amplitudes are observed mainly in the first mode during OND and MAM rainfall seasons (Figure 2.11 & Figure 2.12). An extreme positive score was observed during the OND season of 1961. This rainfall anomaly event, as indicated by earlier researchers, was associated with the anomalous flow patterns emanating from an unusually warm pool of air over the Indian Ocean (Anyamba 1984; Reverdin et al. 1986). High positive scores in the first EOF mode were also observed during the years 1963, 1967, 1972, 1977, 1978, 1982 and 1989 during the OND rainfall season. Similarly, during the MAM season, the years 1963, 1967, 1968, 1970, 1977, 1978, 1981, 1985, 1986 and 1990 displayed low negative scores, while the years 1961, 1965, 1969, 1971-73, 1975/76,

1980, 1983-84 and 1987 displayed high positive scores. Large positive scores were shown in the second EOF modes during the years 1968, 72, 78, 79, 84 and 1986, and 1962, 70, 72, 80, 82, 84, 85 and 1986 for the MAM and OND seasons respectively.

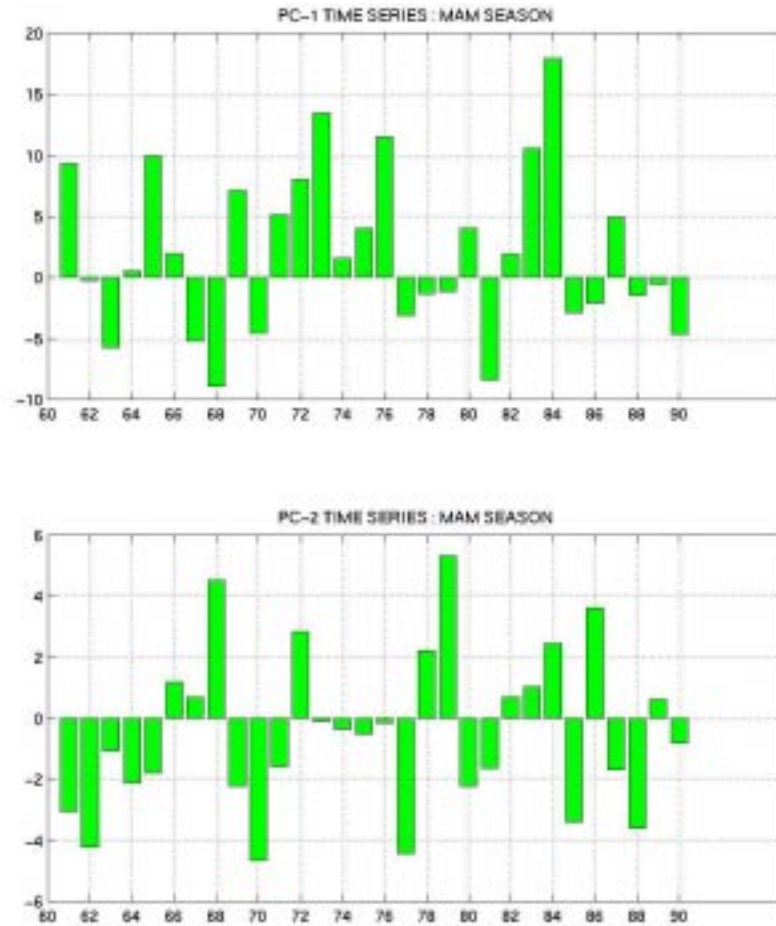


Figure 2.11: The amplitude time series of the first two principal components for the MAM seasonal rainfall.

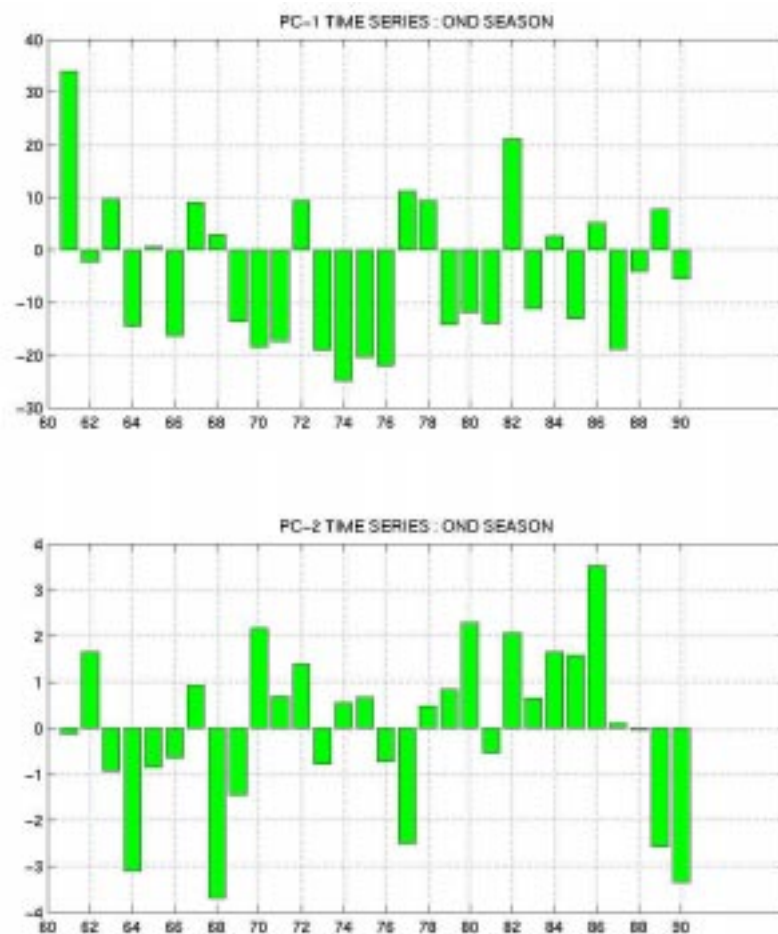


Figure 2.12: Same as in Figure 2.11, but for OND season.

In this study we use annual and seasonal rainfall anomalies obtained from the mean monthly anomalies in the cluster analysis. This analysis will clarify any seasonal dependence of the homogeneous climatic regions over East Africa. It should be noted that Lake Victoria, and southern and western Tanzania, would have more complex spatial rainfall modes during the main rainfall season of MAM (see Figure 2.5) due to the

influence of the complex regional physical features. A further objective is to compare evolutions of ENSO in space and time over homogeneous rainfall regions over East Africa. Hence, the clustered rainfall regions were retained throughout the remaining analyses to enable equal weights to be given to areal rainfall over the different sub-regions of East Africa. The derived EOF rainfall patterns from the annual and seasonal rainfall anomaly fields do not give a complete picture of the homogeneous rainfall stations in the region.

### **2.3.2 Clustering East African Rainfall Stations into Homogeneous Regions**

Figure 2.2 shows the delineated homogeneous rainfall regions over East Africa using annual rainfall using the procedure described in section 2.2.2. After correlating the principal components time series and station rainfall time series, eight homogeneous regions were delineated over East Africa: 1. coastal areas of Kenya and Tanzania 2. eastern highlands of Kenya and Tanzania 3. central Rift Valley of Kenya, 4. western highlands of Kenya, northwestern Kenya and northeastern Uganda, 5. central and southern Tanzania, 6. Lake Victoria region, 7. central and western Uganda and, 8. west of Lake Victoria. The resulting map shows the grouping of stations according to the importance of each eigenvector. The importance of each eigenvector is confined to one specific area of the East African region. In general, the eight regional groupings are similar to the ones constructed by Ogallo (1989). Farmer (1988) found that rainfall over the coastal areas of Kenya (Region 1) were highly correlated and could be averaged to form a single rainfall index.

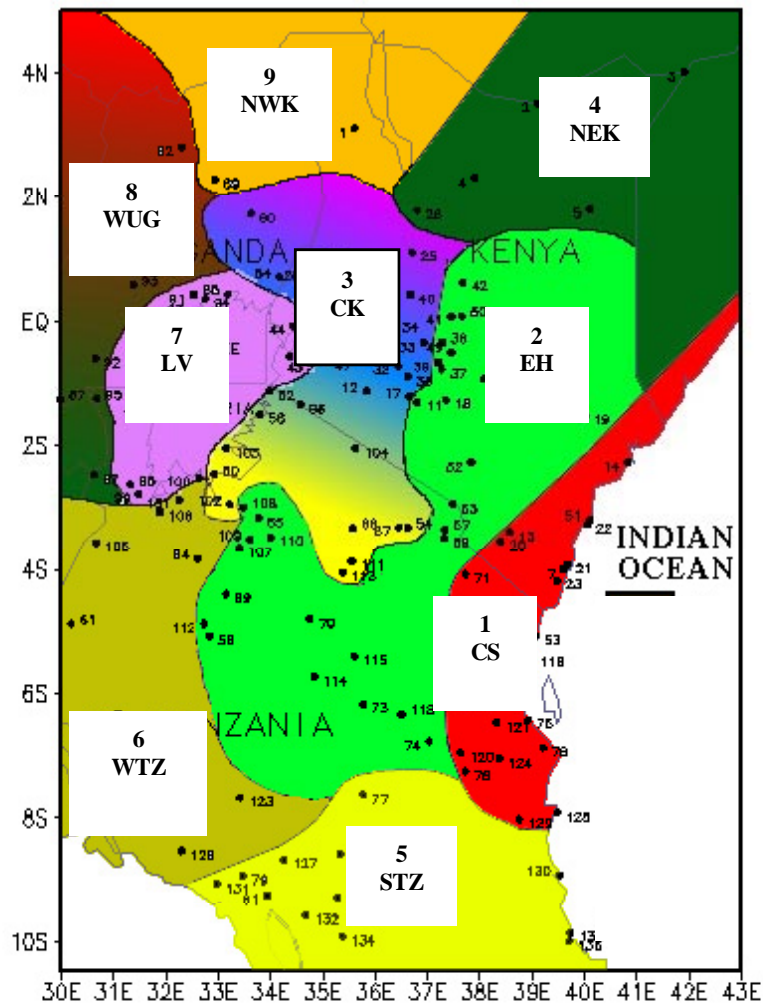


Figure 2.13: The nine homogeneous climatic regions over East Africa obtained from seasonal rainfall series.

Davies et al. (1985) analyzed rainfall over central Kenya (Region 3) and found it to be homogeneous, having a rainfall peak during August when, apart from parts of Uganda, most other parts of East Africa are dry. Eight rainfall time series were constructed corresponding to the sub-regions to be used in the analysis of ENSO/rainfall modulation.

Similar analyses applied on seasonal rainfall yielded nine homogeneous climatic regions (Figure 2.13). The resulting homogeneous climatic regions are very similar to those obtained using annual rainfall but with little modifications, which indicates little seasonal dependence of the climatic regions. The nine regions obtained from this analysis are: CK – central Kenya, EH – eastern highlands of Kenya, CS – coastal strip of Kenya and Tanzania, NEK – northeastern Kenya, STZ – southern Tanzania, WTZ – western Tanzania, LV – Lake Victoria basin, WUG – western and central Uganda, and NWK – northwestern Kenya and parts of northeastern Uganda. These regions will be used in the comparison of numerical model results and the observed rainfall over equatorial eastern Africa.

### **2.3.3 Composite Rainfall Map Patterns for the El Niño/La Niña (0) and Post-ENSO (+1) onset Years**

During the period 1961-1990, there were nine warm El Niño (0) episodes, seven cold La Niña (0), seven post-ENSO (+1) and five post-La Niña (+1) years, and fifteen normal years (Figure 2.14). Warm ENSO events occurred in the years 1963, 65, 68, 69, 72, 76, 82, 86 and 87, and La Niña in the years 1964, 70, 71, 73, 75, 84 and 88. This classification in ENSO years is consistent with those identified earlier (Rasmusson and Carpenter 1983; Wang 1984; Nicholson 1996; Phillips et al. 1998). The years 1964, 66, 70, 73, 77, 83 and 88, and 1965, 71, 74, 76 and 89 were stratified into the post ENSO/post-La Niña (+1)/rainfall composites respectively. The 1982/1988 warm ENSO and cold La Niña respectively stands out as the strongest events observed during the period of study.

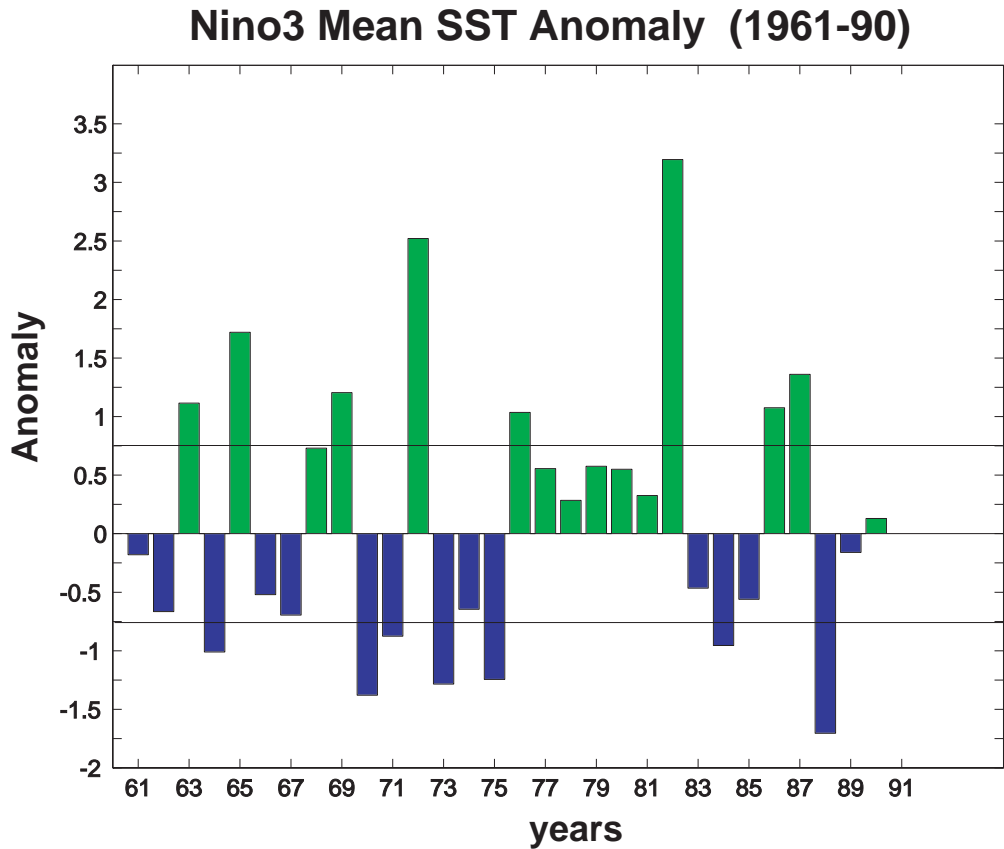


Figure 2.14: Time series of mean El Niño3 Pacific Ocean sea-surface temperature anomalies for November-December-January. The years with the sea-surface anomaly greater than +0.75 are classified warm ENSO and less than -0.75 classified cold ENSO. The years with sea-surface temperature anomalies within this range are classified as normal years.

Based on the 30-year ENSO/La Niña and post-ENSO/post-La Niña (+1) rainfall composites, years with normalized rainfall departures greater than +0.2 of the standard deviation were classified as wet rainfall composites, and years with rainfall anomalies less than -0.2 of the standard deviations as dry rainfall composites. The significance of each of these composites was determined by using a variant of the standard t-test, which takes into consideration samples with equal variances (Wagner and DA Silva 1994).

In order to have better understanding of the seasonal mean patterns and the intra-seasonal variability in the rainfall composites, both the mean seasonal and monthly anomaly stratification patterns were analyzed. Figure 2.15 and Figure 2.16 shows seasonal rainfall map patterns for ENSO and La Niña onset years. The seasonal rainfall composite map patterns for ENSO onset years (Figure 2.15), show above normal rainfall conditions over the coastal areas of Kenya and Tanzania (Region 1) during MAM. Significantly below normal rainfall is observed over the northern areas of Kenya and Uganda during both the boreal winter and summer seasons. Most parts of East Africa receive normal to above normal rainfall during the short-rains season of the ENSO onset years (Figure 2.15d). Above normal rainfall is experienced over southern Tanzania and central Kenya during JF and JJAS of the La Niña onset years (Figure 2.16). Below normal rainfall conditions are observed over eastern and coastal areas for the MAM season and spreads westward to cover most parts of the region in OND season. The monthly rainfall map indices for the ENSO and La Niña onset years for March through June are shown in Figure 2.17. Dry conditions are experienced in much of the northern parts of East Africa and the lake basin and a few areas over central and southern Tanzania during March for the ENSO onset years, with the coastal region experiencing relatively wet conditions.

During the month of April, dry conditions persist over the central Rift Valley of Kenya and northern Tanzania and significantly high rainfall is observed over the lake basin, central and western Uganda and the East African coast (Figure 2.17b). The results show an

east/west dipole pattern in rainfall during the ENSO onset years. A similar pattern was shown by Ogallo (1988) using RPCA on seasonal rainfall patterns over East Africa. During the month of May, wetter than normal rainfall conditions persist over coastal regions, central Uganda and northern Tanzania while dryer than normal conditions are observed over the lake basin, the western highlands of Kenya and southern Tanzania (Figure 2.17c). Wetter than normal conditions are experienced over most of East Africa during the month of June of the ENSO onset years.

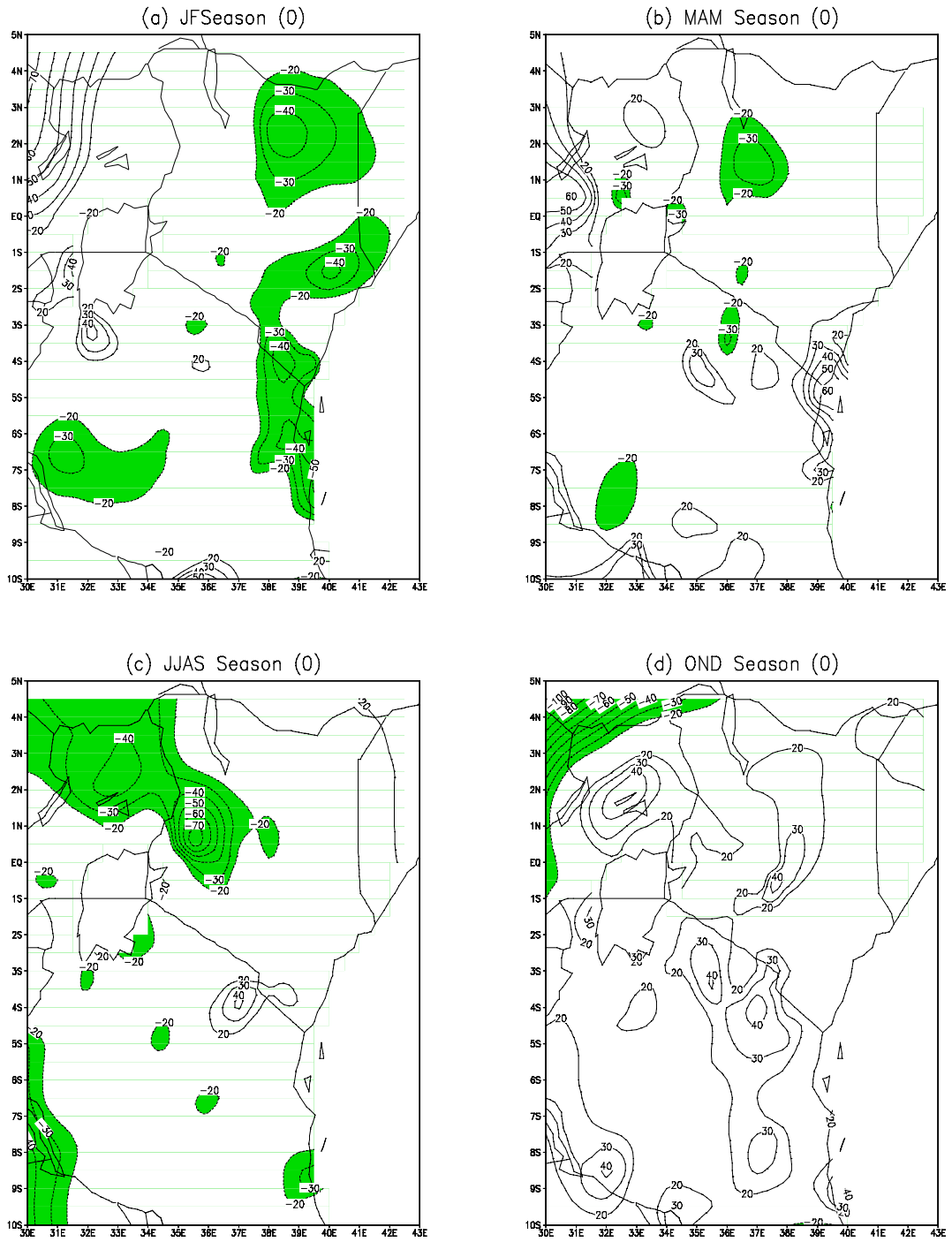


Figure 2.15: The composite map patterns for seasonal rainfall during the El Niño onset years (Loading  $\times$  100). The anomalies  $\pm 20\%$  of the long-term standard deviation are significant at 5% level. Negative significant anomalies are shaded.

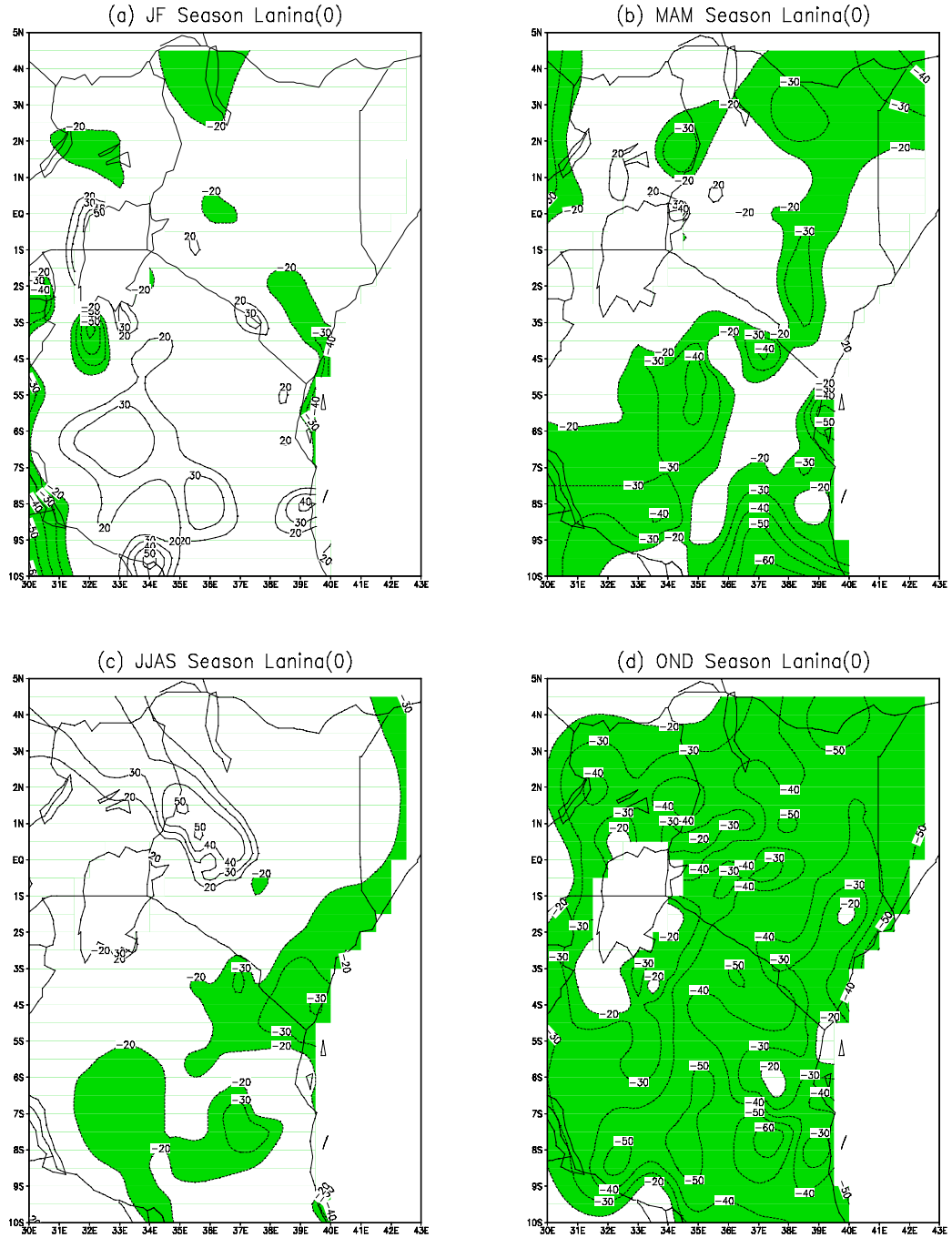


Figure 2.16: Same as in Figure 2.15 but for La Niña onset years.

Figure 2.18 shows the March through June monthly performance of rainfall during the La Niña onset years. During the month of March, there is a dipole in the rainfall pattern with

negative anomaly north of the equator and positive to the south. There is a flip over of this pattern during April and by May, a negative rainfall anomaly is observed in most parts of East Africa apart from the lake basin, central Kenya and central Uganda which receives above normal rainfall. In June, there is noticeable recovery from negative to positive rainfall anomaly over central, northeastern and coastal parts of Kenya (Figure 2.18d).

During the boreal summer period, maximum rainfall is expected over the central Rift Valley of Kenya (Region 3) and western highlands of Kenya, northwestern Kenya and northeastern Uganda (Ogallo 1983; Davies et al. 1985). The rainfall/ENSO composite analysis for seasonal rainfall (Figure 2.15c) is consistent with previous analyses and shows significantly dry conditions over the central Rift Valley, the Lake Victoria basin, northeast Uganda and the western highlands of Kenya during the JJAS rainfall season. Near normal rainfall conditions are observed over most other areas of East Africa. Suppression of the seasonal rainfall peak during the June-September rainfall season may have severe impacts on the soil moisture and agricultural production over the central Rift Valley of Kenya where wheat and barley are widely grown by large-scale farmers. The July-September rainfall peak is as important to the farming community as the long-rains of MAM and the short-rains of OND (Davies et al. 1985).

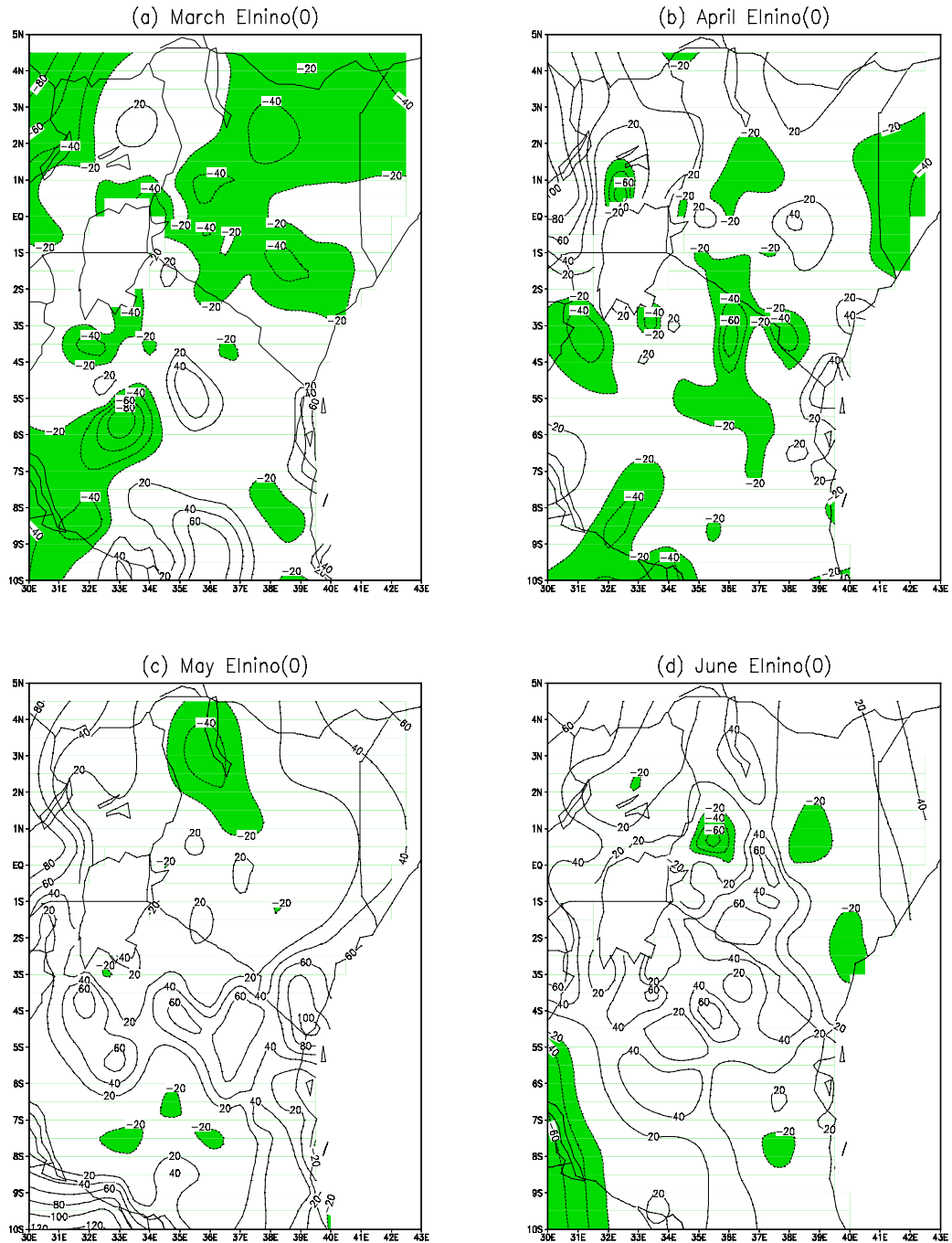


Figure 2.17: The composite map patterns for monthly rainfall during the El Niño onset years for (a) March, (b) April, (c) May and (d) June (loading  $\times 100$ ). The anomalies  $\pm 20\%$  of the long-term standard deviation are significant at 5% level. Negative significant anomalies are shaded.

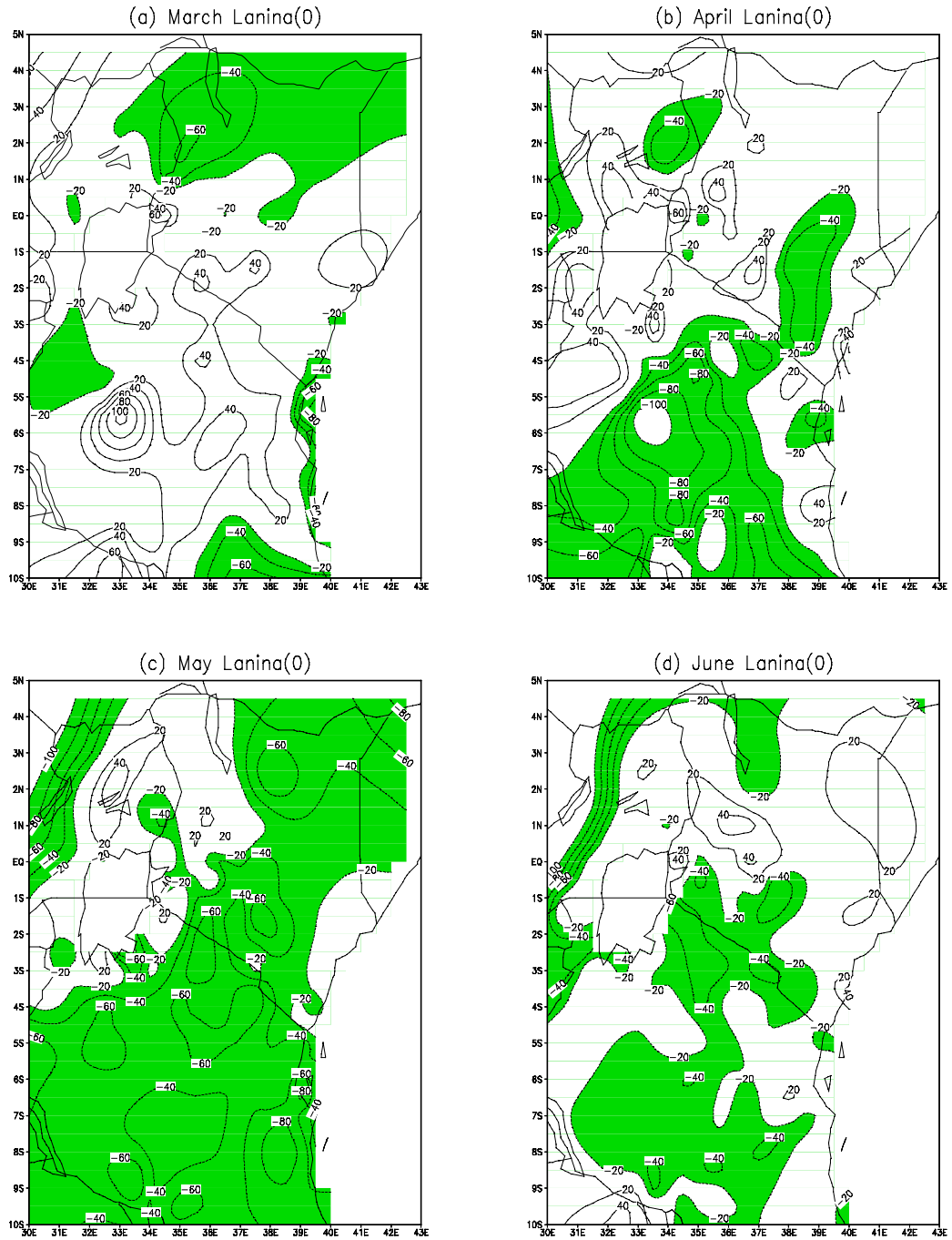


Figure 2.18: Same as in Figure 2.17, but for La Niña onset years.

The monthly ENSO/rainfall composite for the JJAS season (Figures not shown) shows persistent dry conditions over these regions during the entire season.

The ENSO/rainfall index for the months of September to December of the ENSO onset years are shown in Figure 2.19, while Figure 2.20 shows the corresponding La Niña/rainfall composite. Figure 2.19 shows continuing dry conditions over the western highlands of Kenya and northeastern Uganda, the central Rift Valley of Kenya, parts of the Lake Victoria basin and parts of central Tanzania during September. Wetter than normal rainfall conditions are experienced over northeastern Kenya and parts of northern Tanzania during this month. During October, most regions of East Africa receive normal to above normal rainfall conditions with high rainfall observed over central Tanzania. During November and December, wetter than normal rainfall conditions are experienced over the eastern highlands, central Uganda, the lake basin and the coastal regions (Figure 2.19c, d). Drier than normal conditions are experienced over the southern parts of Tanzania and some parts of the East African coast during this period. There is a sudden reduction of rainfall over the coastal areas during December (Figure 2.19d), but wetter than normal conditions are still experienced over most parts of East Africa. The sudden cessation of rainfall and switch from wet (November) to dry conditions in December over the coastal area can have devastating impacts on the soil moisture and hence on agricultural production in these areas. Farmer (1988) noted the importance of the short-rains in maintaining fruits and vegetables over the coastal areas of Kenya. These results suggest that most areas of East Africa are prone to relatively wet rainfall conditions during the October-December of the ENSO onset years. Relatively wet rainfall conditions are observed over Uganda, Lake Victoria basin and, central and western Kenya during

September of the La Niña onset years (Figure 2.20a). Below normal rainfall is observed over southern Tanzania and the coastal areas of Kenya. Below normal rainfall conditions are observed over most parts of East Africa during the months of October through December. An early recovery in rainfall is indicated over the eastern and coastal areas of Kenya, which receive near normal to above normal rainfall in December.

The seasonal rainfall composite maps for the post-ENSO (+1) years (Figure 2.21) indicate wet rainfall conditions over most parts of East Africa during the JF rainfall season. The relatively wet conditions during the OND seasonal rains tend to extend to the following year and are mainly responsible for the wet conditions observed during this season. Dry conditions are observed over southern Tanzania during the MAM season (Figure 2.21b). Dry conditions are also observed in most parts of East Africa during the JF of the post-La Niña (+1) years (Figure 2.22a). Eastern Highlands and the coastal strip experience dry conditions in all seasons. The monthly ENSO/rainfall composite map patterns for the post-ENSO (+1) years (Figure 2.23) show dry conditions in March over the western highlands of Kenya and southern parts of the coastal region and wetter than normal conditions over central Tanzania, the eastern highlands of Kenya, the lake basin and northwestern Uganda.

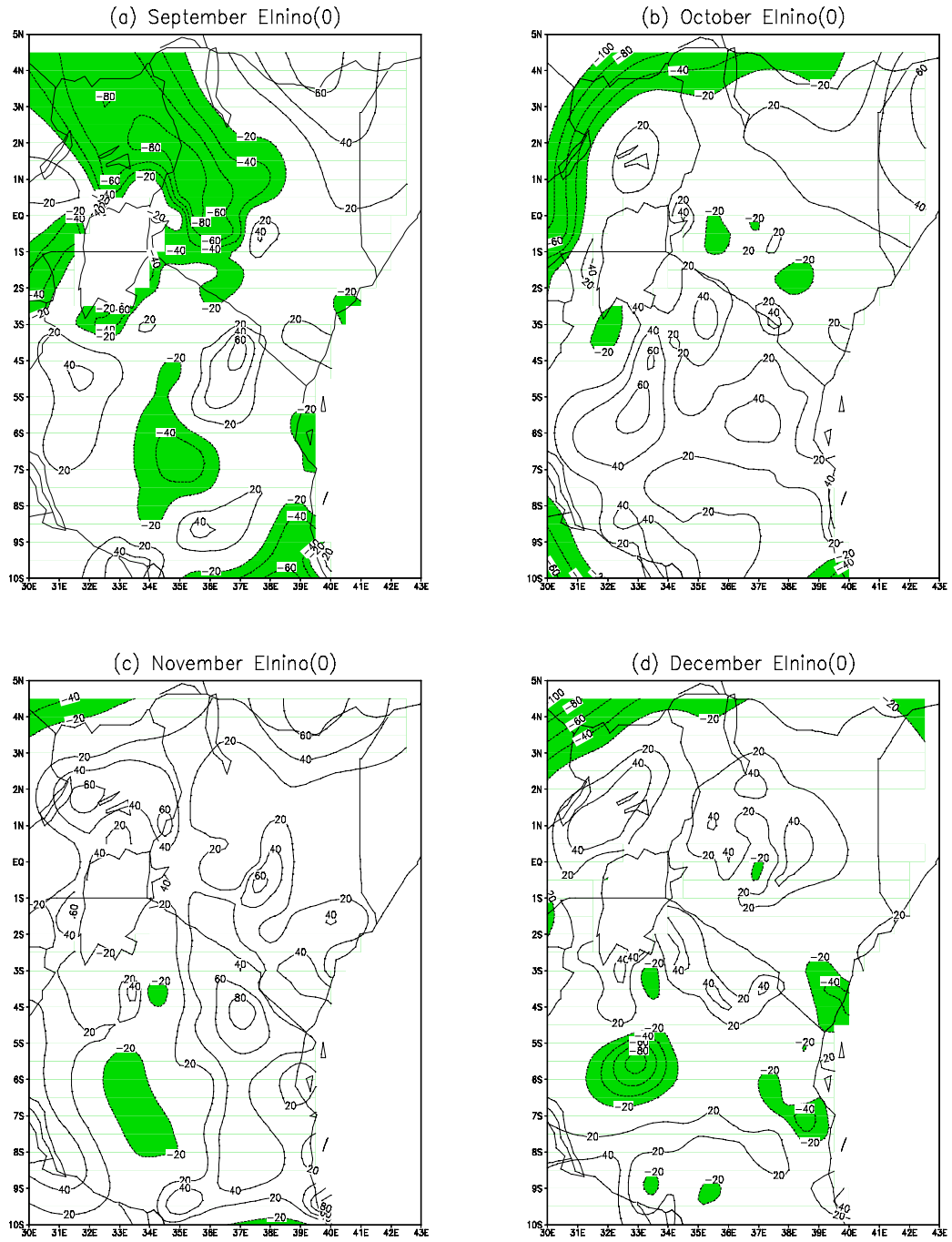


Figure 2.19: Same as in Figure 2.17, but for the months of (a) September, (b) October, (c) November and (d) December.

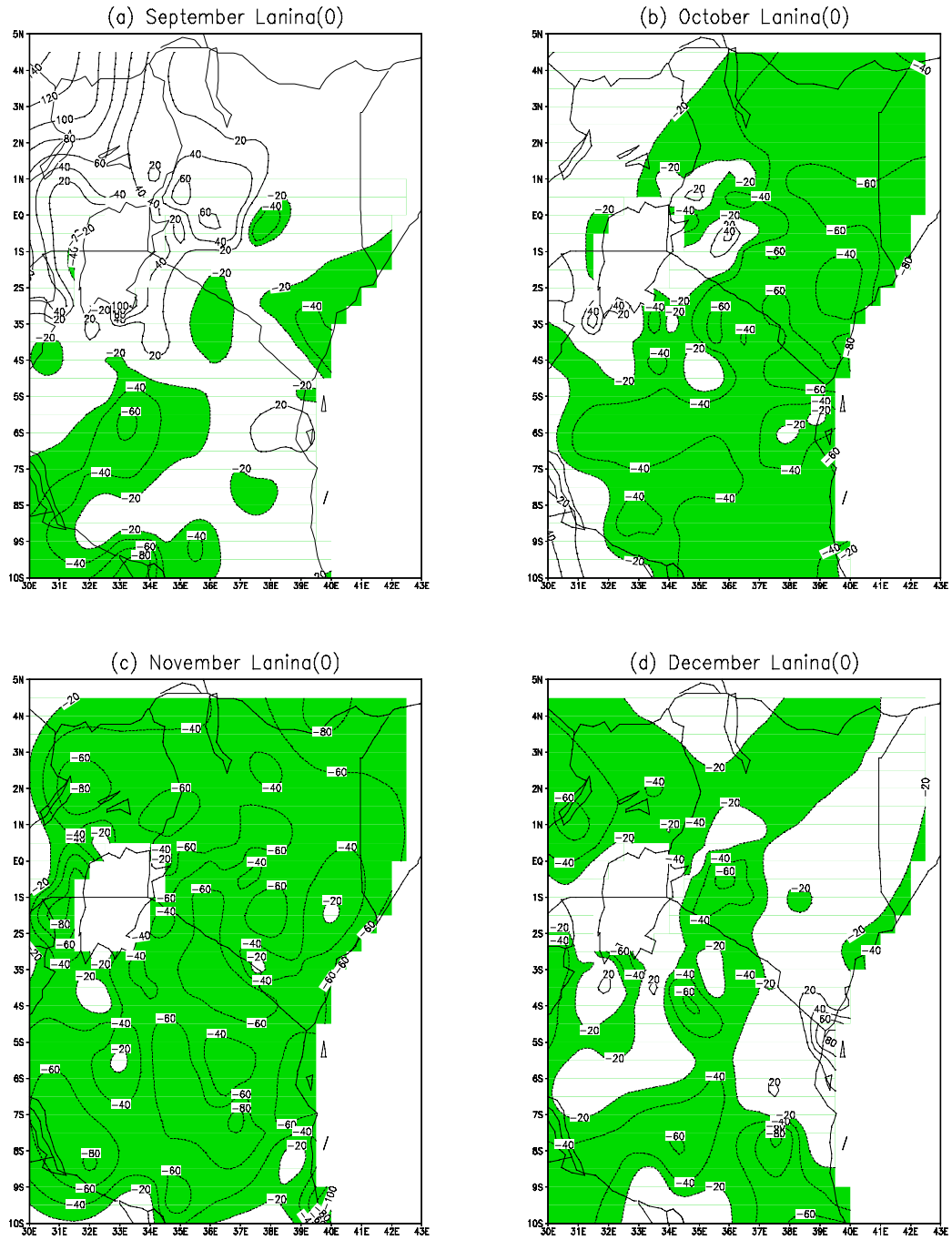


Figure 2.20: Same as in Figure 2.19, but for La Niña onset years.

During April, wetter than normal rainfall conditions are observed over the Lake Victoria basin and some parts of northern Tanzania, and significantly dry conditions over central and southern Tanzania and southern parts of the East African coast. Most areas of East Africa receive significantly below normal rainfall conditions during May in the post-ENSO (+1) years (Figure 2.24c) except for a few areas over the western highlands of Kenya, central Rift Valley of Kenya and central Tanzania which receive near normal rainfall conditions.

Near normal rainfall conditions are received in most parts of East Africa during the month of June of the post-ENSO (+1) years. Figure 2.24 displays the rainfall composite map patterns during post-La Niña (+1) years. Dry conditions are observed over the eastern and coastal regions of East Africa during the months of March through May with above normal rainfall conditions experienced over southern Tanzania during much of this period. Dry conditions persist over northern and western parts of Kenya in June and above normal rainfall conditions are observed over western Uganda (Figure 2.24d).

During the northern hemisphere summer season, wetter than normal rainfall conditions are experienced over the western highlands and central Rift Valley of Kenya, and northeastern Uganda (Figure 2.21c) as opposed to the extremely dry conditions observed during the ENSO onset years. These results suggest the existence of a negative correlation between the June-September rainfall over this region with ENSO. Dry conditions are experienced over the Kenyan coast and parts of northern Tanzania during this season. Dry conditions

are also experienced over the Eastern Highlands and southern Tanzania during JJAS of post-La Niña (+1) years (Figure 2.22c). Since rainfall at this season is crucial for the farming community in the central Rift Valley, and western highlands of Kenya, the lake basin and central Uganda, advance knowledge of the expected timing and performance of the rainfall season could be very important for agricultural and other social economic planning in the region.

The East African region experiences the second passage of the ITCZ as it progresses from north to south during the October-December period. Over most parts of East Africa, this rainfall season is important to the farming community for maintaining cash crops such as tea, coffee and corn. This rainfall season is also important in maintaining the growth of Savannah grasslands and shrubs over parts of the Eastern Highlands of Kenya and northern Tanzania where wildlife animals in National Parks are tourist attraction. The results obtained from the post-ENSO (+1)/rainfall composite maps for this season (Figure 2.21d) shows significantly dry conditions over the eastern highlands of Kenya, the Lake Victoria basin, western Uganda and central Tanzania. Dry rainfall conditions are also observed over these regions during the post-La Niña (+1) years (Figure 2.22). The rainfall deficit creates unfavorable conditions for grazing and for crop growth and development.

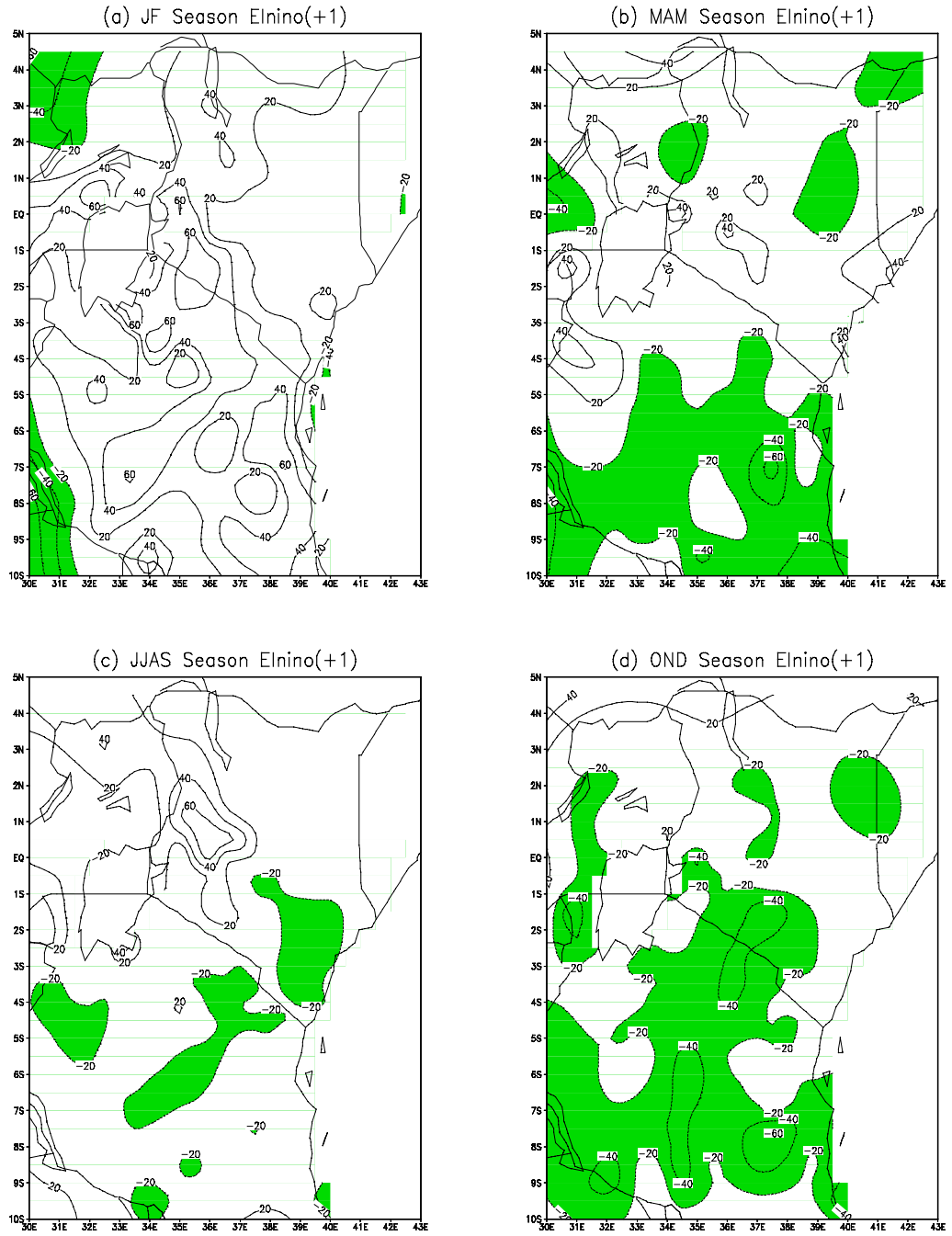


Figure 2.21: Same as in Figure 2.15 but for post-ENSO (+1) years.

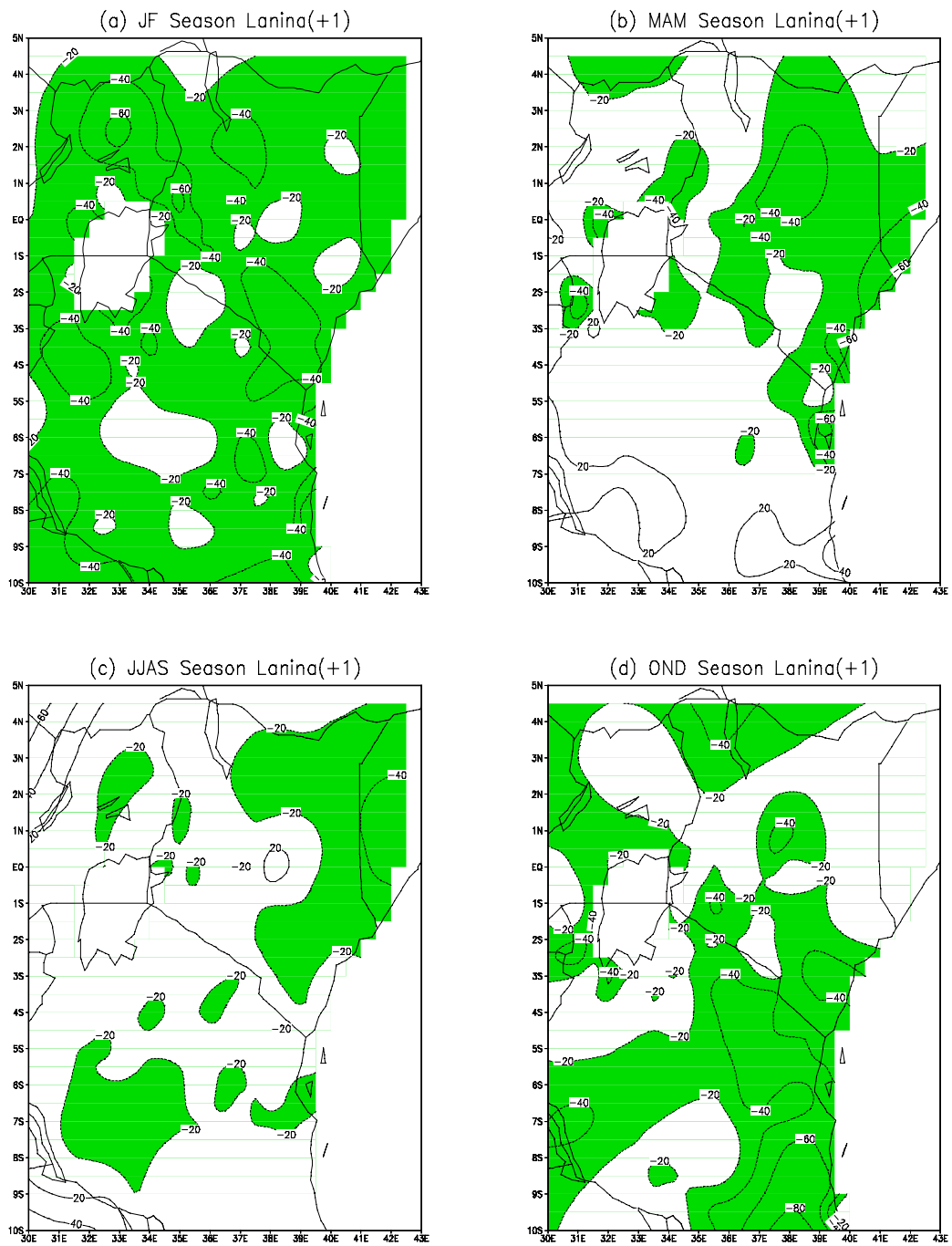


Figure 2.22: Same as in Figure 2.21, but for post-La Niña (+1) years.

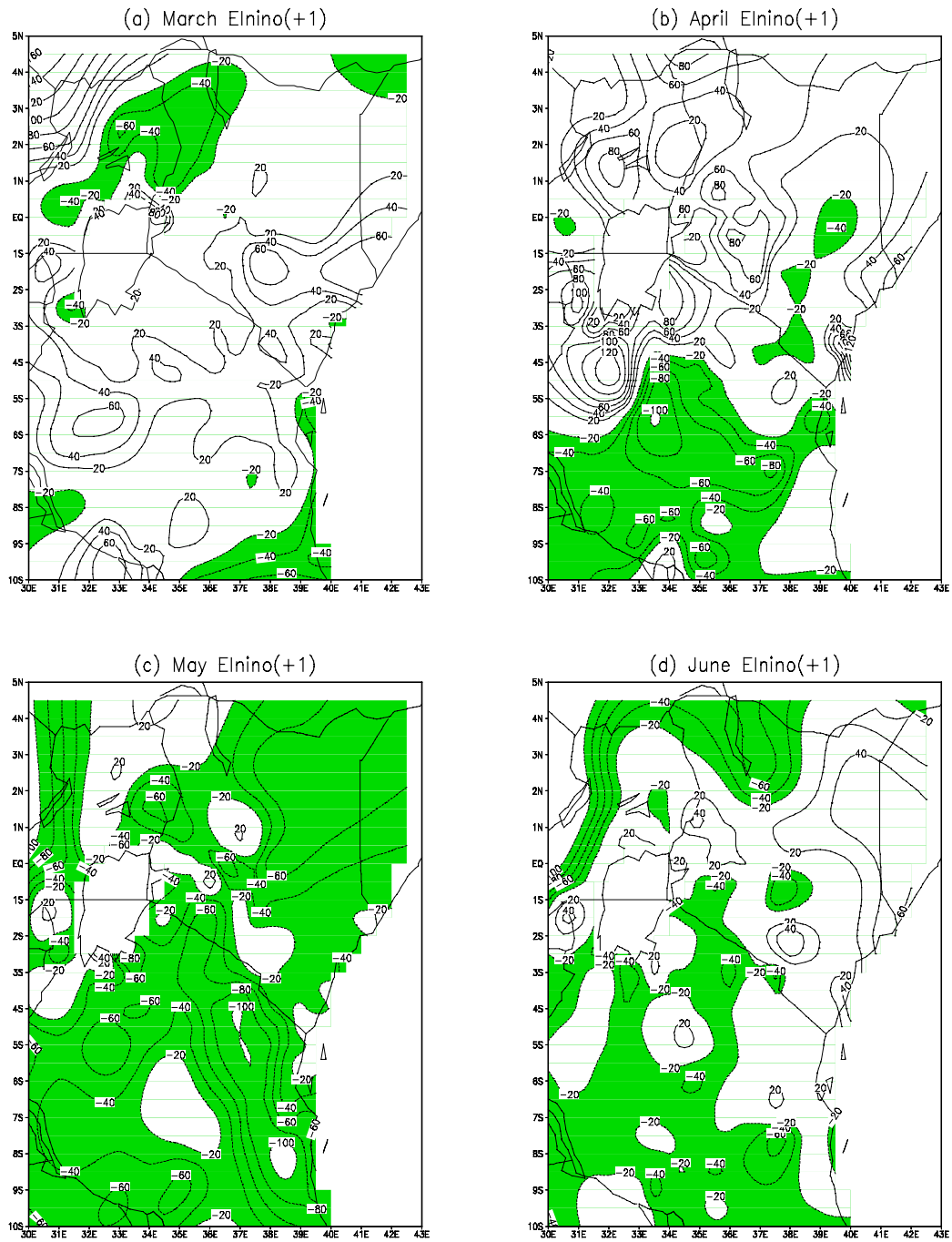


Figure 2.23: The composite map patterns for monthly rainfall during the post-ENSO (+1) years for (a) March, (b) April, (c) May and (d) June (loading  $\times 100$ ). The anomalies  $\pm 20\%$  of the long-term standard deviation are significant at 5% level. Negative significant anomalies are shaded.

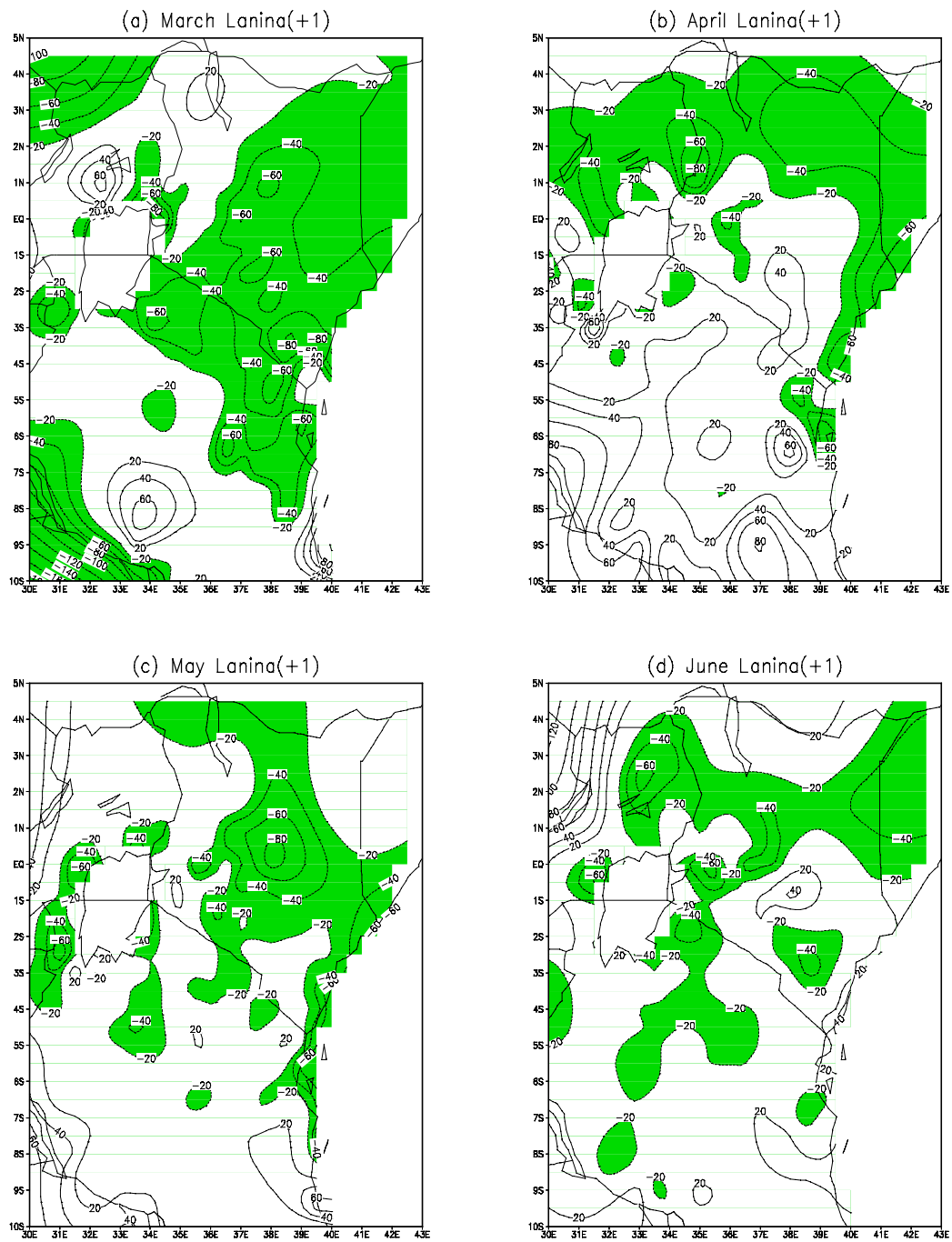


Figure 2.24: Same as in Figure 2.23 but for post-La Niña (+1) years.

Advance knowledge of the timing and the expected performance of this rainfall season could be of much benefit to the farming community for planning the schedule of planting and crop rotation. The monthly rainfall composite map patterns (Figure 2.25) show persistent dryer than normal rainfall conditions over East Africa of October to December, but there is significantly high rainfall over the central Rift Valley of Kenya, the western highlands of Kenya and northeastern Uganda, and the Lake Victoria basin during September (Figure 2.25a). Areas over the eastern highlands of Kenya and the coastal areas of East Africa recover from the dry conditions in the early part of the season during the wetter month of December (Figure 2.25d). Most areas are generally dry during September of the post-La Niña (+1) years except the eastern highlands of Kenya which experience above normal rainfall conditions (Figure 2.26a). Dry conditions persists over most parts of the region during the months of October through December of post-La Niña (+1) years except for the northern and Lake Victoria basin of Tanzania which experiences above normal rainfall conditions (Figure 2.26d).

The earlier work by Ropelewski and Halpert (1987) showed a dipole ENSO/rainfall pattern over eastern and southern Africa. Wetter than normal conditions were indicated over eastern Africa and drier conditions over southern Africa during ENSO years. Whilst Nicholson (1996) indicated that there is a tendency for rainfall to be above average for most parts of East Africa during ENSO years and for drought to occur during the following year.

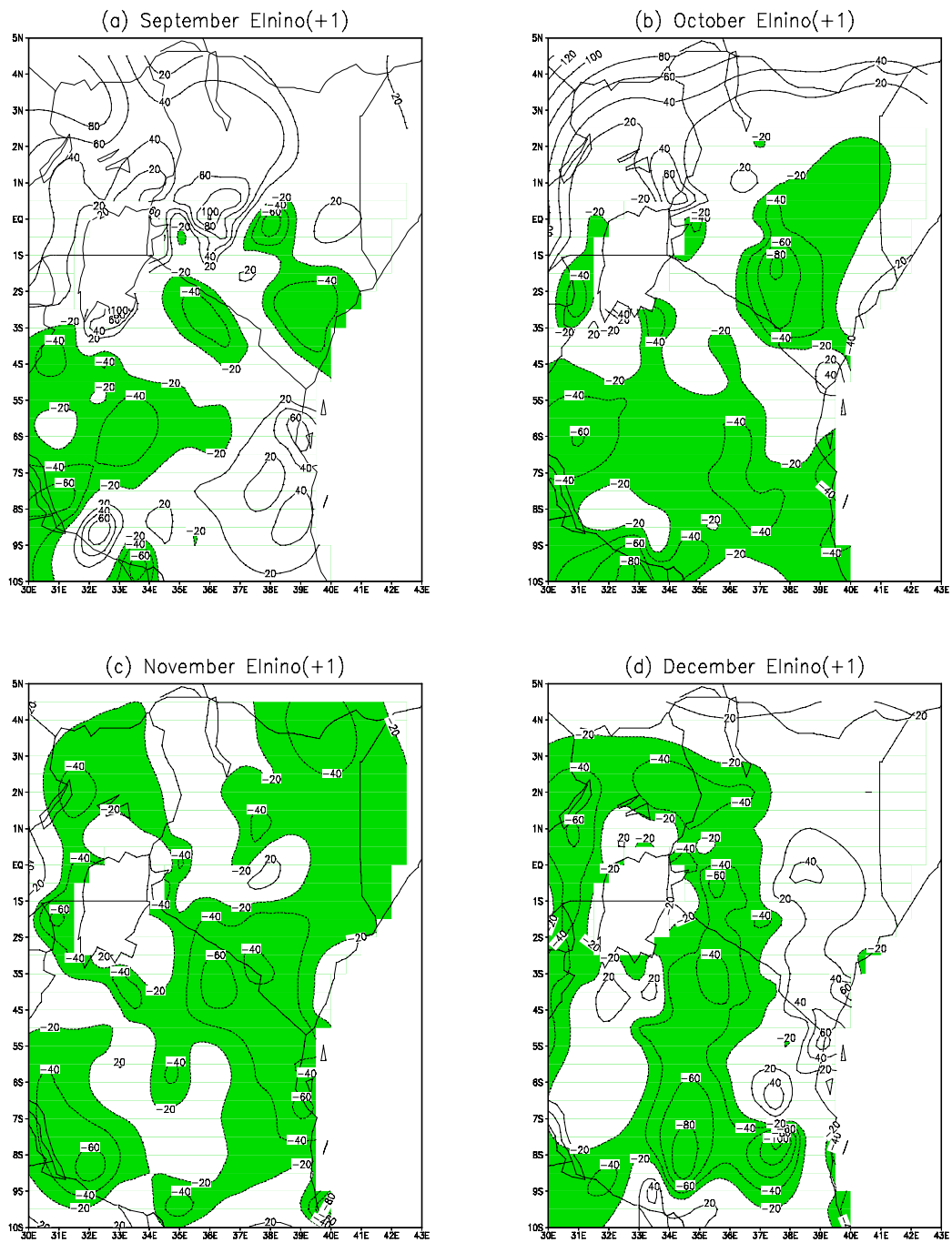


Figure 2.25: Same as in Figure 2.23, but for the months of (a) September, (b) October, (c) November and (d) December.

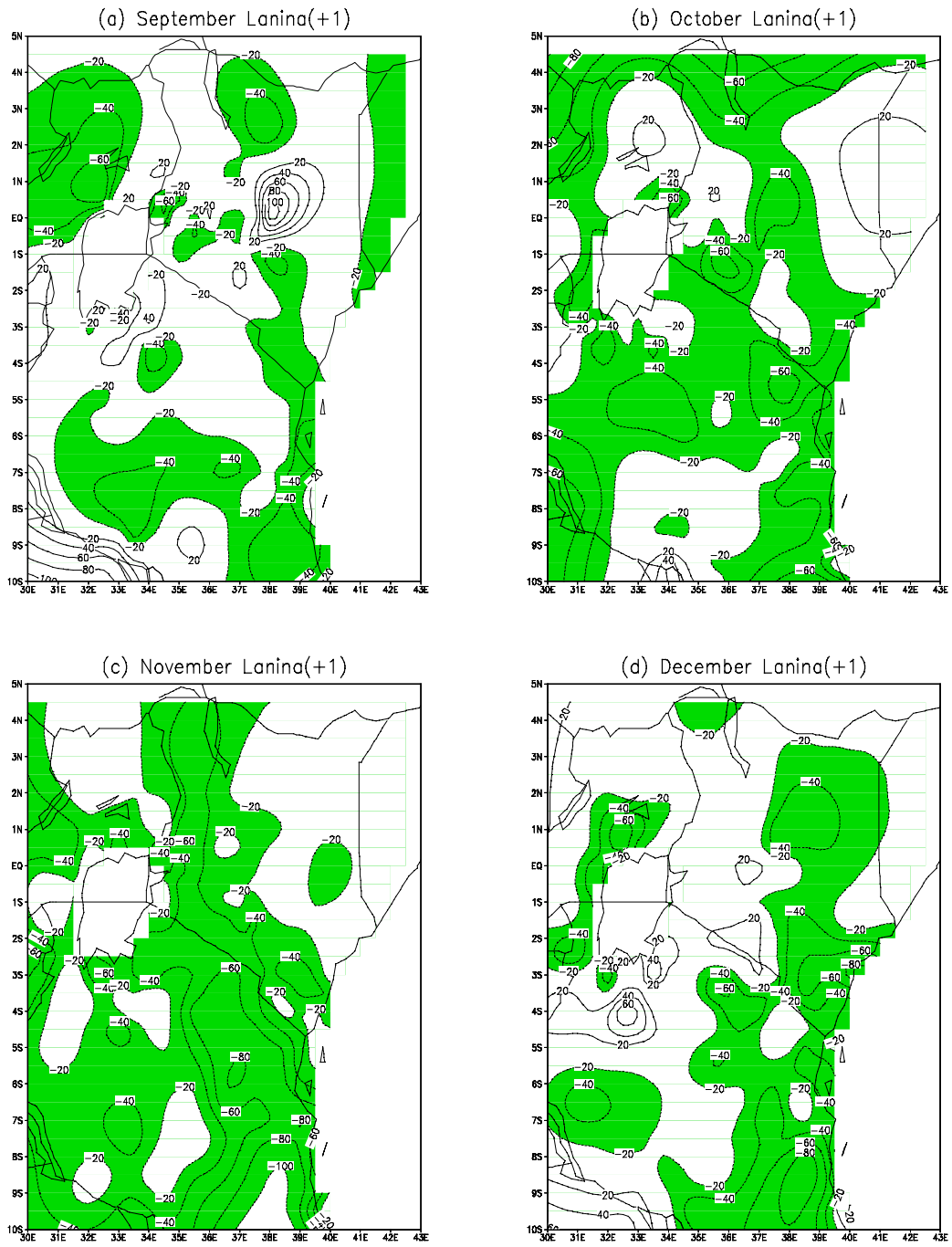


Figure 2.26: Same as in Figure 2.25 but for post-La Niña (+1) years.

One of the major results of the detailed inspection of the rainfall anomaly patterns described here is to reveal a more complicated distribution of rainfall anomalies over eastern Africa than the simple dipole cited earlier. Our results elaborate in detail the earlier ENSO/rainfall work done over the region and are important for the long-range seasonal rainfall monitoring and guidance in the East African region based on prior information of the expected ENSO events. Once the onset of an El Niño/ La Niña event is ascertained either by empirical or numerical prediction techniques, then it will be possible to use the results obtained from our ENSO/rainfall composite maps to monitor and provide guidance on the likely evolution of the rainfall anomaly patterns over different regions of East Africa.

#### **2.3.4 Observed Shifts in the Seasonal Rainfall Cycle Induced by ENSO**

The seasonal rainfall cycle for each of the eight regions of East Africa was analyzed for the mean climatology, ENSO onset and post-ENSO (+1) years to detect shifts in the rainfall seasons between the three groupings and to speculate on possible socio-economic impacts. It should be noted that besides the modulation of rainfall due to ENSO, which accounts for about 50% of the East African seasonal rainfall variance (Ogallo 1988), there are other important factors which influence East African rainfall variability. These include the Quasi-Biennial Oscillation (Ogallo et al. 1994) and the 30-60 day Julian-Madden tropical wave (Anyamba 1990). Nicholson (1996) has noted that East African rainfall is clearly linked to large-scale features of general circulation including sea-surface temperatures. Camberlin (1995) and Mutai et al. (1998) have shown significant relationships between rainfall over East Africa and the atmospheric flow patterns over the

region. In this study we are confining our analysis to the association of ENSO with the East African regional rainfall.

The mean seasonal pattern for the East African coastal areas (Region 1) shows the expected bimodal rainfall distribution with the rainfall peaks observed in April/May and November (Figure 2.27, top panel). An early onset of rainfall is shown during ENSO. The rainfall in April/May is greater than in normal years. During the post-ENSO (+1) years, there is timely onset in the March-May rainfall followed by an early cessation. During the short rains of October to December in ENSO onset years, there is significantly high rainfall with a peak in November well above the climatological mean. In post-ENSO (+1) years, there is relatively poor performance of short-season rains and a shift in the rainfall maxima to December instead of November as is usually expected. Early knowledge of seasonal performance and any expected shift in the seasonal rainfall over these regions would be important for agricultural planning of fruits and vegetables. Prolongation of both long and short rains during ENSO onset years can be relatively important in maintaining soil moisture and therefore the performance of crops. On the other hand, early cessation of the long rains during post-ENSO (+1) years and a shift in the rainfall maxima from November to December would affect the different growing stages of crops and affect yield. Farmers might benefit from late planting under such conditions, although other factors would have to be taken into account.

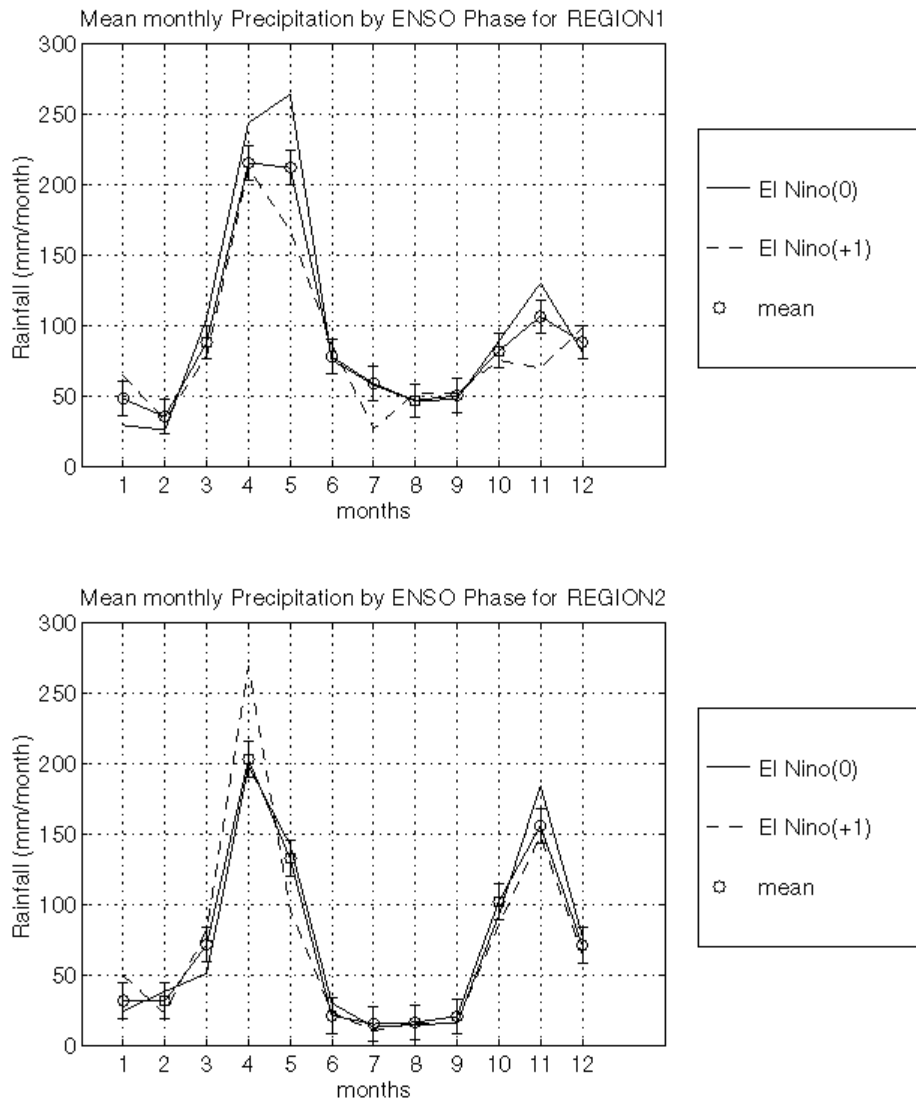


Figure 2.27: The mean monthly precipitation by ENSO phase for the homogeneous rainfall regions 1 over East Africa. The error-bar on the mean climatological annual rainfall cycle represents  $\pm 20\%$  of the climatological monthly mean. Values outside  $\pm 20\%$  of the long-term mean are significant at 5% level.

In Region 2, covering most parts of the highlands east of Rift Valley, normal performance of the long rains is indicated during the ENSO onset years. During the post-ENSO (+1) years, there is an early onset of the long rains, which become more intense surpassing the long-term mean (Figure 2.27, bottom panel). There is normal timing in the short rains during both the ENSO onset and the post-ENSO (+1) years. However, there are noticeable differences in rainfall performance, with wet conditions occurring during ENSO onset years and relatively dry conditions during post-ENSO (+1) years. Crops planted dependent on the March-May rainfall season are expected to perform normally during both the ENSO onset and post-ENSO (+1) years, but to experience later moisture stress during the post-ENSO (+1) years followed possibly by poor harvest.

The effect of an ENSO episode on the seasonal rainfall cycle over the central Rift Valley of Kenya (Region 3) is shown in Figure 2.28 (top panel). The Figure shows that during ENSO onset years, there is a late onset of the long rains followed by an early cessation. During the post-ENSO (+1) years, there is an early onset of long rains and rainfall peak reached normally in April. However, significantly wet conditions, well above the long-term mean, are experienced during this season. During ENSO years, the expected rainfall peak in August is significantly diminished. Such suppression of mid-year rains could have a severe impact on agricultural production in a region where both large-scale and subsistence farmers grow wheat and maize and depend on this rainfall season. During the post-ENSO (+1) years, there is a normal onset of July-September rainfall with very wet conditions that persist and link-up with the short rains season of October-December.

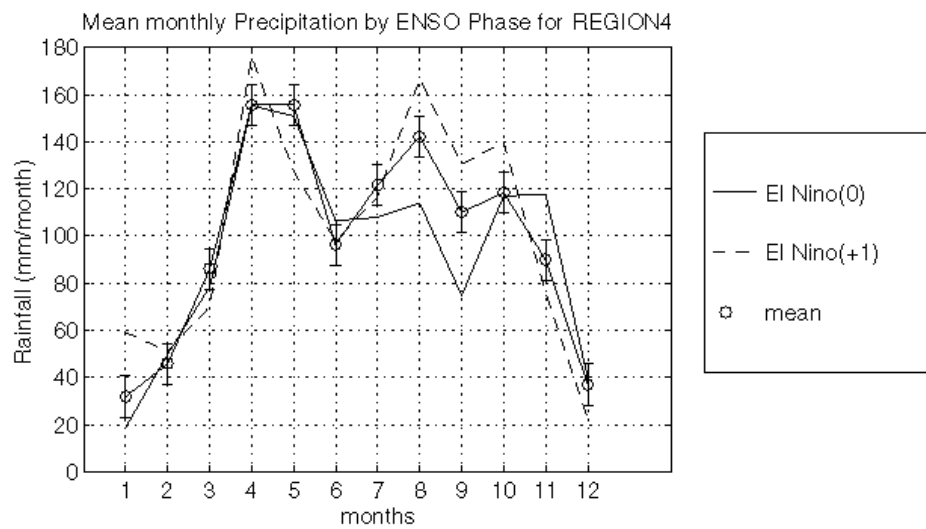
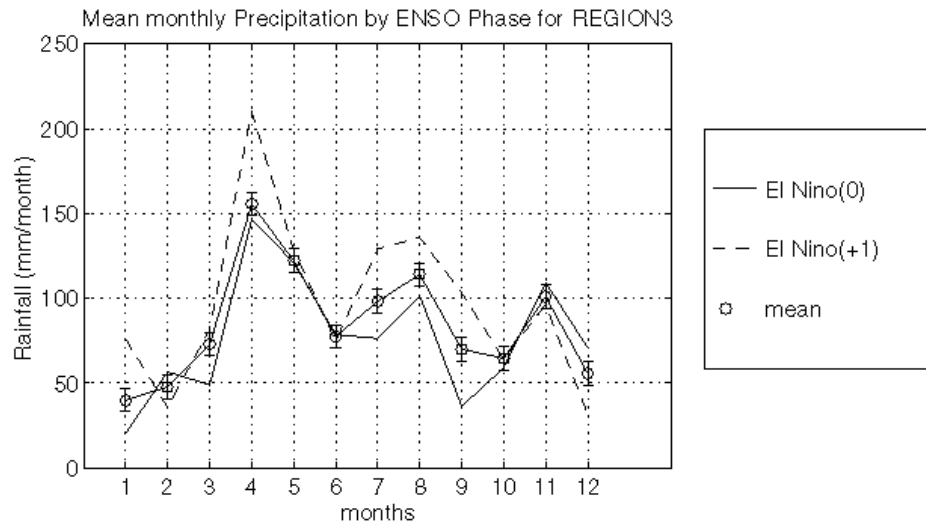


Figure 2.28: Same as in Figure 2.27.

There is a late onset but late cessation of the October-December rains during the ENSO onset years. During post-ENSO (+1) years a normal onset is followed by an early withdrawal.

The impacts of ENSO on rainfall over the western highlands of Kenya, northwestern Kenya and northeastern Uganda (Region 4) is shown in Figure 2.28 (bottom panel). It can be seen that during ENSO years there is a late onset and a poor seasonal rainfall performance of the March-May rains. During post-ENSO (+1) years, the indicated early onset of rainfall attains normal maxima in April as expected but which is significantly higher than the long-term mean. Advance guidance regarding the expected shift in the rainfall season due to ENSO will be crucial for social economic planning in this region during July-October with poor rainfall performance during the short rains of November-December. Since evaporation rates are high during July-September, the poor performance of the late short rains may result in failure to sustain soil moisture. Beans and potatoes planted during this period are likely to produce poor yields.

The mean monthly precipitation by ENSO phase for central and southern Tanzania (Region 5) is shown in Figure 2.29 (top panel). Apart from rainfall suppression during post-ENSO (+1) years and significantly high rainfall anomalies during the ENSO onset years during the main rainfall season of October-May, there is no significant shift in the pattern of seasonal rainfall.

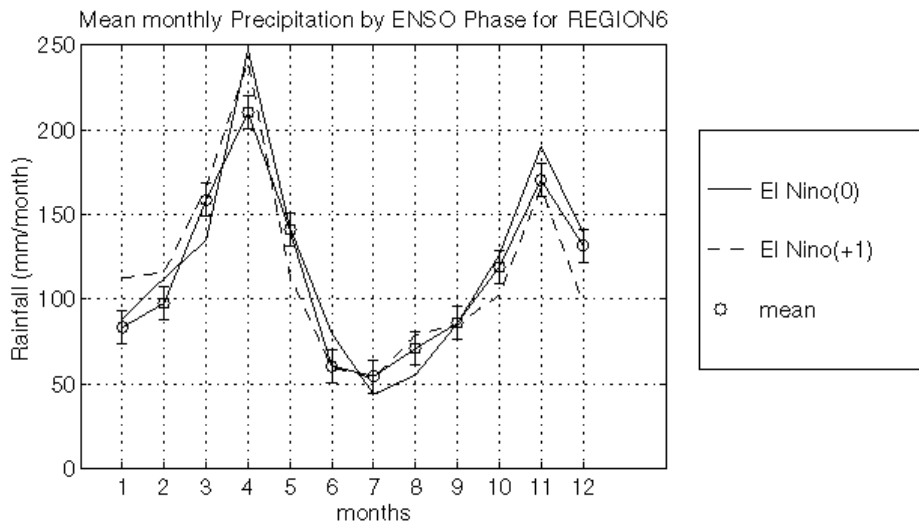
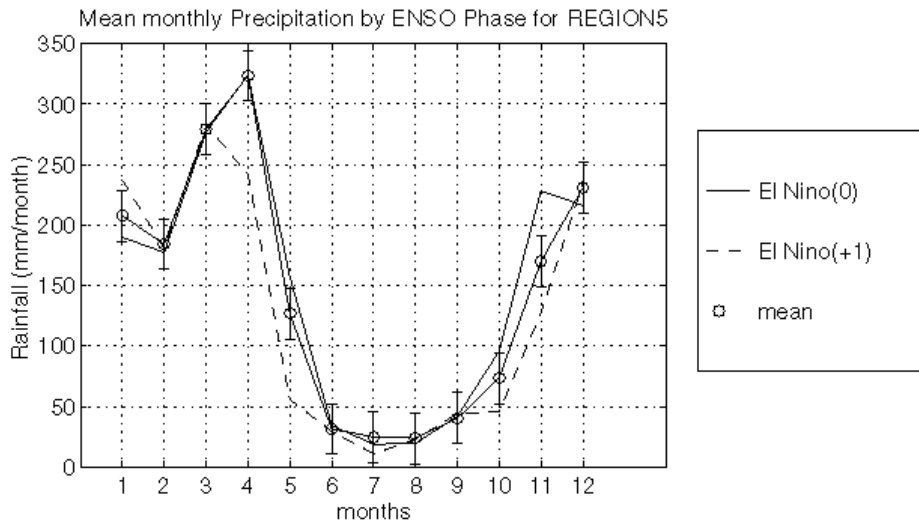


Figure 2.29: Same as in Figure 2.27.

The social economic implications of ENSO in this region may be felt due to the persistence of dryer than normal conditions during post-ENSO (+1) years. Crops grown during the normal growing season will experience significant moisture stress with less rainfall for normal agricultural production. It would be advantageous for farmers to plant alternative crops, which require little rainfall and soil moisture to mature.

Figure 2.29 (bottom panel) shows the mean monthly precipitation by ENSO phase for the Lake Victoria basin (Region 6). The Figure shows that during ENSO onset years, there is a late onset of long rains of March-May. An early onset followed by significantly high rainfall during April but an early withdrawal of the seasonal rainfall during post-ENSO (+1) years is indicated. Late planting would be recommended for the ENSO onset years to coincide with the late onset of the seasonal rainfall. The Figure also shows that during ENSO onset years, the normal increase of rainfall in August in this region is suppressed.

Any crop, which depends on this seasonal rainfall to mature, is likely to do poorly during ENSO years. The high rainfall experienced during December of the ENSO onset years may not be sufficient to replenish and sustain the soil moisture and the crops usually grown in this region since the preceding season is dry. Alternative crops requiring less soil moisture and rainfall to mature may be a suitable alternative for this region during ENSO episodes.

The mean monthly precipitation by ENSO phase for central and western Uganda (Region 7) is shown in Figure 2.30 (top panel). The Figure shows a near normal onset of the

March-May seasonal rainfall during ENSO years, followed by a late withdrawal and a significantly high seasonal rainfall giving normal to above normal rainfall conditions. On the other hand, there is a normal onset of long rains during the post-ENSO (+1) years, but with a peak in April followed by an early withdrawal in May indicating a shortened rainfall season. This can have severe impacts on regional soil moisture. The results show further that during the short rains there is an earlier onset during the post-ENSO (+1) years than during the ENSO onset years. During the ENSO onset years, above normal conditions are observed in a late November peak, followed by a normal rainfall withdrawal. During the post-ENSO (+1) years, the early onset is followed by an early below normal maximum in September/October as opposed to October/November, followed by early withdrawal. This drastic shift and reduction in the short rains during post-ENSO (+1) years can have severe impacts on agriculture. The rainfall comes before the farmers have prepared for the next planting. On the other hand, if the heavy rainfall is received during harvest time for the first crop, especially for maize, which is usually harvested at this time of the year, it may impact on yield due to the presence of high air moisture. If farmers are advised of the impending seasonal climate conditions in advance, they have opportunity for formulating alternative remedies. One alternative would be to plant only once and late into the rainfall season.

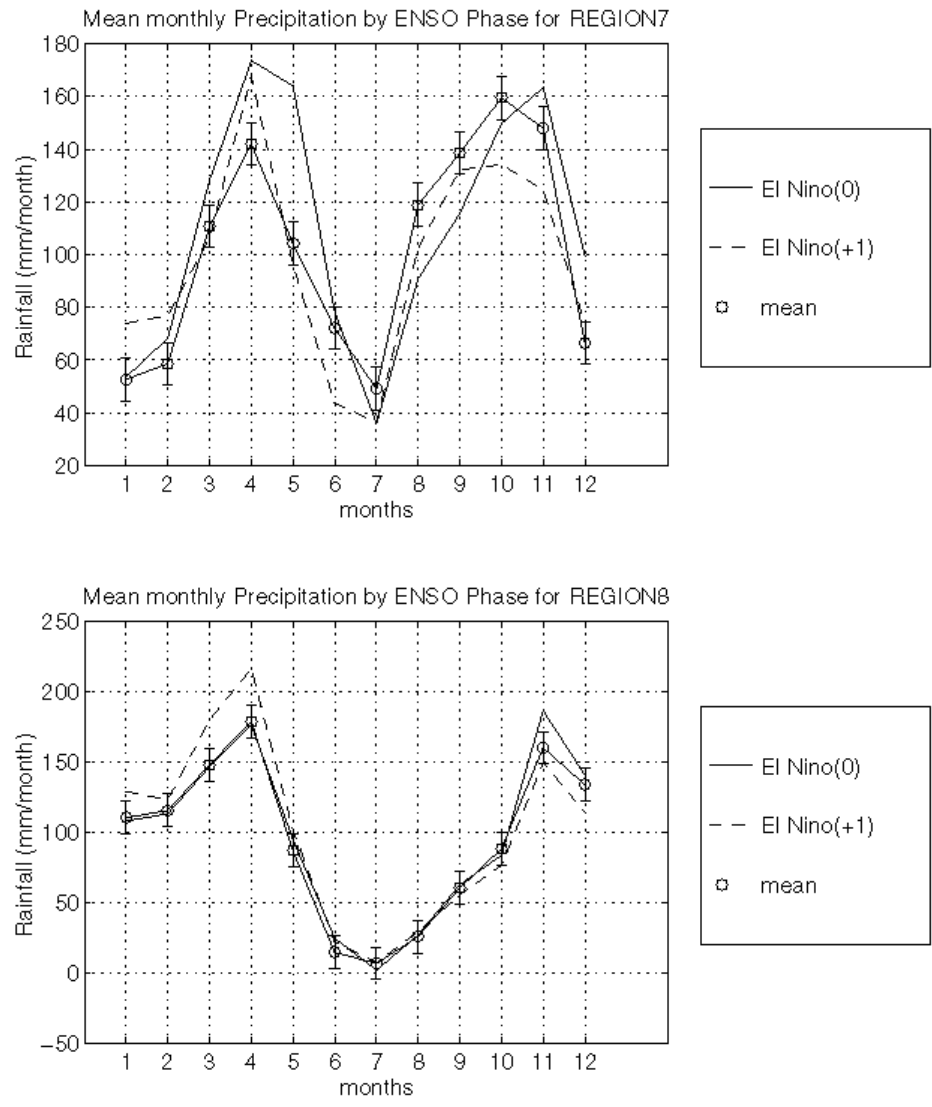


Figure 2.30: Same as in Figure 2.27.

Figure 2.30 (bottom panel) which shows the effect of ENSO on seasonal rainfall over the area west of Lake Victoria (Region 8), indicates that, during ENSO onset and post-ENSO (+1) years, there is not much shift in the long rains, but high rainfall is observed during

post-ENSO (+1) years and poor rainfall during the ENSO onset years. During the ENSO years, the October-December seasonal rainfall sets in normally although in post-ENSO (+1) years there is an early cessation and a generally poorer rainfall performance. The reliability of this rainfall season should ensure the maintenance of conditions and healthy crop performance. However, early planting during post-ENSO (+1) years would appear to be a prudent strategy.

## Chapter 3

### 3 RELATIONSHIPS BETWEEN QUASI-BIENNIAL OSCILLATION (QBO) IN THE LOWER EQUATORIAL STRATOSPHERIC ZONAL WINDS AND SEASONAL RAINFALL

In this chapter, we examine the teleconnections between the seasonal rainfall anomalies of March through May (long-rains) over equatorial eastern Africa and the lower equatorial stratospheric (30-mb) zonal winds (QBO-index) for the 32-year period 1964-1995 using statistical methods. The analysis is based on the application of the simple correlation method and QBO/rainfall composite analysis. A statistical study of spatial correlation patterns is made in an effort to understand the climatic associations between the equatorial stratospheric zonal wind and regional rainfall at the interannual scale. The aim of this analysis is to establish whether this global signal can be employed as predictor variable in the long-range forecasts. The study is part of an ongoing investigation, which aims at designing a comprehensive and objective, multi-variate-forecast system of seasonal rainfall over equatorial eastern Africa.

#### **3.1 Background**

The QBO is a quasi-periodic reversal in the tropospheric and stratospheric zonal wind from easterly to westerly components and vice-versa with periodicity of about 28 months. Several studies have reported the presence of the QBO in various atmospheric parameters and at different regions of the globe. Some of the stratospheric and tropospheric variables

that have exhibited QBO include temperature (Rasmusson et al. 1981), ozone (Funk and Garnham 1962; Hasebe 1980), Indian monsoon rainfall (Mukherjee et al. 1979, 1985) and African rainfall (Rodhe and Virji 1976; Ogallo 1982; Nicholson and Entekhabi 1986; Nicholson 1996). In studies of QBO it may be important to distinguish between the stratospheric QBO and tropospheric QBO. Studies by Brier (1978), Nicholls (1978) have associated QBO in the troposphere to the air-sea interaction processes. Brier (1978) presented a conceptual model, which suggested that the tropospheric QBO could arise if the sense of either the ocean-to-atmosphere forcing or atmosphere-to-ocean forcing varied seasonally. Nicholls (1978) postulated that air-sea interaction in the Indonesia-North Australia region could provide the required seasonal variation in feedback and could be the source of the tropospheric QBO.

Studies by Holton and Lindzen (1972), Plumb (1977) and, Holton and Tan (1980) have indicated that the stratospheric equatorial QBO is forced locally by alternating downward propagating patterns of westerly and easterly mean zonal winds which repeat with somewhat irregular period averaging about 26 months. It has been pointed out that the stratospheric QBO is excited primarily by vertically propagating equatorial wave modes, and that these modes excite a quasi-biennial mean zonal wind response through the mechanism of radiative damping which causes the waves to decay in amplitude with height and thus to transfer momentum to the mean zonal flow (Holton and Lindzen, 1972). This mechanism indicates linkage between the tropospheric disturbances and the QBO in the zonal winds of the lower stratosphere over lower latitudes. Schoeberl (1978) postulated

that cell eddies, commonly referred to as planetary waves, which formed in the troposphere through baroclinic, orographic and diabatic processes would propagate vertically and affect the stratospheric circulation. Labitzke and van Loon (1988, 1990), Barnett (1990), Ropelewski et al. (1992) have reported the QBO of the stratosphere equatorial zonal winds and its association with the interannual variability of the coupled air-sea system. Lau and Sheu (1988) have indicated that the fundamental period of the Southern Oscillation (SO) is approximately double that of the QBO, which in turn is twice that of the annual cycle. QBO has been found to be strongly phase locked with the annual cycle and it also tends to enhance major negative swings in the SO associated with the El Niño-Southern Oscillation (ENSO) events. Evidence suggests that the development of ENSO tends to be associated with the easterly phase of the lower stratospheric QBO (Lau and Sheu 1988).

Many attempts have been made to examine the predictability potential of the QBO signals because of its persistence and appearance in many atmospheric parameters (Mukherjee et al. 1979, 1985; Mason and Tyson 1992; Jury et al. 1994). Mukherjee et al. (1979, 1985) have identified a significant relationship between the phases of the QBO in the zonal wind in the lower stratosphere (30-mb) and the percentage departures of the summer monsoon rainfall of India. They showed that the strong easterly phase of the QBO is associated with weak monsoons and the weak easterly/westerly phase with active monsoons. The weakening of the easterly winds is generally a manifestation of westerly phase of the QBO in the lower stratosphere, as the prevailing winds in the stratosphere during summer

monsoon are broadly easterly. Mason and Tyson (1992) have analyzed the phases of QBO and southern Africa rainfall and found a significant correlation (+0.6) between QBO and regional rainfall when the QBO is in the west phase. The relationship failed during 1991/92 when the regional drought corresponded with the east phase of the QBO. Jury et al. (1994) have identified a correlation pattern between the QBO and tropospheric winds, which corresponds with upper anticyclonic, Walker cell uplift over southern Africa and the descent over Madagascar in the west phase summers. Ogallo et al. (1994) have investigated the characteristics of QBO over tropical eastern Africa using zonal wind composites from Nairobi, Kenya ( $1^{\circ} 18'S$ ,  $36^{\circ} 45'E$ ) for the period 1966-1987. Their results, based on spectral analysis indicated the dominance of a 28 months period in the zonal wind component. The vertical rate of propagation was about 1.2 km per month. The results also indicated some significant (at 5% level) association between rainfall and QBO signal based on the reversal in zonal winds.

Distinct QBO-spectral peaks in the East African rainfall have been reported in several studies (Rodhe and Virji 1976; Ogallo 1982; Nicholson and Entekhabi 1986; Nicholson 1996). Nicholson and Entekhabi (1986) presented evidence of several quasi-periodicities common to African rainfall, especially over southern and equatorial regions of the continent. In the low latitudes, spectral peaks in the ranges of 2.2 to 2.4 and 5.0 to 6.3 years are common. In the eastern tropical sector spectra show peaks in the ranges 2.2 to 2.4 and 3.3 to 3.8 years. These dominant periodicities may be indicative of different mechanisms in the two sectors. These findings and others have led us to investigate the

prospects of adopting the stratospheric oscillator as a potential predictor for regional seasonal rainfall. The regular quasi-periodicity of the QBO of about 2.3 years, further makes it a good candidate for the prediction of rainfall over equatorial eastern Africa.

Significant evidence of the relationships between short-rains over eastern Africa, and SST and ENSO have been observed (Ogallo et al. 1988; Nicholson and Nyenzi 1990; Semazzi et al. 1996; Mutai et al. 1998; Indeje et al. 2000). Relatively less attention has been directed at the predictive potential of the long-rains season over the region, which is more critical than the short-rains in many parts of the region for the agricultural industry and other social economic activities. The long rains season has been associated with complex interactions between many regional and large-scale mechanisms which generally induce large heterogeneities in the spatial rainfall distribution (Ogallo 1982; Beltrando 1990; Semazzi et al. 1996; Nicholson 1996; Okoola 1998; Indeje et al. 2000) and virtually negligible correlations with ENSO (Ogallo 1988). Recent studies of interannual variability in the tropics have largely focused on the ENSO, so much so that other important long-term sources of climate variability may have been overlooked. Recent investigations (Webster et al. 1999 and Saji et al. 1999), have furnished evidence of unusual events in the tropical Indian Ocean that clearly point to the existence of a climate mode of interaction between the ocean and the atmosphere (Anderson 1999). As noted above, this mode of climate variability may be significant in modulating the climate of eastern Africa. The QBO on the other hand, was well known in the atmosphere long before ENSO became the main focus of the studies on inter-annual variability (Lau and Sheu 1988). It has been observed

that once there is a change of sign from positive to negative (or vice versa) of the lower stratospheric winds, the particular state persists for at least nine months (Brier 1978). Although the biennial oscillation appears to have an irregular component, varying between two and three years in length, it provides some measure of order in the otherwise more chaotic behavior of inter-annual variability of the long-rains of equatorial eastern Africa and therefore some hope for predictability. Based on the foregoing observations therefore, the objective of this study is to investigate the relationships between the different QBO phases in the stratospheric zonal wind and the long-rains season of equatorial eastern Africa and also explore the predictive potential of the long rainy season using information about the phases of the QBO. Both simultaneous and lag correlation are explored in the search for optimal predictive potential.

### **3.2 Data Description and Methodology**

The monthly mean climate indices: the SOI and the globally averaged equatorial stratospheric 30-mb zonal wind index (QBO-Index) were obtained from Climate Analysis Center (CPC/NOAA) database. The SOI and QBO-Index covered the period 1964-97 and 1979-97 respectively. Because of the short length (1979-1992) in the equatorial stratospheric 30-mb zonal wind index which was obtained from CPC, it was supplemented by 30-mb zonal wind observational data set for Singapore ( $1^{\circ} 20'N$ ). The time series of the monthly mean zonal winds at 30-mb for Singapore used in this study was for a 15-year period (1964-1978). Inspection of the data from any near-equatorial station reveals that the amplitude and phase of the QBO is independent of longitude (Wallace 1973; Plumb et al. 1984). The stratification of the QBO indices was based on four seasons: March to May

(MAM), June-August (JJA), September to November (SON), and December to February (DJF). The standardized departures of the rainfall for East Africa from its 136 stations and 30-year (1964-1993) normals were calculated for the long-rains season of MAM. In view of the large variability of distribution of rainfall over the region, the analysis was based on the eight sub-regions (Figure 3.1) in order to examine the relationship of rainfall of those regions with QBO. Further details regarding the identification of the eight homogeneous sub-regions over eastern Africa, which are adopted in this study, are described in chapter 2 and in Indeje et al. (2000).

The methodology employed in this study was based on the application of the simple correlation analysis and rainfall composites based on the phase of the QBO. The aim of these analyses was to establish whether the QBO signal can offer any useful predictor variable information for use in seasonal prediction. Each of the 136 (32-year) rainfall indices and the regional rainfall index time series for eight sub-regions were first correlated with the equatorial averaged stratospheric zone wind in order to identify the spatial extent of the associations between QBO and rainfall. The sub-regions that significantly correlate with the QBO were identified and were cross-correlated with the SOI to test the contribution of each of the two global climate indices on the long-rains season. These sub-regional time series were then generalized into categories using contingency tables based on the west and east phases of the QBO. The primary attributes of the correlation analysis include simultaneous or zero lag, and the non-zero lag correlation analyses. The statistical significance of the correlation coefficient  $[r]$  was tested based on the Monte

Carlo t-scores that achieve 95% significance and the standard correlation tables (Neave 1978). Since the data was at varying length, statistical significance was attained at different correlation coefficient [ $r$ ] levels. The space and time patterns of the significant correlations were then used to investigate the relationships between QBO and SOI, and regional rainfall. The lag cross-correlation maps between rainfall and climate indices offer estimates of the domain and intensity of influence of global oscillators (SOI, QBO and SST) over recent decades (Jury et al. 1994). This study is part of an ongoing investigation, which aims at designing a comprehensive and objective, multi-variate-forecast system of seasonal rainfall over eastern Africa. Results obtained from this study are presented in the next section.

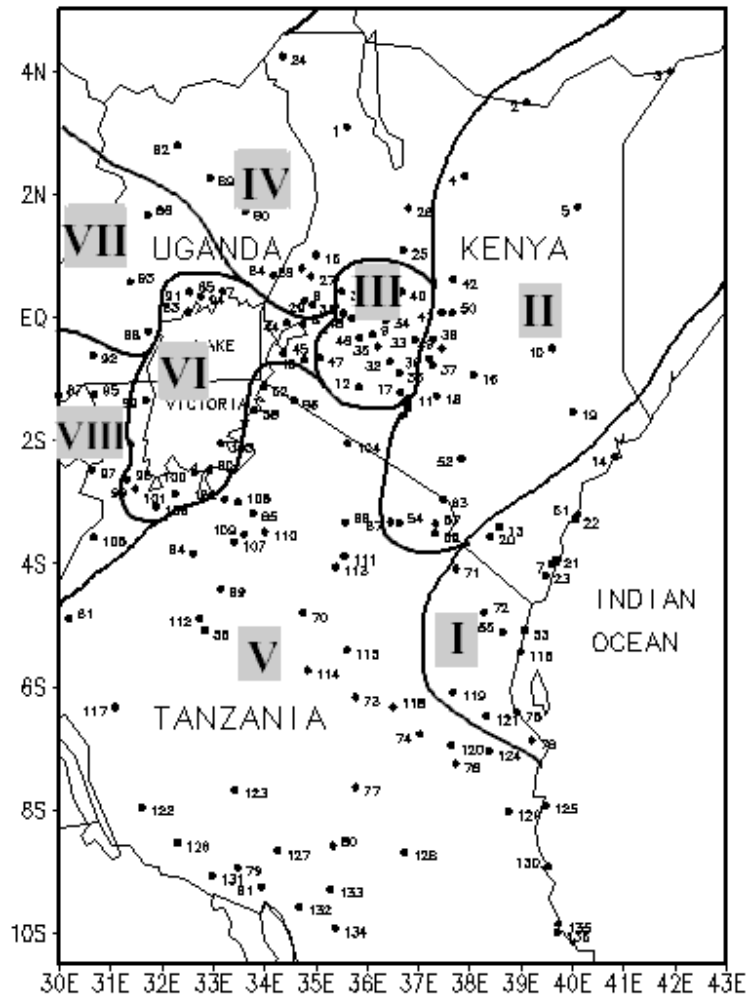


Figure 3.1: The eight homogeneous rainfall groupings over East Africa obtained from combined EOF and simple correlation analyses (Indeje et al. 2000).

### **3.3 Results**

#### **3.3.1 Relationships between seasonal rainfall and the QBO-index**

Spectral analysis has been performed on the rainfall time series in the eight homogeneous rainfall regions over equatorial eastern Africa and the results are shown in Figure 3.2. There is a dominant group of periodicities around 4-7 years, which may be associated with the ENSO phenomena. More interestingly, a pronounced QBO, with periods from 20-30 months are also dominant over regions 7 and 8 which corresponds to the western sector of eastern Africa. Nicholson (1996) showed a rainfall spectrum for eastern Africa as a whole that was dominated by a strong peak at 5 to 6 years, but significant peaks at 3.5 to 2.3 years were also evident suggesting that other than ENSO/SST forcing (5-6 years), there are other forcing mechanisms acting quasi-periodically with a time scale of about 2-3 years responsible for the interannual variability of rainfall in East Africa. These findings and others justify our investigation of the stratospheric (QBO) oscillator as an additional influence factor for tropical African climate variability. The basis for using the lower equatorial stratospheric zonal wind index in seasonal prediction are based on its tendency to persist for several months after the phase change from easterly to westerly and vice versa, is established.

Figure 3.3 show plots of simultaneous and lag correlations between the long-rains over homogeneous rainfall regions in eastern Africa and 30-mb QBO-Index for the period 1979-1992. Based on a the standard correlation tables (Neave 1978) on a sample size of 14 years, correlation coefficients  $[r] \geq 0.532$  are above 5 percent confidence level. Table

3.1 gives a summary of the seasonal and monthly correlation indices between the two variables. Results indicate significant simultaneous and lag correlations between the QBO-Index and rainfall over region 3, which covers the central and western highlands of Kenya (+0.8), the western parts of Uganda (Region 8) of about +0.8, the lake Victoria basin (Region 6) and the northern parts of Kenya and Uganda (Region 4). The QBO/rainfall correlations in these regions are significantly high for at least six months prior to the MAM rainfall season.

The highest significant correlations between seasonal rainfall and the QBO-Index of  $> +0.8$  are observed between the MAM rainfall index and the JJA QBO-Index of the previous year and decreases towards the target rainfall season (MAM). These lagged relationships between the two variables indicate high prospects for using them in the development of prediction methodology. However, the correlations suddenly collapse between 3 and 2 seasons lag for regions 7 and 8. The sudden collapse in correlations suggests that long-term prediction (of two seasons or more in advance) may not be feasible in these two regions. The JJA QBO-Index of the previous year can be used to predict the MAM rainfall season with significant skill. Significantly high zero lag and lagged correlations between the QBO-Index and MAM seasonal rainfall were also obtained in some stations over central parts of Tanzania of about 0.8.

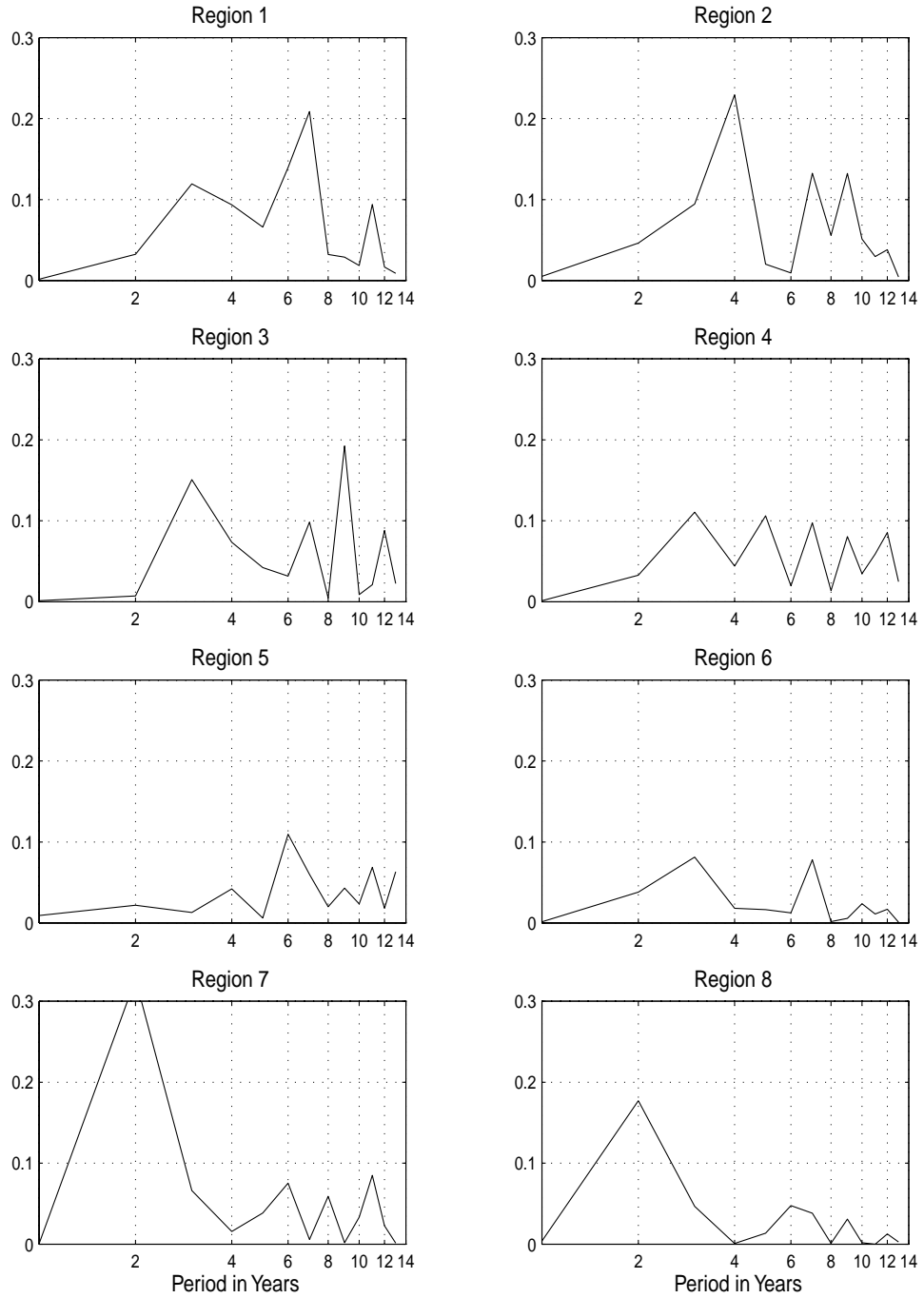


Figure 3.2: A power spectrum of annual rainfall time series for the eight homogeneous regions over eastern Africa. Values  $\geq 0.1$  on the y-axis are above confidence level of 95 percent.

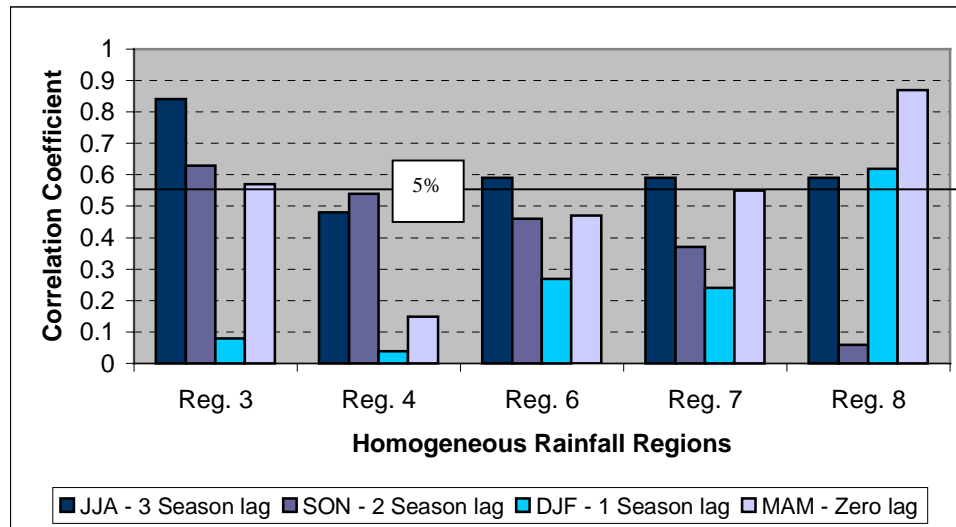


Figure 3.3: The mean correlation patterns of three seasons lag, two seasons lag, one season lag and zero lag between the QBO-Index and March-May (long-rains) season over East Africa. Correlation values above 5% significant levels are also indicated.

This pattern is positive during JJA and SON seasons and reverses sign to negative during the boreal winter. In these areas of Tanzania, some caution should be exercised in using the correlations for forecasting purposes because of the sudden reversal in the sign of correlation coefficient from JJA and SON seasons. Negative significant correlations are observed over the southern coast of East Africa. The observed areas of significant lag correlations suggest that seasonal prediction may be feasible in those areas. The physical aspects of the linkage between QBO and convection over eastern Africa are further discussed in section 3.4.

Figure 3.4 shows the comparison of the time series for rainfall (long-rains) over western highlands of East Africa, the QBO-Index and the SOI for March and July (previous year). Cross-correlation between the QBO-Index, rainfall and SOI was computed and the resulting indices are summarized in Table 3.2. These results show some good associations between QBO-Index and the regional rainfall with significant simultaneous and lag correlations of +0.53 (explaining about 26% of the variance) and +0.84 (explaining about 70% of the variance) respectively. The fact that the two global climate indices (QBO and SOI) are statistically unrelated at both simultaneous and lagged time, gives more confidence of using them as predictors of the seasonal rainfall with low risk of introducing artificial skill. The QBO-Index and SOI are found to be out of phase for most the analysis period. The notable phase locking of the two variables occurred during the year 1984. This year followed one of the strongest ENSO of the century, which was associated with severe drought over most parts of the East African region. These results clearly indicate the potential of using the QBO information for the prediction of the long-rains, which have a poor relationship with ENSO.

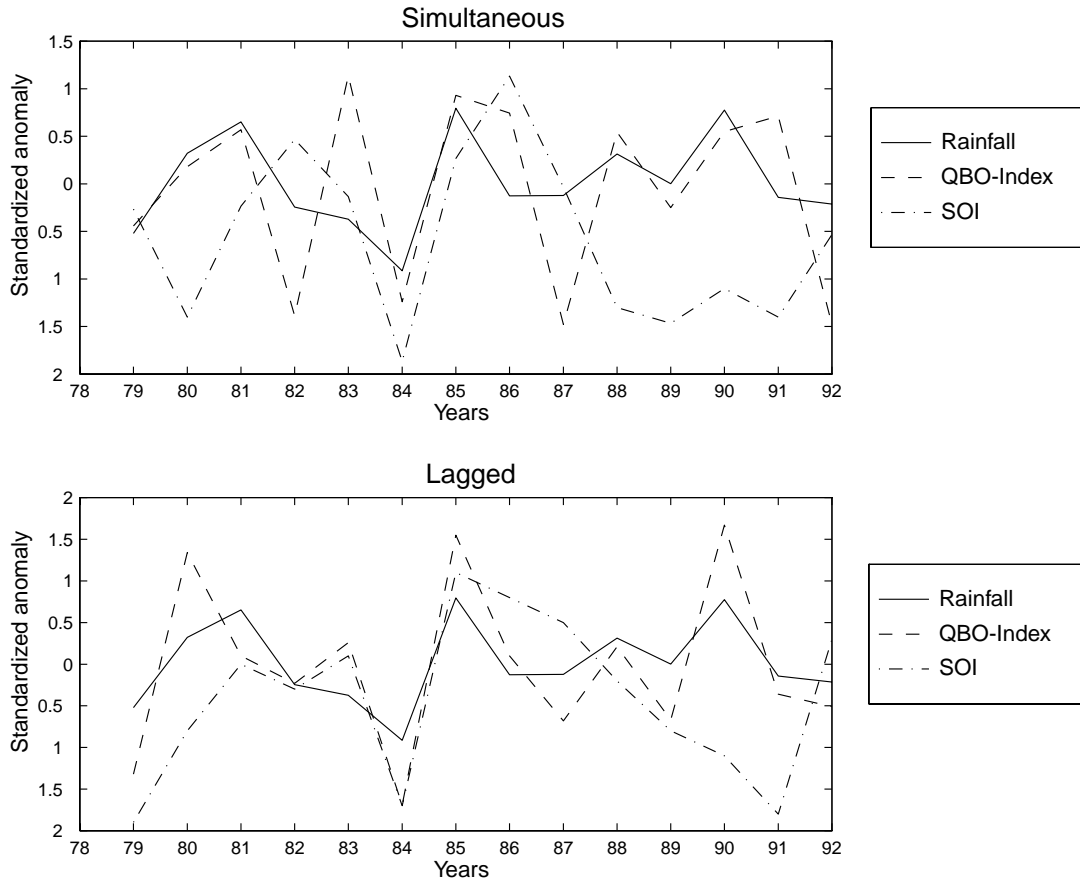


Figure 3.4: Time series of March-May (long rain) seasonal rainfall over central and western highlands of Kenya (Region 3), and March QBO-Index, and March SOI index (top) and, previous year July QBO-Index, and previous year July SOI index (bottom).

Table 3.1: Simultaneous and lag correlations [r], between the averaged equatorial stratospheric 30-mb zonal winds (QBO-Index) and MAM rainfall season over the eight homogeneous regions over East Africa. Bold and underlined values are above significant level of 10 percent based on a sample size of 14 years.

	REGION 1	REGION 2	REGION 3	REGION 4	REGION 5	REGION 6	REGION 7	REGION 8
JJA	-0.41	0.24	<b><u>0.84</u></b>	<b><u>0.48</u></b>	0.13	<b><u>0.59</u></b>	<b><u>0.59</u></b>	<b><u>0.59</u></b>
SON	-0.40	0.06	<b><u>0.63</u></b>	<b><u>0.54</u></b>	-0.02	<b><u>0.46</u></b>	0.37	0.06
DJF	0.32	0.36	0.08	0.04	-0.02	0.27	0.24	<b><u>0.62</u></b>
MAM	-0.08	0.33	<b><u>0.57</u></b>	0.15	0.11	<b><u>0.47</u></b>	<b><u>0.55</u></b>	<b><u>0.87</u></b>
JUNE	-0.37	0.21	<b><u>0.76</u></b>	0.30	0.09	<b><u>0.48</u></b>	<b><u>0.61</u></b>	<u>0.71</u>
JULY	-0.38	0.27	<b><u>0.84</u></b>	<b><u>0.49</u></b>	0.17	<b><u>0.59</u></b>	<b><u>0.60</u></b>	<u>0.61</u>
AUG	-0.41	0.20	<b><u>0.79</u></b>	<b><u>0.58</u></b>	0.11	<b><u>0.61</u></b>	<u>0.47</u>	0.35
SEPT	-0.42	0.12	<b><u>0.70</u></b>	<b><u>0.57</u></b>	0.05	<b><u>0.53</u></b>	0.39	0.18
OCT	-0.39	0.06	<b><u>0.62</u></b>	<b><u>0.54</u></b>	-0.02	<b><u>0.46</u></b>	0.36	0.05
NOV	-0.39	-0.02	<b><u>0.55</u></b>	<b><u>0.50</u></b>	-0.10	0.37	0.34	0.06
DEC	-0.43	-0.10	<b><u>0.46</u></b>	<b><u>0.46</u></b>	-0.08	0.26	0.24	-0.20
JAN	0.29	0.36	0.12	-0.02	-0.04	0.28	0.25	<u>0.63</u>
FEB	0.20	0.33	0.20	0.00	0.04	0.31	0.39	<u>0.70</u>
MAR	0.13	0.36	0.39	0.06	0.15	0.43	<u>0.48</u>	<u>0.83</u>
APR	-0.06	0.36	<b><u>0.53</u></b>	0.16	0.12	<b><u>0.47</u></b>	<u>0.54</u>	<u>0.87</u>
MAY	-0.26	0.25	<b><u>0.67</u></b>	0.20	0.06	0.45	<u>0.56</u>	<u>0.80</u>

Table 3.2: Simultaneous and lag cross-correlation matrix for Rainfall, QBO and SOI indices. The sample size is 14 years (1979-92) and correlation coefficient  $[r] > 0.53$  is significant at 5 percent level. Significant correlation values are bold and underlined.

	Rainfall Index (Region 3)	QBO Index (MAM)	SOI Index (MAM)	QBO Index (July)
QBO Index (MAM)	<b><u>0.57</u></b>			
SOI Index (MAM)	0.07	0.07		
QBO Index (July)	<b><u>0.84</u></b>	<b><u>0.62</u></b>	0.13	
SOI Index (July)	0.38	0.13	<b><u>0.69</u></b>	0.39

Having demonstrated the associations between the equatorial averaged 30-mb zonal wind index and the seasonal rainfall over some regions of eastern Africa, the next step is to test the stability of these relationships by using a longer time series of equatorial lower stratospheric zonal winds and rainfall anomalies. We employed the Singapore observed 30-mb zonal wind to supplement the QBO-Index. Examination of the two data sets indicates that they are very highly correlated. Wallace (1973) indicated that due to the zonal symmetry, the QBO in the equatorial stratosphere could be well represented by a single station. This station being close to the equator, the annual cycle is dominated by distinct oscillation with average periodicity of slightly more than 2 years. In the next sub-

section we examine the robustness of the conclusions based on the QBO index as well as examining the prediction potential of the seasonal rainfall based on the phases of this index.

### **3.3.2 Predictability potentials of seasonal rainfall using the equatorial stratospheric QBO-Index**

Figure 3.5 shows the time evolution of the QBO-Index and the SOI for the period 1964-1997. The figures show years with westerly and easterly phases of the QBO-Index and SOI. The west phases of the QBO-Index were observed during 1963, 1966, 1969, 1971, 1973, 1975, 1978, 1980, 1983, 1985, 1986, 1988, 1990, 1993, 1995 and 1997 and, east phases during 1965, 1968, 1970, 1972, 1974, 1976/77, 1979, 1982, 1984, 1987, 1989, 1992, 1994 and 1996. These observations agree with those of Mukherjee (1985), and Brier (1978) using 30-mb zonal wind data from Balboa (9°N, 80°W) and, Ogallo et al., (1994) using zonal wind components for Nairobi, Kenya (1° 18'S, 36° 45'E). The QBO was relatively stationary during the years 1964-74. During recent period 1975-1994 there was a strong westerly event followed by two consecutive easterlies. The SOI on the other hand, exhibited a positive phase in the 1960's and early 1970's. From the early 1980's to-date, the frequent negative phases have been dominant in the SOI. During the years: 1965, 1972, 1977, 1979, 1982, 1984, 1987, 1992 and 1994, the east phase of the QBO-Index coincided with the low (negative) phase of the SOI. All these years with exception of 1984 and 1994 have been classified as ENSO years (Trenberth 1997). This observation is consistent with the notion that ENSO tends to be associated with the east phase of the QBO.

Figure 3.6 shows the time series of rainfall from three regions of East Africa that we have identified to have significant correlation with the QBO-Index. Generalizations of the seasonal rainfall in these three regions into categories using contingency tables and the west and east phases of the QBO are summarized in Table 3.3. Based on these three regions, stratospheric westerly wind phases corresponding to above normal rainfall, were observed during 8 of the 13 cases for region 3, 6 out of 13 for region 7 and, 7 out of 13 for region 8, giving conditional probabilities of about 0.6, 0.5, and 0.55 for the associations of above normal rainfall during the long-rains over equatorial eastern African region and west phase of the QBO. Similar results were observed by Ogallo et al. (1994). Years with below normal rainfall coinciding with the westerly phase of the QBO were observed during 1966, 1973 and 1983. These years have been classified as strong and prolonged ENSO years (Trenberth 1997). Many studies have been done on ENSO/rainfall relations in the region. Stratospheric east wind phases and below normal rainfall shows 8 out of 12 for region 3, 8 out of 12 for region 4 and, 8 out of 12 for region 8, giving conditional probabilities of about 0.7 for below normal rainfall in the three regions and the east phase of the stratospheric zonal wind. Associations between the two variables (rainfall and QBO) are more marked after the year 1979 onwards.

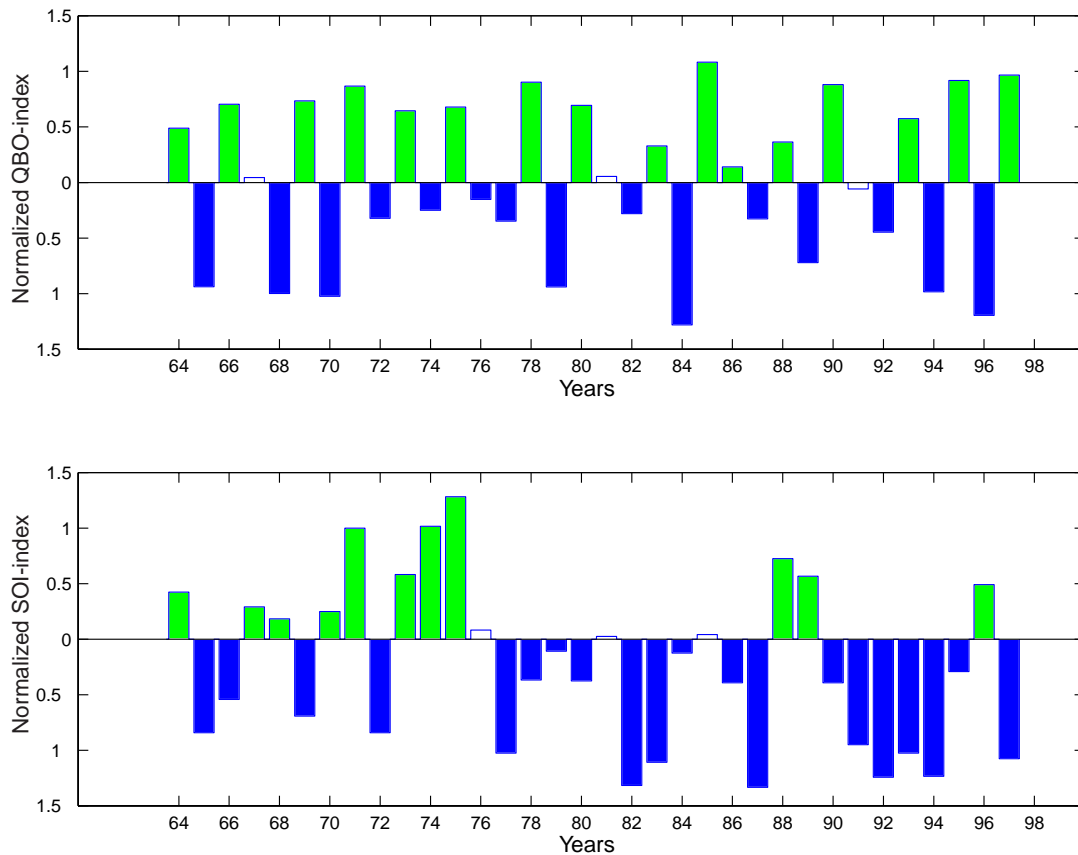


Figure 3.5: Annual mean time series for QBO-Index (top) and SOI index (bottom). Standardized values  $\geq 0.1$  and  $\leq -0.1$  are shaded.

The results obtained in this study support the notion that above/below normal rainfall is associated with the stratospheric westerly/easterly zonal wind phases. About 60 percent probability is found between the west phase of the QBO and rainfall over eastern Africa. The relationship fails during years of strong ENSO events. The low-level easterly transport of moisture in the region from the Indian Ocean by the monsoonal wind system maybe responsible for the association between upper level westerly (easterly) wind phases

and the corresponding above (below) normal rainfall conditions over eastern Africa (Ogallo et al. 1994). These good associations between phases of QBO and seasonal rainfall indicate encouraging potential for rainfall predictability using the information about the QBO phases.

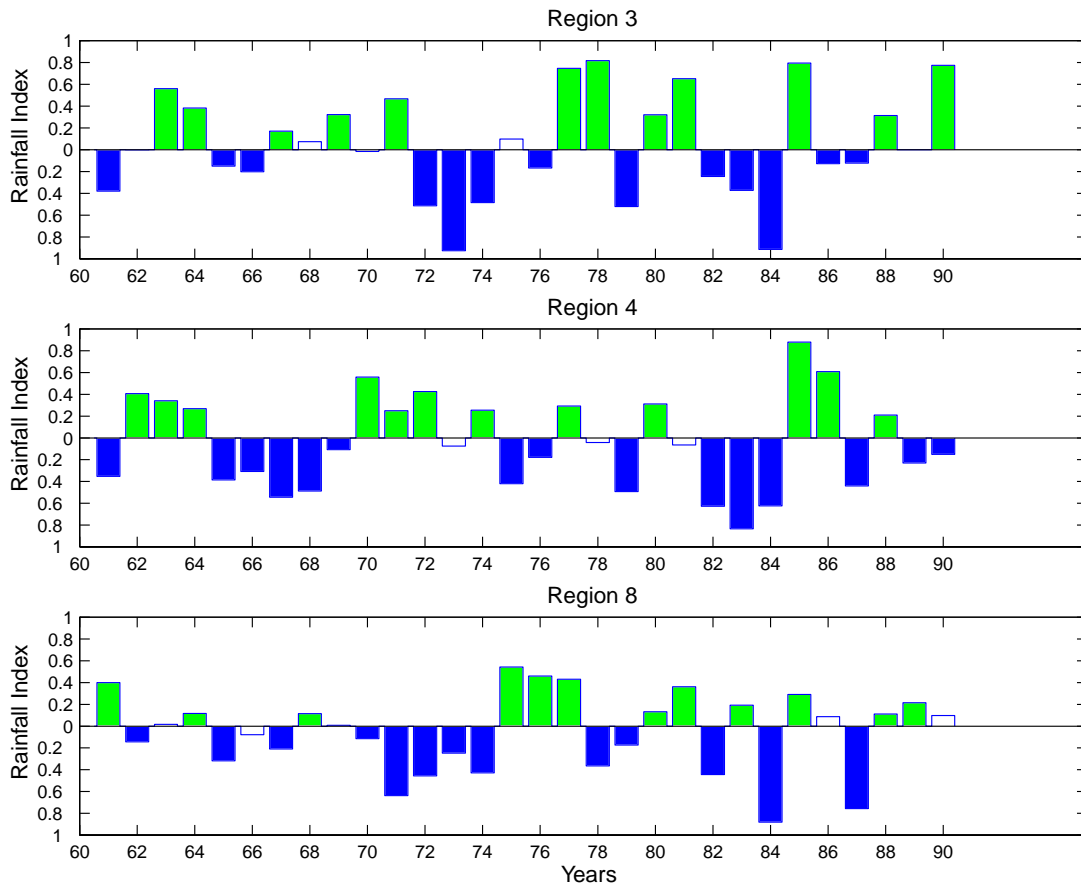


Figure 3.6: Time series of standardized rainfall for three homogeneous regions: Region 3; central Kenya (top), Region 4; northwestern Kenya and northern Uganda (middle), and, Region 8; western Uganda (bottom). Shading information is similar to that in Figure 3.5.

Significant correlations between rainfall in Regions 3 and 4 and the QBO-Index persists for two seasons prior to the long-rains season, but collapses in Regions 6, 7 and 8. We note that the tendency analyses (shown in Figure 3.8) may work well for the two regions (3 and 4), but perhaps not for Regions 6, 7 and 8. In the rest of the analyses, we use the rainfall index for Region 3 as an example for testing the prediction potential of rainfall using the QBO-Index. In Figure 3.7, we present the July QBO-Index prior to the onset of the long-rains which indicated a high significant correlation with the MAM seasonal rainfall over the central and western highlands of eastern Africa. It is evident from this figure that about 60 percent of the large positive/negative anomalies in the rainfall were observed during the periods of large positive/negative QBO-index. Some of the extreme rainfall anomalies were however, not related to the QBO-index. Using a time series of 32 years (1964-1995), for the QBO-Index and sub-regional rainfall, the correlation coefficient is found to be 0.55, which is above significant level of one percent based on the standard correlation tables (Neave 1978). This highly significant correlation with a time series of more than 30 years, indicate some robust associations between the seasonal rainfall and the QBO. The shown robust relationship between the long-rains and the QBO-Index shows high predictive potential.

Table 3.3: Contingency tables for zonal wind phases at 30-mb level and the MAM seasonal rainfall anomalies over three climatic regions of equatorial eastern Africa.

		Rainfall Anomaly			
	QBO Phases	AN	NN	BN	Total
Region 3					
	West Phase	8	1	4	13
	East Phase	1	3	8	12
	Total	9	4	12	25
Region 4					
	West Phase	6	1	6	13
	East Phase	4	0	8	12
	Total	10	1	14	25
Region 8					
	West Phase	7	2	4	13
	East Phase	4	0	8	12
	Total	11	2	12	25

AN - Above Normal rainfall ( $X_i \geq X_{\text{mean}} + 0.1\sigma$ )

BN – Below Normal rainfall ( $X_i < X_{\text{mean}} - 0.1\sigma$ )

NN – Near Normal rainfall ( $X_{\text{mean}} - 0.1\sigma \leq X_i \leq X_{\text{mean}} + 0.1\sigma$ )

$\sigma$  is the standard deviation

$x_i$  denotes an observation

Figure 3.8 shows a composite of normalized seasonal rainfall and mean monthly stratospheric wind phases for high- and low-rainfall years. In the composite analysis we used the years with above normal rainfall and coinciding with west phases of the QBO and years with below normal rainfall and coinciding with the east phases of the QBO. The years 1964, 1969, 1971, 1975, 1978, 1980, 1985, 1988 and 1990 having a standardized rainfall index of  $\geq +0.10$  were classified as high-rainfall and the years 1965, 1972, 1974, 1976, 1979, 1982, 1984, 1986, 1987, 1989 and 1994, having a standardized rainfall index  $\leq -0.1$ , classified as low-rainfall years. The choice of this range of the standardized rainfall index is based on a student t-test applied on a sample size of 32 years. The t-scores on the high- and low-rainfall indices indicate that the two series are significantly different at 95 % significance level. In the figure, the months are presented along the abscissa and the vertical axis corresponds to the normalized QBO-Index. The central block of the graph denotes the boreal spring months for which the seasonal rainfall was considered while the block to the left indicates the QBO-Index tendency prior to the rainfall season. The QBO-Index trend increases/decreases from JJA to DJF before the occurrence of high/low MAM seasonal rainfall. Large positive anomalies of the long-rains are found to coincide with the maximum westerly phase of the lower equatorial stratospheric zonal winds when maximum heating due to the overhead sun occurs, thus suggesting possible role of the annual cycle in modulating the QBO.

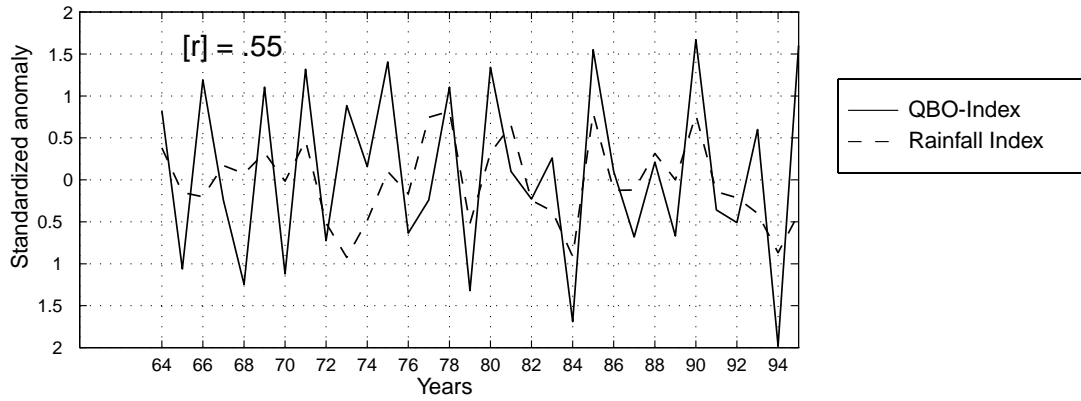


Figure 3.7: Time series of rainfall over central and western highlands of Kenya (Region 3) and the QBO-Index.

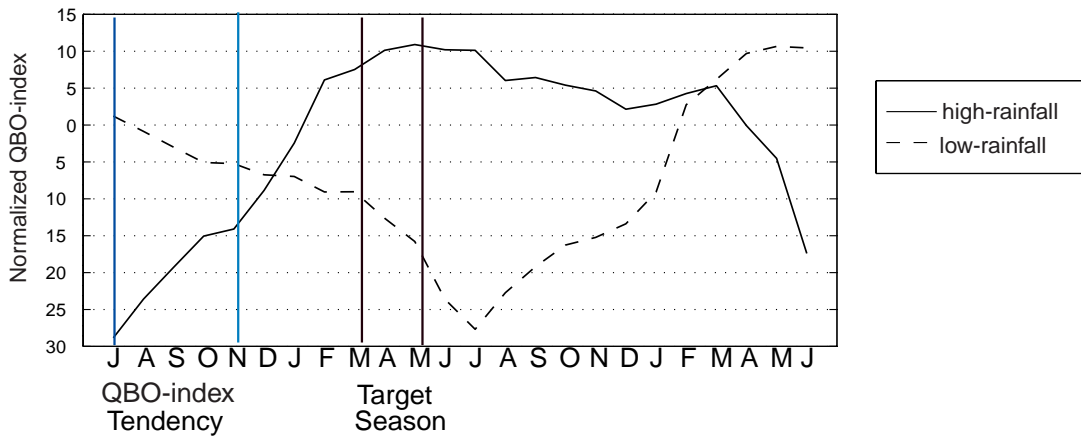


Figure 3.8: Composite plot for the QBO-Index corresponding to high- and low-March to May seasonal rainfall years.

Because of this striking QBO-Index anomaly in the pre-rainfall months and the composite MAM seasonal rainfall, we have examined the association between pre-MAM QBO trend and MAM seasonal rainfall over eastern Africa. For the purpose of predicting the regional rainfall, the most useful index appears to be the trend for QBO-Index before the rainfall season. The positive OND minus JJA QBO trend could be a good indicator for the non-occurrence of drought over eastern Africa. Similarly, a negative trend could be a good indicator for the non-occurrence of high rainfall over the region.

Figure 3.9 shows a scatter diagram between March-May seasonal rainfall anomaly over central and western highlands of East Africa (top panel) and, the October to December minus June to August trend in the QBO-Index (lower panel). The correlation coefficient between the East African rainfall anomaly from region 3 and the difference between OND and DJF QBO-Index is 0.6 (explaining about 36% of the rainfall variance) which is higher than that for JJA season (0.5). As shown on Figure 3.9 (bottom panel), most of the severe drought years are in the lower left quadrant, and most of the very heavy rainfall years are in the upper right quadrant of the scatter diagram. The near absence of points in the lower right corner of this scatter diagram suggests that a positive QBO-Index trend should be a very useful predictor for non-occurrence of droughts over eastern Africa. An ENSO phenomenon is known to be a fundamental and periodic part of the ocean-atmosphere system, with periodicity of about 3 to 8 years (Rasmusson and Carpenter 1983). Some extreme rainfall anomalies in East Africa have been associated to ENSO (Ropelewski and

Halpert 1987; Janowiak, 1988; Ogallo 1988; Nicholson 1996), among others. If an El Niño has already been observed in the preceding winter and spring, a prediction of deficient MAM seasonal rainfall over eastern Africa can be made with some degree of confidence (Nicholson 1996; Indeje et al. 2000). But the relationship between the MAM seasonal rainfall and El Niño applies to a limited number of years, the ones when El Niño occurs, whereas the relationship between the QBO-Index and seasonal rainfall is applicable in all years. Monitoring of both the parameters can provide very useful guidance for the long-range forecasting of seasonal rainfall over the region. This observation suggests a conditional probability, thus during the westerly phases of QBO-index and when a strong ENSO episode is not expected in the following boreal winter, then there are high chances for the occurrence of above normal MAM seasonal rainfall conditions over eastern Africa and vice versa for the easterly phase of the QBO-index. Results from correlation analysis ( $[r]=0.55$  based on 32-year period) indicate that QBO in the equatorial lower stratospheric zonal winds explains a maximum of about 36 percent of the rainfall variance over the central and western highlands of East Africa during March to May season. These areas being highly agricultural productive, accurate seasonal climate prediction would be a step toward improving the planning stages in the industry. Monitoring of the equatorial lower stratospheric zonal wind phases can hence provide useful guidance for the long-range forecasting of the long-rains over eastern Africa.

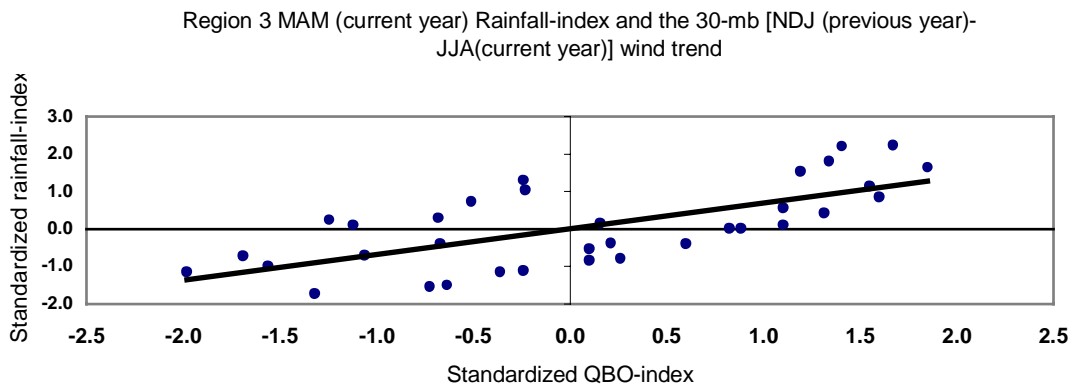
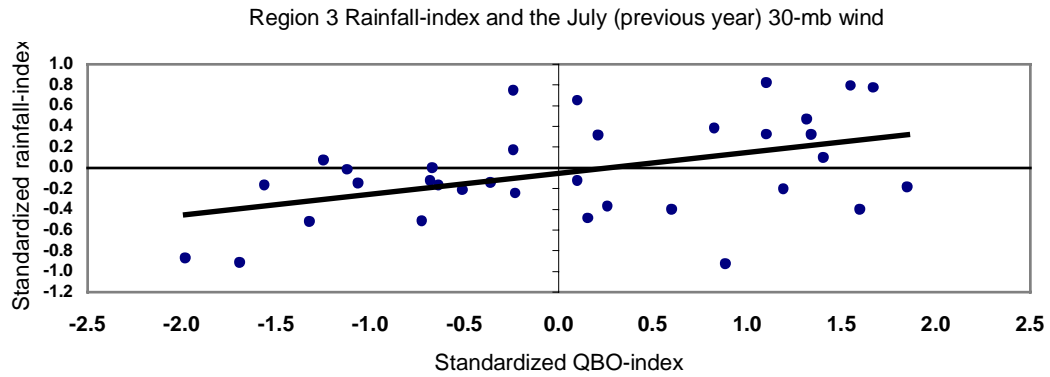


Figure 3.9: Scatter diagram between MAM seasonal rainfall anomaly over central and western highlands of Kenya and the July 30-mb equatorial zonal wind (top), and the October to December minus June to August trend in the QBO-Index (bottom).

### **3.4 Discussion**

There are two primary questions which arise from our analysis, (i) the physical mechanisms responsible for the strong teleconnections between the long-rains of equatorial eastern Africa and the QO-index, and (ii) the weakening of this relationship with decreasing time lag between the two phenomena. As noted above, the physics of the stratospheric equatorial QBO has been extensively investigated (Holton and Lindzen 1972; Plumb 1977; Holton and Tan 1980). The traditional explanation for the development of this type of the QBO is based on the alternating downward propagating patterns of westerly and easterly mean zonal winds which repeat with somewhat irregular period averaging about 26 months. However, recently Webster et al. (1999) have proposed a coupled ocean-atmosphere mechanism over the Indian ocean sector which may offer an alternative explanation, and which seems to have been responsible for the prolonged SST anomaly conditions during the recent 1997/98 ENSO event. Their results show that this mechanism which involves a sequence of thermal and dynamical processes may also account for the major warming event of 1961-62 when the normal SST gradient across the Indian Ocean reversed and resulted in substantial warming in the western basin and flooding over eastern Africa. Webster et al. (1999) and Saji et al. (1999) have shown that the summer monsoons following west Indian Ocean warming should have stronger winds in the western basin, which would induce greater mixing, greater Ekman transport forcing coastal upwelling, and greater evaporation, all of which would contribute to rapid cooling. They refer to the large-scale interactions between the Indian Ocean and the overlying atmosphere as the dipole mode index (DMI). During the low phase of the DMI, there is

massive cooling over the western Indian Ocean and relative warming over the eastern sector of the Indian Ocean. A reversed Walker-like atmospheric circulation associated with the low DMI is a consequence of this temperature gradient over the ocean with rising/sinking motion over the eastern/western parts of the ocean. Between 1950 and 1998 there were 16 years in which the equatorial SST gradient reversed with spectral peaks around 2 years (Webster et al. 1999). We postulate that the reversal in the SST gradient associated with the Indian Ocean climate system may also provide an alternative explanation for the reversal in the upper air winds, usually explained in terms of the alternating downward propagating patterns of westerly and easterly mean zonal winds.

Figure 3.10 is a schematic representation depicting the interaction among, the basic Walker circulation overturning over the Indian Ocean region, the anomaly circulation associated with the Indian Ocean SST dipole, and the equatorial winds associated with the QBO. Under normal conditions the Indian Ocean is warmer in the east and slightly cooler in the west, thus inducing low level winds blowing from the west to the east, and easterlies aloft (Webster et al. 1999). Therefore, the normal SST conditions over the Indian Ocean are in phase with the easterly phase of the QBO. This flow pattern is coupled with the two major ascending branches of the Walker circulation over Africa and the Maritime continent (i.e. the Indonesia region). The net result is a vertical cell structure characterized by rising motion and upper level outflow over central Africa and the Maritime continent, and the compensating descending motion over the western region of the Indian ocean (Holton 1972).

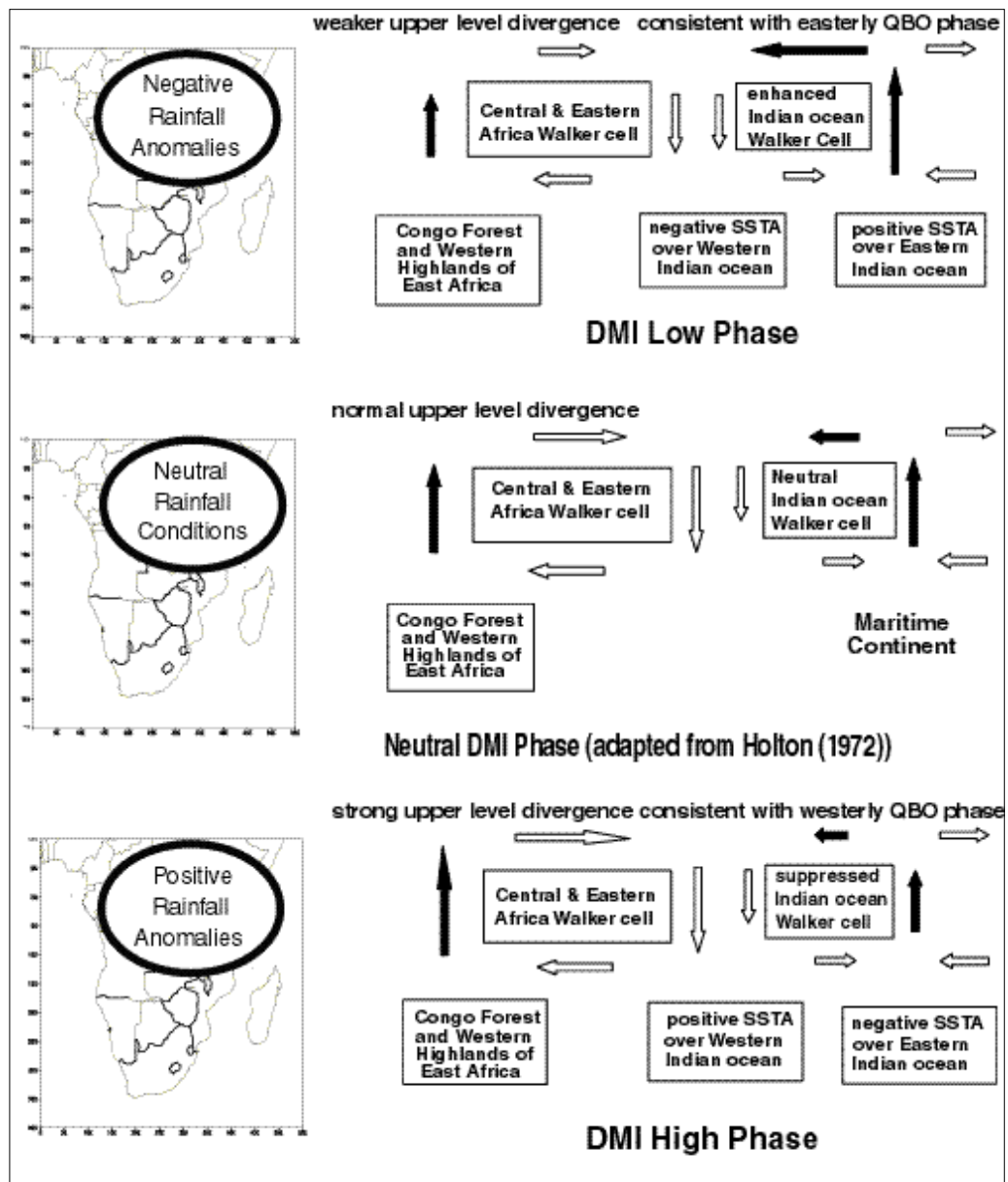


Figure 3.10: Conceptual model representing the west phase of QBO and tropical convection over eastern Africa. DMI is the climate mode dipole index over the Indian Ocean (Webster et al. 1999, and Saji et al. 1999).

During the opposite phase of the Indian ocean SST dipole, the conditions are warmer over the western part of the ocean basin than in the east, and therefore tend to induce low/upper level easterlies/westerlies, thus consistent with the westerly phase of the QBO. We envisage that this flow structure would lead to a sequence of events, characterized by enhanced upper level divergence from the African continental land-mass, and increased ascending motion and rainfall over the Congo tropical rain forest and the western Highlands of East Africa. This conceptual model is consistent with our analysis, which indicates that the westerly phase of the QBO is associated with abundant rainfall over eastern Africa and reduced precipitation during its easterly phase. The simple framework proposed here, indicate that the quasi-biennial variability of the DMI could induce upper level flow, which may partly explain the QBO phenomenon. The three-way co-variability among, the rainfall over East Africa, the QBO and DMI, may provide an important clues regarding the dynamical links which should be examined more comprehensively in the future, using theoretical and numerical models to understand the physical mechanisms involved.

The reasons for the weakening of the correlation between the QBO-Index and rainfall over eastern Africa, with decreasing time lag are not entirely clear based on the hypothesis proposed above. However, we believe this observation may provide important clues regarding the physical mechanisms involved. We speculate that the primary factor responsible for modulating the long-rains is the Indian Ocean 'warm pool', which propagates across the ocean basin and completes the cycle on a quasi-biennial time scale.

Its propagation appears to be phase-locked with the annual cycle, with maximum amplitude along the coast of Africa occurring during the months of the long-rains. Several recent studies (Nicholson 1996; Jury et al. 1994) provide indirect support for our proposed conceptual model. Nicholson (1996) also described evidence that the low-level divergence and sinking motion over the cool western Indian Ocean may be associated with low- and mid-tropospheric moisture transport in the interior of the East African region. This advected moisture would support the convective activities over the western highlands of eastern Africa, which through the release of latent heat would sustain the east-west Walker-like circulation between the western highlands of eastern Africa and the western Indian Ocean. Over the Indian Ocean, the reversed DMI circulation would be accompanied by rising/sinking motion over eastern/western parts of the ocean.

## Chapter 4

### 4 SEASONAL PREDICTABILITY OF RAINFALL IN EQUATORIAL EASTERN AFRICA BASED ON TROPICAL PACIFIC OCEAN SEA-SURFACE TEMPERATURES

In this study, we utilize the Canonical correlation analysis (CCA) method to construct all empirical models for the prediction of seasonal rainfall of equatorial eastern Africa based on the tropical Pacific sea surface temperature (SST). Empirical Orthogonal Function (EOF) analysis is employed first to reduce the large dimensionality of the SST and rainfall data and the leading nine eigenmodes of SST are retained as predictors for the homogeneous climatic regions of equatorial eastern Africa. The condensed SST and rainfall data are then subjected to a CCA procedure in order to establish the existing relationships between SST prior to the forecast time and rainfall in the specific climatic zones of eastern Africa. The observed lagged relationships are then used in developing a CCA prediction model for the seasonal rainfall.

#### 4.1 *Background*

Climate prediction has been recognized as an important objective in recent research initiatives at the national and international levels. The need to investigate the mechanisms responsible for tropical rainfall anomalies motivated the development of tropical climate prediction methods in the 1980's (Hasternrath 1985). These methods are being applied to climate predictions over many parts of the world. The economies of the African countries

including the equatorial eastern African region depend on agriculture and water resources, which are strongly dependent on the occurrence of anomalous climate variability. Thus, a better understanding of the variability and predictability of the precipitation regime over the region is of primary importance.

Monitoring of sea surface temperatures, in near real time provide vital input to seasonal climate prediction. This is much so with the sea level anomaly that provide a useful index, which may reflect the combined effects of barometric and wind forcing on the seasonal time-scale especially those associated with El Niño/Southern Oscillation (ENSO) events (Smith 1994). Several investigators have associated regional climate variability to the SST of the oceans in the neighborhood of those regions (Parker et al. 1988; Ward and Folland 1991; Nicholls 1984; Smith 1994 among others). Parker et al. (1988), and Ward and Folland (1991) demonstrated how statistical seasonal rainfall predictions for the Sahel region and northern Brazil could be made using the evolution of the SST patterns in the Atlantic and Pacific Oceans. Smith (1994) related the principal components derived from Indian Ocean SST anomalies to the Australian winter rainfall using regression analysis, and found significant simultaneous correlations between the dominant patterns in the Indian SST and the wintertime rainfall over large parts of Australia. Mason (1998) used SST from the global basin to develop a quadratic discriminant analysis model for forecasting rainfall over southern Africa. His model produced skilful forecast shortly before or soon after the start of summer rainfall that could have significant operational value.

Studies by Rowell et al. (1994), Ininda (1998), Nyenzi (1992), Ogallo (1988), Indeje (1995), and Semazzi and Indeje (1999) have explained the link between the seasonal rainfall over East Africa and the SST in the global oceans. Ogallo et al. (1988) observed significant lagged correlations between SST anomalies and rainfall Principal Component (PC) modes in East Africa. Significant negative correlations between the summer rainfall over the western regions and SST anomalies over parts of the equatorial Atlantic Ocean, North Indian and Arabic Sea regions were observed. Rowell et al. (1994) showed strong correlations between East African rainfall and global SST on the monthly time scales during the short rains season. The lack of the significant correlations during the month of April was attributed to the internal chaotic atmospheric circulations. Ininda (1998) observed positive correlations between short rains and SST over Arabian Sea, central and eastern tropical Pacific Ocean. Negative significant correlations between East African rainfall and SST over the east and central Pacific, and South Atlantic Ocean were observed during the month of March. Semazzi and Indeje (1999) have showed a pattern that travels around Africa in response to migratory rainfall-ENSO variability during the annual cycle.

Various statistical approaches based on EOF, CCA and multiple linear regression (MLR) have been employed to investigate regional climate variability with success (Barnett and Preisendorfer 1987; Graham 1990; Barnston 1994; Barnston and Smith 1996; Barnston et al. 1996 among others). CCA is a multivariate statistical technique that calculates linear

combinations of a set of predictors that maximizes relationships in a least square sense to the similarly calculated linear combinations of a set of predictand. The superiority of CCA over other several techniques is its ability to operate on full fields of information and to objectively define the most highly related patterns of predictor and predictand. Barnett and Preisendorfer (1987) showed a comprehensive description of CCA maps and their corresponding vectors. The map patterns show the relation at a specific location between the predictor and predictand fields and their respective canonical component time series. By investigating the temporal variability of the canonical coefficients and the predictor and predictand correlation patterns, it is possible to draw inferences about the nature of the predictor (ocean-atmosphere interaction) field that contribute to the variability in the predictand (rainfall) field. CCA can also be viewed as a special form of EOF analysis where the correlation structure between predictor and predictand data sets is described more completely with each successive CCA mode (Barnston and Smith 1996).

The mechanisms responsible for the spatial and temporal variability of rainfall in equatorial eastern Africa are beginning to be understood at the regional level (Ogallo 1988; Nyenzi 1992; Beltrando 1990; Camberlin 1995; Nicholson 1996), but investigations into the predictive potential of seasonal rainfall has been less well elucidated. Barnston et al. (1996) investigated the predictability potential of rainfall over regions of Africa including East Africa using statistical methods. Their results were not very encouraging over many parts of East Africa apart from Meru (central Kenya) where the relationships between the predictor and predictand were significant. The reason for the weak relationships may have

been attributed to the sparse station network (16 stations over East Africa) that they used in their study. An investigation into the study and evaluation of the teleconnections between the rainy seasons over eastern Africa and the SST anomalies over the Pacific Ocean is addressed in this study. A total of 144 rainfall stations well distributed over the region are used in the study. The aim is to statistically evaluate the role of the tropical Pacific SST anomalies on the seasonal rainfall over the region, focusing on the occurrences of anomalously dry and wet conditions. The study also assesses the long lead predictability of seasonal rainfall using SST in tropical Pacific as a predictor. The Pacific Ocean basin was chosen for this study because it is the source of the ENSO signal and the advances made in monitoring and measuring the SST in the ocean makes it possible to be utilized in climate forecasting in near real time. Also, whereas the Indian Ocean SST variability may have changed in the recent years especially after the warming in the late-1970s, the SST variability in the Pacific Ocean has remained stable (Landman and Mason 1999).

#### **4.2 Data and Methodology**

The precipitation anomaly (predictand) data used in this study consisted of monthly rainfall records for one hundred and forty four stations scattered over the equatorial eastern African region. Time series of monthly rainfall were computed at each station based on the 1961-90 climatology. Of the 144 stations, 54 synoptic stations were used in the forecast evaluation of the 1997 prediction. Two seasonal averaged precipitation anomalies for the long-rains of MAM and the short-rains of OND were extracted from the monthly series. The SST data used in constructing the prediction model was obtained from

the United Kingdom data set archived at the National Centers for Environmental Prediction-National Center for Atmospheric Research (NCEP-NCAR). This data covered the period 1961-1990 and was available on a  $1^{\circ} \times 1^{\circ}$  horizontal grid. This SST data was then interpolated to a  $2^{\circ} \times 2^{\circ}$ -grid spacing over the Pacific Ocean basin ( $30.5^{\circ}\text{N} - 29.5^{\circ}\text{S}$ ;  $120.5^{\circ}\text{E} - 67.5^{\circ}\text{W}$ ) in order not to overload the processor. The anomaly SST values at each grid point were defined as departures from 1961-90 climatology. For the period 1997, monthly values corresponding to Optimum Interpolation (OI) SST data (Reynolds and Smith 1994) were used in the model prediction. These SST data utilizes in situ observed data from ships and buoys and from bias-corrected satellite data.

Prior to performing the EOF and CCA, each predictor and predictand data element was standardized, ensuring that equally good predictors have equal opportunity to govern the forecasts, regardless of their original variance. This was accomplished by removing the long-term mean from the monthly data set and dividing it by the corresponding standard deviation. The rainfall and SST data fields were subjected to EOF analysis in order to compress and allow the temporal evolution (principal components) of dominant modes in these fields to be depicted. This was accomplished by projecting original data onto independent and mutually orthogonal space vectors (eigenvector) and then retaining only a limited dominant number of the EOF modes in the analysis. The EOF technique used in this study is described in chapter 2. The EOF modes explaining more than 80% of the cumulated variance for both predictor and predictand were retained for input in the prediction model.

The CCA statistical technique was then employed to test the predictability of seasonal rainfall over equatorial eastern Africa using the training period of 1961-1990. A three months time lag using July and December SST anomalies respectively was used to forecast the OND and the following year MAM rainfall seasons. The objective of this exercise was to assess the seasonal and spatial characteristics of the rainfall predictability based on the tropical Pacific SST. The constructed CCA model was finally utilized in the prediction of the OND rains of the 1997 (the year that was associated with one of the strongest ENSO of the century). The overall prediction skill of the CCA model was determined using standard statistical techniques including correlation, root-mean-square error (rmse), cross-validation and Heidke skill scores (SS). The CCA approach used in this study is described in the next subsection.

#### **4.2.1 Canonical Correlation Analysis (CCA)**

CCA technique is used in this investigation to measure the strength of the combination of the strong predictor/predictand relationships, and to suggest their spatial and temporal structure in terms of the leading modes, and thus aiding in their physical interpretation. The CCA approach used in this study follows that of Barnett and Preisendorfer (1987) and Graham (1990). The steps followed in this procedure are as follows

(a) Consider  $Y(x,t)$  and  $T(x',t)$  as predictor and predictand fields respectively given by their truncated principal components

$$Y(x,t) = \sum_{j=1}^p \kappa_j^{1/2} \alpha_j(t) e_j(x), \quad x = 1, 2, \dots, p, \quad 4.1$$

$$T(x',t) = \sum_{k=1}^q \lambda_k^{1/2} \beta_k(t) f_k(x), \quad x' = 1,2,\dots,q, \quad 4.2$$

where ( $p$  and  $q$ ) are the truncated limits,  $k_j$  and  $l_k$  are the eigenvalues of predictor and predictand respectively,  $e_j$  and  $f_k$  are the eigenvectors of predictor and predictand respectively, and  $\alpha_j(t)$  and  $\beta_k(t)$  are normalized principal components of predictor and predictand respectively and are evaluated as follows;

$$\alpha_j(t) = \kappa_j^{-1/2} \left[ \sum_{x=1}^p Y(x,t) e_j(x) \right], \quad j = 1,2,\dots,p, \quad 4.3$$

$$\beta_k(t) = \lambda_k^{-1/2} \left[ \sum_{x'=1}^q T(x',t) f_k(x') \right], \quad k = 1,2,\dots,q; t = 1,2,\dots,N. \quad 4.4$$

(b) Compute the canonical vectors ( $r_j$  and  $s_k$ ) and canonical correlation ( $\mu_j$  and  $\mu_k$ ) and predictand respectively given by;

$$[CC^T]r_j = \mu_j^2 r_j, \quad 4.5$$

$$[CC^T]s_k = \mu_k^2 s_k, \quad 4.6$$

$C$  is a ( $p \times q$ ) matrix whose elements are

$$C_{jk} = \langle \alpha_j(t) \beta_k(t) \rangle_t, \quad 4.7$$

where  $\langle \rangle_t$  denotes an average over  $t = 1,2,\dots,N$ .

(c) Compute the canonical temporal functions  $u_j$  and  $v_k$  of the predictor and predictand respectively using the equation;

$$v_k = \sum_{i=1}^p \beta_i S_{ij}, \quad 4.8$$

$$u_j = \sum_{i=1}^p \alpha_i r_{ij}, \quad 4.9$$

where  $u_j$  and  $v_k$  each form ortho-normal set of vectors.

(d) Compute the canonical correlation maps  $g_j$  between  $u_j$  and the predictor field, and  $h_k$  between  $v_k$  and the predictand field using the equations;

$$h_k(x') = \frac{\langle T(x',t)v_k(t) \rangle_t}{\left[ \frac{1}{q-1} \sum_{x'=1}^q T(x',t)^2 \right]^{1/2}}. \quad 4.10$$

$$g_j(x) = \frac{\langle Y(x,t)u_j(t) \rangle_t}{\left[ \frac{1}{p-1} \sum_{x=1}^p Y(x,t)^2 \right]^{1/2}}. \quad 4.11$$

#### 4.2.2 Model Validation Techniques

Model validation is usually an important component of model construction. Wilks (1995) suggested a method for model validation that has been adopted in many studies. The method involves constructing the model using a subset of data available and then testing the constructed model over the remaining periods. In order to compare our empirical model performance with other similar studies done on long-range climate predictability in the tropics (Nicholls 1984, Hastenrath 1987, and Folland et al. 1991), we adopted the following validation methods

- (i) The correlation between the model forecast and observed rainfall anomalies.
- (ii) The root-mean-square-error (rmse) between the forecast and the observed values.

- (iii) Cross-validation techniques.
- (iv) Categorical forecast based on tercile stratification in combination with the Heidke Skill Scores.

#### 4.2.2.1 The Correlation Coefficient

Simple correlation analysis can be used to determine the degree of linear relationship between any pair of variables. For any month  $k$ , simple correlation coefficient  $r_k$  between two variable  $X$  and  $Y$  can be expressed as

$$r_k = \frac{\sum_{k=1}^M (X_k - \bar{X})(Y_k - \bar{Y})}{\left[ \left( \sum_{k=1}^M (Y_k - \bar{Y})^2 \right) \left( \sum_{k=1}^M (X_k - \bar{X})^2 \right) \right]^{1/2}}, \quad 4.12$$

where  $M$  is the total number of records,  $\bar{X}$  and  $\bar{Y}$  are long-term means,  $-1 \leq r_k \leq 1$ , positive and negative values of  $r_k$  are indicative of the positive or negative relationships respectively.

#### 4.2.2.2 Root Mean Square Error

Root mean square error is a measure of the square difference between the predicted and observed values at each station (grid point). If  $X$  and  $Y$  are the predictor and observed field the rmse can be estimated using the relationship

$$rmse = \left[ \frac{1}{n} \sum_{i=1}^n (X_i - Y_i)^2 \right]^{1/2}. \quad 4.13$$

Systematic rmse represents the error that is similar at all points in the gridded data. Accurate models have low systematic rmse. However, rmse is not a perfect tool and weaknesses include favouring model forecasts that underestimate variability (Brier and Allen 1951). Notwithstanding, an advantage of this measure of skill is that it retains the unit of the forecast variable.

#### ***4.2.2.3 Cross-Validation Techniques***

The cross-validation technique involves the successive deletion of each observation from the data, reconstructing the model, and then making estimates for the cases omitted (Michaelsen 1987). The deleted observation is then hindcasted and compared with the observed value. Reconstruction at each step is performed so that the model used in hindcast is calculated without any information about the deleted observation. Specifically, the predictor and predictand time series of  $N$  points are divided into  $M$  segments. Canonical correlation analysis is used to develop a prediction model using the  $M-1$  segments and is then used to hindcast the predictand in the withdrawn segment. This process is then repeated successively by changing the segment that has been excluded from the model development. By doing so,  $N$  hindcasts of the predictand are obtained which can be compared directly with  $N$  observations, to determine the overall skill of the CCA model. Barnston (1994) indicated that by comparing with real-time skill, CCA appeared to produce an unbiased estimate using cross-validation. However, Barnston and van den Dool (1993), and Mason (1998) suggested that cross-validation technique is important for small data sets, otherwise in some cases the forecast skill, especially of the most extreme values, maybe exaggerated.

#### 4.2.2.4 *Heidke Skill Score*

Heidke skill score evaluates the skill of prediction models removing the less skill part of the forecast trials (Barnett and Preisendorfer 1987; Preisendorfer and Mobley 1984). If a random forecast were made, one would expect over many forecasts a hit rate of 33.3% for a tercile-forecast system. The hit rate is often adjusted to a score (Hit) that has a chance of 0, a score of +100% for a set of perfect hits and a score of –100% for a set of forecasts with no hits. Predicting of rainfall categories rather than raw rainfall has been found to have more skill. Ranking the predicted values and the observations independently usually does this; so that; in the long run the predicted and the observed categories have the same distribution (Livezy 1987). If ( $H$ ) is the total number of correct forecasts, ( $T$ ) the total forecasts obtainable with a perfect forecast model and ( $E$ ) the number of hits expected by chance then the equation for the score is given by

$$SS = \frac{H - E}{T - E} \times 100 \text{ per cent.} \quad 4.14$$

With three categories a score of 33.3% should be obtained. The score is often rescaled so that random guessing gives 0 per cent. For normal conditions, Heidke SS takes a value zero. For a better and usable forecast model, the value of the skill must be at least positive (Livezy 1987). In this study the forecast and observation time series are ranked (above normal -  $AN$ , near normal –  $NN$  and below normal -  $BN$ ) and divided into three categories thus  $N/3$ , where  $N$  is the length of the forecast and observation. The Hit ratio for above normal forecast is defined by the number of forecasts and observations falling in a given

category in the contingency table divided by the total number of observations in that category.

### **4.3 CCA Model Results**

The results obtained from this study are discussed in the following sub-sections. Application of EOF analysis to the East African seasonal rainfall is discussed in chapter 2. In the next subsections we present the results obtained from the EOF analysis on SST anomalies and CCA results.

#### **4.3.1 Application of EOF analysis on the SST anomalies over the Tropical Pacific Ocean**

The Pacific SST data was arranged into a rectangular matrix (2697 rows  $\times$  360 columns) where the rows represent all grid points for a given month, and the columns represent all months for a given grid point and used as input to the EOF analysis. Table 4.1 shows the variance accounted for by the first nine EOF modes for the July and December SST anomalies, and Table 4.2 shows the corresponding correlation coefficient between the canonical vectors. The first EOF mode for tropical Pacific Ocean SST anomalies (Figure 4.1) accounts for 33.7 and 54.7 for July and December respectively. These patterns are associated with El Niño and La Niña events. The indication of a warm/cold tongue is shown over the eastern Pacific in this EOF mode. During the month of December, warming/cooling extends from the east to cover much of the tropical Pacific Ocean. The variance that is explained by the first EOF mode in December is also higher than that shown in July. These results confirm the observed peak of the ENSO events during the

month of December. The PC time series of the first dominant modes (Figure 4.2) indicate significant positive/negative anomalies during the years that coincide with El Niño and La Niña years. Some of these years are 1972/73, 1979/80, 1982/83, 1986/87 and 1987/88 El Niño, and 1970/71, 1973/75, 1984/85, and 1988/89 La Niña events. The time series evolution of the first EOF mode also shows a tendency of long-term shift towards positive coefficients starting from about 1976. This may reflect the decadal-scale variability in the coupled tropical ocean-atmosphere system (Trenberth and Hurrell 1994; Graham 1995).

Table 4.1: Variance and accumulated variance extracted from the tropical Pacific SST anomalies.

PERIOD	FACTOR	VARIANCE EXTRACTED (%)	CUMMULATIVE VARIANCE (%)
JULY	1	33.7	33.7
	2	15.4	49.1
	3	10.1	59.2
	4	6.1	65.3
	5	5.2	70.5
	6	4.2	74.7
	7	3.5	78.2
	8	3.0	81.2
	9	2.5	83.7
DECEMBER	1	54.7	54.7
	2	7.8	62.5
	3	6.9	69.4
	4	5.1	74.5
	5	3.5	78.0
	6	3.0	81.0
	7	2.4	83.4
	8	2.1	85.5
	9	2.0	87.5

Table 4.2: Correlation coefficient between the canonical vectors time series (u and v) between the predictor and predictand.

PERIOD	MODE	CORRELATION COEFFICIENT
JULY	1	-0.89
	2	-0.79
	3	-0.65
	4	-0.56
	5	-0.36
	6	-0.29
DECEMBER	1	0.91
	2	0.79
	3	0.77
	4	0.49
	5	0.48
	6	0.15

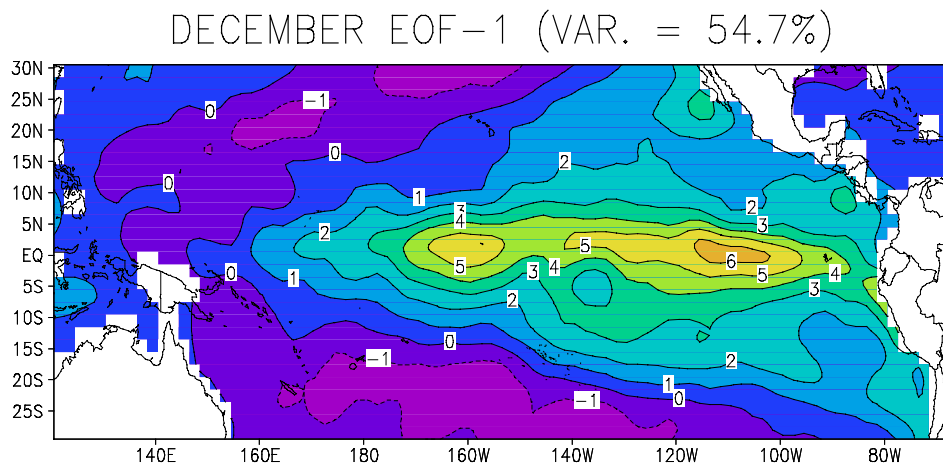
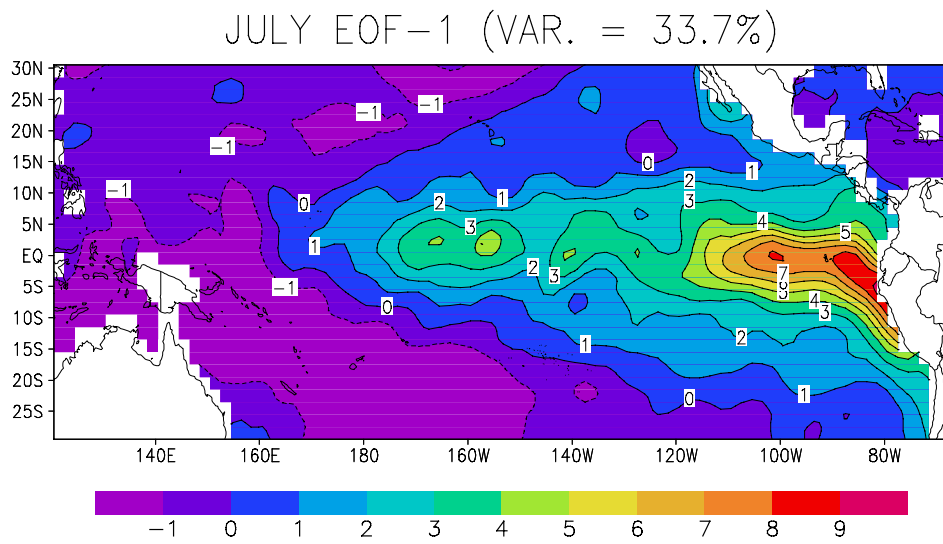


Figure 4.1: The contour patterns of the first EOF modes (loading  $\times$  100) for the July and December tropical Pacific Ocean SST anomalies.

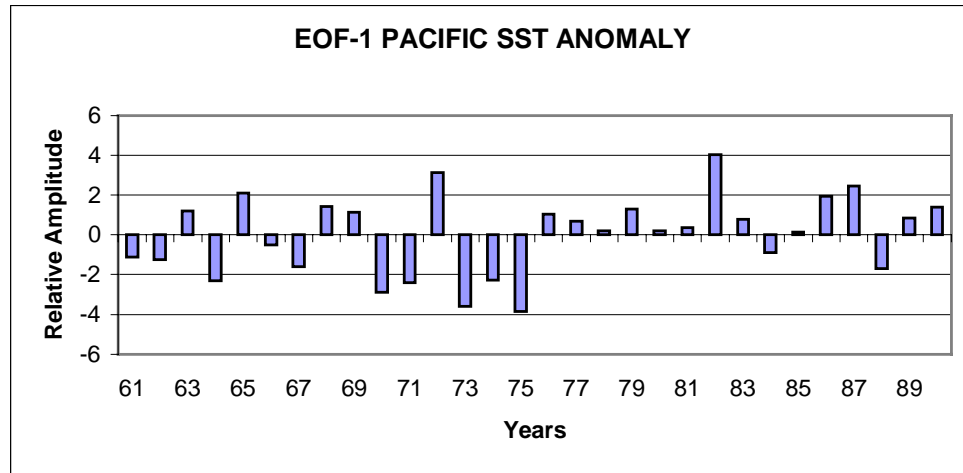


Figure 4.2: The PC time series of the first EOF mode for December tropical Pacific Ocean SST anomalies.

### 4.3.2 Seasonal Predictability of East African Rainfall

#### 4.3.2.1 The CCA Model

In this section, CCA was used to evaluate the seasonal rainfall predictability in equatorial eastern Africa when tropical Pacific Ocean SST is used as a predictor. The July and December Pacific Ocean SST anomalies were employed with a three months lead-time to investigate the predictability potential of OND and MAM rainfall respectively over eastern Africa. A total of eight modes for the predictand (OND and MAM rains) and eight modes for the predictor (SST) were selected as input to the CCA model. These modes accounted for more than 80% of the variance for the predictand and predictor fields respectively (Table 4.1). The overall significance of these modes is determined based on Monte Carlo simulation and student t-test.

Figure 4.3 shows the first spatial canonical pattern pair for the canonical correlation between July Pacific SST and the canonical vector (u), and the October-December rainfall and the canonical vector (v). The figure also shows normalized temporal functions (u and v) for the first CCA patterns for rainfall and SST respectively. Figure 4.4 shows the corresponding map patterns for December SST and March-May seasonal rains. An area of high significant positive correlations ( $> +0.6$ ) between the sea-surface temperatures and the canonical component time series is evident over the western Pacific coast and the western coast of North America in July (Figure 4.3a). During the month of December, significant negative correlations ( $< -0.6$ ) are shown over the eastern and western equatorial Pacific and the western coast of the USA (Figure 4.4a). Similarly, there is significant negative correlation ( $< -0.5$ ) with the station rainfall over the western parts of the Lake Victoria basin, eastern and southern coast of eastern Africa with the corresponding canonical component time series of rainfall in OND season (Figure 4.3b). In MAM season (Figure 4.4b), significant correlations are indicated over the western sectors of eastern Africa. Strong correlations indicate areas where the association between sea-surface temperature and rainfall are greatest.

The form of the association between SST and seasonal rainfall can also be determined from the sign of the correlations of the canonical component time series shown in Figure 4.3c and Figure 4.4c. The correlations between the first canonical time evolution for sea-surface temperature and seasonal rainfall is  $-0.89$  and  $0.91$  for OND and MAM seasons

respectively. By combining the contributions of the other significant canonical modes the predictor and predictand fields could be described sufficiently. The first canonical component for rainfall is positive during 1983 while it is negative for the sea-surface temperature (Figure 4.3c). The positive/negative correlations over the sea-area and negative/positive over land imply that the sea-surface temperature was warmer/cooler than normal and rainfall was below/above average. A positive/negative association is implied with cold (warm) sea-surface temperatures associated with wet (dry) conditions over land. The fact that the CCA rainfall pattern in the two seasons (OND and MAM) exhibits a mixed structure, with large positive (negative) in the east (west) flanked by pair of smaller regions of opposite sign, suggests that rainfall response to the variation in the Pacific SST is not uniform across eastern Africa. The significantly high correlation between the pairs of rainfall and SST records indicates a coherent variation in the time series in the two variables throughout the entire time period.

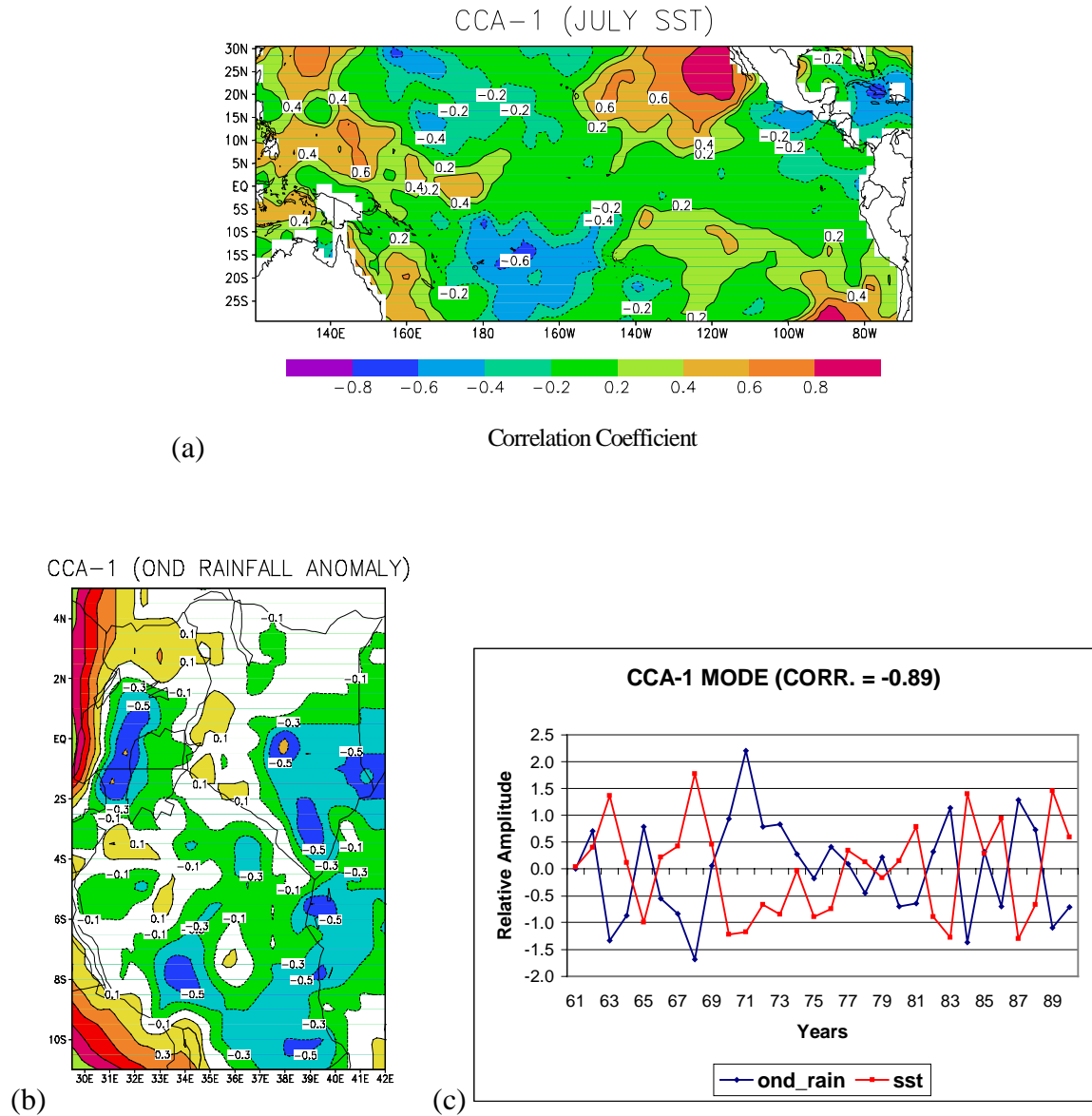


Figure 4.3: The first spatial pattern pair for the canonical correlation between July Pacific SST and October-December rainfall over eastern Africa. (a) correlation between the predictor (SST) and the canonical vector (u), (b) correlation between the predictand (rainfall) and canonical vector (v) and, (c) normalized temporal functions (u and v) of the first CCA patterns for rainfall and SST.

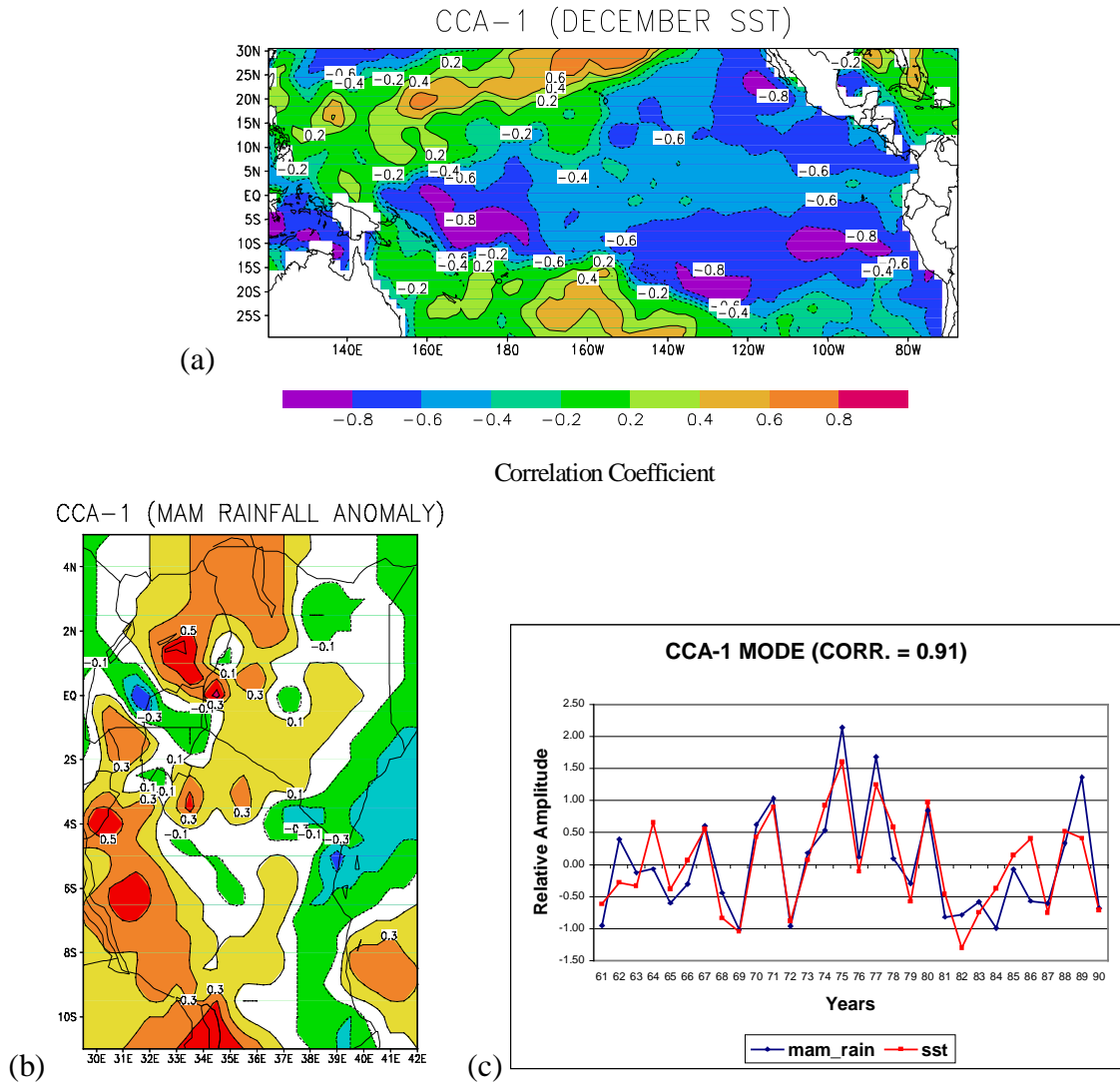


Figure 4.4: The first spatial canonical pattern pair for the canonical correlation between December Pacific SST and the following March-May rainfall over eastern Africa. (a) correlation between the predictor (SST) and the canonical vector ( $u$ ), (b) correlation between the predictand (rainfall) and canonical vector ( $v$ ) and, (c) normalized temporal functions ( $u$  and  $v$ ) of the first CCA patterns for rainfall and SST.

#### **4.3.2.2 Model Validation**

To demonstrate forecast skills, we display the time series of cross-validated forecasts and observations for the homogeneous climatic regions over eastern Africa. The correlation coefficient values between the observed and cross-validated rainfall ranges from 0.75 for region 1 down to 0.26 for region 5, (Table 4.3). The CCA model forecasts move in the correct way and tends to pick part of the variance extremes (Figure 4.6). However, the results are expected to have been much better by omitting extreme years from the analysis. Farmer (1988) found the correlations between observations and model forecasts to increase considerably when the extreme rainfall events were omitted in the forecast model. There are a few extreme events like 1963/64, 1971 and 1987, which were not captured by the model. Since the verification period of 30 years is long, the model cross-validation of extreme values maybe exaggerated such as 1967 (Barnston and van den Dool 1993; Mason 1998).

As a further measure of evaluating the forecast accuracy, the root-mean-square error (rmse) between the forecast and observation is used. The average correlation and rmse between the cross-validated forecast and the observation for the 1961-1990 are shown in Figure 4.5 and Figure 4.7 for the two rainfall seasons. Of the nine regions tested, Region 1, 2 and 8 exhibits the largest correlations (0.75, 0.74 and 0.54), smallest rmse (3.9, 4.7 and 3.6) respectively (Table 4.3). During the March-May season, the forecast model is stable for only one region (Region 8) which indicates correlation of 0.24 and a low rmse of 0.32 (Figure 4.7 and Figure 4.8).

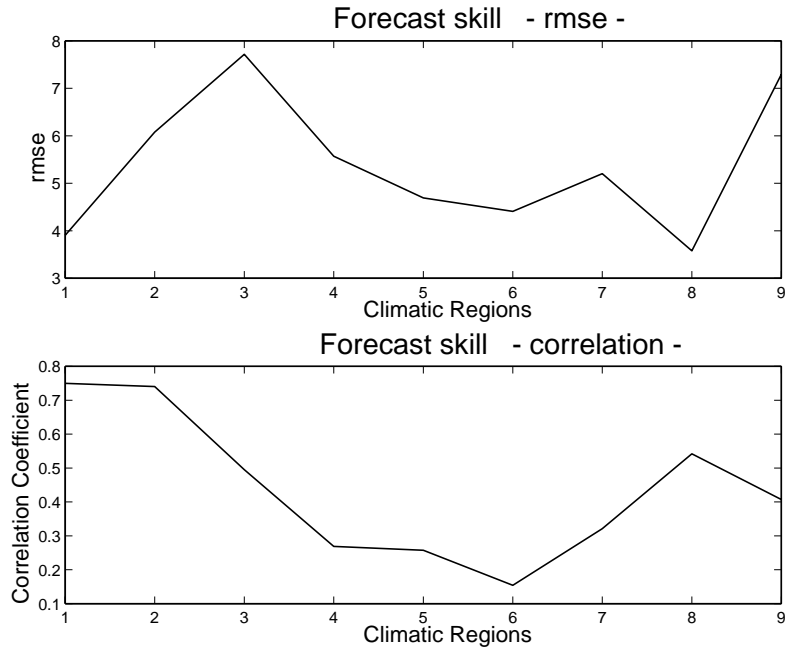


Figure 4.5: Root mean square error and correlation forecast model skill for the prediction of OND rains over the nine climatic regions of eastern Africa.

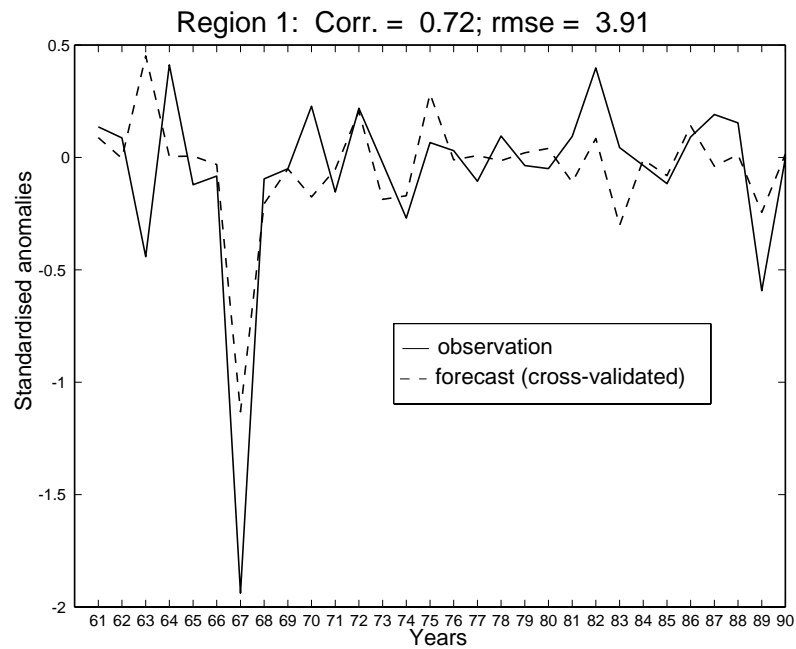


Figure 4.6: Time evolutions of the forecast (cross-validated) and the observed OND standardized rainfall anomalies for the climatic homogeneous region 1 of eastern Africa.

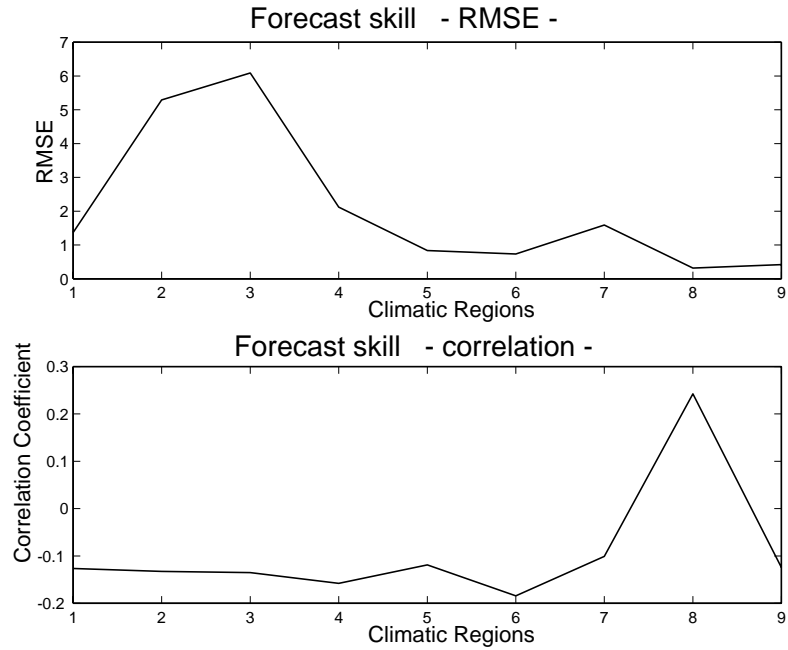


Figure 4.7: Root mean square error and correlation forecast model skill for the prediction of MAM rains over the nine climatic regions of eastern Africa.

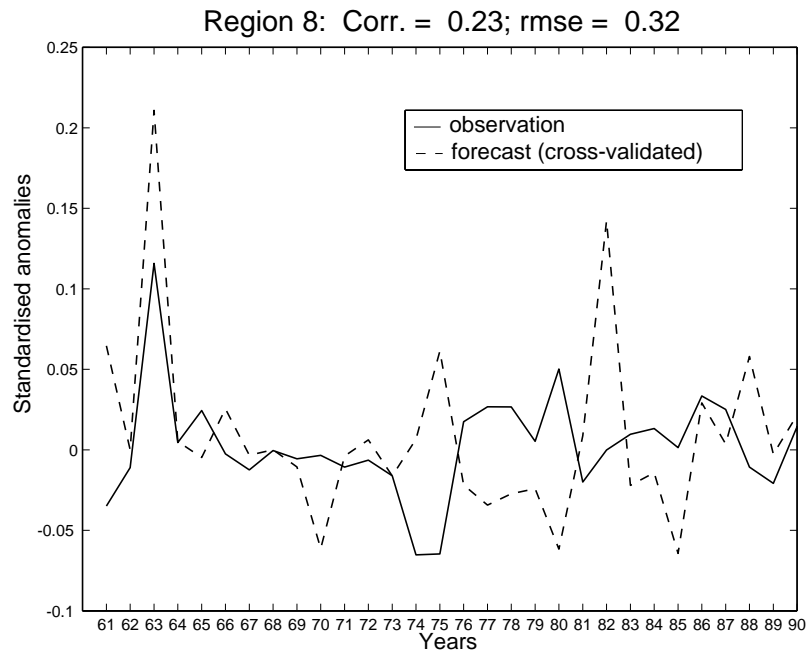


Figure 4.8: Time evolutions of the forecast (cross-validated) and the observed MAM standardized rainfall anomalies for the climatic homogeneous region 8 of eastern Africa.

Results shown on Table 4.3 and Table 4.4 indicate that the CCA model developed for the region has skill in forecasting the OND seasonal rainfall. On overall, the CCA model perform better over the East African highlands, the coast and the eastern lowlands, the regions that are productive in terms of cash crops and tourism. Search for more predictors is recommended for the regions close to the lake and western parts of the eastern African region. A “break down” of the cross-validation model for the MAM season for most of the climatic regions indicate that this season has low predictive potential based on Pacific Ocean alone. A further analysis of the relationship between the Atlantic Ocean SSTs and the wind patterns including the quasi-biennial oscillation (QBO) in the tropical lower stratosphere (Indeje and Semazzi 2000) would improve the predictability of this seasonal rainfall. The main source of moisture for these western regions is from the Atlantic Ocean that traverses the moist Congo/Zaire forest, which qualifies the Atlantic Ocean as another possible predictor of the regional rainfall. These results indicate the ability of the CCA model to skillfully forecast seasonal rainfall over parts of eastern African using the Pacific SST.

Table 4.5 summarizes the performance of the CCA model for climatic region1 for the October-December seasonal rainfall. There is a moderate correlation coefficient of 0.75 between the cross-validated forecast series and the observed series in the model-training period of 1961-1990. The contingency tables indicated a Heidke SS of 0.25, with a rmse of 3.9. The chances of achieving the right forecast is  $((6+4+5)/30 = 0.50)$ , about 50%. There exist robust relationships between the Pacific Ocean SSTs and rainfall over most

parts of eastern Africa especially those areas over the Eastern Highlands and the coastal areas.

Table 4.3: Assessment of October-December seasonal rainfall using cross validation techniques (1961-1990).

REGION	CORRELATION	RMSE	HEIDKE SS
1	0.75	3.9	0.25
2	0.74	6.1	0.35
3	0.50	7.7	0.25
4	0.27	5.6	0.25
5	0.26	4.7	0.15
6	0.15	4.4	0.15
7	0.32	5.2	0.25
8	0.54	3.6	0.25
9	0.41	7.3	0.25

Table 4.4: Assessment of March-May seasonal rainfall using cross validation techniques (1961-1990)

REGION	CORRELATION	RMSE	HEIDKE SS
1	-0.13	1.4	-0.05
2	-0.13	5.3	-0.05
3	-0.14	6.1	-0.05
4	-0.16	2.1	-0.05
5	-0.12	0.8	-0.20
6	-0.18	0.7	-0.05
7	-0.10	1.6	-0.05
8	0.24	0.3	-0.10
9	-0.12	0.4	0.0

Table 4.5: Contingency table for cross-validated October-December seasonal rainfall for climatic Region 1.

	OBSERVATION				
		AN	NN	BN	TOT.
FORECAST	AN	6	3	1	10
	NN	2	4	4	10
	BN	2	3	5	10
	TOT.	10	10	10	30

### **4.3.3 Application of the CCA model to the Prediction of the 1997 October-December Seasonal Rainfall**

The CCA model constructed using 1961-1990 data was applied to predict OND rainfall anomalies over eastern Africa for the 1997 season. This year was associated with a strong El Niño on record causing floods, that resulted catastrophic disruption of socioeconomic infrastructures and loss of life, loss of property, spread of diseases and had devastating impacts on the social economic activities in the East African region (Trenberth 1997). Figure 4.9 shows the predicted and observed standardized rainfall anomaly for the October-December rainfall using the July Pacific SST. The values of the numbers tell how large a deviation from normal is expected. These are not in millimeters, but are in standardized units that indicate how typical (or non-typical) the rainfall conditions are expected to be relative to the station's normal climate for the season in question. Large positive (negative) deviations indicate substantially wetter (or dryer) conditions than normal for the region and time of year. The model forecast compares well with observations. On average the model predicts above normal rainfall over most parts of eastern Africa during this season. Relatively high rainfall anomaly is predicted to the Eastern Highland, the coastal areas bordering the Indian Ocean, the Lake Victoria basin and, central and western Uganda. The spatial distribution of the predicted rainfall compares well with the observations although the model slightly underestimates rainfall anomaly. These results indicate the ability of the model to predict the spatial distribution of seasonal rainfall anomalies over eastern Africa with skill.

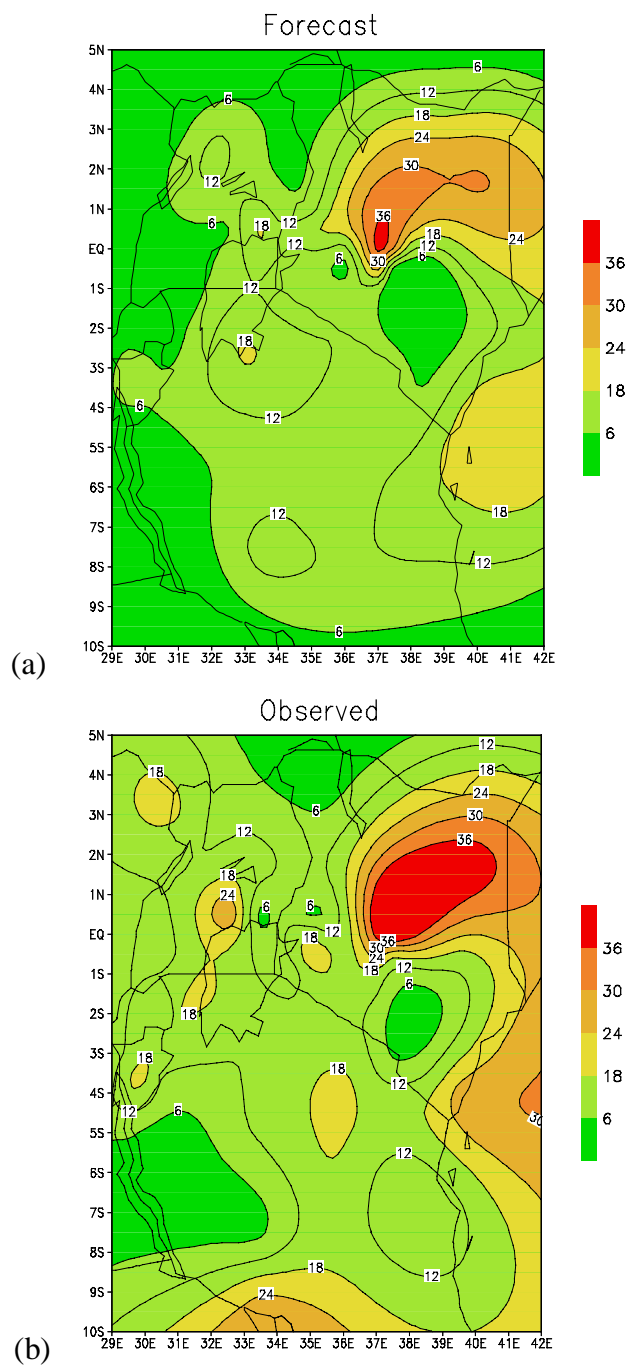


Figure 4.9: CCA model performance for the 1997 October-December seasonal rainfall over eastern Africa using the July Pacific SST. (a) Predicted and (b) observed standardized rainfall anomaly.

This model can be implemented in the prediction of seasonal climate over the region and the results could be useful in the social economic planning since the forecast would be made three months in advance (using July mean monthly SST) prior to the target season. Since the SST anomaly is the only predictor in the CCA model, the predictability of rainfall anomalies depends largely on the characteristics of the air-sea interaction that is manifested in the large-scale teleconnections through the Walker-circulation.

## Chapter 5

### 5 MECHANISTIC SIMULATIONS OF THE EAST AFRICAN CLIMATE USING NCAR REGIONAL CLIMATE MODEL: INFLUENCE OF LARGE-SCALE OROGRAPHY ON THE TURKANA LOW-LEVEL JET

In this chapter we investigate the role of orographic forcing in modulating the equatorial eastern African climate. A series of basic sensitivity studies are performed using the NCAR regional climate version 2 (RegCM2) to investigate the dynamics and thermodynamics underlying the orographic influence specifically on the Turkana easterly low-level jet that lies between the Ethiopian and the East African highlands. This investigation is aimed at contributing to our basic understanding of the processes involved in establishing a time-mean climate over equatorial eastern Africa, which is necessary in order to improve our ability to understand and predict the climate variability in the region.

#### 5.1 *Background*

The term orography implies obstacles on the large-scale such as mountain ranges, which affect stratified flows in the atmosphere. It is one of the lower boundary factors controlling global climate dynamics. Orography may influence climate through 1) its role in determining the positions of the semi-permanent upper tropospheric troughs and ridges in the westerlies, 2) the orographic convective precipitation systems, 3) the role it plays in the development and maintenance of meso-scale circulations, and 4) the blocking and

channeling effects on the low-level jetstreams. Whereas, the land/sea thermal contrast affects climate through thermal forcing, the effect of large-scale orography is mainly dynamical in nature (Kasahara 1966). Its main effect on the mean flow is through form drag that is associated with differences in tangential pressure across a mountain. In the globally-averaged atmosphere, this is approximately 50% of the total drag from the ground, the other half being frictional drag associated with the turbulent boundary layer (Stull 1988). Regional climate may be influenced by the structure of the large-scale flow for that region and the presence or absence of other forcings such as orography, and mean heat sources and sinks. This is mainly the case in the tropics where the dynamical flow instabilities are relatively weak as compared to those in the midlatitudes (Xue and Shukla 1997).

Orographic forcing on regional weather and climate has been the subject of several major investigations ever since the pioneering work by Kasahara (1966). Sarker et al. (1978) showed that rainfall distribution over the Ghat mountains of India was dependent on orography and the latent heating that induces upward motion in both the heating area and downstream of the mountain. Semazzi (1980ab, 1985) investigated the influence of large-scale orographic forcing on the African climate using a primitive equation barotropic model, and showed an equatorial geopotential height trough and a pair of tropical anticyclones on either side of the equatorial trough. He suggested that the observed semi-permanent trough (Equatorial trough) in the middle troposphere over equatorial Africa might be maintained partly by orographic forcing. Semazzi and Sun (1997) suggested that

orographic control could play a critical role in maintaining the observed teleconnections between global SST anomalies and the West African droughts.

## **5.2 Observational studies**

The region of study is enclosed by latitudes 9°N - 10°S and longitudes 28°E - 42°E. It has diverse topographic features that include the Ethiopian highlands to the northeast and East African highlands to the southwest (Figure 5.1). In between the Ethiopian highlands and the East African highlands lies a low-level region. This valley is referred to as the Turkana channel (Kinuthia and Asnani 1982). It is above 500 m from the mean sea level and has a depth that varies between 610 and 1524 m, and a width that varies between about 140 to 700 km. The channel is approximately 700 km long and oriented from southeast to northwest. In the channel is the Chalbi Desert, which is 150 km long and situated from 2° 35'N to 3° 20'N and from 37° 00'E to 37° 50'E. It also extends from southeast to northwest to join the Koroli Desert to the south. It is interesting to note that all these desert regions stretch from southeast to northwest as the direction of the prevailing wind and are also located in the wider part of the valley. Kinuthia and Asnani (1982), and Kinuthia (1992) have also observed the presence of a low-level jet in this valley. A low-level jet is typically a thin stream of fast moving air with maximum wind speeds of 10 to 20 m s<sup>-1</sup> that is usually observed in the lowest 1 to 2 km of the atmosphere. It is classified in the meso-β scale circulation with horizontal scales between 20 to 200 km, and time scales from hours to several days. Studies have shown that jet streams through the associated convergence/divergence and vertical motion patterns exert

a control on the surface weather and climate (Hastenrath 1985). Low-level jets are also significant in the transport of pollution and pests, are potential sources of wind energy, may cause aircraft accidents due to the strong wind shears associated with them and may also cause a sudden intensification and rapid spread of forest fires and sand storms.

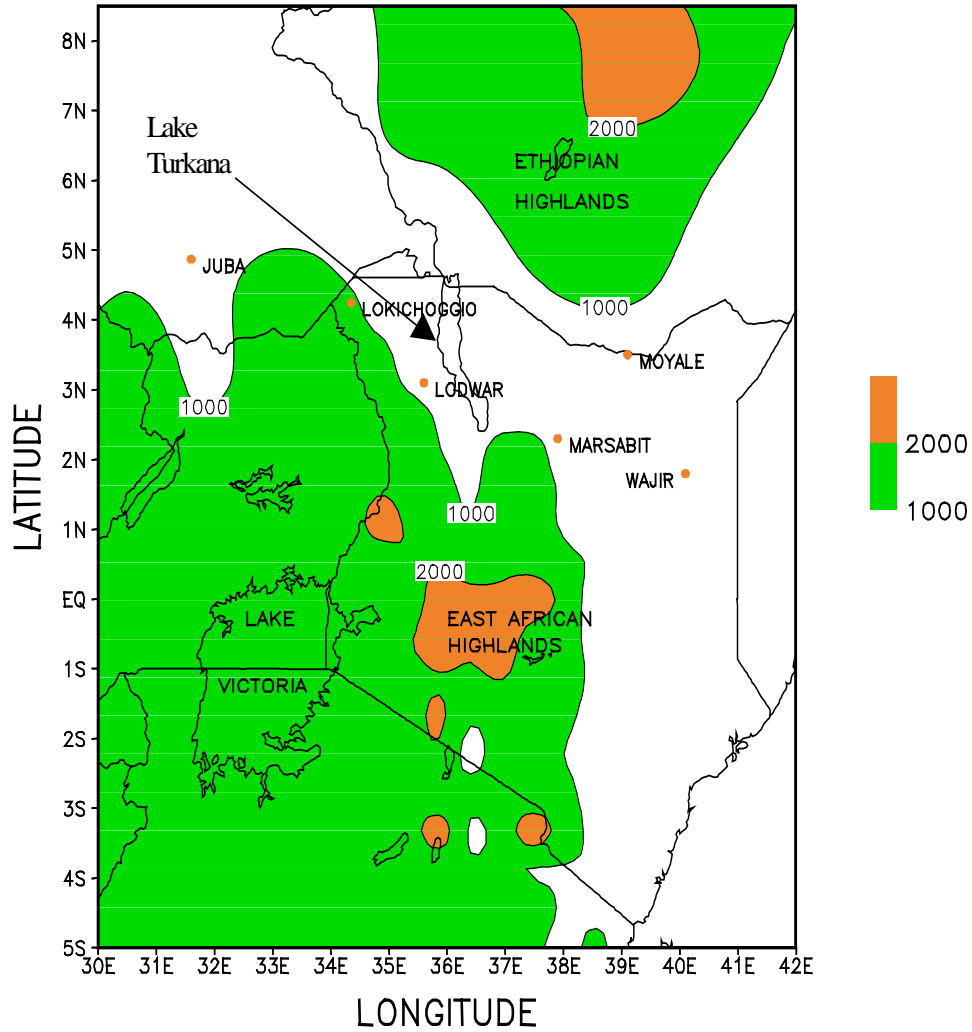


Figure 5.1: Topography over the Turkana Channel. Terrain height values greater than 1000 m are shaded.

The East African low-level jet (EALLJ) is one of the major well-recognised cross-equatorial flows that have been studied through theoretical and numerical models (Findlater 1966; Anderson 1976; Krishnamurti et al. 1976; Findlater 1977; Ardanuy 1979; Bannon 1979; among others). It is located over the eastern coast of Africa during the northern summer season and is associated with flows across the equator carrying southern-hemisphere air northwards up the African continent and ending at the Indian subcontinent. The jet core is generally located between 1 to 1.6 km above the mean sea level. This jet stream induces strong currents and upwelling over the western equatorial Indian Ocean. It thus plays an integral role in the seasonal development of the Somali Current, an intense ocean current, which flows northward only during the southwest monsoon but whose strength then is comparable to that of the Gulf Stream over the eastern coast of the United States of America (Anderson 1976).

During the months of June to August, the southeasterly (SE) flow associated with the pronounced EALLJ is dominant over the eastern part of equatorial eastern Africa. The jet builds during the months of April and May and decays in September and October, during which the flow reverses to northeasterly (NE) monsoons. Northwesterly (NW) to westerly flow dominate over the western sector of the region. Kinuthia and Asnani (1982) and Kinuthia (1992) observed that throughout the year the NE and SE monsoons air near the equator branches off from the Indian Ocean, enters the Turkana channel and intensifies (Figure 5.2). Their observations showed quite distinct low-level jet in the channel (Turkana easterly low-level jet) that persists throughout the year. They further postulated

that the configuration of the Ethiopian highlands and the East African highlands could be playing a critical role in the development and maintenance of the Turkana low-level jet observed over northern Kenya through the orographic channeling effect. This phenomenon has not been fully understood. Previous studies, (e.g. Krishnamurti et al. 1976; Ngara and Asnani 1978) have also indicated the importance of orography on the EALLJ. Krishnamurti et al. (1976) investigated the role of the Ethiopian highlands, the East African highlands and the Madagascar Mountains on the EALLJ. Their results showed that the Ethiopian and the East African highlands are crucial for the observed strong winds off the coast of Somali while the Madagascar mountains are most important for the strong winds just downstream from Madagascar. Preliminary studies by Owino (1997), and Patwardhan and Asnani (2000) have indicated that orographic configuration plays major role in the meso-scale rainfall distribution observed over mountain gaps.

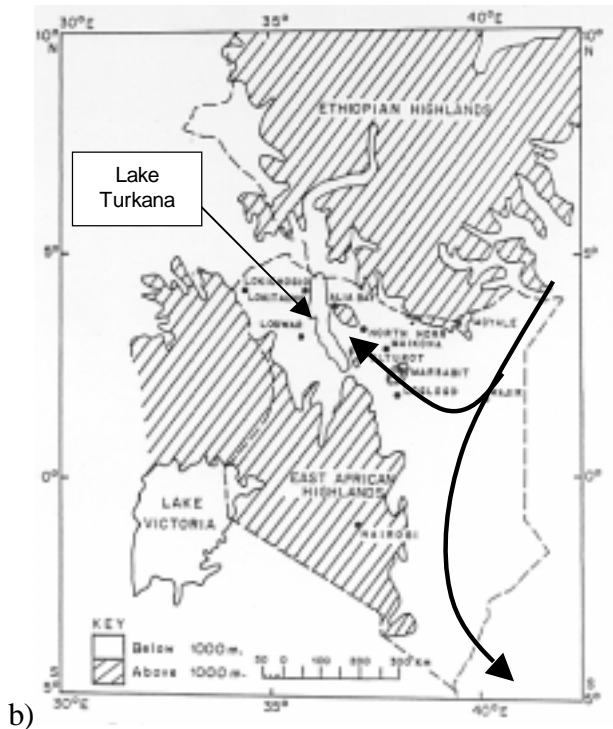
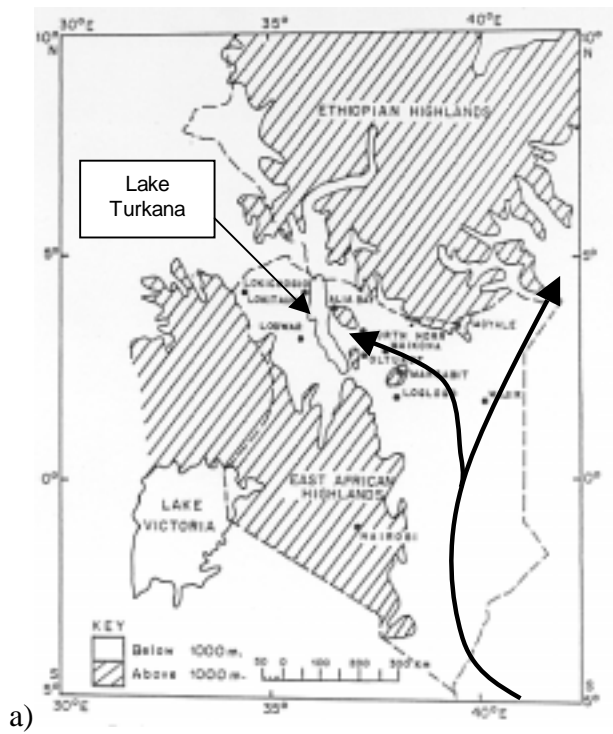


Figure 5.2: A simplified model showing the cross-equatorial monsoon flow diverting into the Turkana channel during (a) northern summer, and (b) northern winter.

### 5.2.1 The Turkana Low-level Jet

Ever since the discovery of a skeleton related to human evolution by Dr. Leakey in the Turkana channel (Kinuthia and Asnani 1982), many archeological expeditions continue to be carried out in this valley. Pilots flying here occasionally experience strong winds associated with severe turbulence during takeoff and landing. A number of aircraft accidents have been reported in the valley of recent years, which calls for need to understand the dynamics of the flow patterns in the valley in order to identify areas associated with strong winds for aviation safety. There is also need to investigate the causes of the observed semi-arid climates in this valley.

Various criteria have been used to classify the low-level jets (LLJ). Stull (1988) defined the LLJ as occurring whenever there is a relative wind speed maximum that is more than  $2 \text{ m s}^{-1}$  faster than wind speeds above it within the lowest 1500-m of the atmosphere. Chen et al. (1994) classified the LLJ into two categories: the boundary layer jet (BLJ) which occurs in the PBL with very strong vertical wind shear and shows a remarkable diurnal variation reaching maximum intensity by early morning and breaking down in the afternoon and, the LLJ which occurs between 600 and 900-hPa levels, usually associated with synoptic-scale systems. The Turkana jet has been observed to exhibit strong diurnal variations (Kinuthia and Asnani 1982; Kinuthia 1992) and is associated with the synoptic-scale cross-equatorial monsoon flow, both of these phenomena are included in the definition of a LLJ by Chen et al.

Several studies have been carried out to investigate the influence of orography on regional climates (Sarker et al. 1978; Semazzi 1980ab, 1985; Semazzi and Sun 1997). These studies have indicated the importance of orography in shaping regional climates. The purpose of the present study is to investigate the role of orographic forcing in modulating the East African climate. A series of basic sensitivity studies are performed using a regional climate model (RegCM2) with detailed surface parameterizations to investigate the dynamics and thermodynamics underlying the orographic influence and other forcing mechanisms (the large-scale monsoon flow and the depth of the channel) on the Turkana low-level jet. The study also investigates the possible explanations for the observed desert conditions over parts of the channel especially over the Lake Turkana watershed. This investigation is aimed at contributing to our basic understanding of the processes involved in establishing a time-mean climate over eastern Africa during austral spring season. Such an understanding is necessary in order to improve our ability to understand and predict the climate variability in the region.

The main observed features of the Turkana easterly low-level jet and the general flow in the Turkana channel according to Kinuthia (1992), and Kinuthia and Asnani (1982) are,

- (i) the existence of strong winds within the channel throughout the year with the speeds decreasing in regions where the channel becomes wide;

- (ii) the existence of two distinct jet streams, detached from each other, throughout the channel except at the middle of the channel where they seem to combine into a single and very high jet;
- (iii) the level of maximum wind occurs in the layer 305-2438 m;
- (iv) general backing of the mean wind to the east and northeast aloft throughout the channel;
- (v) a maximum wind of about 26 knots ( $\sim 13 \text{ m s}^{-1}$ ) near the channel entrance during the boreal winter season. Winds stronger than 40 knots ( $\sim 20 \text{ m s}^{-1}$ ) have been observed occasionally during this season.

Some scientific questions that are still unanswered on the jet are 1) what role the large-scale orographic forcing plays in its formation and maintenance, 2) whether the depth of the channel is important in determining the vertical structure of this jet, 3) what role is played by the cross-equatorial monsoon in determining the strength of the jet and, 4) whether thermal effects play any significant role on the jet or is this purely mechanical channeling that is important.

### **5.2.2 Hypothesis of formation and maintenance of Turkana low-level Jet**

We hypothesize that some of the scientific questions listed above are important in the formation and maintenance of the jet. The orography over East African highlands and the Ethiopian highlands may be important in providing a valley suitable for the channeling of the monsoon wind system. The presence and strength of the large-scale monsoon flow may be crucial in maintaining the strength in the jet cores and, the depth of the channel

may play a role in determining the vertical extent of the jet cores and the total mass transfer along the channel. In the present study, we do not consider the other possible effects such as the air-sea interactions, detailed boundary layer dynamics, detailed vertical resolution or possible effects of the middle latitude interactions that may be important to the Turkana jet. In this study, we shall be primarily concerned with the problem of the numerical simulation and analysis of the impacts of orography and other possible forcing mechanisms (large-scale monsoon and the depth of the channel) on some of the observed features of the jet).

Kinuthia and Asnani (1982) and Kinuthia (1992) have alluded that orographic channeling effect may be responsible for the Turkana low-level jet. The dynamics of the channeling effects could be explained through the application of the Bernoulli equation for barotropic ( $\rho = \rho(p)$ ) flows derived from a modified Eulerian equation of the form,

$$\frac{DR}{DT} = \frac{1}{\rho} \frac{\partial p}{\partial t} + \mathbf{u} \cdot \mathbf{F} + \frac{p}{\rho^2} \dot{H}, \quad (5.1)$$

where the Bernoulli function,  $R$  is defined by

$$R(x, y, z, t) = \frac{1}{2} q^2 + gz + \frac{p}{\rho}, \quad (5.2)$$

where  $q^2 = u^2 + v^2$ ,  $u$ ,  $v$  are east-west and north-south components of horizontal wind,  $g$  the gravitational acceleration,  $z$  the depth of the channel,  $p$  is the pressure,  $\rho$  the air density, and  $F$  and  $H$  represent internal processes, such as turbulence or viscous effects, or external ones such as additional body forces or radiative heating.  $H$  ( $\text{kg m}^3 \text{s}^{-1}$ ) represents some

heating process that may affect the density without changing the total mass. In a steady flow without forcing or heating,  $R$  is constant along a streamline. On the other hand, if the fluid passes through a region where there are significant frictional or turbulent stresses (represented by  $F$ ) like the rough sides of the mountain valleys, then the flow on each streamline would be affected by these stresses, which will reduce  $R$ . When the flow is constrained to a channel, as in straits, the effect of rotation in the down stream direction can be small, even at quite large distances (Baines 1995). Viscous forces are dominant close to the rough walls and at the bottom of the channel and are insignificant away from these surfaces. Hence, if we consider an inviscid, steady, irrotational, barotropic flow and neglect the viscous forces then,

$$R = \frac{1}{2}q^2 + gz + \frac{P}{\rho} = \text{Constant everywhere.} \quad (5.3)$$

The streamlines are concentrated at the channel entrance and exit and, the jet does not contract because of the well-rounded nature of the Turkana channel. Hence, the streamlines at the entrance and exit are uniform. In simple language, under simplified assumptions, Bernoulli's theorem may be stated as follows: under steady-state conditions, a fluid mass flowing horizontally conserves the sum of its potential and kinetic energy. When the boundary conditions constrain the fluid to pass from a narrow cross-section to a wider cross-section, then its velocity decreases, kinetic energy decreases and potential energy in the form of pressure increases; this increase of pressure is called dynamic pressure (Patwardhan and Asnani 1999). Consequently, the mass flow rate across the channel may be approximated by

$$M = \rho A (2gz)^{1/2}, \quad (5.4)$$

where  $A$  is the area at the channel entrance.

### **5.3 Regional Climate Model Simulations**

In this study, we explore the use of a regional climate model, capable of distinguishing between the primary geographical climate anomaly regimes over equatorial eastern Africa, a region where the local forcings have been identified as a major contributor to climate (Okeyo 1986; Mukabana and Pielke 1996; Nicholson 1996).

#### **5.3.1 Description of the Numerical Model**

The model used in this study is the second-generation Regional Climate Model (RegCM2). RegCM2 is based on the NCAR/Penn State mesoscale model version MM4 (Anthes et al. 1987), but all its physics parameterizations have been recently enhanced. Giorgi et al. (1993a,b), Kiehl et al. (1997) and SSOG99 have discussed details regarding the various attributes of the RegCM2 and its customization to the tropical region. This climate model is based on the primitive equations and a terrain-following ( $\sigma$ ) vertical coordinate system, where  $\sigma$  is given by

$$\sigma = \frac{p - p_t}{p_s - p_t}, \quad (5.5)$$

where,  $p$  is the pressure at any reference level,  $p_t$  the pressure at the top of the model atmosphere and  $p_s$  the prognostic surface pressure. The model vertical structure includes

16  $\sigma$ -levels with the model top at 50-mb and six levels are below  $\sigma = 0.79$  level, with the lowest model layer at about 40 m from the surface. The model uses c-staggered horizontal grid, which is preferred at long model simulations because it conserves mass and energy at such runs. The model domain size is 5580 km  $\times$  5040 km centered at 31°E, 4°S, and a horizontal grid spacing of 60-km (Figure 5.3). At this horizontal grid spacing, the main features of the bottom topography in the domain are well resolved (Figure 5.4). The eastern branch of the Great Rift Valley that lies roughly North-South through Kenya and Tanzania and the western branch located at the western boundaries of Tanzania and Uganda is well resolved. Figure 5.5 shows the surface vegetation types adopted in the model. This vegetation distribution is obtained from the standard MM4 land-use data set described in Anthes et al. (1987), and some clear discrepancies in the data have been rectified based on the mean land surface conditions based on Hammond World Atlas (1991).

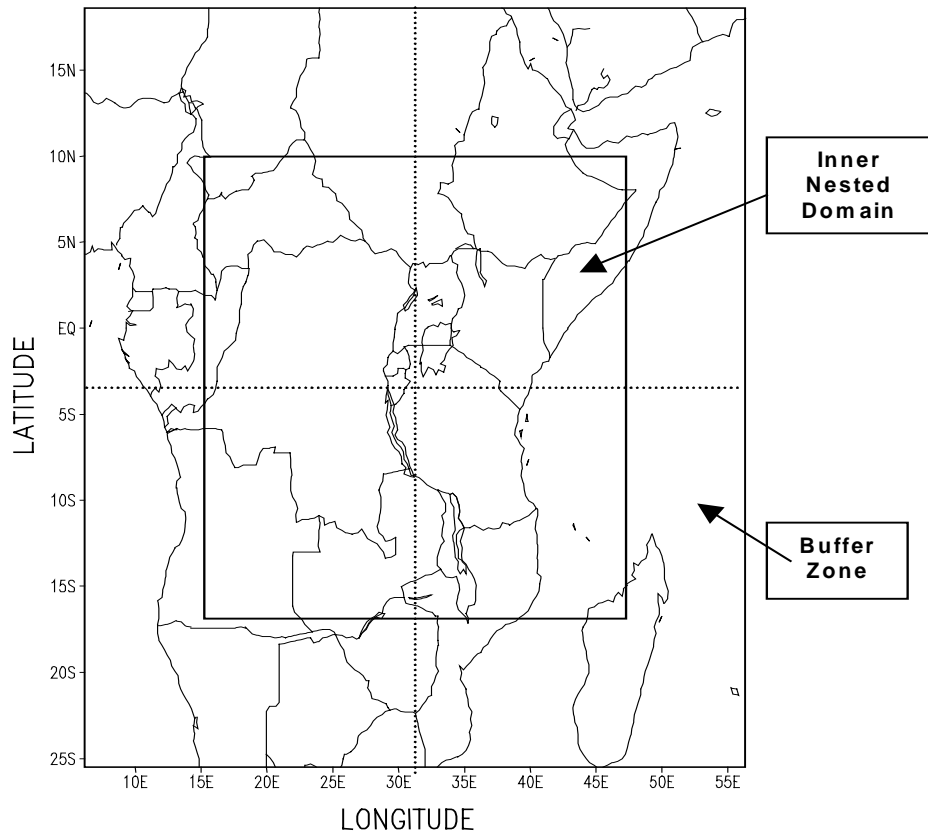


Figure 5.3: RegCM2 model domain.

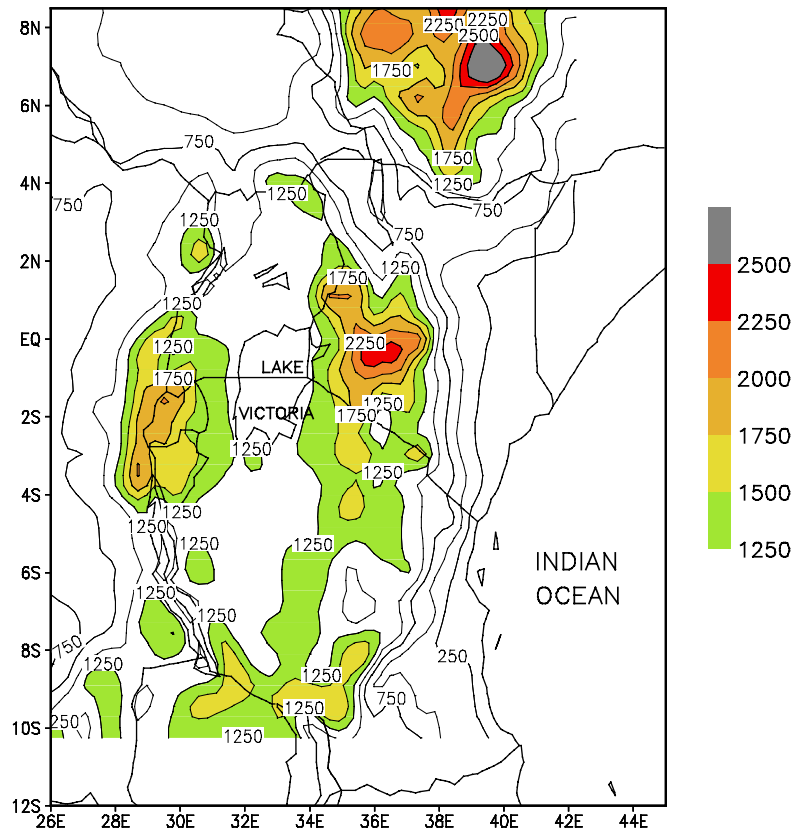


Figure 5.4: Topography of study area. Shaded are areas of elevation above 1250 m AMSL. Contour interval is 250m.

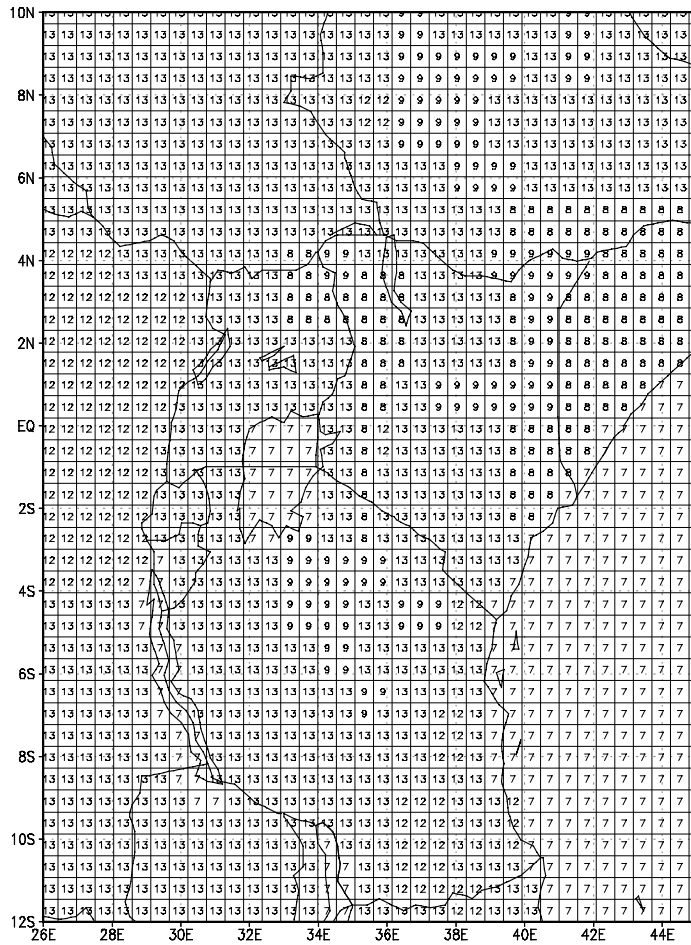


Figure 5.5: Land-use patterns over eastern Africa. Land cover type: 7 – water, 8 – semi-arid land, 9 – desert, 12 – tropical and subtropical forest, 13 – Savannah.

### 5.3.2 Model Equations

The horizontal momentum equation is given in (5.6) and (5.7).

$$\frac{\partial p^* u}{\partial t} = -m^2 \left[ \frac{\partial p^* uu / m}{\partial x} + \frac{\partial p^* vu / m}{\partial y} \right] - \frac{\partial p^* u \sigma}{\partial \sigma} - mp^* \left[ \frac{\sigma}{\rho} \frac{\partial p^*}{\partial x} + \frac{\partial \phi}{\partial x} \right] + p^* fv + D_u \quad (5.6)$$

$$\frac{\partial p^* u}{\partial t} = -m^2 \left[ \frac{\partial p^* uu / m}{\partial x} + \frac{\partial p^* vu / m}{\partial y} \right] - \frac{\partial p^* u \sigma}{\partial \sigma} - mp^* \left[ \frac{\sigma}{\rho} \frac{\partial p^*}{\partial y} + \frac{\partial \phi}{\partial y} \right] + p^* fv + D_v \quad (5.7)$$

Thermodynamic equation;

$$\frac{\partial p^* T}{\partial t} = -m^2 \left[ \frac{\partial p^* uT / m}{\partial x} + \frac{\partial p^* vT / m}{\partial y} \right] - \frac{\partial p^* T \sigma}{\partial \sigma} + p^* \frac{\omega}{\rho c_p} + p^* \frac{\dot{Q}}{c_p} + D_T, \quad (5.8)$$

Where the  $D$  terms represent the vertical and horizontal diffusion terms and vertical mixing due to the planetary boundary layer turbulence or dry convection adjustment. The heat capacity for moist air at constant pressure is given by  $c_p = c_{pd}(1 + 0.8q_v)$ , where  $q_v$  is the mixing ratio for water vapor and  $c_{pd}$  is the heat capacity for dry air. In the thermodynamic equation (5.8),  $\omega = \frac{dp}{dt}$  and is calculated from

$$\omega = p^* \dot{\sigma} + \sigma \frac{dp^*}{dt}, \quad (5.9)$$

where

$$\frac{dp^*}{dt} = \frac{\partial p}{\partial t} + m \left[ u \frac{\partial p^*}{\partial x} + v \frac{\partial p^*}{\partial y} \right]. \quad (5.10)$$

The hydrostatic equation is used to compute the geopotential heights from the virtual temperature,  $T_v$ ;

$$\frac{\partial \phi}{\partial \ln \left( \sigma + \frac{P_t}{P^*} \right)} = -RT_v \left[ 1 + \frac{q_c + q_r}{1 + q_v} \right]^{-1}, \quad (5.11)$$

where  $T_v$  is given by  $T_v = T(1 + 0.608q_v)$ , and  $q_c$  and  $q_r$  are mixing ratios of cloud water and rain water. Surface pressure is computed from

$$\frac{\partial p^*}{\partial t} = -m^2 \left[ \frac{\partial p^* u / m}{\partial x} + \frac{\partial p^* v / m}{\partial x} \right] - \frac{\partial p^* \dot{\sigma}}{\partial \sigma}, \quad (5.12)$$

which is used in its vertically integrated form

$$\frac{\partial p^*}{\partial t} = -m^2 \int_0^\sigma \left[ \frac{\partial p^* u / m}{\partial x} + \frac{\partial p^* v / m}{\partial x} \right] d\sigma. \quad (5.13)$$

Then the vertical velocity in the  $\sigma$ -coordinate,  $\dot{\sigma}$ , is given by

$$\dot{\sigma} = \frac{1}{p^*} \int_0^\sigma \left[ \frac{\partial p^*}{\partial t} + m^2 \left( \frac{\partial p^* u / m}{\partial x} + \frac{\partial p^* v / m}{\partial y} \right) \right] d\sigma', \quad (5.14)$$

where  $\sigma'$  is a dummy variable of integration and  $\dot{\sigma}(\sigma=0) = 0$ .

### 5.3.3 Time Splitting

The time splitting scheme is used to increase efficiency, because of the model equations are completely compressible and hence permit sound waves. These waves are fast and require a short time step for numerical stability. For the hydrostatic equations, fast moving

external gravity waves are the limiting factor. These fast moving waves are split from the rest of the solution. In this study we have adopted a scheme developed by Madala (1981), which separates the terms governing the gravity modes from those governing the Rossby modes. The term “split” here refers to separation of the motion in terms of eigenmodes. This scheme allows the time-steps of the slow tendencies to be twice as large as they were with the Brown-Campana (1978) algorithm and they are comparable to the ones used in the nonhydrostatic numerics.

### 5.3.4 Horizontal Diffusion

The second and fourth order diffusions are used to control nonlinear instability and aliasing. The second-order diffusion is of the form

$$F_{H2\alpha} = p^* K_H \nabla_{\sigma}^2 \alpha, \quad (5.15)$$

where  $\alpha$  is any prognostic variable. A more scale-selective fourth-order form of diffusion is given by

$$F_{H4\alpha} = p^* K'_H \nabla_{\sigma}^4 \alpha, \quad (5.16)$$

where

$$K'_H = \Delta s^2 K_H. \quad (5.17)$$

The second order diffusion is used in the coarse domain for the row and column of the grid points next to the lateral boundaries, while the fourth-order form is used in the interior of the entire domain of the fine mesh.

### 5.3.5 Precipitation Physics

Precipitation physics in the model is treated using the explicit and implicit schemes. Explicit schemes treat resolved precipitation physics while implicit schemes the non-resolved precipitation physics. Both may be operating on a grid-point at the same time. The terms convective and stable (non-convective) precipitation may generally not be acceptable on finer grid-resolutions, where convective precipitation is quite often resolved. The terms resolved/non-resolved are often used to describe convective/non-convective precipitation. Different schemes are available for the generation of precipitation in the RegCM2. An implicit scheme, whereby supersaturated water immediately precipitates or explicit scheme including prognostic equations for cloud-water and rainwater (Hsie et al. 1984) describes non-convective precipitation. Convective precipitation can be described using two schemes, a simplified Kuo-type scheme (Anthes et al. 1987) and Grell scheme (Grell 1993).

#### 5.3.5.1 *The Kuo-type Cumulus Cloud Parameterization Scheme*

In this scheme the amount of convection is determined by the vertically integrated moisture convergence. The feedback to the large-scale (the vertical distribution of heating and moistening), is determined with the help of the normalized vertical profiles of convective heating and moistening and vertical eddy-flux divergence of water vapor associated with cumulus convection. In this parameterization scheme, rainfall is initiated when the moisture convergence in a column exceeds a given threshold and the vertical sounding is convectively unstable. The vertically integrated moisture convergence  $M_t$  is given by,

$$M_t = \left( \frac{m^2}{g} \right) \int_0^1 \frac{\nabla p^* \dot{V} q_v}{m} d\sigma. \quad (5.18)$$

A fraction  $(1 - b)$  of  $M_t$  condense and precipitate, while the remaining fraction (the  $b$  factor) is redistributed between the cloud top and the cloud bottom following a specified parabolic vertical heating profile that yields maximum moistening and heating in the upper half of the cloud layer. The  $b$  factor is a function of the mean relative humidity ( $\overline{RH}$ ) of the column, where

$$b = 2(1 - \overline{RH}), \quad (5.19)$$

for  $\overline{RH} \geq 0.5$ , and  $b = 1$  otherwise. Over equatorial eastern Africa, the moisture convergence is shallow and weak due to the weak low-level monsoon wind convergence in the tropics. It is thus difficult for the model to initiate the cumulus convection for the specific version of the Kuo cumulus scheme. SSOG99 found this version of Kuo scheme to simulate weak climatic conditions over this region during the short rain season.

#### ***5.3.5.2 The Grell-type Cumulus Cloud Parameterization Scheme***

Grell (1993) developed this scheme. In the scheme, clouds are envisaged as two steady state circulations caused by an updraft and a downdraft with no direct mixing between cloudy air and environmental air except at the top and bottom of the circulations. For both updraft and downdraft, maximum buoyancy is allowed. The inflow to an updraft is not a mixture of downdraft air and the more buoyant air; it is more likely the air with high static energy from the layer above the downdraft outflow. Compensatory subsidence only

continues to the level from which the updraft draws in air. Compensatory uplift may be required in very low layers of the troposphere because of the downdraft mass flux. A simplistic cloud model is used that assumes that the mass flux in the updraft and downdraft is constant with height, and the originating levels of updraft and downdraft are given by the levels of maximum and minimum ambient moist static energy, respectively. The scheme is activated when a parcel lifted from the updraft originating level eventually attains moist convection. Physically, maximum buoyancy is allowed for both updraft and downdraft. For deep convection scheme, the cloud base for the updraft is not restricted to the boundary layer, but can be anywhere in the troposphere. The feedback for this scheme is entirely determined by compensating mass fluxes and detrainment at cloud top and bottom. SSOG99 have indicated that the Grell cumulus scheme yields better results than the Kuo scheme over the equatorial eastern African region perhaps because it responds more readily to variations in atmospheric stability conditions. Since, typical tropical atmosphere is conditionally unstable; the Grell scheme appears to be a better choice for our present purpose. The cloud model that is used to calculate the cloud properties in this scheme is formulated with a few equations. Mass flux is constant with height, and there is no entrainment or detrainment along the cloud edges. The originating mass flux of the downdraft is made as a function of the updraft mass flux and the re-evaporation of convective condensate. Thus

$$m_o = \frac{\beta I_1 m_b}{I_2}, \quad (5.20)$$

where  $m_o$  and  $m_b$  are the mass fluxes of the updraft and downdraft at their originating level and the conditions at the originating levels are given by the environment,  $I_1$  is the amount of condensation integrated over the whole depth of the updraft normalized by the updraft mass flux,  $I_2$  is the evaporation in the downdraft normalized by the downdraft mass flux, and  $\beta$  is the fraction of updraft condensate that re-evaporates in the downdraft. Here,  $1-\beta$  is the precipitation efficiency. Rainfall is computed from

$$R = I_1 m_b (1 - \beta). \quad (5.21)$$

The term  $\beta$  is analogous to the  $b$  factor of the Kuo scheme and is a key parameter in determining the intensity of convection as affected by the stabilizing effect of the downdraft. The lower the  $\beta$ , the higher the convective precipitation efficiency and, in general, the greater the precipitation due to convective processes.  $\beta$  can vary between 0 and 1. Following Fritsch and Chappell (1980), the  $\beta$ -term can be described as a function of the vertical wind shear,  $u_z$ , given by

$$\beta = 1 - (1.591 - 0.639u_z + 0.953u_z^2 - 0.00496u_z^3). \quad (5.22)$$

In this study we have prescribed  $\beta$  as a function of the vertical wind shear and allowed it to vary between 0.25 and 0.6 based on the recommendations by SSOG99.

### 5.3.6 Model physics

Several of the original MM4's physics parameterizations were modified to adapt the RegCM2's use to long-term climate simulations. The surface physics-soil hydrology processes; the Biosphere-Atmosphere Transfer Scheme (BATS) were coupled to the

model (Dickinson et al. 1993). The model PBL and precipitation schemes were modified to improve the simulation of precipitation and surface air temperature. The interactive biosphere atmosphere transfer schemes represent the role of vegetation and interactive soil moisture that modifies the surface-atmosphere exchanges of momentum, energy and water vapor. BATS and the model radiative transfer schemes require specification of atmospheric carbon dioxide concentration for which we adopted a constant mixing ratio of 330 parts per million by volume (ppmv) as recommended for the region by SSOG99. Initial surface soil and canopy temperature is set equal to that of the lowest model level. The soil water content is initialized as a function of vegetation as described in Giorgi and Marinucci (1991).

### ***5.3.6.1 Surface Energy Formulation***

Over land, the surface temperature  $T_g$  is computed from the surface energy budget that is based on the ‘force-restore’ method developed by Blackadar (Zhang and Anthes 1982).

The budget equation is

$$C_g \frac{\partial T_g}{\partial t} = R_n - H_m - H_s - L_v E_s, \quad (5.23)$$

where  $C_g$  is the thermal capacity of the slab per unit area,  $R_n$  is the net radiation,  $H_m$  is the heat flux into the substrate ( $\text{W m}^{-2}$ ),  $H_s$  is the sensible heat flux from the surface into the atmosphere ( $\text{W m}^{-2}$ ),  $L_v$  is the latent heat of evaporation and  $E_s$  is the flux of water vapor from the surface into the atmosphere. The following formulation enables the amplitude and phase of the slab temperature to be identical to the surface temperature of a real soil

layer of uniform thermal capacity. The heat flow into the substrate is through molecular conduction given by

$$H_m = K_m C_g (T_g - T_m), \quad (5.24)$$

where  $K_m$  is the heat transfer coefficient expressed as  $K_m = 1.8\Omega$ ,  $\Omega$  is the angular velocity of the earth, and  $T_m$  is the temperature of the substrate, which is presently taken to be a constant value equal to the mean surface-air temperature over the period of simulation.

The fluxes at the surface are described using the bulk-aerodynamics option. The surface-heat fluxes are given by

$$H_s = \rho_a c_{pm} C_\theta C_u (\theta_g - \theta_a) V, \quad (5.25)$$

where  $\rho_a$  and  $\theta_a$  are density and potential temperature at the lowest model layer,  $C_\theta$  and  $C_u$  are exchange coefficients, and  $c_{pm}$  is the specific heat at constant pressure for moist air.

Surface moisture flux is given by

$$E_s = \rho_a C_\theta C_u M (q_{vs}(T_g) - q_{va}) V, \quad (5.26)$$

where  $M$  is the moisture availability parameter which varies from 1.0 to 0.0 for a surface with no potential for evaporation. The availability is specified as a function of land category and the model results are often quite sensitive to the value used for  $M$ . The surface momentum flux is given by

$$\tau_s = \rho_a C_D V^2, \quad (5.27)$$

where  $C_D$  is the surface drag coefficient.

### 5.3.6.2 Boundary Layer Physics

For the convective boundary layer calculations, the non-local eddy diffusion formulation of Holtslag et al. (1990) is used. For stable and near-neutral conditions, the vertical momentum, heat, and moisture in the PBL is represented local K-theory of the form

$$F_c = -K_c \left( \frac{\partial C}{\partial z} - \gamma_c \right), \quad (5.28)$$

where  $F_c$  is the vertical flux for the quantity  $C$  ( $u$ ,  $v$ ,  $w$ ,  $q$ ,...),  $z$  is the vertical coordinate and  $K$  is the eddy diffusivity,  $\gamma_c$  is a "counter gradient" transport term describing non-local transport due to dry deep convection. The eddy diffusivity is given by the non-local formulation

$$K_c = \kappa \omega_t z \left( 1 - \frac{z}{h} \right)^2, \quad (5.29)$$

where  $\kappa$  is the Von Karman constant ( $= 0.4$ ),  $\omega_t$  is a turbulent convective velocity that depends on the frictional velocity, height, and the Monin Obukhov length ( $L$ ) that is given by

$$L = -\frac{c_{pm} \rho_a \theta_a u_*^3}{kgH_s}, \quad (5.30)$$

and  $h$  is the PBL height. The countergradient term for temperature and water vapor is given by

$$\gamma_c = C \frac{\Phi_c^0}{\omega_t h}, \quad (5.31)$$

where  $C$  is a constant equal to 8.5, and  $\Phi_c^0$  is the surface temperature or water vapor flux.

The PBL height ( $h$ ) is estimated from the Richardson number given by

$$Ri_{cr} = \frac{gh}{\theta_s} \frac{[\theta_v(h) - \theta_s]}{[u(h)^2 + V(h)^2]}, \quad (5.32)$$

where the  $u(h)$ ,  $v(h)$ , and  $\theta_v(h)$  are the wind components and the virtual potential temperature at the PBL height,  $g$  is the gravity,  $Ri_{cr}$  is a critical bulk Richardson number, and  $\theta_s$  is an appropriate temperature of air near the surface. Detailed descriptions of various terms are presented in the paper by Holtslag et al. (1990). Over land, the roughness length  $z_o$  is specified as a function of land-use category. Over water,  $z_o$  is calculated as a function of friction velocity (Delsol et al. 1971) such that

$$z_o = 0.032u_*^2 / g + z_{oc}, \quad (5.33)$$

where  $z_{oc}$  is a background value of  $10^{-4}$  m.

The non-local PBL scheme causes more rapid moisture detrainment from the PBL top and, as a consequence, dryer conditions and less pronounced clouds formation in the lowest model levels (Giorgi et al. 1993). Rather, maximum cloudiness occurs in the upper regions of the, and above, the PBL. In addition to affecting the cloudiness, the enhanced transport and subsequent saturation above the PBL top induced by the non-local PBL scheme also modifies the precipitation predicted by the model. The lifted moisture to mid

troposphere condenses and precipitates as gridpoint rain. In addition, because the lower model levels in this scheme are drier, there is less availability of moist static energy to support cumulus convection. Hence, The non-local scheme has effect of increasing the precipitation through enhanced vertical transport of moisture, which in turn increases the shadowing, lower tropospheric cooling, and decreased land evaporation and surface sensible heat flux. This negative feedback mechanism has been handled by incorporating the new radiation scheme in the RegCM2 (Briegleb 1992) that tend to control the excessive moisture influx to the PBL top.

### **5.3.7 Boundary conditions**

#### ***5.3.7.1 Surface boundary conditions***

Orography is incorporated in the model as the lower boundary condition in a terrain following vertical coordinate system. Pressure has been widely used as a vertical coordinate in modeling and theoretical studies ever since the pioneering work by Eliassen (1949). Using pressure as an independent variable eliminates the not routinely observed air density from the governing equations and simplifies thermodynamic calculations. Furthermore, numerical models in such a coordinate system can easily incorporate observational data that are generally available at pressure levels (Xue and Thorpe 1990). There are however deficiencies of the sigma treatment of orography. This scheme may not handle sharp terrain gradients effectively. The orography data used in this study was taken from the global 5' horizontal resolution orography file archived at International Research Institute (IRI). This data was interpolated to the model horizontal grid resolution

of 60- and 30-km using the bilinear interpolation scheme (Cressman 1979). The land-use data adopted in the model was interpolated from 30' and 10' resolution data archived at National Centers for Atmospheric Research (NCAR). The time-dependent SST was interpolated from a  $1^\circ \times 1^\circ$  grid of the monthly mean observed data (Shea et al. 1992).

### 5.3.7.2 *Lateral Boundary Conditions*

The RegCM2 has several options for lateral boundary conditions described in Anthes et al. (1987). However, in this study we have adopted the exponential relaxation method (Davies and Turner 1977; Giorgi et al. 1993b). This scheme consists of Newtonian and diffusion terms that gradually drive the model solution of wind components, temperature, water vapor mixing ratio, and surface pressure toward specified large-scale values inside the lateral 'buffer' zone. A boundary condition term is added to the model tendency equation for the variable  $\alpha$  given by the equation

$$\left( \frac{\partial \alpha_M}{\partial t} \right)_n = F(n)F_1(\alpha_{LS} - \alpha_M) - F(n)F_2 \nabla^2(\alpha_{LS} - \alpha_M), \quad (5.34)$$

where the subscripts  $LS$  and  $M$  refers to the driving large-scale and the model simulated fields, respectively.  $F$  decreases linearly from the lateral boundary, such that

$$F(n) = \left( \frac{5-n}{3} \right) \quad n = 2, 3, 4, \quad (5.35)$$

$$F(n) = 0 \quad n > 4, \quad (5.36)$$

and  $F_1$  and  $F_2$  are given by

$$F_1 = \frac{0.1}{\Delta t}, \quad (5.37)$$

$$F_2 = \frac{\Delta s^2}{50\Delta t}. \quad (5.38)$$

$\Delta t$  and  $\Delta s$  are the model time step and grid spacing respectively, the index  $n$  refers to the number of grid points from the lateral boundaries; that is,  $n = 1$  is on the boundary, and the function  $F(n)$  varies from 0 to 1 within the lateral buffer zone. This lateral boundary formulation is designed to provide a gradual, smooth blending of the model-produced and driving lateral boundary fields throughout the buffer zone. Giorgi et al. (1993) suggested the use of wider buffer zones and an exponential function form of  $F(n)$  of the form

$$F(n) = \exp\left[-\frac{(n-2)}{N_l}\right], \quad (5.39)$$

where  $N_l$  is a constant. Compared to the linear formulation, the exponential representation ensures a stronger control by the lateral boundary conditions near the lateral boundaries and smoother transition towards the interior of the domain of interest. In this study, we adjusted the value of  $N_l$  to vary from values of 0.2 to 0.5 in the lower 10-model levels, to values ranging between 1 and 6 in the upper model levels. These specifications allow for weaker forcing in the low levels and relatively strong forcing in mid and higher levels for the tropical regions as recommended by SSOG99.

These lateral boundary conditions were prescribed at every 1200 LST of integration using the European Center for Medium Range Weather Forecasting (ECMWF) reanalysis data. In principal the replacement of the new GCM boundary conditions should be made at each time step, but studies by Kida et al. (1991) has shown that the error introduced by 12-hourly lateral boundary updates is negligible.

### **5.3.8 Initial conditions**

Initial conditions in a numerical simulation represent the mean space-time characteristics of the atmosphere at the beginning of the numerical experiment. The model was initialized with the 12-hourly mean meteorological fields obtained from the ECMWF reanalysis (Trenberth 1992). This data is based on a T42 spectral grid that corresponds to approximately  $2.8^\circ \times 2.8^\circ$  horizontal resolution in physical space and is available on 14 pressure levels. No further adjustments were done to the initial and boundary conditions although the spatial interpolation to our model resolution may introduce slight imbalance. Many researchers (Murakami and Sumathipala 1989; Mukabana and Pielke 1996; Okoola 1999, among others) have utilized ECMWF data sets for various studies and have found the data sets to give reasonable approximations of the flow fields over eastern Africa and the Indian Ocean. The simulation period was September through December coinciding with the short rainy season over eastern Africa. The first month (September) results were discarded to allow for the model to spin-up. The year 1988 that displayed near normal rainfall conditions (Ininda 1998; SSOG99) was used in our control runs. Model results were analyzed at 1200 and 2400 local standard time (LST). Multiple simulations starting

from slightly perturbed initial conditions were performed to provide input for the computation of ensemble statistics for assessing the averages and spread of the forecasts.

### 5.3.9 Design of numerical experiments

In order to test the hypotheses listed in section 5.2.2, a series of numerical experiments designed to explore the relative importance of each of the three parameters (Orography, large-scale monsoon flow and depth of the channel) in the formation of the Turkana LLJ, the following sets of experiments were conducted

- (i) Experiment 1: all forcing mechanisms were incorporated in the domain (here after referred to as Control)
- (ii) Experiment 2: the entire bottom topography was suppressed over the model domain and the large-scale wind forcing remained the same as in experiment 1. The purpose of this experiment is to investigate the role of large-scale orography in formation of the jet.
- (iii) Experiment 3: the model was started from rest ( $u = 0 = v$ ) to eliminate the impact of the large-scale monsoon flow. Orography and channel depths were kept the same as in experiment 1. The purpose of this experiment is to find out the importance of large-scale forcing in the realistic simulation of the jet. By eliminating the large-scale forcing, it is also possible to investigate the combined impacts of other processes such as thermal heating, surface drag on the jet. Starting the model from rest does not purely eliminate these effects of thermal heating, frictional drag and the pressure gradients, which are still present in the large-scale forcing fields.

- (iv) Experiment 4: the bottom of the Turkana channel was artificially raised up to a mean depth of 1000-m above mean sea level (AMSL). The large-scale forcing fields were kept the same as in experiment 1. The purpose of this experiment is to investigate the role of the channel depth on the jet development and strength.

By performing these experiments, we anticipate to have a better understanding of (1) the role each of these three factors (orography, large-scale monsoon wind and depth of the channel) in the formation and variation of the jet, and (2) the cross-sectional temperature distribution in the core of the jet, and (3) the observed semi-arid climates over the Lake Turkana watershed.

The NCAR/NCEP reanalysis data described in Kalnay et al. (1998) was used to validate the model performance in reproducing the observed atmospheric circulations. We utilized an independent data set from the one used in forcing the model for model validation. SSOG99 have also shown that the recently compiled NCAR/NCEP data compares well with the observed climate patterns over eastern Africa.

#### **5.4 Model Simulations**

Results of numerical experiments conducted in this study are discussed in this section. The results for the four series of experiments are presented independently below.

### **5.4.1 Model Results of the Control Run**

This section highlights the major features that were observed with the control model experiment.

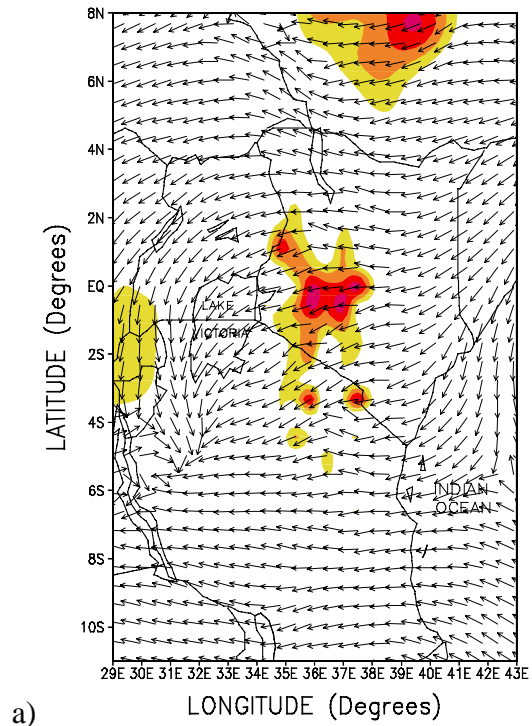
#### ***5.4.1.1 Circulation Features***

Simulated wind vectors for November are shown in Figure 5.6. The large-scale monsoon flow during this season emanates from a high-pressure cell located over Arabian peninsular and the Mascarene anticyclone located in the southern Indian Ocean. Northeasterly to northerly flow is simulated at 850-hPa level over the eastern parts of the domain north of 6°S. The wind is convergent over the western parts of Tanzania and the coastal regions. Strong zonal and meridional wind components are simulated over the eastern lowlands and the Turkana channel (Figure 5.7b,d), while relatively weaker winds are simulated over the western highlands of East Africa including the Lake Victoria basin. This wind patterns is consistent with the NCAR/NCEP reanalysis fields (Figure 5.7a,c). However, the RegCM2 simulates detailed wind patterns associated with the complexity in the regional orography and land-use patterns than is shown on the reanalysis wind patterns. These results partly explain the deficiency in the GCM based analysis in reproducing detailed regional climate patterns over equatorial eastern Africa.

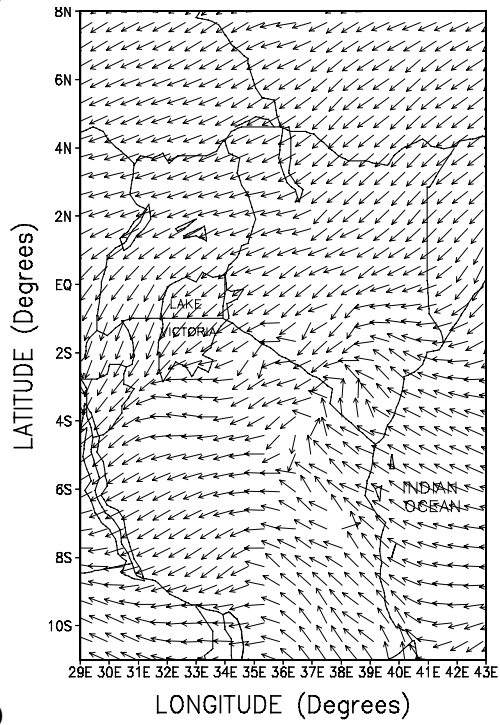
The flow at 700-hPa (Figure 5.6b) is more easterly along the Indian Ocean coast. At this level, the meridional flow corresponding to the northeast monsoon switches to a quasi-easterly flow, advecting moisture from the Indian Ocean to the inland areas (Camberlin and Wairoto 1997). There is an indication of wind convergence over the Eastern

Highlands of Kenya and northwestern Tanzania. These convergence zones may be linked to interaction between the meso-scale land/sea breeze and anabatic/katabatic flows, and large-scale mean monsoon flow (Mukabana and Pielke 1996; Indeje and Anyamba 1998).

Figure 5.8a shows the vertical cross section of horizontal wind field for November at 1°S running across Lake Victoria and the East African highlands to the Indian Ocean. Winds stronger than  $8 \text{ m s}^{-1}$  are shown centered at about 800-hPa level (located between 36°E and 39°E), winds of about  $4 \text{ m s}^{-1}$  centered at 700-hPa and winds stronger than  $6 \text{ m s}^{-1}$  centered at 200-hPa level. These wind patterns are also evident in the north-south vertical cross section at 33°E running across Lake Victoria (Figure 5.8b). Important features noticeable on these cross sections are the low-level monsoons, mid-level and upper-level jetstreams. Strong winds shown between 36°E and 39°E maybe related to the easterly monsoon flow. These monsoons are the source of the Turkana low-level jet and will be discussed in section 5.4.2. The simulated strong winds in the mid- and upper-troposphere maybe linked to the mid-tropospheric African easterly jet and the upper-tropospheric tropical easterly jet. These jetstreams have been discussed in the works by Krishnamurti (1961); Krishnamurti et al. (1976, 1980); Koteswarran (1958); Burpee (1972), among others.



a)



b)

Figure 5.6: Simulated November mean horizontal wind vectors at a) 850-hPa and b) 700-hPa levels. Surface terrain above 1500 m is indicated as shaded.

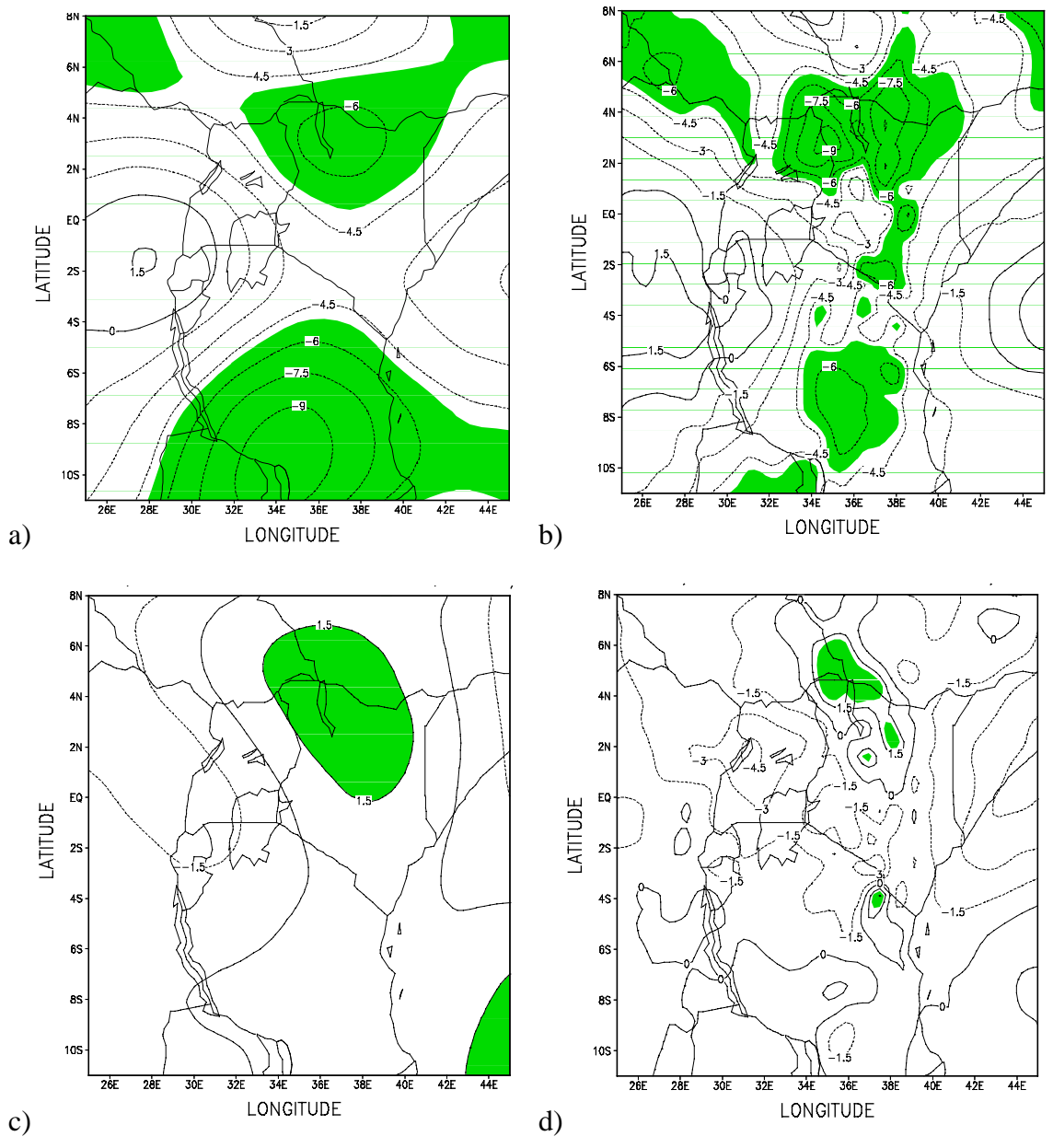


Figure 5.7: Mean November NCAR/NCEP reanalysis (left panel) and RegCM2 (right panel) simulated zonal (upper panels) and meridional (lower panels) wind speed ( $\text{m s}^{-1}$ ) at 850-hPa level. Regions of strong easterly and southerly wind flow are shaded.

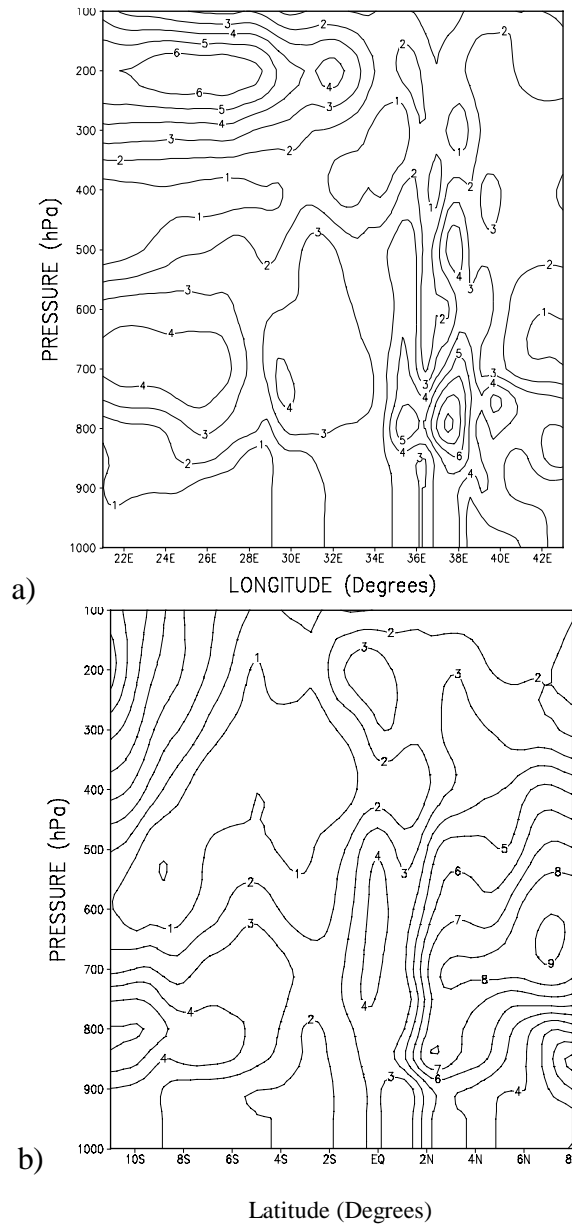


Figure 5.8: Longitude-height cross section of horizontal wind speed ( $\text{m s}^{-1}$ ) along a)  $1^\circ\text{S}$  and b)  $33^\circ\text{E}$ .

#### ***5.4.1.2 Temperature and Humidity Fields***

The RegCM2 model simulated and NCAR/NCEP reanalysis temperature and specific humidity fields at 850-hPa level are shown in Figure 5.9 and Figure 5.11. Higher temperatures are simulated over the Lake Victoria basin, and central and western Tanzania. Lower temperatures are shown to the east of the East African Highlands and the Indian Ocean coast (Figure 5.9a). This spatial distribution of temperature over the domain of study compares well with the NCAR/NCEP reanalysis fields (Figure 5.9b). The simulated surface temperature (Figure 5.10a) display an alignment following the terrain over the region. Higher temperatures (greater than 27°C) are simulated over the Indian Ocean coast, Lake Victoria basin and over Lake Tanganyika. Temperatures lower than 18°C are shown over the East African and Ethiopian highlands. Higher temperatures are also shown over the semi-desert areas of northeastern Kenya and central Tanzania. These patterns compare well with the NCAR/NCEP reanalysis field (Figure 5.10b), which basically shows the large-scale structure of temperature field with many regional details missing. Some of these regional climatic patterns include the observed high temperatures over the Lake Victoria basin, the Indian Ocean coast and the semi-arid areas of Northeastern Kenya, and low temperatures over the high mountains. The pressure gradient created between these contrasting temperatures is favorable for the formation of thermally induced meso-scale circulations over the region. These meso-scale circulations have a major control on the regional rainfall patterns (Okeyo, 1986; Mukabana and Pielke, 1996).

Specific humidity values higher than  $12 \text{ g kg}^{-1}$  are simulated over the East African highlands and the Lakes Victoria and Tanzania and values lower than  $10 \text{ g kg}^{-1}$  are simulated over the hot and dry semi-arid areas in the region (Figure not shown). The moisture field of the NCAR/NCEP reanalysis compare well with the RegCM2 simulated moisture field, however, the RegCM2 output shows a more detailed variation in the moisture field that is similar to the observed temperature patterns over the equatorial eastern African region (Figure 5.11).

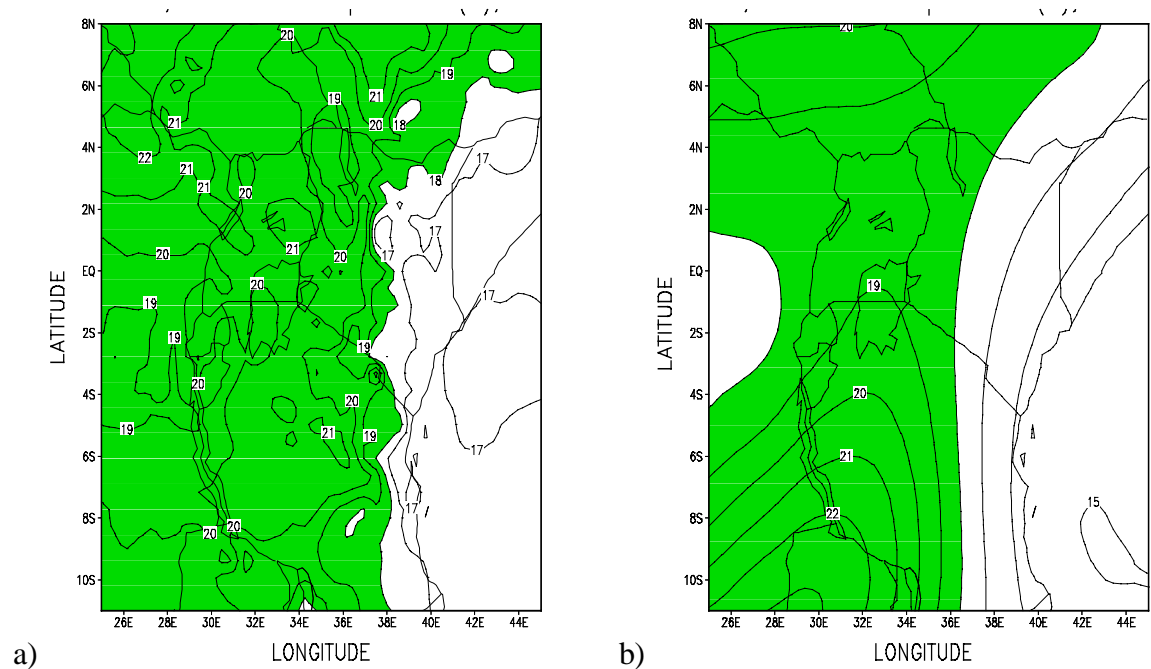
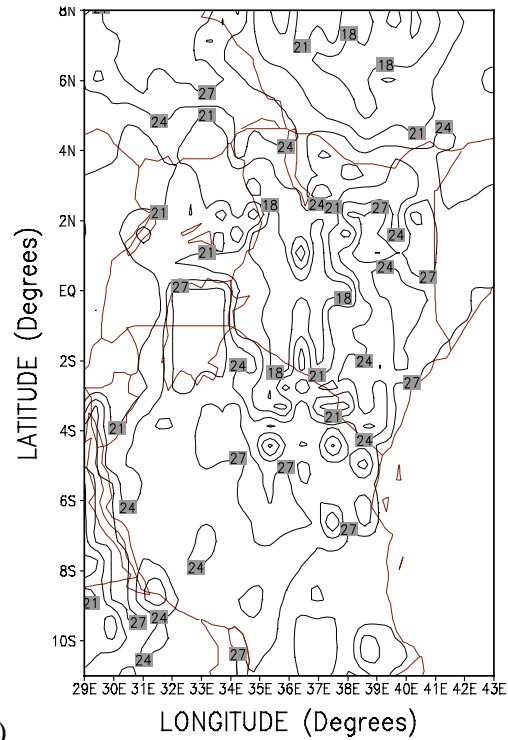
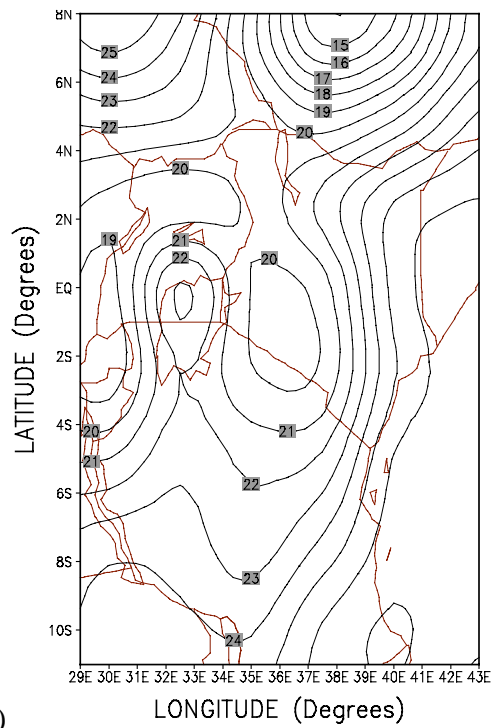


Figure 5.9: November temperature ( $^{\circ}\text{C}$ ) at 850-hPa level for (a) RegCM2 model simulation, and b) NCAR/NCEP reanalysis.



a)



b)

Figure 5.10: Simulated November surface temperature ( $^{\circ}\text{C}$ ) for a) RegCM2 and b) NCAR/NCEP GCM.

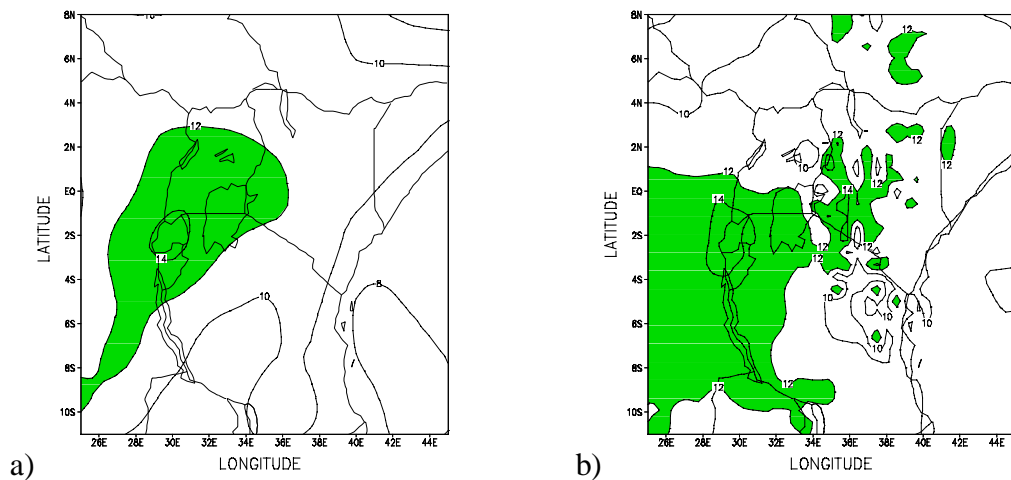


Figure 5.11: November specific humidity ( $\text{g kg}^{-1}$ ) at 850-hPa level for (a) RegCM2 model simulation, and b) NCAR/NCEP reanalysis.

#### 5.4.2 Simulation of the Turkana Low-level Jet

The Turkana easterly low-level jet lies in the Turkana channel (Figure 5.1). The channel is wider at the center as compared to the entrance and the exit. Lake Turkana lies in the middle part of this channel at approximately latitudes  $35.5^{\circ}\text{E}$  and  $36.5^{\circ}\text{E}$  and longitudes  $2^{\circ}\text{N}$  and  $4^{\circ}\text{N}$ . In this study, we investigate the dynamics and thermodynamics of the Turkana easterly low-level jet. The simulated characteristics of the jet are compared with the limited observations that were carried out in the channel by Kinuthia (1992) during the month of February 1983.

#### ***5.4.2.1 Dynamical Structure of the Jet***

In this subsection, results from the control model run are further analyzed. Orography and other forcing mechanisms (large-scale flow and depth of the channel) are incorporated in these experiments. Figure 5.12a-c illustrates the simulated flow patterns in the Turkana channel during the northeast monsoon period of November. Streamlines at 950-, 850- and 750-hPa levels show southeasterly to northeasterly flow before entering the channel. On entering the channel, the streamlines become confluent and turn to southeasterly. This southeasterly flow is clearly shown at 950- and 850-hPa levels but northeasterly wind direction is indicated at 750-hPa level. Convergent wind is shown at the channel exit while divergent wind is indicated at the middle of the channel. These results agree with the observational studies reported by Kinuthia (1992). Ramachandran et al. (1980) indicated that there is a fanning out of surface winds emerging from a mountain gap. These results indicate that the flow becomes confluent at the jet exit as the channel becomes narrower again. Kinuthia (1992) observed similar characteristics associated with this jet.

The latitude-height cross section of mean horizontal wind speed for October, November and December along the channel is shown in Figure 5.13. The wind flow is from southeast and northeast throughout the channel in the three months. This flow extends from surface to about 800-hPa level where it becomes predominantly easterly. Above 700-hPa level, the flow is mainly northeasterly as shown during the months of November and December. Transition of the mean wind to the east and northeast aloft throughout the season and throughout the channel is also indicated. The level of maximum winds occurs

in the layers 930-hPa and 650-hPa. The levels of maximum winds decline down from the entrance to the middle region and then rise up again towards the exit. Before and near the channel entrance and at the channel exit the levels of occurrence of maximum winds are almost the same. At the channel entrance, the jet core is at 900-hPa and 800-hPa levels. In the middle of the channel they combine into one single jet centered at 700-hPa level especially in November, and at the exit it is centered at about 820-hPa level. Kinuthia (1992) observed that the magnitude of maximum wind in Lodwar, a station to the western side of Lake Turkana was about 1.5 - 3 times less than the maximum winds in the stations to the eastern side of the lake. He explained the weakening of the winds to be possibly due to the widening of the channel to about 2.5 times the width at the entrance. The southeasterlies and the easterlies increase in intensity throughout the channel, and from the surface to the level of the occurrence of mean maximum wind, then decreases aloft. The largest value of the mean maximum wind speed is about  $11 \text{ m s}^{-1}$  (~22 knots).

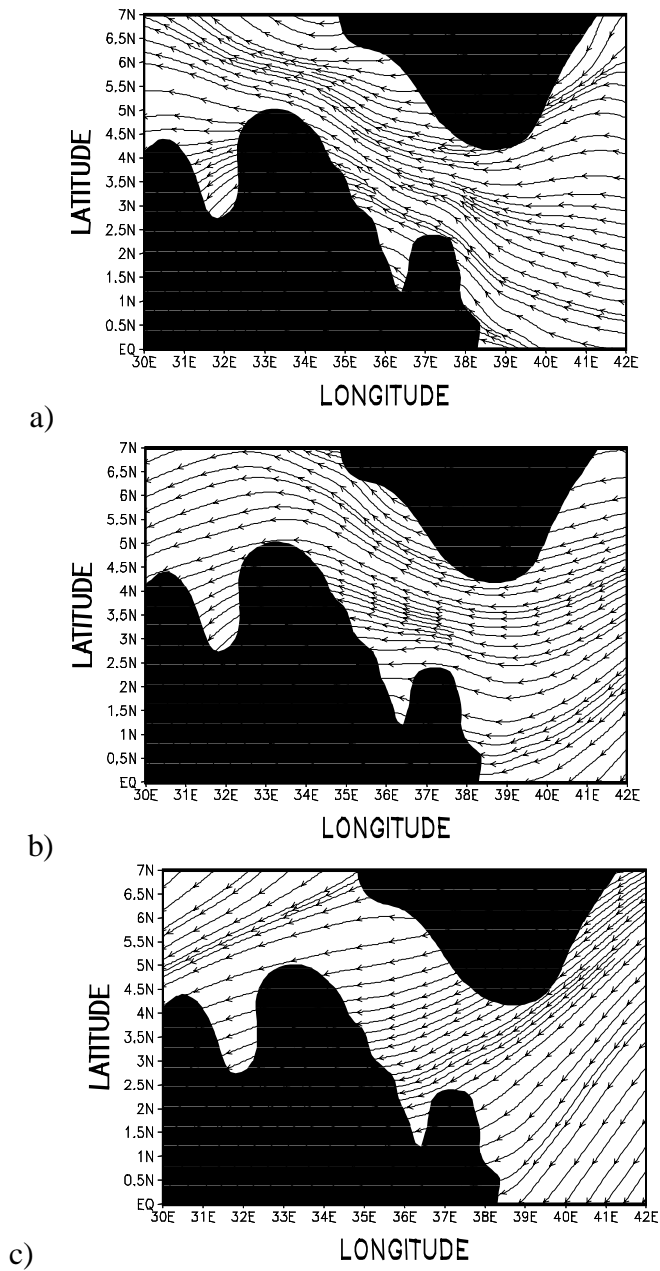


Figure 5.12: Streamlines of the simulated November mean conditions at a) 950-hPa, b) 850-hPa and c) 750-hPa levels over the Turkana channel in the control run. The mean configuration of the surface orography is indicated in dark shaded.

The jet is weaker in October and intensifies in November and December to almost twice the speeds observed in October. Similar results were shown by SSOG99 using an earlier version of the RegCM2. Weakening of the winds in the middle of the channel to about a half the values observed at the entrance and exit could be due to the widening of the channel width in that section. The observed increase in the wind speed at the channel exit may be explained in terms of, a) narrowing of the channel from the center toward the exit and, b) a conversion of potential energy to kinetic energy that may occur at the valley's exit as the jet exits the valley causing air to sink and flow out over the flat plain. The deep Turkana channel that ends abruptly at the plain over southern Sudan may enhance this energy conversion. Baines (1995) gives a broader discussion of this energy conversion associated with flows exiting a valley.

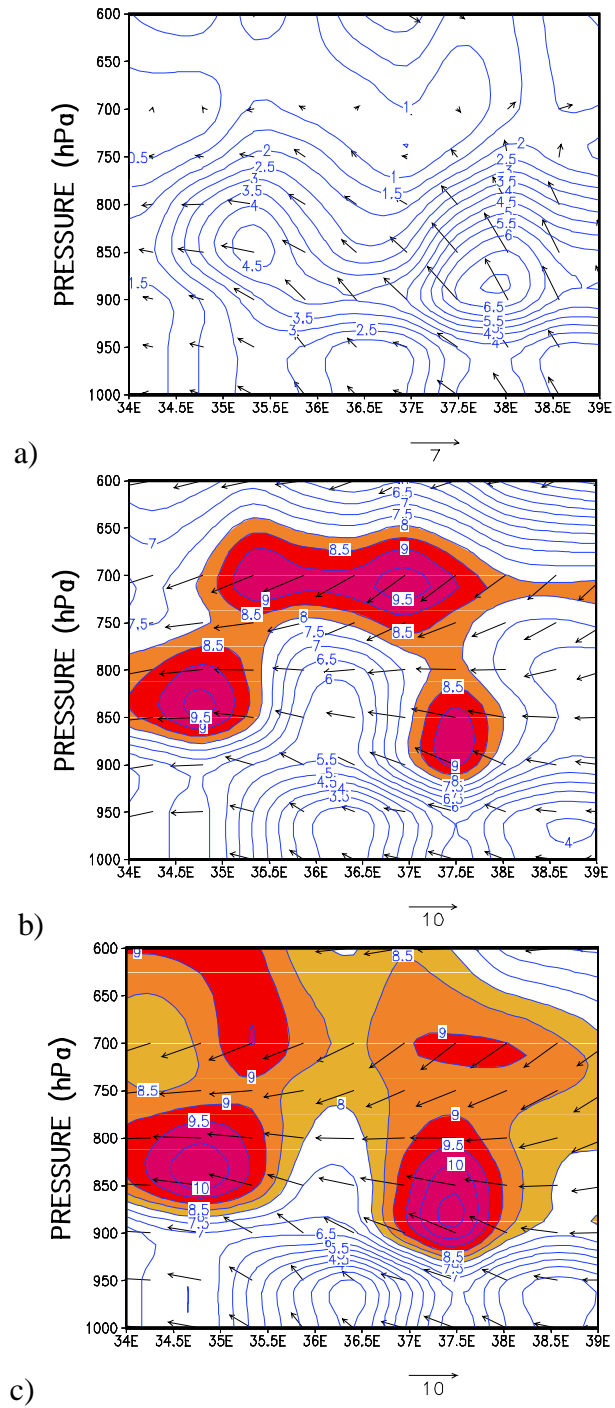
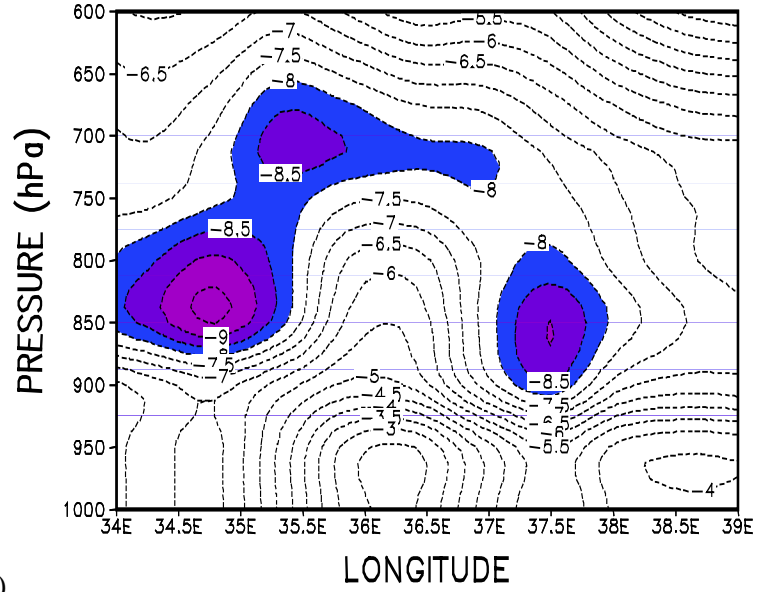
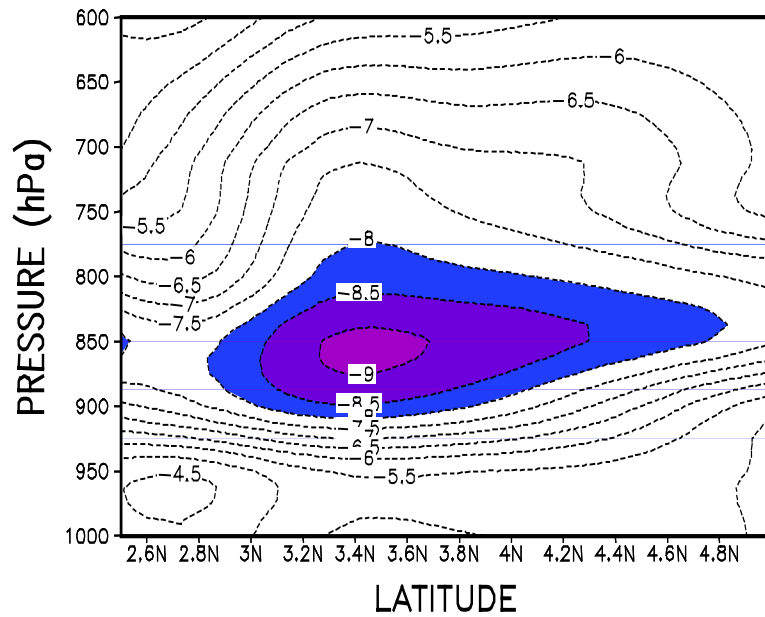


Figure 5.13: Simulated mean horizontal wind speed for a) October, b) November and c) December at lat. 3.5°N along the Turkana Channel in the control run. Shaded are values with wind stronger than 8 m s<sup>-1</sup> and vectors indicate the wind direction.



a)



b)

Figure 5.14: Simulated November mean zonal wind component a) at lat. 3.5°N along the Turkana Channel, and b) at lon. 37.5°E across the entrance of the Turkana Channel, for and control run. Shaded are values with wind speed stronger than 8 m s<sup>-1</sup>.

Figure 5.14 shows the zonal component of the horizontal wind along and across the channel entrance for the month of November. Easterly wind component is found to dominate the flow along the channel. The magnitudes and location of wind maxima are similar to those shown on the horizontal wind across the channel. This implies that the configuration of the bottom orography in this region dictates the wind direction from a southeasterly and northeasterly to a mainly easterly flow. The cross section of the zonal winds at longitude  $37.5^{\circ}\text{E}$  across the entrance of the channel (Figure 5.14b) shows the jet core located at 850-hPa level and extending from 900-hPa to about 800-hPa levels. These results agree with the kinematics of the jet shown in the east-west cross section along the channel (Figure 5.13b).

The horizontal wind divergence was computed for the entrance, middle and exit of the channel and the results are shown in (Figure 5.15). These results indicate that at the entrance and the channel exit, convergence ( $\sim 1.0 \times 10^{-5} \text{ s}^{-1}$ ) occurs below 900-hPa level and divergence ( $\sim 0.3 \times 10^{-5} \text{ s}^{-1}$ ) between 860 and 760-hPa levels. In the middle of the channel, relatively weak horizontal wind divergence ( $\sim 0.2 \times 10^{-5} \text{ s}^{-1}$ ) is indicated below 900-hPa level and increase to a maximum of about  $1.8 \times 10^{-5} \text{ s}^{-1}$  located at 860-hPa level followed by a general decrease aloft. The observed low-level horizontal divergence in the middle of the channel and over the Lake Turkana basin may inhibit any convection associated with the meso-scale circulation around the lake basin. Several studies have shown these areas to display arid to semi-arid climates (Ogallo 1980; Indeje et al. 2000).

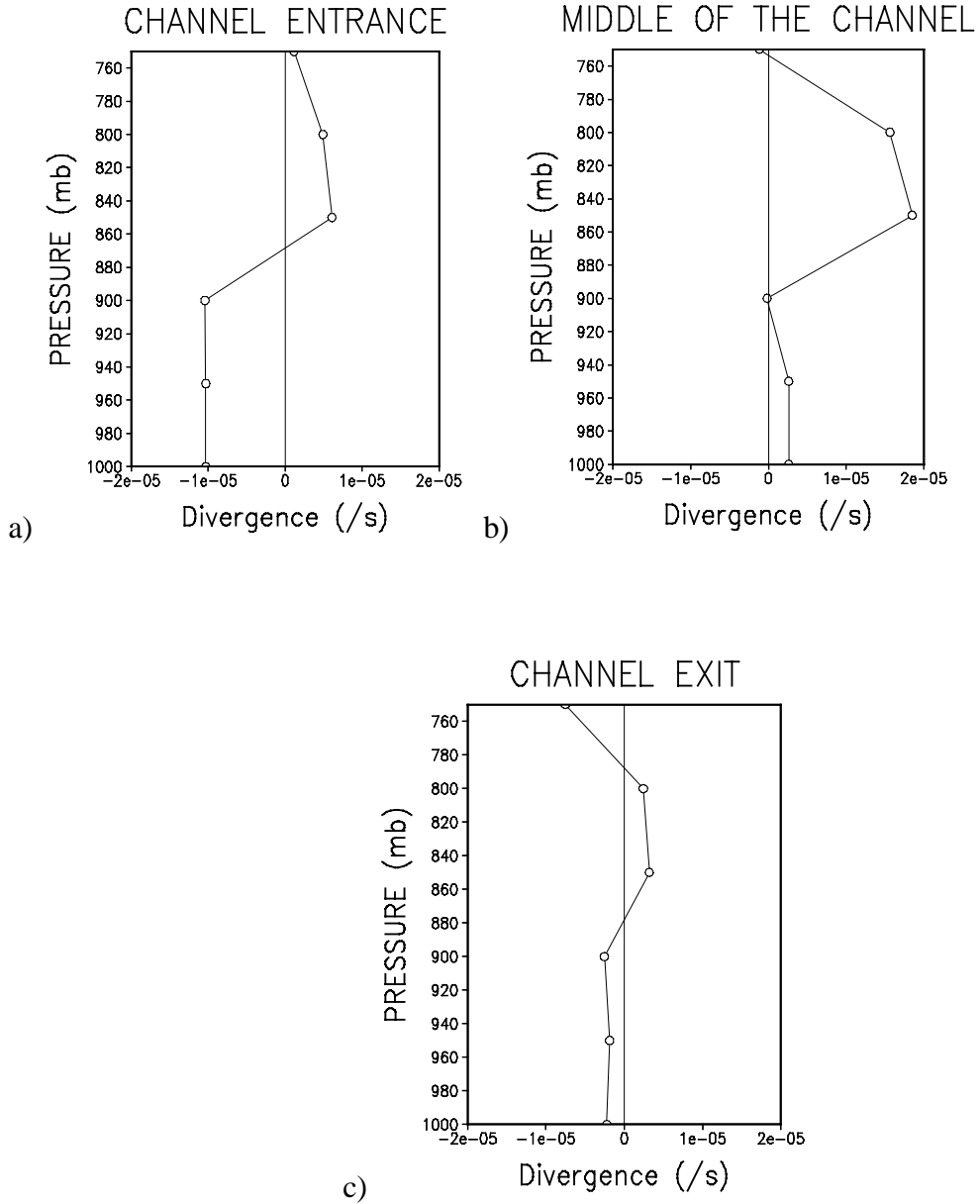


Figure 5.15: Simulated November mean horizontal divergence at a) the channel entrance near Marsabit, b) middle of the channel around Lake Turkana and c) at the exit of the channel near Logichoggio, for the control model run. These locations are shown in Figure 5.1.

These results of divergence/convergence fields are consistent with those obtained from the observational and analytical studies by Kinuthia (1992). Anyamba (1983) noted that over northern Kenya during the month of January (boreal winter season), the month when the northeast monsoon reaches its maximum intensity, in spite of the rather diffluent streamlines over Kenya, the Turkana Channel area still displayed convergence at the low levels. The low-level horizontal wind divergence in the middle of the channel may explain the splitting of the jet cores at these parts of the valley. Consequently, convergence of the horizontal wind above 750-hPa level may explain the re-appearance of a combined jet at 700-hPa level in this part of the channel. Previous studies have shown similar phenomenon in barotropic flows (Thompson 1957; Wiin-Nielsen 1961; Krishnamurti et al. 1976; and others). Krishnamurti et al. (1976) have associated strong divergence in the flux of westerly momentum to the splitting of the East African Low-level Jet (EALLJ) observed over the western Indian Ocean during the period May through October. Regions of large net divergence of easterly momentum flux may result in the weakening of a parent Turkana jet and a new jet may form in the vicinity where there is large net convergence of easterly flux of momentum.

Figure 5.16 shows the longitude-height cross section of vertical velocity along the Turkana Channel. Centers of upward/downward vertical velocity are located between 850- and 500-hPa levels. Downward vertical motion of about  $2.0 \times 10^{-2} \text{ m s}^{-1}$  is shown before the channel entrance located at  $37.5^{\circ}\text{E} - 38^{\circ}\text{E}$ . This downward motion may be related to the divergent nature of the easterly monsoon flow in the low levels (Lamb 1983;

Anyamba 1983). Upward vertical motion ( $\sim 1.5 \times 10^{-2} \text{ m s}^{-1}$ ) is simulated at the channel entrance (centered at  $37^\circ\text{E}$ ), and at the exit of the channel, it is about  $2.5 \times 10^{-2} \text{ m s}^{-1}$  (located between  $34^\circ\text{E}$  and  $34.5^\circ\text{E}$ ). In the middle of the channel and over the Lake Turkana basin (between  $34.5^\circ\text{E}$  and  $36.5^\circ\text{E}$ ), downward vertical motion is dominant with two centers of about  $2.0 \times 10^{-2} \text{ m s}^{-1}$  as indicated in Figure 5.16.

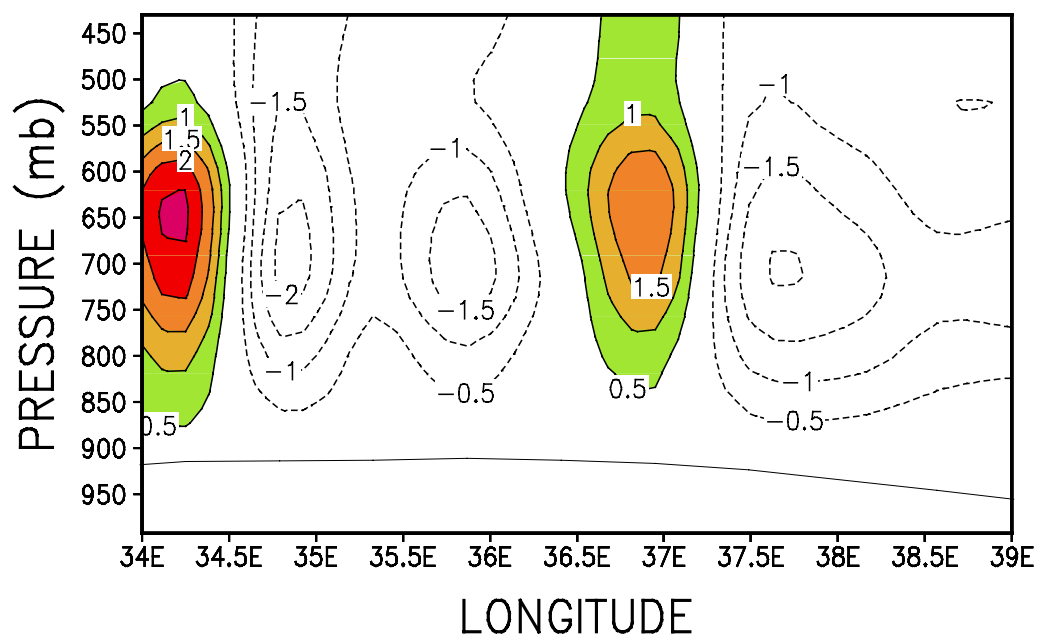


Figure 5.16: Longitude-height cross section of vertical velocity at lat.  $3.5^\circ\text{N}$  along the Turkana channel. Shaded are areas of upward vertical velocity. The bottom orography, which is almost flat in the channel, is also shown.

The dominant downward motion over the Lake Turkana basin may inhibit any convective activity and thus weakening any development of the meso-scale circulations over this region. The vertical motion field in the channel is consistent with the simulated horizontal

divergence field (Figure 5.15). Upward/downward motion is associated with low-level convergence/divergence zones.

Vorticity of mean winds at the channel entrance, middle and exit is shown in Figure 5.17. At the channel entrance anticyclonic vorticity is simulated above 950-hPa level with a maximum ( $\sim 2.0 \times 10^{-5} \text{ s}^{-1}$ ) shown at 900-hPa level. In the middle of the channel, anticyclonic vorticity is simulated below and above 900-hPa level and cyclonic vorticity indicated at 900-hPa level. The anticyclonic vortices that exists at the entrance and middle of the channel is possibly due to the friction effects which slow down the southeasterly to northeasterly currents along the mountain edges. Kinuthia (1992) observed that anticyclonic relative vorticity existed in the northern half and cyclonic relative vorticity in the southern half over the eastern parts of the channel. At the exit of the channel, relatively weak anticyclonic/cyclonic vortex is shown. This may indicate that the flow is nearly irrotational at this section. Also, at the channel exit the vortices could decay unless they receive some energy to sustain them. Kinuthia (1992) postulated that the vortices generated in the Turkana channel may contribute to the mid-tropospheric African Easterly jet associated with the easterly waves over West Africa that ultimately develop into hurricanes observed over the eastern coast of the United States of America.

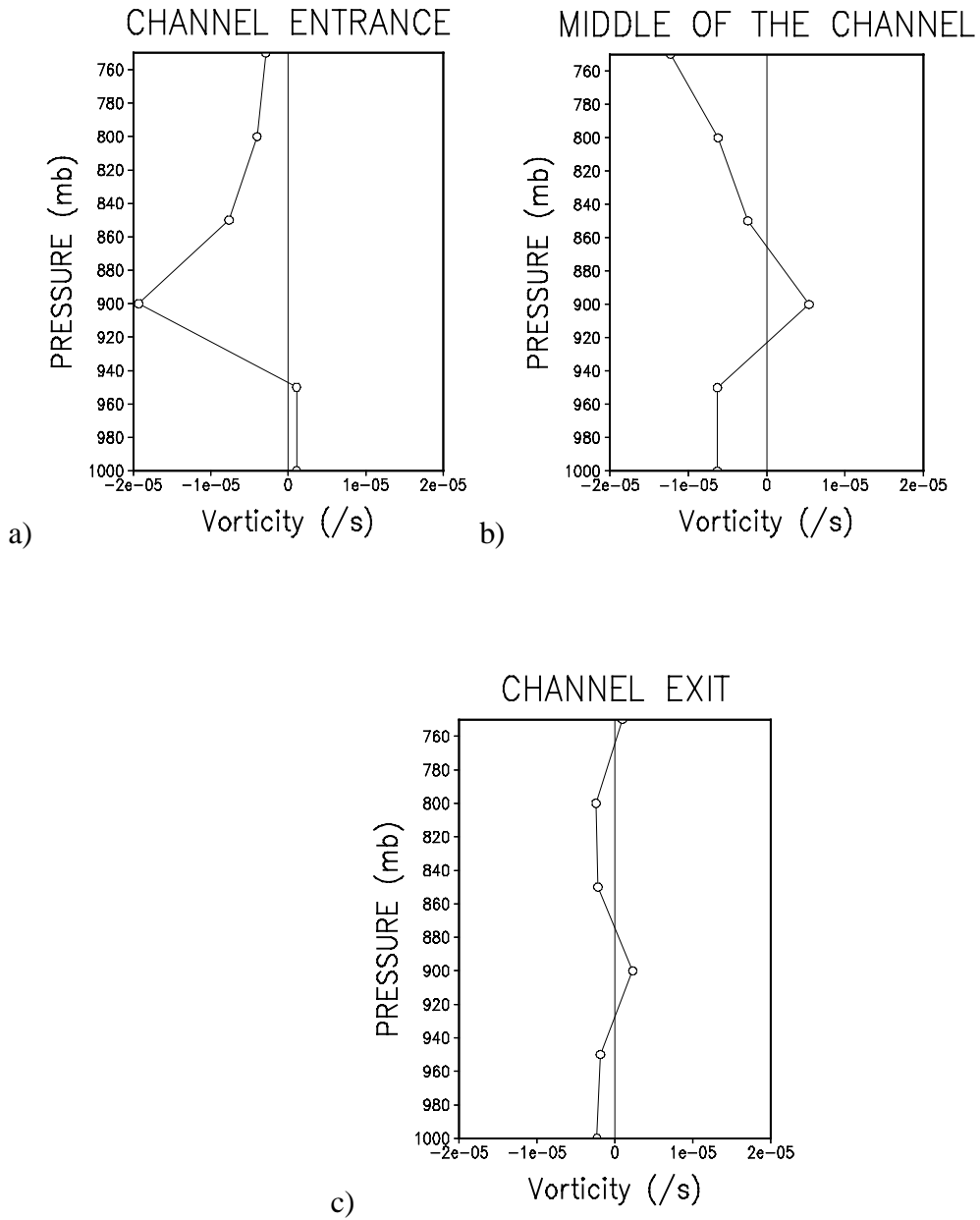


Figure 5.17: Simulated November mean vorticity at a) the channel entrance near Marsabit, b) middle of the channel around Lake Turkana and c) at the exit of the channel near Logichoggio, for the control model run.

#### ***5.4.2.2 Thermal and Moisture Structure in the Jet Axis***

Figure 5.18a shows the mean temperature at 850-hPa level over the Turkana channel for the month of November. The figure indicates a nearly homogeneous temperature along the channel. High temperatures ( $> 18.5^{\circ}\text{C}$ ) are indicated close to the edges of the valleys, which are exposed more to the solar radiation than the valleys below. The temperature gradient resulting from warmer valley edges and cooler valley bottom may be conducive to the development of thermally induced mountain/valley flows. In this valley these thermally induced flows are cross wind to the Turkana jet axis and may be suppressed by the presence of the jet. With a near homogeneous temperature along the channel, one would expect the existence of a weak temperature gradient. This suggests that orographic channeling effects may dominate the thermal forcing in the development of this jet. However, low temperatures ( $\sim 16^{\circ}\text{C}$ ) are indicated over the eastern end of the channel and high temperatures of about  $20^{\circ}\text{C}$  over the western sector of the channel. The temperature difference of  $4^{\circ}\text{C}$  between the two ends of the valley may be favorable for the generation of an east-west pressure gradient that may sustain the wind flow along the channel from east to west.

Figure 5.18b shows the mean surface pressure over the channel. There is an indication of almost constant pressure ( $\sim 895\text{-hPa}$ ) along the center of the channel. The almost constant pressure and temperature fields along the channel may justify the assumption that the flow is nearly barotropic in this valley. We can also infer from these results that the

Bernoulli function given by equation (5.3) is almost constant in the channel since the wind speed is almost constant ( $\sim 11 \text{ m s}^{-1}$ ) in the jet cores throughout the channel.

To study the evolution of water vapor distribution in the channel, the moisture flux divergence was computed using the following equation

$$F_v = \nabla \cdot (q\vec{V}) \quad (5.40)$$

$F_v$  was multiplied by minus one for convenience. Thus,  $F_v < 0$  indicates moisture flux divergence and  $F_v > 0$  indicate moisture flux convergence. Moisture flux divergence fields combine the horizontal advection of moisture with mass convergence, which are the two prime factors in developing strong convection (Doswell 1977). Areas of increasing moisture contribute to de-stabilization, while mass convergence results in vertical motion. The forcing and de-stabilization resulting from moisture convergence may be used to diagnose areas of convection.

Figure 5.19 shows the simulated moisture flux divergence field along the Turkana channel. Moisture flux convergence ( $\sim 4.0 \times 10^{-6} \text{ kg kg}^{-1} \text{ s}^{-1}$ ) is indicated over the channel entrance ( $\sim 37^\circ\text{E}$ ) and exit ( $\sim 34^\circ\text{E}$ ). In the middle of the channel ( $\sim 34.5^\circ\text{E} - 36^\circ\text{E}$ ), divergence of moisture flux ( $\sim 5.0 \times 10^{-6} \text{ kg kg}^{-1} \text{ s}^{-1}$ ) is shown. There is a tendency for the centers of the moisture flux convergence/divergence to tilt with height from the channel entrance to the channel exit. The simulated moisture flux divergence over the Lake Turkana basin ( $\sim 34.5^\circ\text{E} - 36^\circ\text{E}$ ) may further inhibit developments of meso-scale circulations over these

areas. Moisture flux convergence/divergence zones compare well with the simulated upward/downward vertical velocity over different parts of the channel. Sections with upward/downward motions are associated with positive/negative fluxes of moisture.

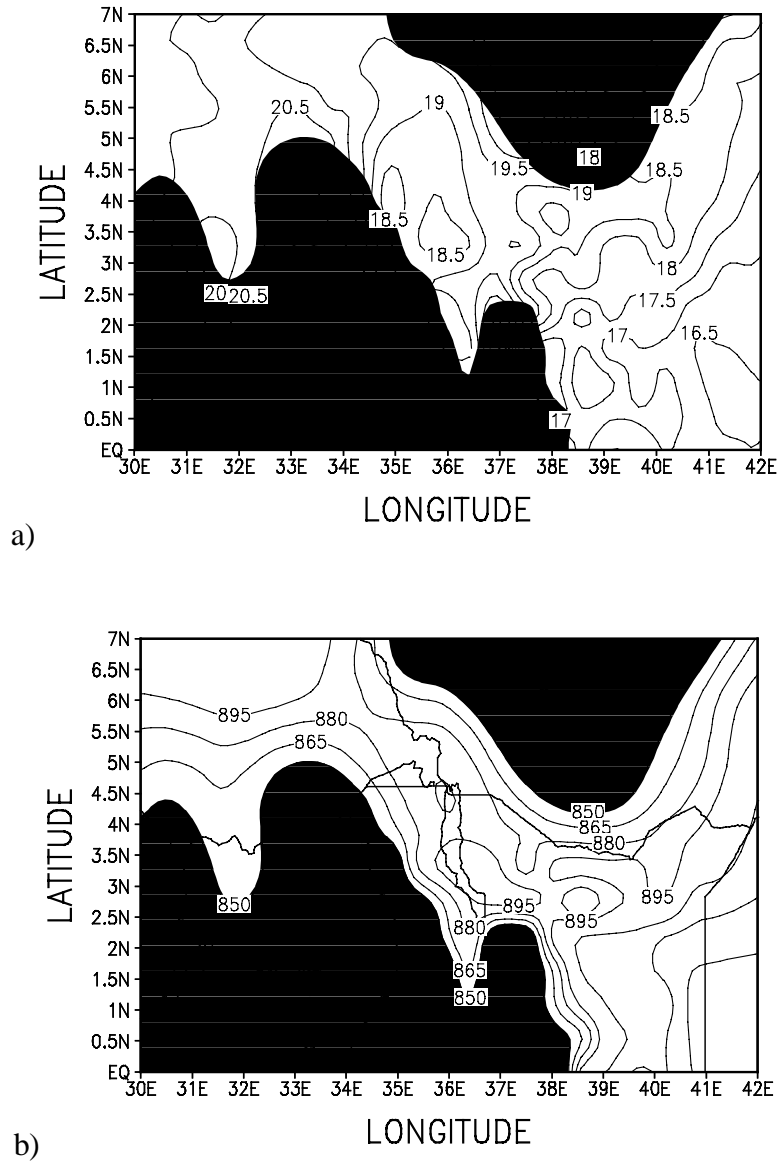


Figure 5.18: Simulated November a) mean temperature ( $^{\circ}\text{C}$ ) at 850-hPa, and b) mean surface pressure (hPa) over the Turkana channel in the control model run.

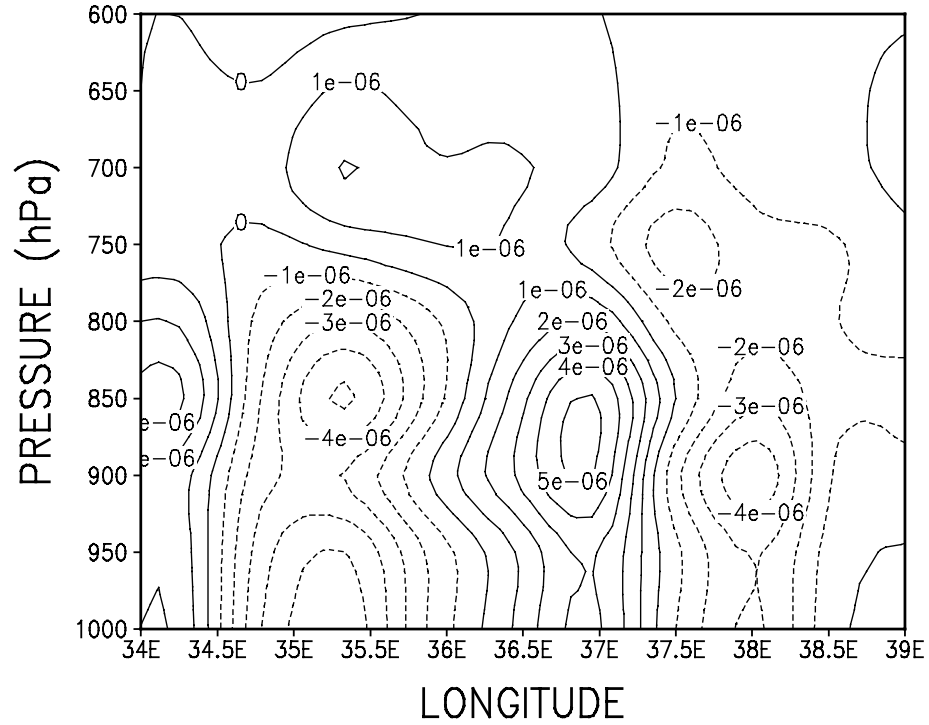


Figure 5.19: Simulated November mean moisture flux divergence ( $\text{kg kg}^{-1} \text{s}^{-1}$ ) along the Turkana channel in the control model run. Positive values indicate divergence and negative convergence of moisture flux.

In order to obtain some information about the fluctuations of temperature fluxes and study their evolution at particular locations in the channel, the following flux divergence equation was used

$$G_V = \nabla \cdot (T\vec{V}) \quad (5.41)$$

$G_V$  was multiplied by minus one for convenience. Thus,  $G_V < 0$  indicates temperature flux divergence and  $G_V > 0$  indicate temperature flux convergence. Figure 5.20 displays the temperature flux divergence field along the Turkana channel. At the channel entrance (~

37°E) and exit (~ 34°E), temperature flux divergence ( $\sim 12.0 \times 10^{-2} \text{ K s}^{-1}$ ) is indicated. Temperature flux convergence ( $\sim 12.0 \times 10^{-2} \text{ K s}^{-1}$ ) is shown at the middle of the channel and to the east of Lake Turkana (between latitudes 34.5°E - 36°E). The observed cooling of the lower troposphere over the Lake Turkana basin might inhibit convection and cause decreased (moisture) convergence and precipitation. These patterns compare well with the moisture flux convergence and the centers of the jet cores.

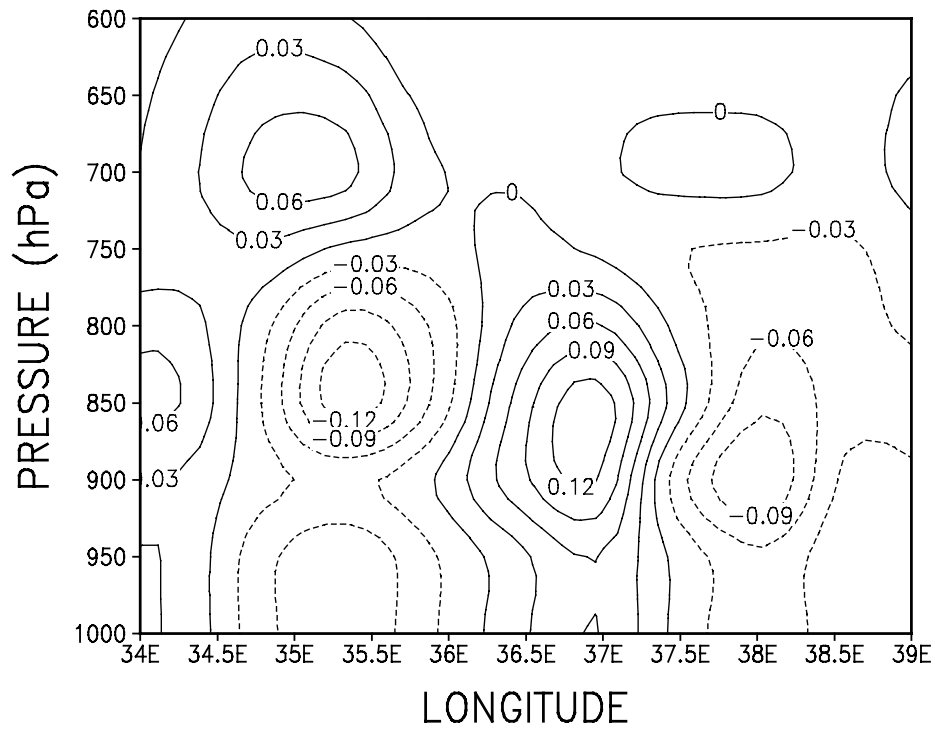


Figure 5.20: Simulated November mean temperature flux divergence ( $\text{K s}^{-1}$ ) along the Turkana channel in the control model run.

Based on equation (5.4), if we take the depth at the entrance of the channel to be about 1027 m, and the width as  $2.5^\circ$  ( $\sim 2.5 \times 111.1 \times 1000$  m),  $\rho = 1 \text{ kg m}^{-3}$  and  $g = 9.81 \text{ m s}^{-2}$  then the mass flow rate across the channel is about  $3.9 \times 10^7 \text{ kg s}^{-1}$ . This is the amount of mass being transported from the eastern part to the western part of the channel.

### **5.4.3 Effects of Large-scale Orography on the Jet**

We intend to ignore the spatial variation of orography in this case study with all other parameters remaining the same. Figure 5.21a illustrates the solution of the streamlines at 850-hPa level in November for this experiment. The flow is generally northeasterly throughout the channel and the observed southeasterly flow in the channel is missing. Figure 5.21b shows the wind vectors and isotachs. When compared with Figure 5.13b, the wind speed in this case is weak with a maximum of about  $6 \text{ m s}^{-1}$  over the channel and the jet cores are either missing or very unrealistic. There is also small variation of wind speed with height. The observed strong winds are not present in the jet cores at the entrance and exit of the channel. These results generally indicate missing of the key features associated with the jet when the entire topography is suppressed. These results indicate the importance of the large-scale orography for the simulation of the Turkana jet.

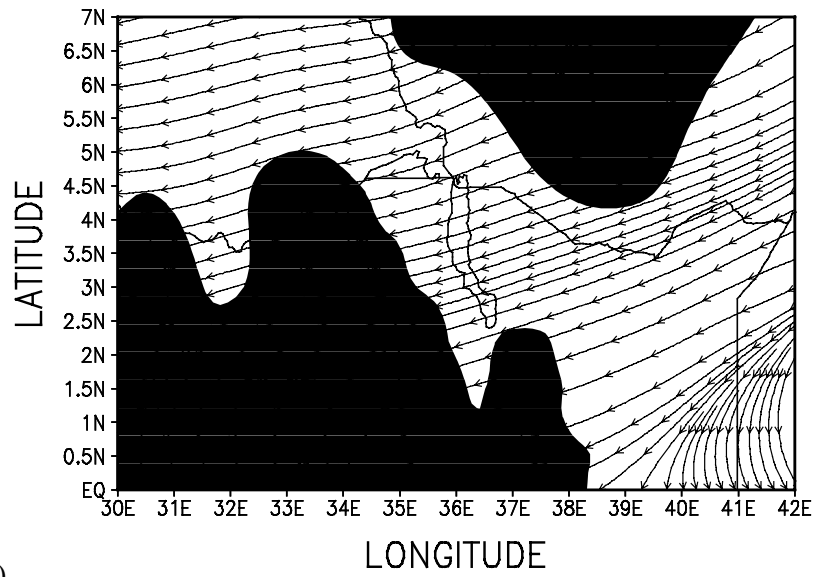
### **5.4.4 Influence of the Large-scale Monsoon Flow on the Jet**

Sensitivity of the Turkana low-level jet to the calm wind speed is investigated in this case study by initializing the model with no (zero) ambient wind ( $u = v = 0$ ). The large-scale kinematics forcing at the lateral boundaries was also set equal to zero throughout the simulation. Cross-examination at the boundaries indicates that the effect of the large-scale

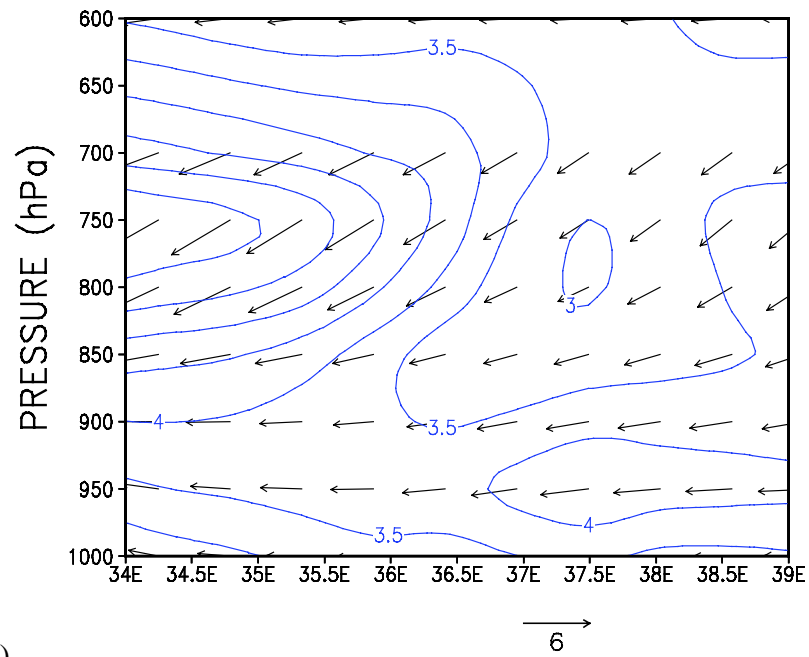
flow is not felt beyond the buffer zone. Figure 5.22 shows the results from these experiments. The wind flow over the channel turns from northeasterly to southeasterly at the channel entrance. These streamline analyses compare well with results in the control run Figure 5.12. The tendency of the wind speed to increase with height throughout the channel is also observed (Figure 5.22b). However, the maximum wind speed in the jet cores is about  $6 \text{ m s}^{-1}$  at the valley entrance and exit, and about  $9 \text{ m s}^{-1}$  at the middle of the valley centered at about 700-hPa level. Compared to the control simulation, the winds in this case are weaker by 50%. These results indicate that the large-scale flow enhances the strength of the wind speed in the jet cores. Thermal forcing and possibly the effect of surface drag in concentrating the flow along the jet core may play equal roles as that of the large-scale monsoon in the development and maintenance of the Turkana low-level jet. These results show that the jet cores could still exist even in the cases of weak large-scale monsoon flow but will be weaker (by about 50%) than the observed.

#### **5.4.5 Effects of the Channel depth on the Turkana Jet**

In this experiment the large-scale orography and the large-scale monsoon flow are included and the depth of the channel was artificially raised to a constant level of 1000-m AMSL. Results obtained from this simulation are depicted in Figure 5.23. There is reduced streamline convergence over the channel. The jet cores tend to combine and move to the center of the channel where strong winds ( $\sim 7 \text{ m s}^{-1}$ ) are shown. There is also a general rising in the level of the jet cores to center at about 850- and 650-hPa levels. These results indicate that the depth of the channel plays a role in determining the correct height of the observed jet cores in the Turkana easterly low-level jet.

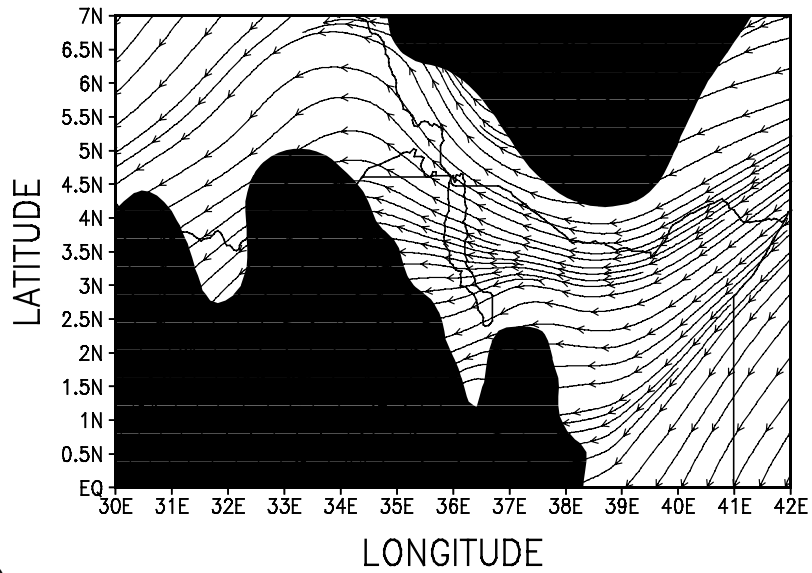


a)

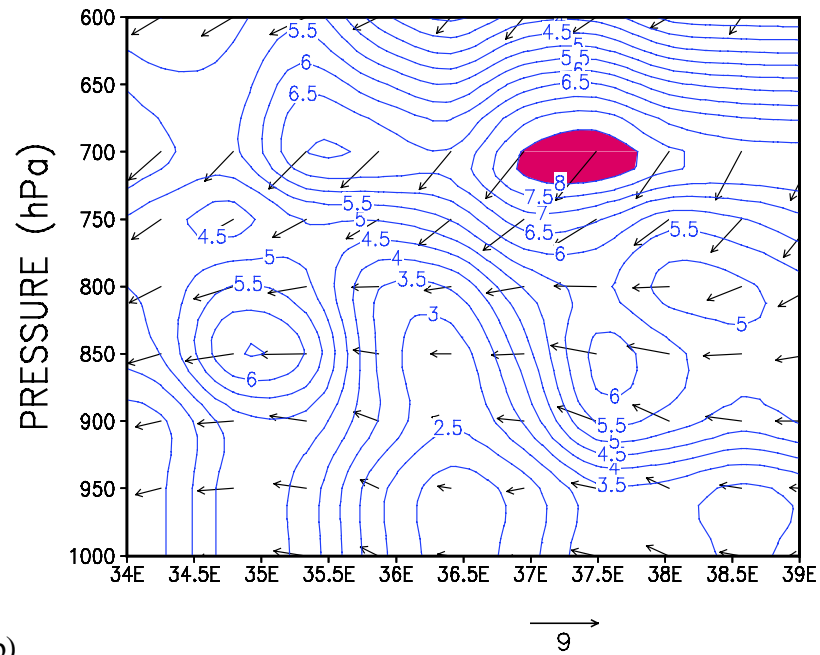


b)

Figure 5.21: Simulated November a) mean wind flow at 850-hPa over the Turkana channel, and b) mean wind speed along the Turkana channel, for the NOTOPO experiment.

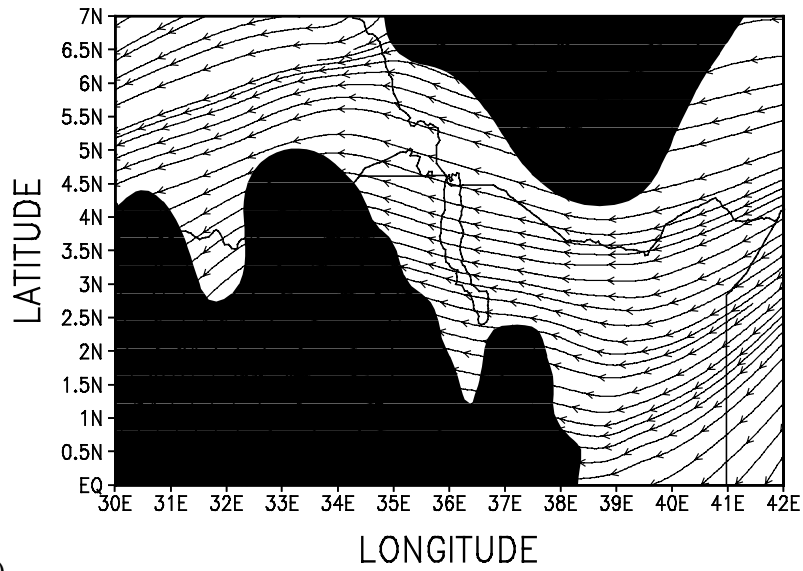


a)

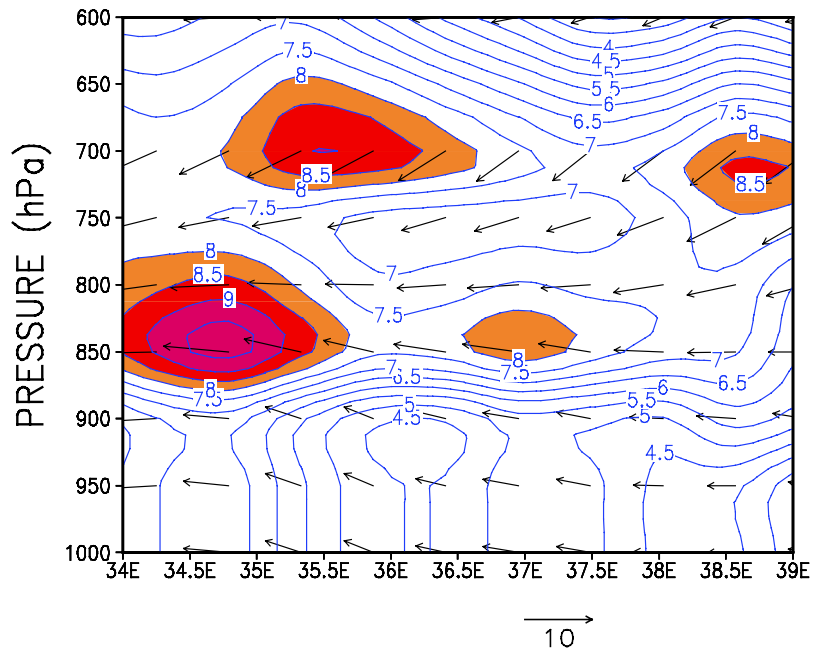


b)

Figure 5.22: Simulated November a) mean wind flow at 850-hPa over the Turkana channel, and b) mean wind speed along the Turkana channel, for the zero large-scale ambient wind experiment.



a)



b)

Figure 5.23: Simulated November a) mean wind flow at 850-hPa over the Turkana channel, and b) mean wind speed along the Turkana channel, for the channel depth experiment.

## Chapter 6

### **6 DYNAMICS AND THERMODYNAMICS OF THE EL NIÑO AND NON-EL NIÑO ASSOCIATED CLIMATIC CONDITIONS OVER EASTERN AFRICA**

The physical mechanisms responsible for the occurrences of wet and dry episodes over eastern Africa during the October-December rainy season are investigated using a numerical regional climate model. Two contrasting years the El Niño (1982) and non-El Niño (1987) that were associated with wet and dry episodes respectively are studied. The year 1988 that displayed near normal conditions is used in the control model simulations. This study is aimed at understanding the physical mechanisms responsible for modulating the floods and droughts over eastern Africa during the short rains season. Such an understanding is necessary before attempting to predict climatic variability in the region. Results obtained from this study may be used in short and medium range climate guidance and forecasting in the region.

#### **6.1 Background**

Several mechanisms including El Niño/Southern Oscillation (ENSO), sea-surface temperatures (SST), the Quasi-Biennial Oscillation (QBO) in the equatorial lower stratospheric zonal winds and 20-60 Madden-Julian waves have been proposed as being some of the primary factors responsible for the regional interannual climate variability over eastern Africa (Ogallo 1988; Farmer 1988; Anyamba 1992; Nyenzi 1992; Rowell et al. 1994; Ininda 1998; Nicholson 1996; Mutai et al. 1998; Indeje et al. 2000). On the

interannual and shorter time scales, there may be shift in the Walker circulation over land and the adjacent Indian Ocean with associated changes to the preferential location and strength of the sub-tropical high pressure cells, the major synoptic rainfall producing system of the region (e.g., SSOG99; Semazzi and Indeje 1999; Webster et al. 1999; Saji et al. 1999) as well as interaction with the QBO and other wind-rainfall mechanisms (e.g., Anyamba 1992; Ogallo et al. 1994; Camberlin 1995; Camberlin and Wairoto 1997; Okoola 1999; Indeje and Semazzi 2000).

A number of investigators have utilised kinematics and the associated transport and convergence of moisture, to study the evolution of dry and wet episodes over several regions. Matarira and Jury (1992) showed that the meridional wind was generally southerly over and to the east of Zimbabwe at the 700-hpa level during the dry spells, whereas it was northerly during the wet spells. Semazzi et al. (1996) observed that in response to the SST anomaly regimes, the rainfall deficits over the west and southern Africa in 1973 compared to 1950 were associated with continental scale diffluent low-level circulation anomalies. Johnson and Morth (1961), and Nakamura (1968) indicated that the wet rainfall conditions in the region were associated with the cool, moist and unstable westerly air mass from the Congo forests transported into the East African region by the equatorial mid-tropospheric westerly winds. These equatorial mid- and lower-tropospheric westerly winds have also associated with abundant rainfall over Kenya (Camberlin and Wairoto 1997). Okoola (1999) showed that a cyclonic circulation over southern Madagascar in the mid-troposphere forced southerly winds through Mozambique

Channel which turned eastward near the equator driving broad westerly flow in the equatorial regions during the Northern Hemisphere Spring season. These southerlies followed by westerlies were associated with wet spells over the East African region while stronger than normal easterlies near the equatorial regions were associated with dry conditions.

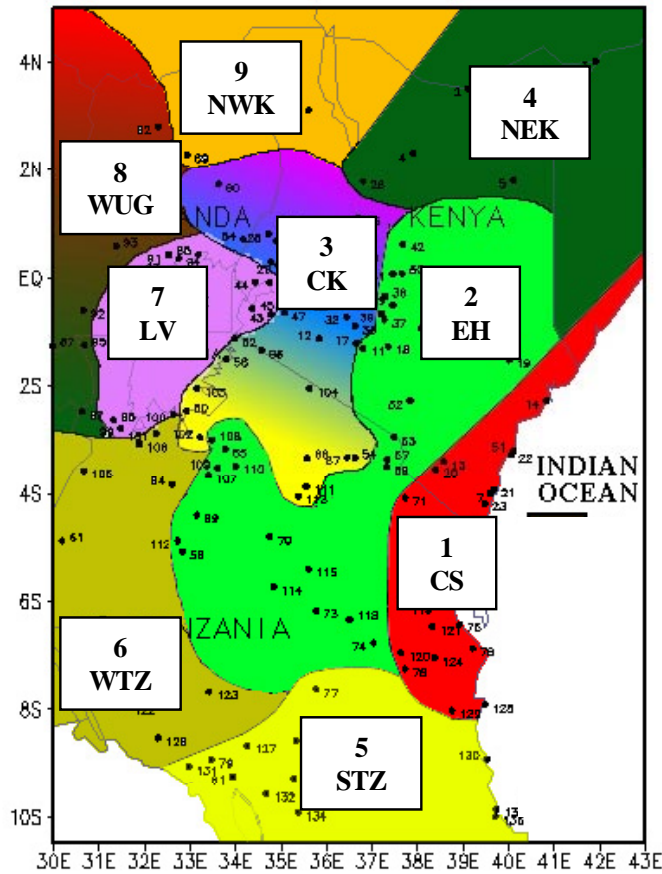


Figure 6.1: The domain of study and the nine homogeneous climatic regions based on cluster analysis. The nine regions are as follows: CK - Central Kenya, EH - Eastern highlands of Kenya, CS - Coastal strip of Kenya and Tanzania, NEK - Northeastern Kenya, STZ - Southern Tanzania, WTZ - Western Tanzania, LV - Lake Victoria basin, WUG - Western and central Uganda, and NWK - Northwestern Kenya and parts of northeastern Uganda.

Several studies have been undertaken in order to understand the climate variability over eastern Africa and their linkage to global oceanic and atmospheric dynamics. However, these efforts have been hampered by the lack of suitable tools to investigate the mechanisms and processes involved in the initiation, development, and cessation of the climatic anomalies. GCMs have been employed as tools in the previous climate studies over eastern Africa. These models may have difficulties with the regional climate, particularly where it is influenced by local factors such as steep orography, which can not be represented by the relative coarse resolution. Meso-scale numerical models may provide regional spatial scales; however, their computational expense prohibits integration on the seasonal to interannual time scales considered in climate studies. Downscaling of the dynamical fields generated by GCMs to regional spatial scales is proving to be a practical alternative (Giorgi and Marinucci 1991; Liu et al. 1994; SSOG99). Therefore, a comprehensive regional climate model integrated over monthly to seasonal time scales is employed in this study to (a) identify the unique differences in the circulation patterns and convergence zones during the two contrasting climatic years; wet El Niño and dry non-El Niño, (b) investigate the space-time variability of the convergence zones associated with the Inter-Tropical Convergence Zone (ITCZ) during the El Niño and non- El Niño years, and (c) establish and determine the major dynamical and thermal dynamical factors responsible for the droughts and floods over eastern Africa by analysing zones of vertical motion and precipitation that are associated with the interactions between the large- and meso-scale circulations.

The data used in this study comprised of monthly rainfall totals at 136- rain-gauge station observational network well distributed over East Africa (Figure 6.1) and covering the period 1961-1990. The data for October through December corresponding to the short-rains was extracted for further analyses. This data was used in identifying the dry and wet years in the region.

## **6.2 Identification of the dry and wet years during the short rains season**

Standardized rainfall anomaly index was defined for the entire eastern African region using a method similar to that of Wagner and DA Silva (1994). This index was based on the 160 stations normalized rainfall departures for the short-rains season. The network averaged rainfall index for a given year  $j$  was given by

$$R_j = \frac{1}{N_j} \sum_{i=1}^{N_j} X_{ij}, \quad (6.1)$$

where  $X_{ij}$  is the normalized rainfall departures for the station  $i$  in year  $j$  and  $N_j$  is the number of the stations available for that year. The rainfall monthly anomalies were computed by subtracting the monthly climatological means based on the 1961-90 climatology from the values, and normalized by dividing each record by the corresponding monthly standard deviation. The normalized rainfall departures for the season were then obtained by averaging the normalized values for the corresponding months in the season.

Thus,  $X_j$  was given by

$$X_j = \frac{1}{3} \sum_{k=1}^3 \left( \frac{r_k - \bar{r}}{\sigma} \right) \quad (6.2)$$

Where  $k$  is the month,  $\bar{r}$  the monthly mean,  $r_k$  the monthly rainfall, and  $\sigma$  the standard deviation for the month.

### **6.3 Numerical Model Description and Experimental Detail**

The RegCM2 described in chapter 4 is employed in this study. The model was initialized with ECMWF reanalysis meteorological fields and restarted after every 15 days of the model simulation. The analysis period was September through December coinciding with the short rain season over eastern Africa. The first month (September) was neglected to allow for the model spin-up. A number of experiments were carried out that investigated the dynamics and thermodynamics associated with dry and wet episodes over the eastern Africa. The year 1988 that displayed near normal rainfall conditions (Figure 6.2) was used in our control model simulations. The next series of model simulations were for the wet El Niño year (1982) and dry non-El Niño year (1987). Comparisons between these model results were analyzed to infer the major kinematics and thermodynamical factors associated with the wet and dry episodes over eastern African region during the El Niño and non-El Niño years. The difference between the dry/wet minus control experiments was referred to as anomaly for convenience. The model forecasts were analyzed at 1200 h and 2400 h LST. Multiple simulations starting from slightly perturbed initial conditions were performed to provide input for the computation of ensemble statistics for assessing the averages and spread of the forecasts. For brevity we only considered the wind and rainfall patterns in our analyses, and model results are discussed in the next section.

## **6.4 Results**

Results obtained from this study are discussed in the following sub-sections.

### **6.4.1 Determining the Dry and Wet Rainfall Years**

Based on the computed standardized rainfall indices using equation 2.1, years with normalized rainfall departures greater than +0.15 of the standard deviation were classified as wet years, while those years with rainfall anomalies less than -0.15 of the standard deviation defined as dry years. The significance of these rainfall indices was based on a standard student t-test applied on a sample size of 30 years. This statistical test takes into consideration samples with equal variances (Wagner and DA Silva 1994).

Figure 6.2 shows the time series of the normalized rainfall index over eastern Africa for the period 1961-1990. On average the region received above normal rainfall in the 1960's and late 1970's. The year 1961 was wettest in the 30-year period as shown by other investigators (Anyamba 1984; Reverdin et al. 1986; Indeje et al. 2000). Recent studies indicate that this 1961 anomalous year may be related to the climatic dipole mode index (DMI) over the Indian Ocean (Webster et al. 1999; Saji et al. 1999). Below normal rainfall was observed in late 1960's, early 1970's and 1980's. During the period 1961-90, 15 dry years (1964, 1966, 1969-71, 1973-76, 1979-81, 1983, 1985 and 1987) and 10 wet years (1961, 1963, 1967-68, 1972, 1977-78, 1982, 1986 and 1989) were observed in the region. The t-scores performed on the rainfall indices of the wet and dry years indicate that the two series are significantly different at 95 significance level. Near normal rainfall conditions occurred during the years 1962, 1965, 1984, 1988 and 1990. These findings are

consistent with those obtained by earlier researchers using Principal Component Analysis (Ogallo 1989; Nyenzi 1992; Okoola 1998; Indeje et al. 2000). The four DMI episodes that were observed during the years 1961, 1967, 1972 and 1982 coincided with positive rainfall anomaly over eastern Africa indicating some relationship between the mode and regional rainfall. The rainfall indices shown on Figure 6.2 further indicate that the wettest/driest years over eastern Africa during the period 1980-1990 were 1982/1987 respectively. The year 1982 is linked to one of the strongest El Niño of the century (Trenberth, 1997) and also to the DMI episodes while 1987 may be related to the reversed DMI (Webster et al. 1999 and Saji et al. 1999). A numerical modeling study is performed in order to physical mechanisms responsible for the two contrasting years wet 1982 and dry 1987 respectively while the year 1988 that displayed near normal conditions was used in our control model simulations.

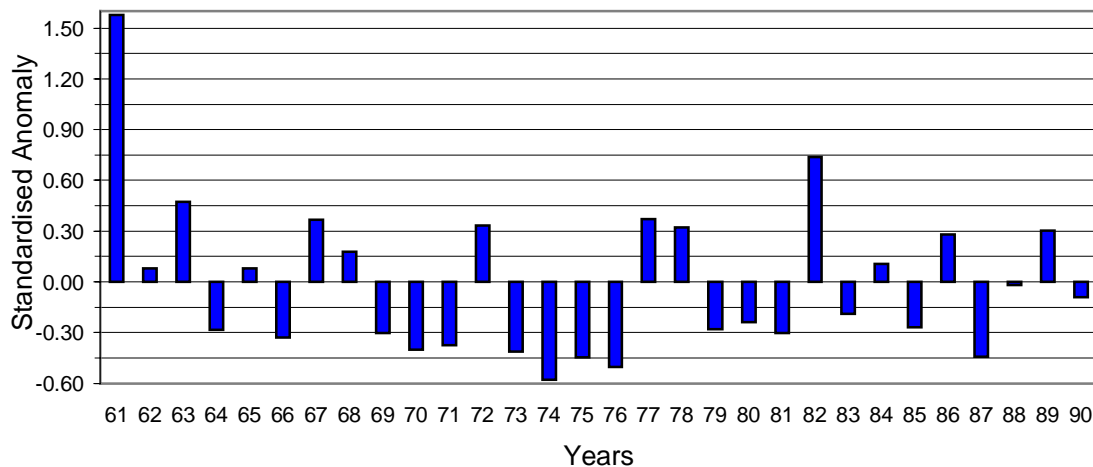


Figure 6.2: Time series of area-averaged October-December seasonal rainfall indices over eastern Africa.

## **6.4.2 Kinematics associated with the wet and dry episodes over eastern Africa**

### ***6.4.2.1 Horizontal wind structure***

The wind flow patterns at 850-, 700-, and 500-hPa levels in the control run for November the peak month for the short-rains over eastern are shown Figure 6.3. Northeasterly to northerly flow (stronger than  $4 \text{ m s}^{-1}$ ) are shown over the highland areas and northern Kenya. This wind flow decelerates as it approaches the western highlands and the Lake Victoria basin, and forms an axis of convergence with the westerly flow in the areas of minimum wind speed. The north-south orientation of the convergence zone of these two air masses shown on 850-hPa level may be related to the meridional component of the ITCZ over the region. At the 700-hPa level, the flow is mainly easterly over the region and an east-west oriented wind convergent is indicated. This north-south convergence is associated with the zonal arm of the ITCZ over the region. Previous studies by Anyamba (1984), Mukabana and Pielke (1996), and Okoola (1999) have observed similar convergence associated with the ITCZ in the wind field at 700-hPa level. The flow remains mainly easterly at 500-hPa level over the northern parts of the domain and weak or variable over the southern parts of the region. The easterly air mass shown from surface to 500-hPa level is responsible for advecting moisture from the Indian Ocean to the inland areas of eastern Africa.

Johnson and Morth (1961) indicated that easterlies are generally wetter in November rains than in the long-rains of March-May, although in the former period a northerly component

seems more distinctive. Camberlin and Wairoto (1997) indicated that at 700-hPa level, the meridional flow corresponding to the northeast monsoon switches to a quasi-easterly flow, advecting moisture from the Indian Ocean to the inland areas. The moisture advected in the region activates the meso-scale circulations over the coastal areas, the Lake Victoria basin and also enhances the orographically induced precipitation over the eastern slopes of the highland areas (Mukabana and Pielke 1996).

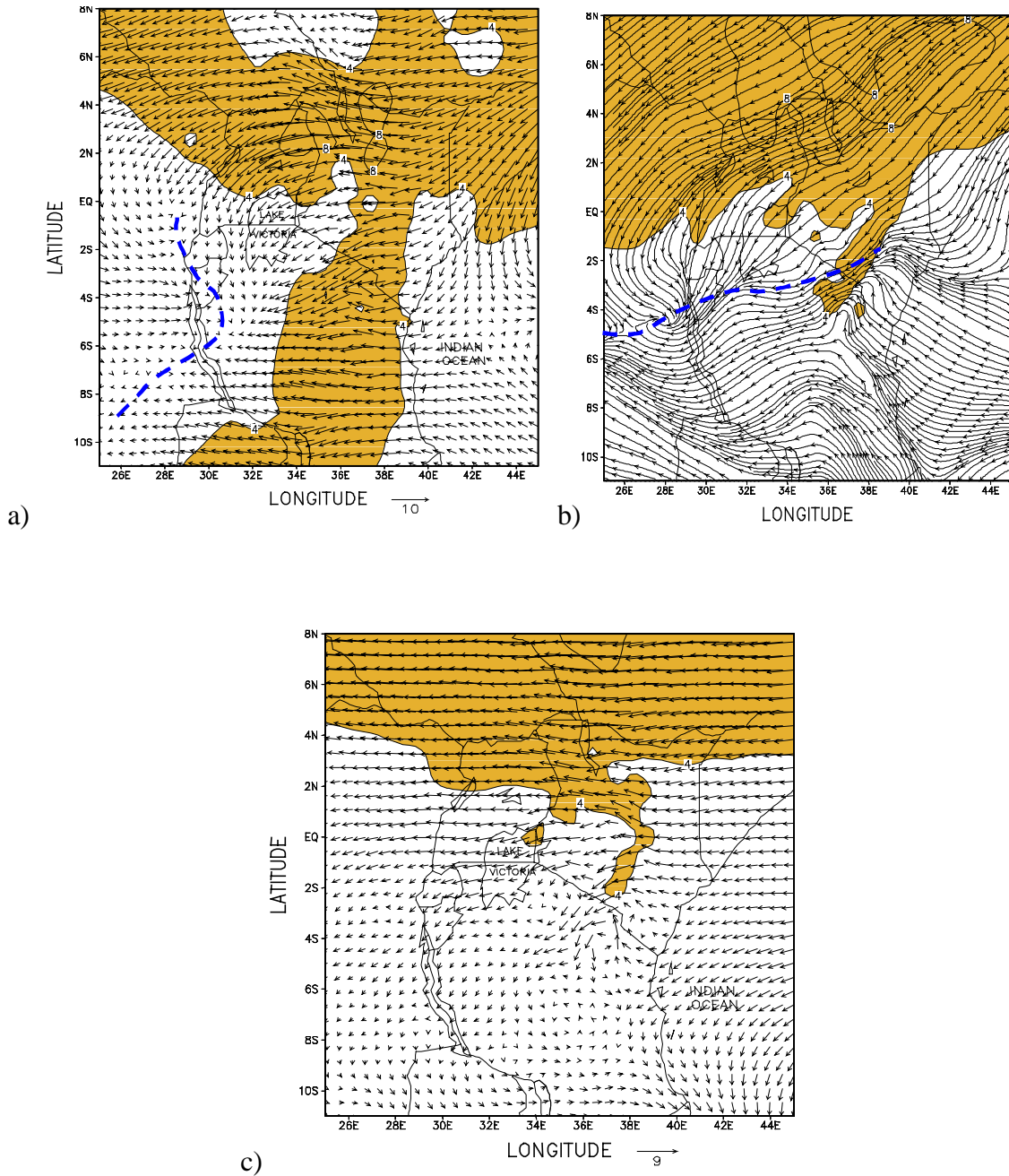


Figure 6.3: Simulated November mean horizontal wind flow at a) 850-, b) 700- and c) 500-hPa levels for the control model run. Shaded are areas with wind speed greater than  $4 \text{ m s}^{-1}$ . Convergence zones are shown with thick hatched lines.

During the wet El Niño (1982) year (Figure 6.4), easterly and westerly wind flows are relatively strong ( $\sim 10 \text{ m s}^{-1}$ ) over the region. Wind convergent between these two air masses is indicated over a larger area of eastern Africa. Deceleration of the relatively strong easterly flow indicated on the 850- to 500-hPa levels could support horizontal convergence by linear deceleration. Mid-tropospheric wind convergent is also indicated over the coastal areas of Kenya and Tanzania. It is shown from these wind patterns that horizontal advection and convergence associated with linear deceleration of the relatively strong easterlies from the Indian Ocean and westerlies from the Congo Forest may play a vital role in sustaining the wet spells over eastern Africa. In the western slopes, the convergence between low- and mid-tropospheric easterlies and, the cold, moist and unstable westerly airmass from the Atlantic/Congo basin and the tropical Atlantic Ocean is indicated. The resulting convergence may activate the ITCZ and enhance intense convection over these areas. While, the enhanced moist easterly flow from the Indian Ocean that penetrate inland to the eastern-highlands and lowlands, where it undergoes orographic lifting could result in cooling and generation of orographic precipitation over areas east of the highlands.

During the dry non-El Niño (1987) year, the easterly wind speed over eastern Africa is on average, weak or missing (Figure 6.5). The southeasterly and northeasterly flows during this year exhibit a more continental track and relatively shorter maritime track and could be dry. Northerly to westerly and southeasterly to westerly wind flow is dominant over the eastern sector and the western Indian Ocean. Backing of the northerly flow and veering of

the southeasterly flow from the Indian Ocean suppresses moisture advection into the region, which could inhibit orographic precipitation over eastern-highlands and lowlands of East Africa. At 500-hPa level, the horizontal winds are generally weak and highly variable. The indicated wind convergent between the northerlies and southerlies on the 700-hPa level may result in dry convection and diminished precipitation in the zones of convergence since these large-scale winds have relatively longer continental-paths.

In general, these results indicate that wet El Niño years in eastern Africa may be related to the deceleration of the mid-tropospheric easterlies into the region, enhancing horizontal convergence within the ITCZ region. Westerly and easterly wind flows during wet years are relatively strong and converge into eastern Africa. The resulting convergence of these two air masses and the associated moisture support vertical motion and enhanced convective precipitation over the western part of the region. Orographic lifting of moist and strong easterly flow from the Indian Ocean is a key mechanism for the occurrences of heavy rainfall over the eastern windward side of the mountain during this season. Thus, the two mechanisms favorable for the precipitation enhancement in the region namely moisture convergence and moisture advection are present during the wet years. The results further indicate that reduction moisture advection from the Indian Ocean, is a feature of the dry years. This reduction moisture advection and associated dry convection and suppressed orographic precipitation could partly explain the observed dry conditions over eastern Africa during this year. These results may be treated as general observations as there may be significant variability in the nine climatic regions of eastern Africa.

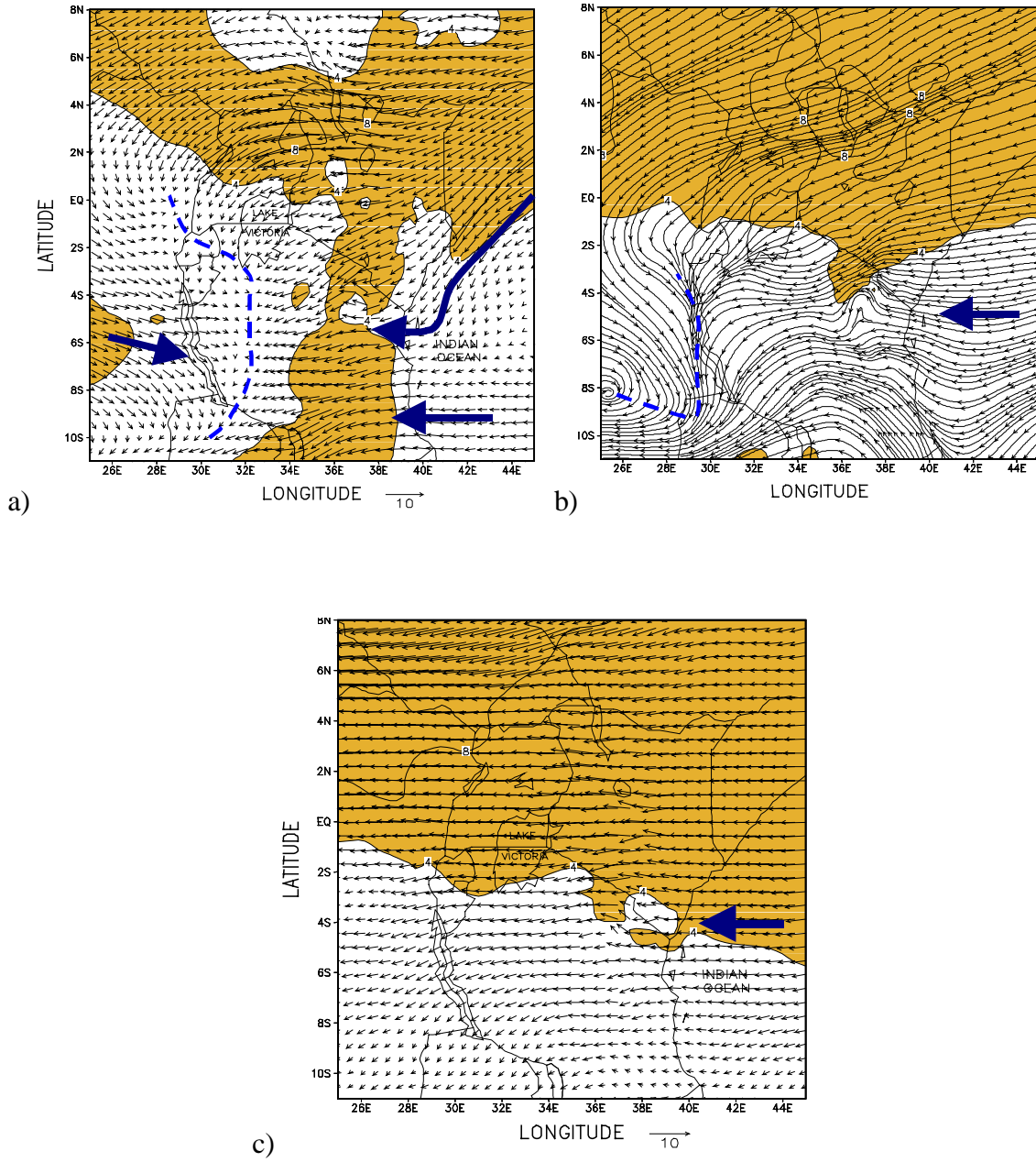


Figure 6.4: Same as in Figure 6.1, but for the wet year 1982.

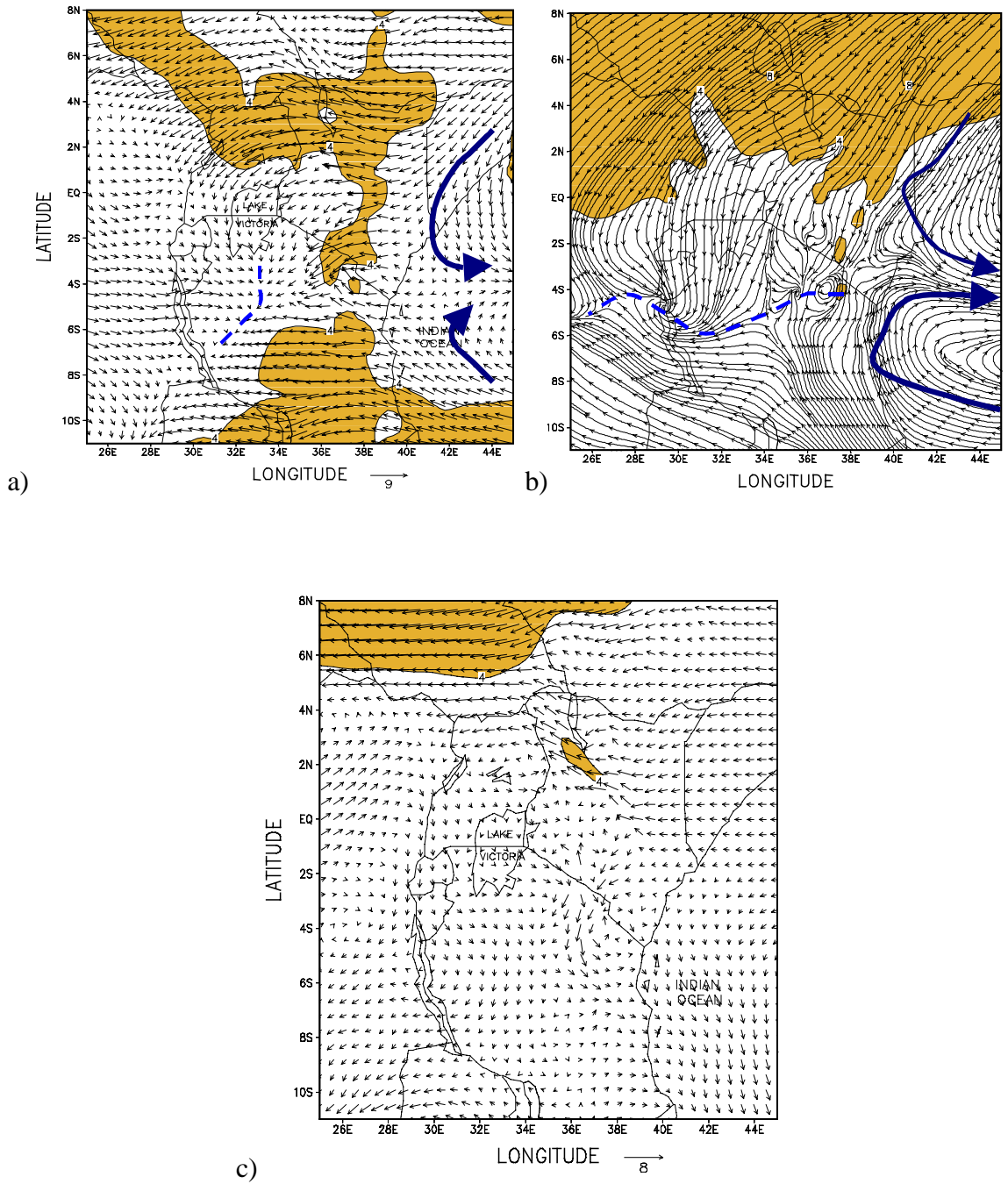


Figure 6.5: Same as in Figure 6.1, but for the dry year 1987.

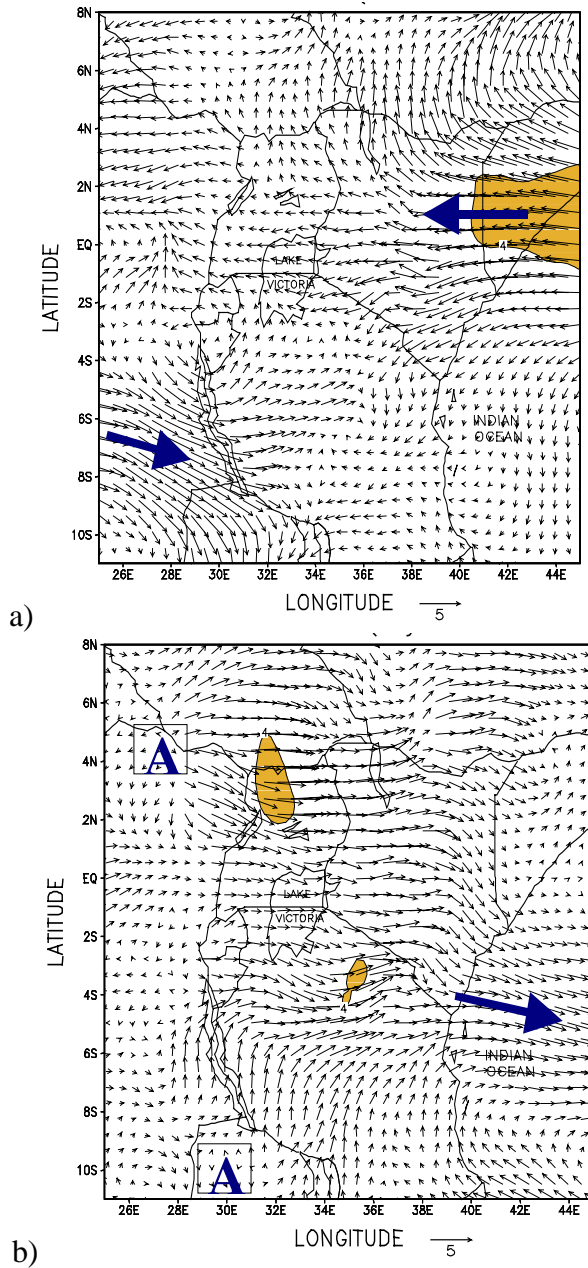


Figure 6.6: Simulated November mean horizontal wind anomaly vectors at 700-hPa level for a) wet year minus control (1988-1982), and b) Dry year minus control (1988-1987). A are areas of anticyclonogenesis.

The wind anomaly patterns for wet year (1982) minus the control year (1988) and the dry year (1987) minus the control year were analyzed to show the contrasting kinematics between the two years. Results for the simulated wind flow patterns at 700-hPa level are presented in Figure 6.6. Okoola (1999) suggested that the occurrences of anomalous rainfall in the equatorial eastern Africa could be studied using the velocity field at 700-hPa level. During the wet year, a north-south wind shear is indicated by the relatively strong easterlies ( $\sim 5 \text{ m s}^{-1}$ ) centered at approximately latitude  $1^\circ\text{N}$  and westerlies ( $\sim 5 \text{ m s}^{-1}$ ) centered at about latitude  $7^\circ\text{S}$ . These two easterly and westerly wind anomalies decelerates over eastern Africa and converges in the interior of the domain of study. The easterly flow into the region north of the equator is moist having traversed the Indian Ocean while the westerly anomaly south of the equator has its track over the moist Congo forest. The zonal wind flow from the Indian Ocean promotes uplift over much of the region during the wet spells, which may be an important mechanism for the short rainfall season over eastern Africa. The north-south wind shear shown on the 700-hPa level indicating a positive vorticity across the equator is a unique feature for the wet years over eastern Africa.

During the dry (1987) year (Figure 6.6b), strong mid-tropospheric westerly wind anomaly is observed over much of the region. These wind anomalies originate from about  $10^\circ\text{S}$ ,  $30^\circ\text{E}$  and from about  $4^\circ\text{N}$ ,  $28^\circ\text{E}$ . The indicated acceleration of these westerlies away from eastern Africa could enhance horizontal divergence by linear wind acceleration. Clearly, the westerly flow out of the region is stronger than normal during the dry year. The

anticyclonic circulations located over western parts of the region at 700-hPa enhancing the westerly wind anomaly over the region, is a distinct feature for dry years.

#### **6.4.2.2 Vertical wind structure**

The latitude-height and longitude-height cross sections of zonal wind speed are analyzed in order to determine a three dimensional kinematics of the atmosphere during the extremely wet and dry years. The height-latitude sections of the zonal winds averaged between longitudes 25° and 45°E for the wet minus control and dry minus control are displayed in Figure 6.7. In the wet year, lower tropospheric southerly wind anomalies are observed extending from surface to about 700-hPa level with overlying northerly wind anomaly centered at about 200-hPa level. The low-level southerly wind anomaly declines northward with increasing altitudes to a minimum depth at the equator and then increases in height again toward the north. A negative vertical wind shear is indicated in the region by the southerly and northerly tropospheric wind anomalies, which may be related to an active Hadley circulation over the region. This negative vertical wind shear between 200-hPa and 700-hPa levels may be conducive for enhanced convection.

Thus, the vertical alignment of the northerlies and the southerlies are quite anomalous during the wet year. A negative wind shear between the low-levels and mid- to upper-troposphere which is conducive for overturning and convection is present during wet years. This vertical wind shear seem to be an important feature of the wet years over the region. During the dry year (Figure 6.10b), lower tropospheric southerly wind anomaly is observed throughout the entire troposphere. Maximum westerly wind anomalies are

centered at approximately 500-hPa level and extend from the equator to about latitude 8°N. It is apparent that during dry years, there is reduced or no vertical shear in the mean equatorial wind over the region.

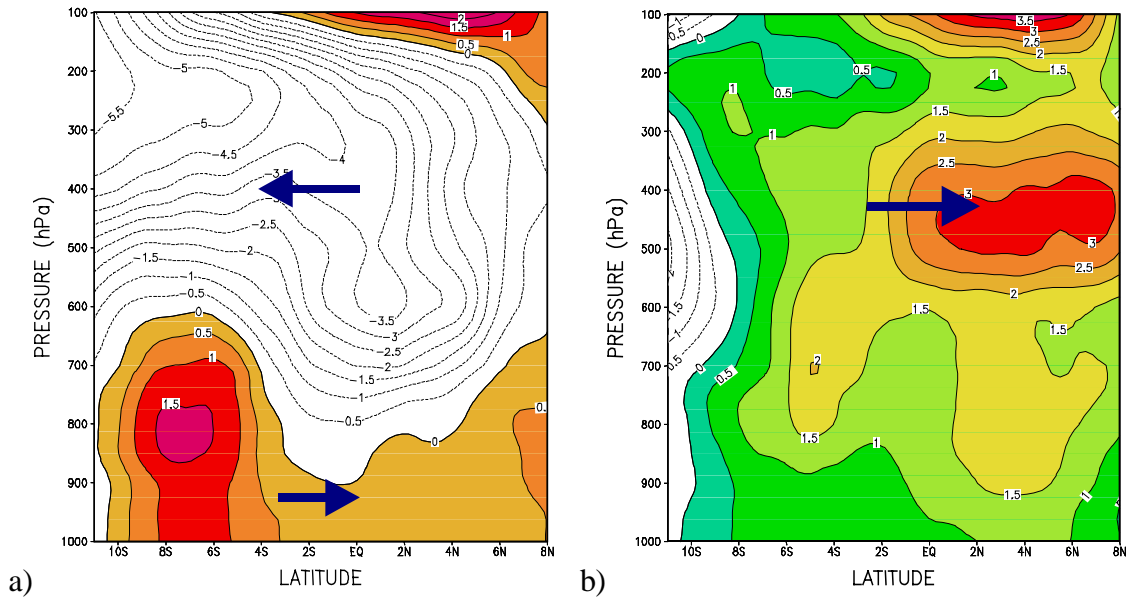


Figure 6.7: Latitude-height cross section of horizontal wind speed ( $\text{m s}^{-1}$ ) averaged over longitudes 25° to 45°E for a) wet year minus control model run, b) dry year minus control model run.

Longitude-height cross sections of zonal wind for the wet minus control, and dry minus years within the latitudes 10°S and 8°N are displayed in Figure 6.8. Westerly wind anomaly is observed below 700-hPa level and declines from the west to the east. In the upper troposphere, the region of maximum easterlies is located at 300-hPa level. A negative vertical wind shear is also shown on this east-west cross section during the wet

year. During the dry year, a westerly wind anomaly is shown throughout the troposphere (Figure 6.8b). The RegCM2 simulated horizontal cross-section of horizontal wind speed for both dry and wet years compare well with the NCAR/NCEP reanalysis (Figure 6.9).

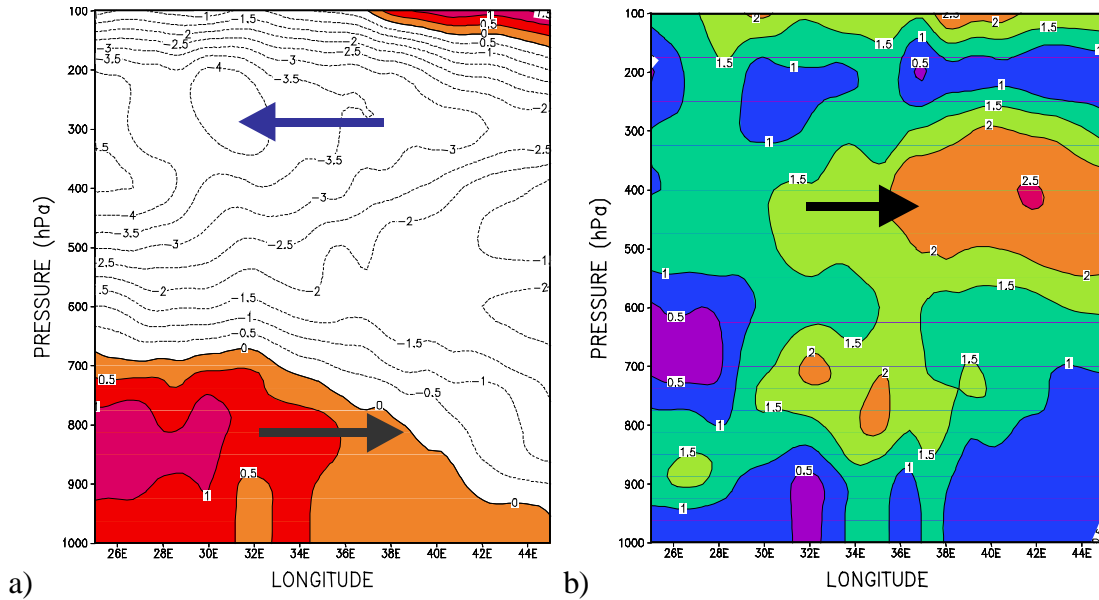


Figure 6.8: Longitude-height cross section of the RegCM2 simulated horizontal wind speed ( $\text{m s}^{-1}$ ) along latitude  $1^\circ\text{S}$  for a) wet year minus control model run (1982-1988), b) dry year minus control model run (1987-1988).

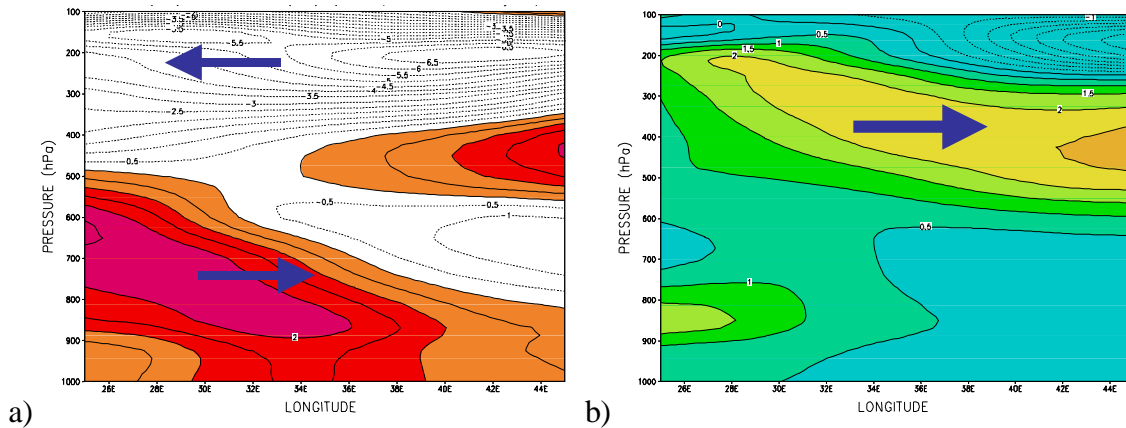


Figure 6.9: Same as in Figure 6.8, but for NCAR/NCEP reanalysis for (a) wet year (1982) minus control (1988), and (b) dry year (1987) minus control.

The most significant result from the vertical cross sectional wind analyses, is the observed correspondence between the anomalous wet year and the negative vertical shear of zonal wind intensity. Negative wind shear between 800- and 200-hPa levels may be associated with active convection over eastern Africa. Hills (1979) indicated that divergence in upper levels (300- and 200-hPa) was present during the short-rains but convergence in long-rains over eastern Africa. This pattern accompanied by the diffluent wind anomalies observed at low levels for dry occurrences in November was indicative of the barotropic nature of rain-bearing mechanisms during the short rains. The short-rains season has shown to be dependent on barotropic east-west atmospheric circulation along the Indian Ocean and Pacific Ocean (Hastenrath et al. 1993). The dry years in the region are associated with westerly wind anomaly that spans the entire troposphere.

### 6.4.3 Thermodynamic Structure and Rainfall Distribution

#### 6.4.3.1 *Moisture Flux Convergence*

The moisture flux convergence field was analyzed using equation 4.5, in order to investigate the evolution of water vapor distribution over eastern Africa during the wet and dry years. Figure 6.10 shows the horizontal divergence of moisture flux from all possible sources. During the wet year, moisture flux convergence ( $\sim 0.2 \times 10^{-06} \text{ kg kg}^{-1} \text{ s}^{-1}$ ) is shown well distributed over the northern and eastern parts of eastern Africa. Moisture flux divergence is indicated over the leeward sides of the western highlands and Lake Victoria. It is apparent that during wet years, larger proportions of the water vapor from the Indian Ocean is advected inland by the easterly flow and deposited over the windward side of the eastern-highlands and lowlands. Moisture flux divergence shown over the Great Rift Valley on the leeward sides of the mountains maybe associated with the descending motion over the valley. This descending motion may partly explain the semi-arid climatic conditions observed over these areas.

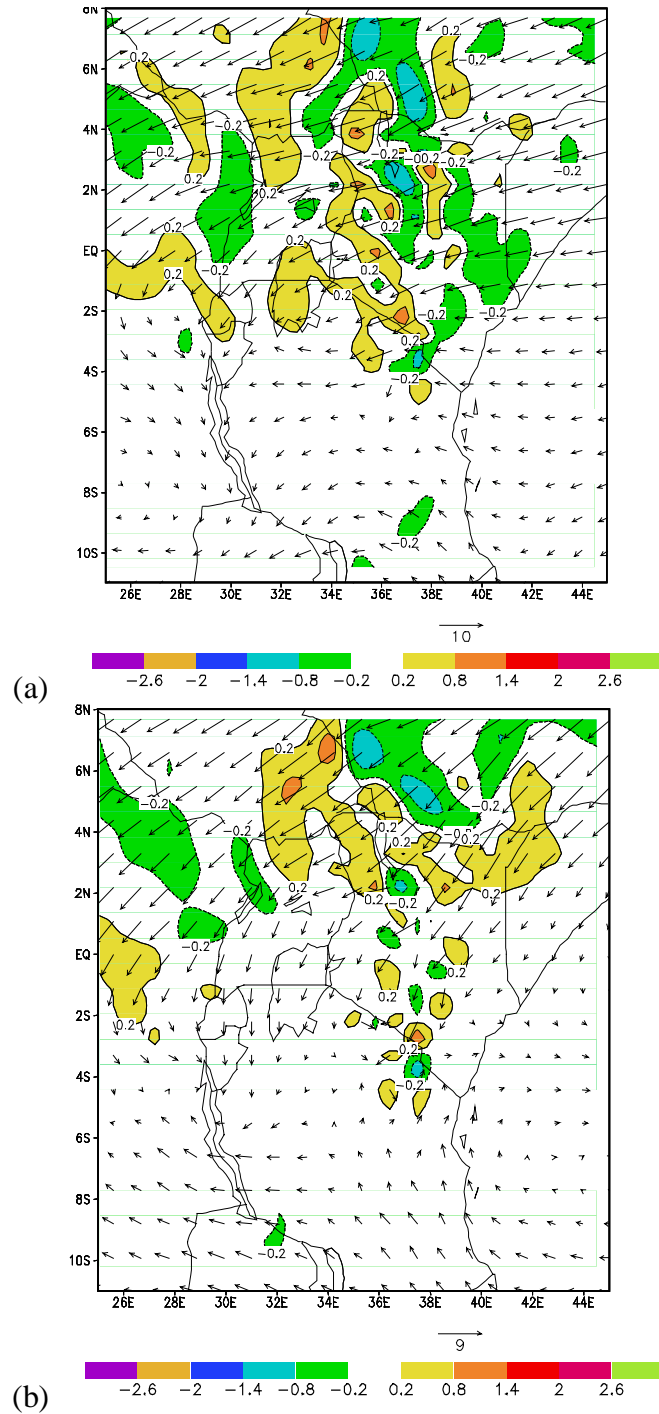


Figure 6.10: November mean horizontal moisture flux divergence field for (a) wet year, and (b) dry year. Negative values indicate convergence of moisture flux and positive divergence of moisture flux. Contour interval is  $0.2 \times 10^{-6}$  ( $\text{kg kg}^{-1} \text{s}^{-1}$ ). Wind vectors are also indicated.

Divergence of moisture flux is also shown over the Turkana Channel and southwestern Sudan, that may be associated with the presence of the low-level jet over this region (Kinuthia and Asnani 1982; Kinuthia 1992), coupled with the descending motion on the leeward side of the Ethiopian highlands.

The north-south dipole orientation of the convergence zone during the wet year with increased convergence of moisture flux ( $\sim 0.4 \times 10^{-06} \text{ kg kg}^{-1} \text{ s}^{-1}$ ) north of the equator and moisture flux divergence south of the equator is typical of the ENSO years over the region (Ropelewski and Halpert 1987; Ogallo 1988; Nicholson 1996; Indeje et al. 2000; Semazzi and Indeje 1999). The year 1982 was associated with one of the strongest ENSO event in history. An east-west dipole pattern indicated over Lake Victoria and the western highlands of eastern Africa during the wet year with convergence of moisture flux over the highlands and divergence over the lake maybe related to the interaction between the meso-scale flows and large-scale easterly monsoon flow in the region (Mukabana and Pielke 1996). This interaction is more pronounced during the wet year. In the dry year, Small pockets of moisture flux convergence are indicated over the region (Figure 6.10b). During this year, moisture is advected toward the Indian Ocean by the relatively strong westerlies as shown in Figure 6.6b. Moisture advected toward the region by the northeasterly flow is deposited over the Ethiopian Highlands resulting in very little or no moisture reaching the interior parts of eastern Africa.

In general, results obtained from the moisture flux convergence field indicate that advection of moisture from the Indian Ocean is crucial for the precipitation distribution over the eastern-highlands of eastern Africa during the short-rains season. During the wet years, larger proportion of moisture is advected from the Indian Ocean apparently by the stronger and more easterly winds resulting in high moisture flux convergence in the region that could support enhanced convection. Reduction in moisture advection during the dry year may explain the deficit in rainfall over the region. The continued presence of moisture divergence over the Turkana channel and southwestern Sudan could support the observed dry conditions over these areas throughout the year. Strong moisture flux divergence shown in areas that usually experience low amounts of seasonal rainfall like the northeastern Kenya, central Tanzania and southern Sudan could manifest in severe drought conditions in these areas. These results further indicate that during wet El Niño years, the interactions between the meso-scale and large-scale flows is strong enhancing convection over the Lake Victoria basin and western sectors of the region. The dipole pattern associated with the meso-scale/large-scale interaction over the Lake Victoria basin is very weak during the dry non-El Niño year, which is a further indication of the importance of moisture advection and convergence in activating the meso-scale/large-scale interactions and determining the spatial and temporal distribution of rainfall over eastern Africa.

#### **6.4.3.2 Vertical Motion**

Regions of vertical motion are analyzed to indicate zones of convergence associated with the interactions between the meso-scale and large-scale flows, which largely determine the

distribution of precipitation over eastern Africa (Okeyo, 1986; Mukabana and Pielke, 1996; Indeje and Anyamba 1998). Figure 6.11 shows the simulated vertical velocity field at 620-hPa level over eastern Africa during the month of November for the control model simulation, the wet El Niño year minus control, and the dry non-El Niño year minus control respectively. Upward motion is simulated over the East African highlands, and Lake Victoria basin (Figure 6.11a). Over the Lake Victoria basin, rising motion ( $\sim 2.2 \times 10^{-3} \text{ m s}^{-1}$ ) is shown confined to the eastern and western parts of the lake. This pattern of the vertical velocity is related to the interaction between the mean large-scale easterly and westerly flows and the Lake Victoria “lake front”. Rising motion is also shown upstream of the mountains and descending motion on the down stream. Maximum upward vertical velocity greater than  $5.4 \times 10^{-3} \text{ m s}^{-1}$  is simulated over the high ground areas and, subsidence of about  $3.6 \times 10^{-3} \text{ m s}^{-1}$  over the valleys next to the mountains. The subsiding air over the region may be related to the down current of the mean northeasterly to easterly monsoons as they cross the north-south mountain chains over the East African highlands. These results are quantitatively similar to the findings by Okeyo (1986), and Mukabana and Pielke (1996). The ascending motion increases to relatively large values ( $\sim 15 \times 10^{-3} \text{ m s}^{-1}$ ) over the high mountain ridges that may be responsible for deep convection and associated high precipitation rates simulated over these mountain areas.

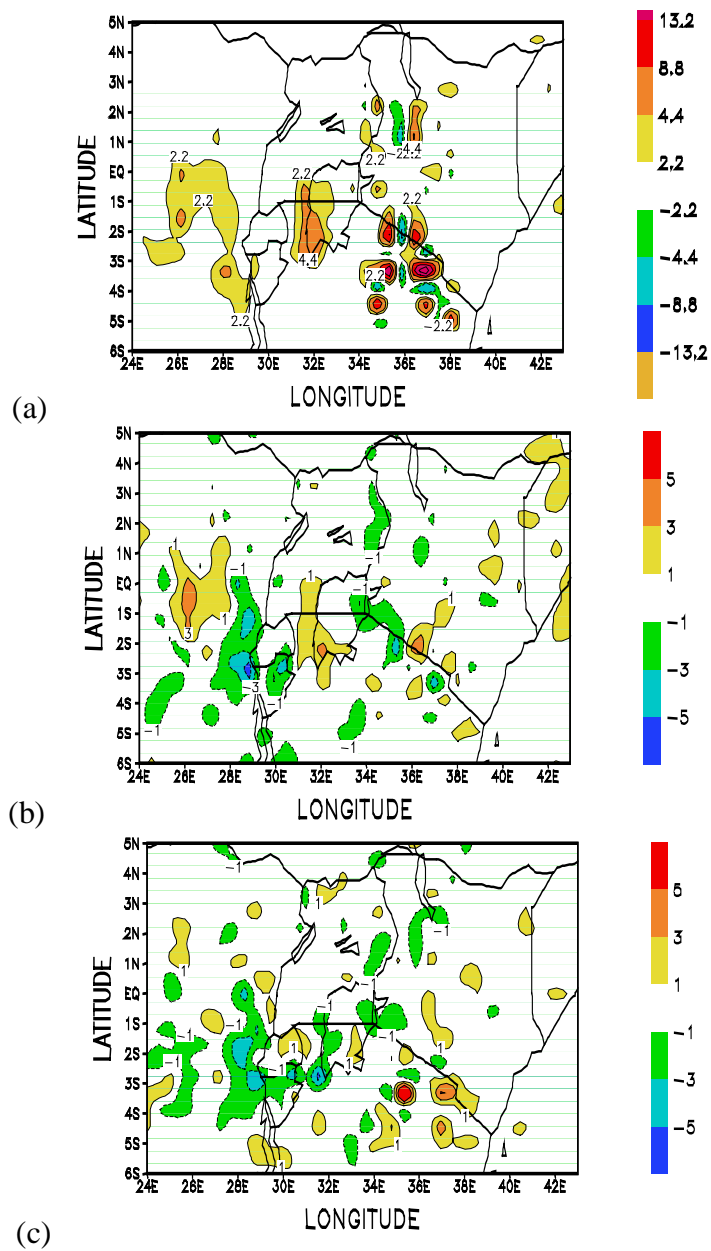


Figure 6.11: Mean Vertical Velocity ( $\times 10^{-2} \text{ m s}^{-1}$ ) for November at 620-hPa level in the a) control model run, b) wet year minus control, and c) dry year minus control. Shaded are areas of upward motion and sinking motion is shown by hatched contours.

The longitude-height cross section of the mean vertical velocity field for the month of November at latitude 1°S across Lake Victoria and the East African highlands for the control, wet (1982) and dry (1987) simulation are shown in Figure 6.12. Figure 6.13 shows the corresponding mean vertical field for the wet year minus control and the dry year minus control respectively. This cross section velocity is analyzed to indicate areas of maximum interactions between the Lake Victoria meso-scale front, the mountain/valley flows and the large-scale flow and also give an insight of the vertical extend of these convective plumes. Four major rising motion “limps” are shown across the domain (Figure 6.13). This vertical motion may be associated to the shift of the rising branch of the Walker circulation to the East African region during this rainy season. The first major location of rising motion is shown over the eastern slopes of the Ruwenzori Mountain directly west of Lake Victoria with mean maximum vertical velocity of about  $5.6 \times 10^{-3} \text{ m s}^{-1}$  that extends from 750-hPa to 100-hPa levels. Rising motion and associated precipitation at this location may be linked to the moist westerly flow emanating from Atlantic Ocean that traverses the Congo forest and the easterly monsoons that passes over Lake Victoria. These two air masses are cool, moist and unstable. There is massive release of latent heat to the atmosphere at the location where these two air masses converge. The vertical velocity and the associated precipitation pattern over the convergent areas can be explained by consideration of the fact that there is high land east of the lake and the region has a quasi-permanent high level of insolation leading to an interaction of the land/lake breeze with the prevailing large-scale flows. Reinforcement of this convergence by the dynamical effect of the bottom orography over the Ruwenzori

Mountains is also apparent. This convergence is strongest in November and weakest in December. Rising motion over the Ruwenzori Mountain is enhanced during the wet El Niño years (Figure 6.13b and Figure 6.13a) and is relatively weak during the dry non-El Niño year (Figure 6.13c and Figure 6.13b)

The second center of vertical velocity ( $\sim 4.2 \times 10^{-3} \text{ m s}^{-1}$ ) is located to the western shores of Lake Victoria. At this location, the vertical velocity extends from 800-hPa to about 100-hPa level. This rising motion with the related rainfall may be associated with the interactions between the land breeze associated with the “lake trough” and the prevailing easterly monsoon flow. Interaction between these two air masses plays major role in determining the precipitation distribution over the lake (Datta 1981). The convergence zone associated with the “lake trough” is advected by the mean easterly monsoon flow from the center of the lake to the western parts of the lake. This wind convergent results in heavy rainfall over the western banks of the lake. Datta (1981) observed that the interaction between the westerly land breeze with the prevailing easterly flow provided positive mechanisms for vigorous convection in the early morning over areas west of the lake. There is however, less thunderstorm activity because of the stable lapse rates associated with nocturnal atmosphere. Ba and Nicholson (1998) have indicated that over the lake, the maximum occurrence of cold cloud tops is observed between 0200 and 0800 LST and between 0500 and 1100 LST during the months of April and November, respectively. The vertical motion over the western parts of the lake is strongest in October and weakest in December. During the wet year, upward vertical velocity anomaly ( $\sim 1.5 \times$

$10^{-3} \text{ m s}^{-1}$ ) is shown in the low-levels (below 600-hPa level) over the Lake Victoria and downward vertical velocity ( $\sim 0.5 \times 10^{-3} \text{ m s}^{-1}$ ) is shown aloft (Figure 6.13a). This vertical wind anomaly in low-level may favor enhanced convection over the lake. During the dry year (Figure 6.13b), sinking motion is dominant over the lake, a mechanism that could inhibit convective developments.

The third major rising branch of the upward vertical velocity is located over the western parts of the East Africa highlands, just to the east of the lake (Figure 6.13). There are two centers ( $\sim 2.8 \times 10^{-3} \text{ m s}^{-1}$ ) located at about 750-hPa and 200-hPa levels in the control run. This rising motion may be attributed to the interaction between the “lake trough” and the easterly monsoon flow augmented by the topographically induced flows over the East African highlands. The coupling between this front and the terrain dynamically induced anabatic flow is responsible for the rising motion and the observed severe weather over this region (Alusa 1976; Asnani and Kinuthia 1979). Over the eastern part of the lake, the region of high radiative input, the insolation together with the interaction of the easterly lake breeze with the prevailing easterlies, leads to thunderstorm activity during the afternoon and evening (Datta 1981). Observations and modeling studies have shown that these areas west of the highlands receive rainfall accompanied by thunder and hail throughout the year (Alusa 1976; Asnani and Kinuthia 1979; Okeyo, 1986).

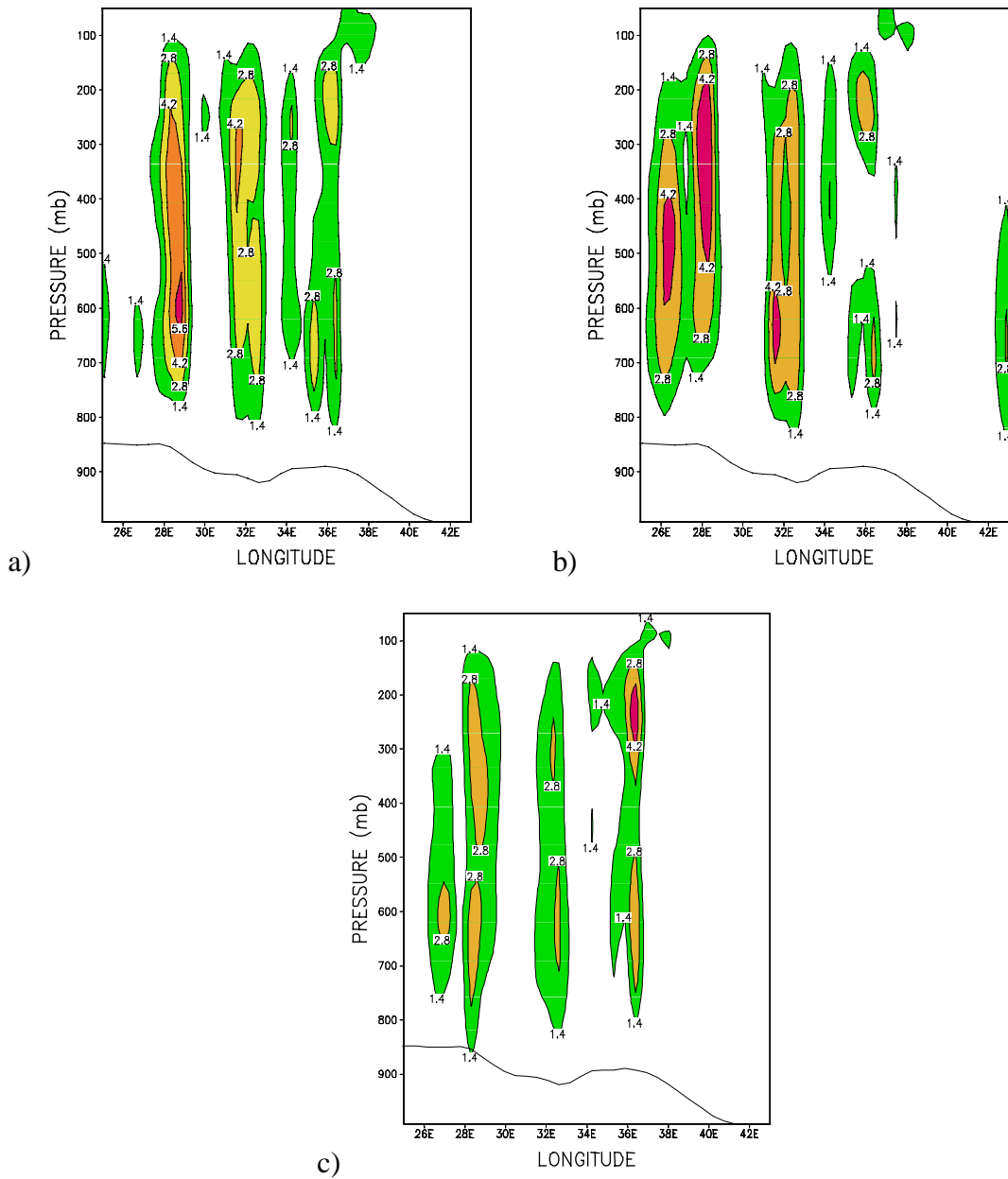


Figure 6.12: Longitude-height cross section of vertical velocity ( $\times 10^{-2} \text{ m s}^{-1}$  at latitude  $1^\circ\text{S}$  during the month of November for a) control model simulation, b) wet (1982) year, and c) dry (1987) year. Bottom orography is also indicated

Precipitation over these areas west of the East African highlands is observed during the late afternoons and early nights. At this time the sea breeze front attains its maximum displacement towards the land. During wet El Niño years (Figure 6.13a), sinking motion is dominant over these areas west of the highlands, which is an indication of suppressed convection.

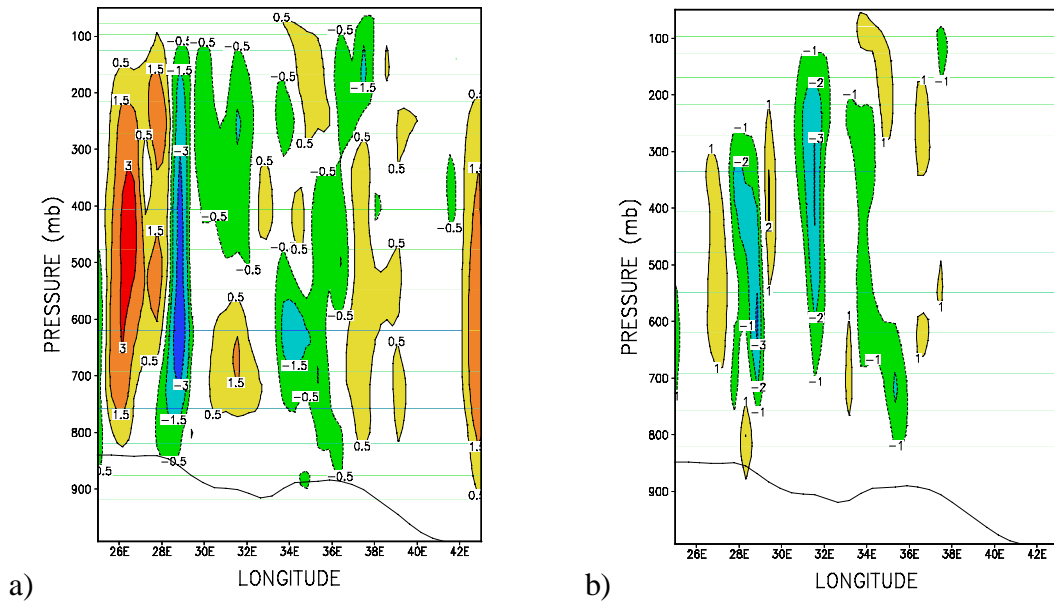


Figure 6.13: Same as in Figure 6.12, but for a) wet year minus control (1982-1988), and c) dry year minus control (1987-1982).

Recent studies by Indeje et al. (2000), also in chapter 2) indicates that the central areas of Kenya and the western highlands of East Africa are prone to dry conditions during El Niño years. It should be noted that the year 1982 was one of the strong El Niño years in history.

Results obtained from this modeling study supports the previous studies (Indeje et al. 2000) and indicate that dry conditions may result from weak meso-scale/large-scale interactions over the western highland areas of eastern Africa during the El Niño years. Enhanced vertical motion is shown over eastern slopes of the East African highlands and western Indian Ocean. This ascent motion may support the observed high rainfall conditions over the East African lowlands and the coastal areas of the Indian Ocean during ENSO years. Similar anomalous climatic conditions were evident during the most recent 1997/98 El Niño year. During the dry non-El Niño year, sinking motion is indicated over the western and eastern highland areas of East Africa respectively. This condition may be responsible for the suppressed interaction between the meso-scale and large-scale flows and hence reduce precipitation in the region.

These results indicate that during the El Niño years, the main convective zones associated with this east-west Walker circulation and the north-south Hadley circulation shift eastwards to the East African region intensifying convection over the region. The occurrence of deep convection observed during this season implies that these particular latent heat sources may influence the large-scale dynamics through the teleconnections. The vertical motion and associated convection is enhanced in the region during the wet El Niño years and highly suppressed during the dry non-El Niño years. These results further indicate that meso-scale/large-scale interaction is enhanced/suppressed during the wet/dry years respectively.

### ***6.4.3.3 Precipitation Distribution***

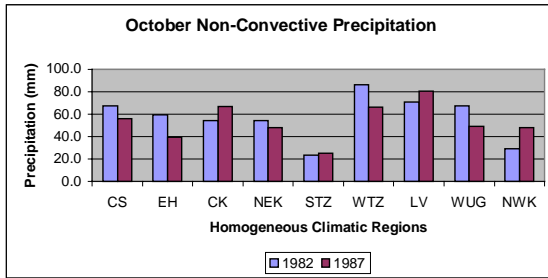
The simulated convective and non-convective precipitation for the wet and dry years averaged over nine climatic regions of eastern Africa is presented in Figure 6.14. During the simulation period (October through December), the ITCZ shifts southward and carries a rain belt along its southward movement. The most striking and encouraging feature shown on the simulated convective and non-convective precipitation is that the model reproduces the month-to-month tendency (increase or decrease) of the rainfall for most parts of the region. This demonstrates the ability of the model to resolve the complex migration patterns of the ITCZ over such complicated terrain, vegetation, and land-water contrasts over eastern Africa. It is shown from the figure that in the wet year more moisture is advected to the region resulting in increased non-convective (non-resolvable or large-scale) precipitation. The circulation differences described in section 6.4.2 are consistent with the buildup and subsequent precipitation of the advected water vapor from the Indian Ocean water and the moist and unstable air from the Congo forest during the wet year.

High orographic precipitation is simulated over the highland areas of eastern Africa, which suggests that the orographically enhanced precipitation could fall out in form of non-convective precipitation over the high ground areas where there is strong interaction between the mountain flows and the prevailing large-scale easterly flow. Moisture advected in the region is lifted to the mountain areas where it undergoes condensation-cooling resulting in the non-convective precipitation. The upstream blocking that

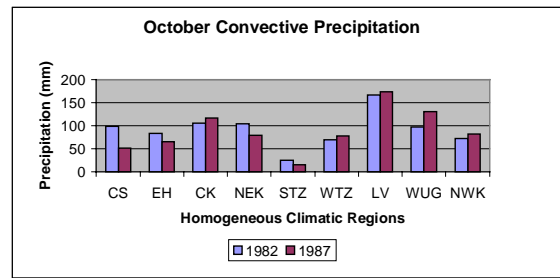
decelerates the low-level winds causing gentle lifting well offshore supports this mechanism. When offshore lifting occurs in the conditionally unstable tropical air, deep convection is initiated depending upon the thermodynamics and dynamic structure in the mid-troposphere. In the dry year the westerlies between the equator and 6°N (Figure 6.6a) directs moisture eastward towards the Indian Ocean resulting in insufficient moisture over the region to trigger the non-convective precipitation over the region.

The second largest contributor to the seasonal rainfall over eastern Africa is from local evaporation and convergence of moisture. This contribution is manifested in the convective (resolvable) precipitation. Convective precipitation in the region may be linked to the coupling between the meso-scale land/sea, land/lake and the anabatic/katabatic flows with the large-scale monsoon flow. During the daytime, when the sea breeze occurs, there is a marked convergence between warm and almost dry easterlies and the cool and moist Lake Victoria breeze over areas west of the East Africa highlands. The simulated convective precipitation for both the wet and dry year was comparable in magnitude, which suggests that moisture advection contributes most in sustaining wet conditions over eastern Africa.

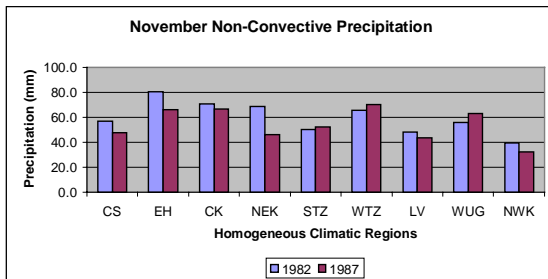
a)



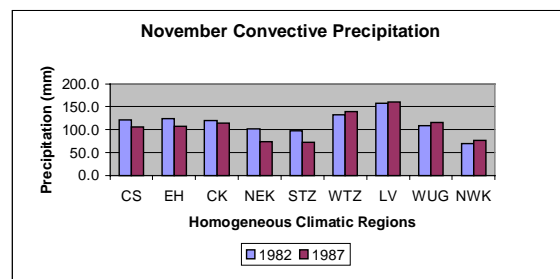
b)



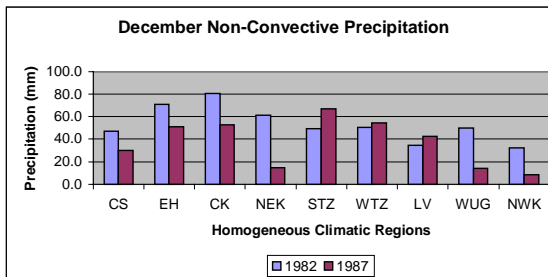
c)



d)



e)



f)

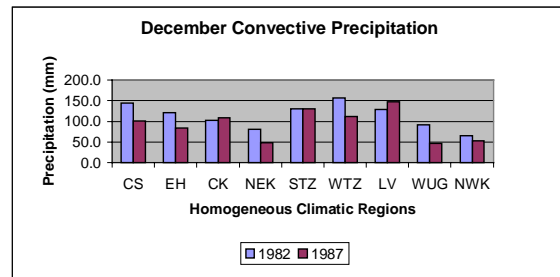


Figure 6.14: Contributions of the convective and non-convective seasonal rainfall to the months of October, November and December over nine homogeneous climatic regions of eastern Africa for the wet and dry simulations.

These findings agrees with those of Reason and Godred-Spenning (1998), who indicated that the major mechanism responsible for the modulation of rainfall over eastern Africa was related to the amount of moisture advected in the region by the easterly trades from the tropical South Indian Ocean rather than to the local evaporation. In the dry year, the eastward moisture advection deprived the western highlands of local moisture convergence resulting in dry convection and associated reduction in convective precipitation.

## **6.5 Discussion**

Since horizontal temperature gradient in the tropics is relatively small (Bjerknes 1969; Philander 1990), small heat sources resulting from hot continental regions and warm SST could give rise to strong upward motion resulting in turbulent and convective mixing between surface and overlying air. These turbulent mixing and the associated moisture convergence and convection in the tropical region may be reflected in the large-scale global teleconnections through the east-west Walker and the north-south Hadley circulations. Bjerknes (1969), Newell (1979) and Lindesay (1988) have shown that during the high phase of the Southern Oscillation corresponding to wet conditions over the South African summer rainfall, the Walker-type circulation over the Indian and Atlantic Oceans and over Africa are such that the weak Zaire cell produces ascending air over Africa while descending air prevails over the western Indian and eastern Atlantic Oceans.

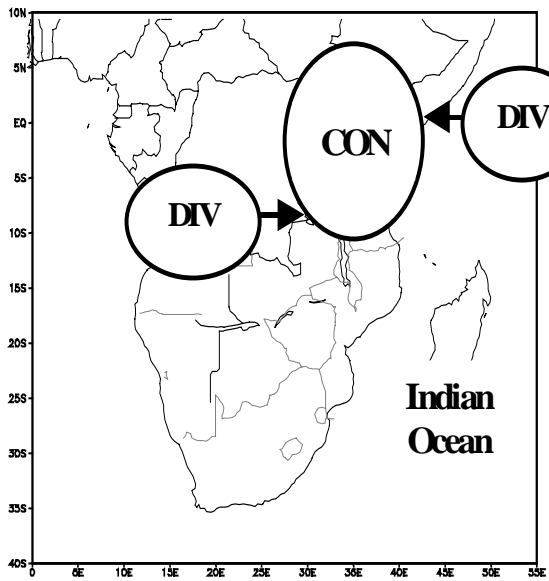
The simulated climatic patterns over the eastern African region are consistent with the changes in the intensity and the lateral position of the Walker and Hadley circulation cells

over the region. Heavy rainfall years in the region correspond to climatic anomalies coherent with the intensification of the Walker- and Hadley-type circulation cells. These large-scale circulations are manifested in the intensified vertical motion during the wet El Niño years and substantially weakened during the dry non-El Niño years. Strong/weak vertical motion associated with these large-scale circulations support the enhanced/suppressed moisture convergence and precipitation in the region during wet/dry years. Hastenrath et al. (1993) suggested that the short-rains over eastern Africa had dependence on barotropic east-west atmospheric circulation along the Indian and Pacific oceans.

Climate variability over the African subcontinent could also be linked to the air-sea interaction processes over the Indian Ocean. Druryan and Koster (1989) have shown that weak Indian Ocean monsoon circulation associated with warm Arabian Sea SST could weaken fluxes from the southwest that supply moisture to northeastern Africa. D'Abreton and Tyson (1995) indicated that the descending and diverging air over the western tropical Indian Ocean during the wet years over eastern Africa serves to modulate not only the supply of water vapor for convection, but also the locus of the ascending branch of the Walker circulation over the continent in the tropical and subtropical Africa. Increase in the easterly winds over the tropical western Indian Ocean and Africa increases the easterly wave and promotes convection over the African subcontinent. However, warm Arabian Sea SST has been associated with weak Indian Ocean monsoon circulation and the associated supply of moisture from the southwest Indian Ocean to northeastern Africa

(Druryan and Koster 1989). Webster et al. (1999) and Saji et al. (1999) have likewise indicated that warming over the western Indian Ocean would be associated with stronger winds in the western basin, which would contribute to rapid cooling and hence modify the large-scale circulation over the ocean. Studies by Trenberth (1997) indicate that warming over the western Indian Ocean during the ENSO years is associated with high moisture fluxes over the marine boundary layer. These increased tropospheric moisture associated with the warm Indian Ocean associated with El Niño years is advected into eastern Africa by the relatively strong easterly wind flow during the wet years. This advected moisture support enhanced convection and orographic precipitation through latent heat release thus sustaining wet conditions over the East African region (Figure 6.15a). Similarly, cool SST over the western Indian Ocean and warm over the eastern Indian Ocean associated with non-El Niño creates an east-west pressure gradient that is favorable for enhanced westerly tropospheric wind flow over eastern Africa. These westerly winds advect moisture toward the Indian Ocean promoting dry conditions over the eastern African region (Figure 6.15b).

a. wet conditions



b. dry conditions

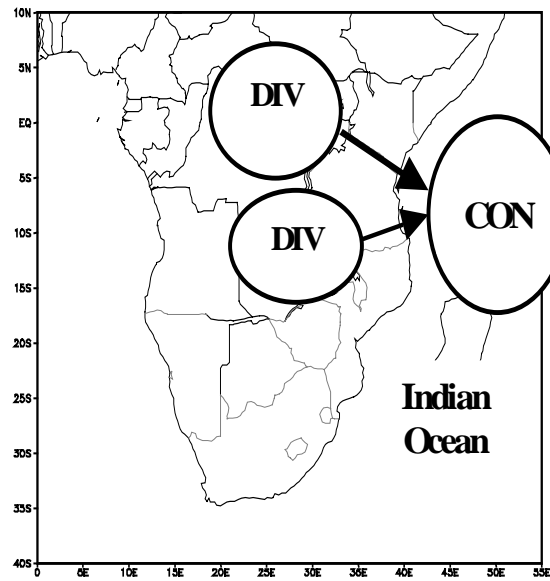


Figure 6.15: Schematic diagram showing the low-level water vapor advection (arrows) and, convergence and divergence (circles) associated with the wet and dry episodes during the October-December rainfall season over eastern Africa.

The large-scale Walker and Hadley circulations, the easterly waves and the air-sea interaction over the Indian Ocean could be playing major roles in sustaining wet conditions over eastern Africa. Of more importance for the occurrence of good rainfall in wet years over eastern Africa is the tropospheric horizontal cyclonic circulation over the region with easterly flow north of the equator and westerly flow to the south of the equator. These two air masses advect moisture to the interior of the region enhancing convection within the ITCZ and also increase the orographically induced rainfall over mountainous areas (Figure 6.15a). The other important climatic feature over eastern Africa is the

correspondence between the anomalous wet years and the negative vertical shear of zonal wind. The lower tropospheric westerly flow (centered about 800-hPa level) and the overlying easterly flow (centered at about 200-hPa level) is supportive of active convection over eastern Africa through enhanced overturning. Upper level easterlies over equatorial regions have been related to divergence associated with the presence of the easterly jet streams (Hastenrath et al. 1991), while the lower tropospheric equatorial westerlies have been associated with convergence and heavy convective precipitation (Nakamura 1969; Davis et al. 1985; Okoola 1999).

Moisture convergence in the region sustains the vertical motion and enhances the Walker and Hadley circulations over eastern Africa through the release of latent heat. In contrast, dry years are characterized by the presence of anticyclonic cells to the north and south of the equator that forces strong westerly flow over the region which increases the divergence of moisture in the troposphere over the region. These westerly flows are also responsible for the increased advection of moisture from the region toward the Indian Ocean (Figure 6.15b). Lack of moisture advection and convergence during the dry years is partly responsible for the simulated weak vertical motion over the region that results in suppression of the large-scale Walker and Hadley circulations.

## Chapter 7

### **7 INVESTIGATING THE PREDICTABILITY OF EQUATORIAL EASTERN AFRICAN CLIMATE USING NCAR REGIONAL CLIMATE MODEL. A CASE STUDY OF THE 1997 SEASON**

In this chapter, we describe research based on systematic application and enhancement of a high resolution nested climate model, toward the development of a high-resolution seasonal climate prediction system for equatorial eastern Africa. This research is built on the recent success in the customization and enhancement of RegCM2 for eastern Africa (SSOG99). The climate models used here are the Community Climate Model (CCM3.3.6) of the National Center of Atmospheric Research (NCAR) and the RegCM2. The European Center for Medium Range Weather Forecast (ECMWF) reanalysis data and CCM3 GCM predicted fields are used to generate the lateral boundary conditions for the RegCM2.

#### **7.1 Background**

The ability of the GCMs in simulating the regional average rainfall is quite encouraging, but the potential application of these global models for seasonal climate prediction is significantly limited by the coarse resolution (Giorgi and Marinucci 1991). Because of the coarse resolution of the GCMs, downscaling techniques have emerged as means of relating meso-scale atmospheric variables to grid- and sub-grid surface variables (Wilby and Wigley 2000). For the equatorial eastern African region, this is particularly important since the

rainfall is highly inhomogeneous. A significant component of the local forcing which determine the distribution of climate over equatorial eastern Africa occurs on scales of less than a few hundred kilometers thus they are not adequately resolved by contemporary GCMs. Although, this region exhibits very pronounced coupling with SST (Cadet and Diehl 1985; Ogallo et al. 1988; Nicholson and Nyenzi 1990) there has been much less research effort to exploit these relationships for the purpose of improving seasonal climate forecasting. The purpose of this study is to explore the performance of a regional climate model nested in a GCM in seasonal rainfall prediction over equatorial eastern Africa.

## **7.2 Numerical Model and Experimental Design**

Two sets of experiments are conducted using RegCM2. The first sets of experiments are conducted at 60- and 30-km horizontal grid spacing. The purpose of these experiments is to verify that, using observed large-scale lateral boundary conditions, the RegCM2 model is capable of simulating realistic climate variability in the interior of the domain and also investigate the role of model grid spacing to the simulated regional climate. Model experiments are performed with the model driven by realistic large-scale meteorological fields obtained from a 12-hourly observation reanalysis dataset obtained from the ECMWF. The computational domain is centered at 31°E, 4°S and has a  $5580 \times 5040 \text{ km}^2$  and  $3330 \times 3240 \text{ km}^2$  longitude-latitude size at the 60- and 30-km grid point spacing respectively.

The second sets of model experiments are performed to evaluate the model performance in a predictive mode. The numerical experiments are conducted for the year 1997, which was associated with extreme rainfall episodes and resulted in devastating social economic losses

in the eastern African region (Trenberth 1998). In this set of experiments, the atmospheric component of the CCM3 GCM output is used to generate initial and boundary conditions for the RegCM2. CCM3 has been chosen for this purpose because of the following considerations (i) RegCM2 has similar formulation of the physical processes as CCM3, and (ii) based on comparison of the observed rainfall patterns (Figure 7.1) and the corresponding GCM simulated pattern (Figure 7.3), shows the ability of the CCM3 to produce realistic simulation of the equatorial eastern African climate, particularly with regard to the distribution and evolution of the short-rains, across the region. Acker et. al. (1996) and Liu et al. (1994) have provided technical details of the CCM3 model. It is forced by persisted observed SST and the RegCM2 simulations are performed at a three months lag. Both the ECMWF reanalysis and the CCM3 data sets are based on a T42 spectral grid that corresponds to about  $2.8^\circ \times 2.8^\circ$  resolution in physical space, and are on 14 and 16 pressure levels for the ECMWF and CCM3 respectively.

The lateral boundary conditions are constructed based on the exponential relaxation method developed by Anthes et al. (1987), and described by Giorgi et al. (1993b). Time-dependent sea surface temperature used, which determines the surface boundary condition over the oceans is the  $1^\circ \times 1^\circ$  Shea observed monthly mean SST global data archived at NCAR (Shea et al. 1992). This data is interpolated to the model grid. For each RegCM2 model forecast case (i.e., set of initial conditions), multiple simulations are conducted starting from slightly perturbed initial conditions. Several statistical analyses including root mean square error, correlation analyses and Heidke Skill Score method are performed on the model

output and observed rainfall data to test the optimal predictability of the regional climate. In this study, we focus on seasonal rainfall for autumn. Daily, 10-day (dekadal) totals and monthly averages of precipitation are used as the primary meteorological variables for performing the quantitative assessment of the model performance.

### **7.3 Model Results**

#### **7.3.1 Sensitivity of Model Horizontal spacing on Regional Climate Simulation**

The horizontal model resolution is one of the essential issues in both short and long-range predictions of climate in regional and global scale models. Giorgi and Marinucci (1996) showed the influence of horizontal grid spacing to the simulated model precipitation over Europe. Local effects and surface forcing due to topography, large lakes and their associated sub-grid processes are resolved better in fine grid spaced models. Most of the physical parameterizations in numerical models are sensitive to horizontal model resolutions because the assumptions and the model variable tuning to specific resolutions. However, the model resolution can not be increased arbitrarily, because of the time step-restriction imposed by the Courant-Friedrichs-Lewy (CFL) stability constraint.

The observed, RegCM2 and CCM3 GCM simulated rainfall for the period October through December 1988 are shown in Figure 7.1, Figure 7.2, and Figure 7.3 respectively. Comparisons of the observed precipitation and model simulations show the ability of the model to realistically simulate precipitation over most parts of equatorial eastern Africa at

60-km. There is generally good agreement between the observed and simulated seasonal rainfall, although the model underestimates rainfall in a few areas especially over the southern parts of the domain in December. The failure of the model to capture rainfall maxima over the southern Tanzania in December can be viewed in terms of 1) the misrepresentation of orography over the southern Tanzania, 2) the centering of the model domain over central Africa (lat. -4, Lon. 31) reduces the inclusion of the Indian Ocean (the major moisture source), and 3) the misrepresentation of other large lakes over the domain especially Lake Tanganyika. The solution to this model deficiency is to move the domain further south and east to include more of the Indian Ocean. Recent model experiments performed with the model centered further east at the Lake Victoria (lat. -1, lon. 33), has shown improved rainfall simulations over the southern parts of the model domain.

The RegCM2 performance over the domain is superior to the corresponding simulations based on the CCM3 (Figure 7.3). The GCM fails to capture the precipitation over the Eastern Highlands and coastal areas of the Indian Ocean. The GCM however reproduces the general seasonal migration of the rainfall belt from north to south. This ability of the GCM to simulate the general migration of the rain-belt is one of the primary reasons for adopting it for generating the lateral boundary conditions for the RegCM2 in the predictive mode.

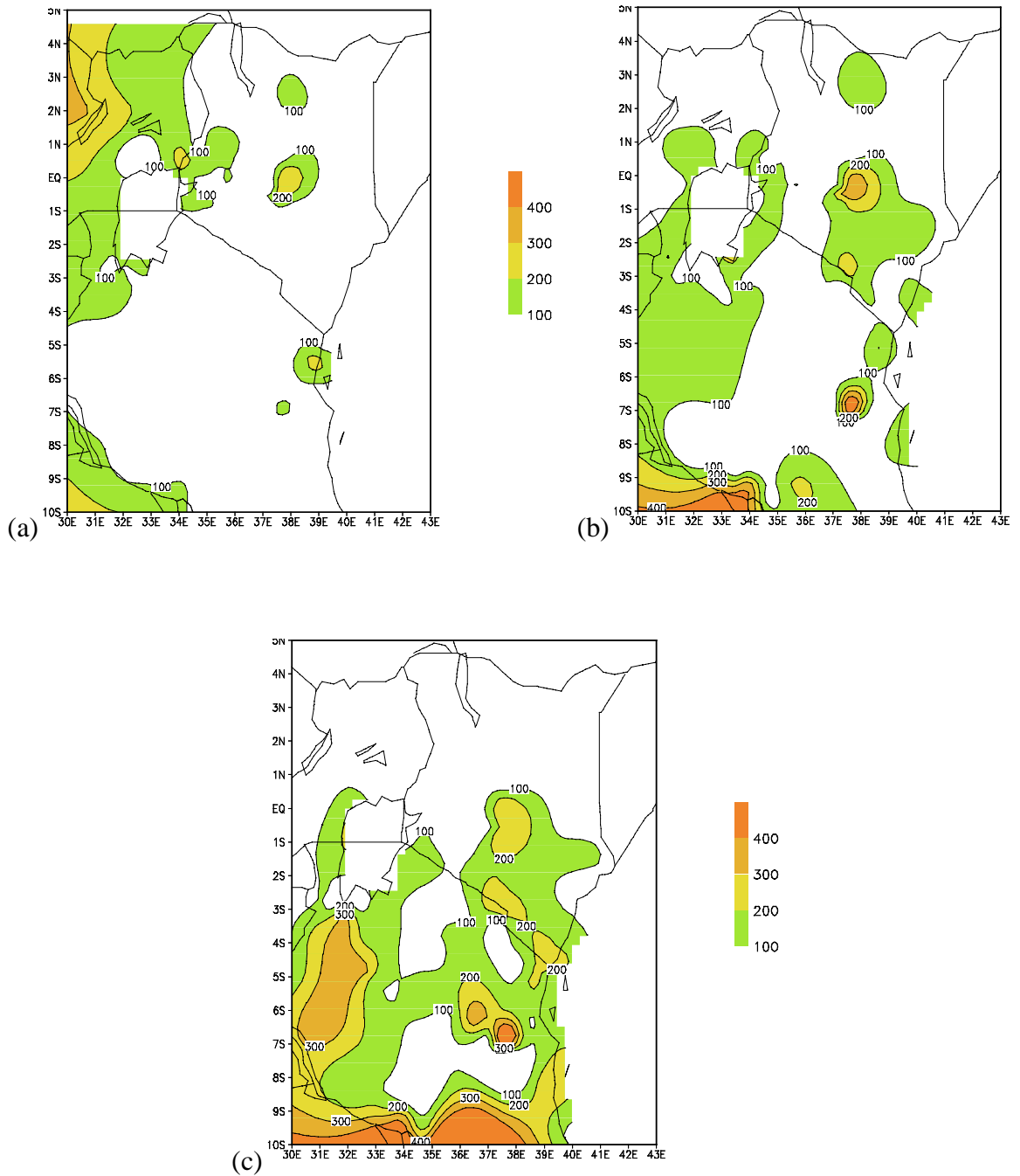


Figure 7.1: Observed seasonal rainfall distribution for 1988; a) October, b) November, and c) December.

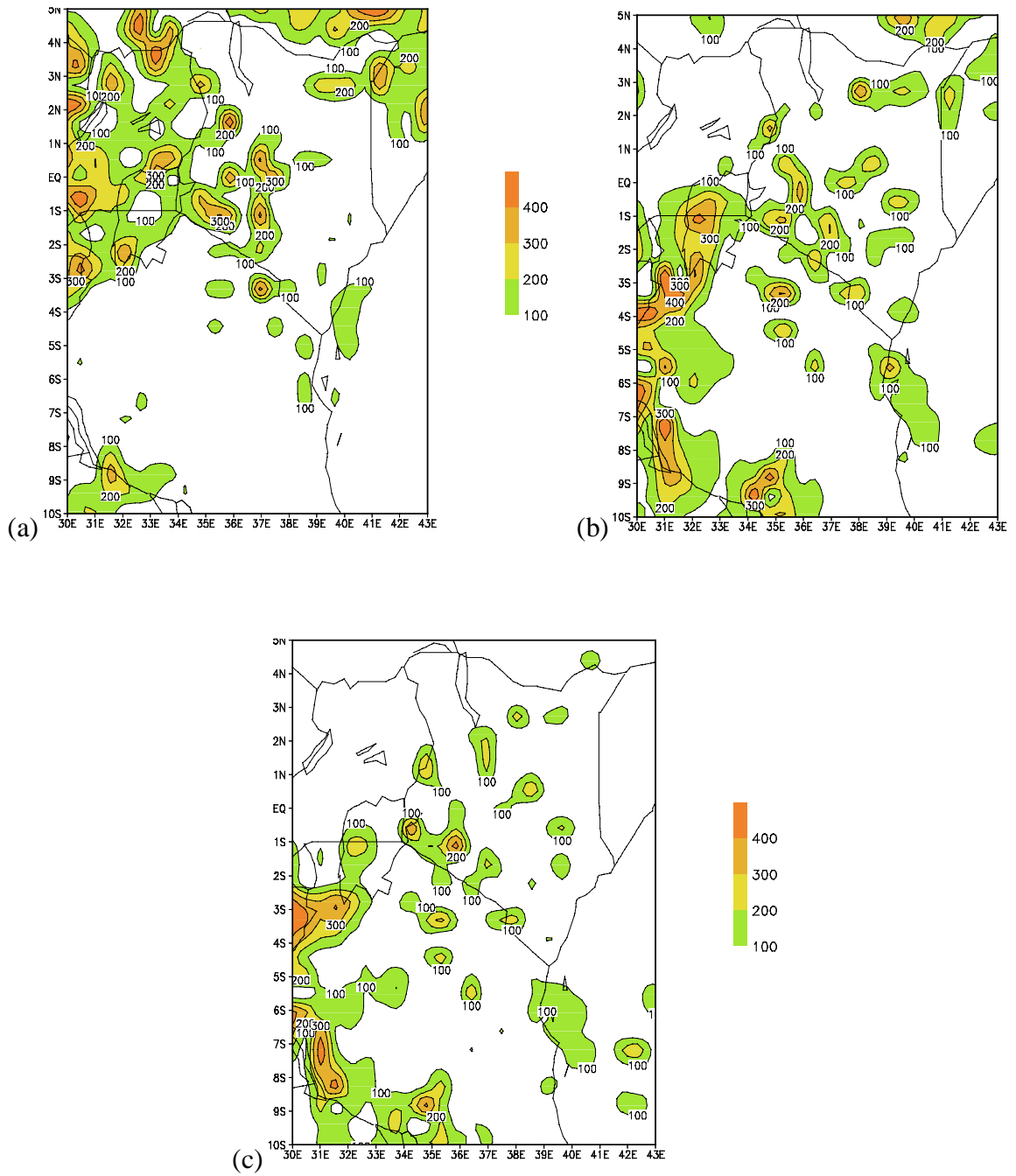


Figure 7.2: Simulated spatial distribution of seasonal rainfall in the control run (1988) for a) October, b) November, and c) December.

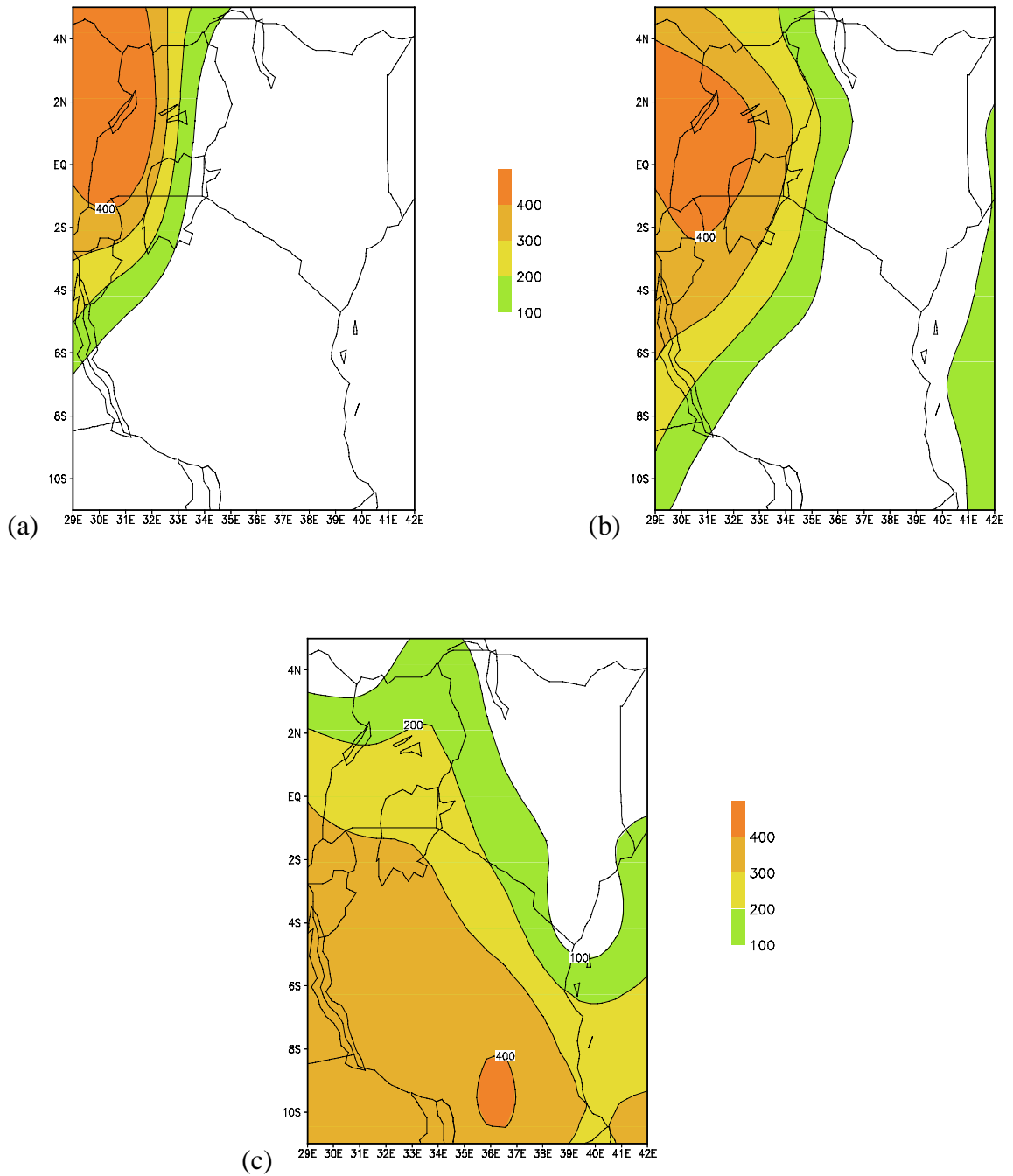


Figure 7.3: CCM3 simulated precipitation for a) October, b) November, and c) December (1988).

To quantitatively evaluate the model performance in reproducing precipitation over the homogeneous climatic regions of equatorial eastern Africa, regional averages of simulated and observed precipitation are compared. Observed precipitation fields are obtained by interpolating the station data into the model grid of 60 and 30 km followed by averaging data over model grids within a given region. The model regional rainfall is calculated by averaging grid rainfall values within the homogeneous climatic regions. The Observed precipitation data over the Lake Victoria and its watershed was not readily available for this study. Nicholson et al. (1988) used satellite-derived data to estimate rainfall distribution over the Lake Victoria and observed an annual precipitation amount well over 2000 mm which is about twice the rainfall amount simulated by the model during the short-rains season.

The rainfall progression for the simulation for the control experiment is illustrated in Figure 7.4. During the simulation period, the ITCZ shifts southward in the western portions of the domain, and carries a rain belt along its southward movement. The most striking and encouraging feature of the comparison between the simulated and observed rainfall is that the model reproduces the month-to-month tendency (increase or decrease) of the rainfall for most parts of the region. This demonstrates the ability of the model to resolve the complex migration patterns of the ITCZ over such complicated terrain, vegetation, and land-water contrasts over the region. This performance may be considered as an important step toward the application of RegCM2 in the prediction mode. These results indicate that given realistic

large-scale lateral boundary conditions, the model is capable of simulating realistic climate variables in the interior of the model.

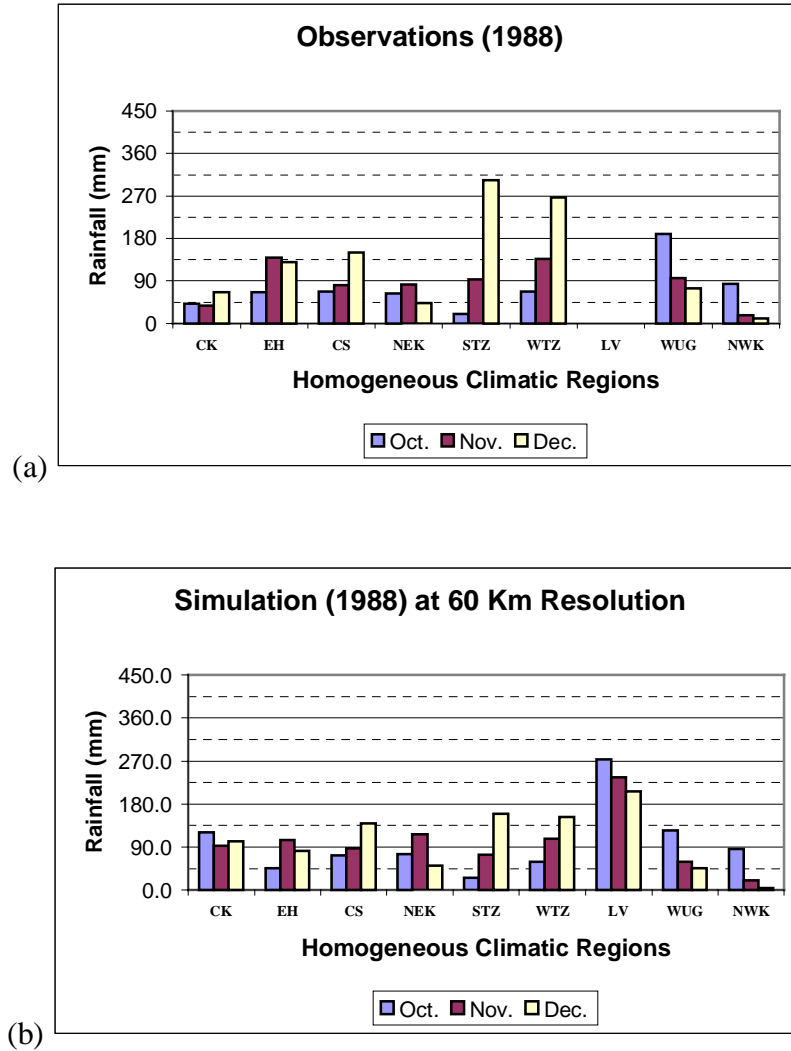


Figure 7.4: (a) Observed and (b) RegCM2 simulated precipitation in the control run (1988) for the nine climatic regions.

Comparison of the simulations based on the 30-km and 60-km (Figure 7.5) indicates that higher resolution is beneficial in reducing model bias over areas associated with very steep terrain (such as the eastern Kenya highlands). By increasing model resolution to 30 km, the simulations improve over the coastal regions (CS), Eastern Highlands (EH) and central Kenya (CK). The percentage-standardized errors are less than 25 % over most parts of the climatic regions at the 30-km horizontal spacing. However, the 60-km horizontal is adopted in most of the experiments because of computer time limitations. It should be noted that it takes about 6 wall clock hours to make a one-month simulation with RegCM2 at 60-km horizontal spacing on the NCSC flyer T90 supercomputer. It would therefore take about eight times that time for model simulation at 30-km horizontal spacing. Based on these results, we have reasonable confidence that the regional climate model is also realistically reproducing the rainfall over lake Victoria (LV), but high-resolution observations over the lake are needed to validate the model results. The discrepancies, between the model and observed monthly rainfall totals, for some regions, are a subject of further investigation. The failure of the model to improve the simulation at higher resolution over some region and especially the Western Highlands of Kenya and the Lake Victoria watershed may be due to i) the treatment of the one-dimensional diffusion model over Lake Victoria, (ii) centering of the domain further west as to include less of the Indian Ocean, and iii) the interpolation of the observed rainfall totals to match the model grid. This deficiency is more critical over areas where the rainfall station density is marginal or inadequate. We expect the model results to be more realistic over the lake because the performance of the model is more reasonable over all the other regions. There

prospects for improvement of model simulations over the lake and its watershed by including a comprehensive three dimensional lake-RegCM2 coupled model which is currently being developed at NCSU.

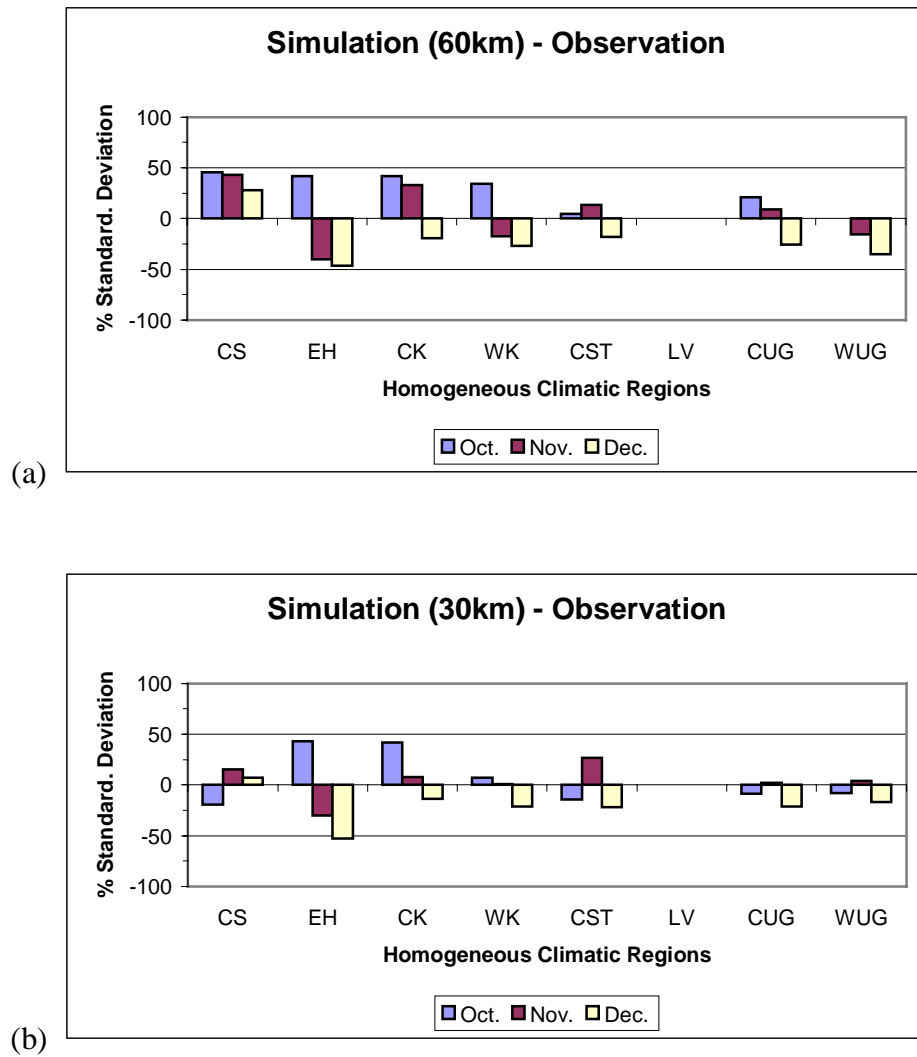


Figure 7.5: Percentage standardized rainfall deviations for the eight homogeneous climatic regions over East Africa at 60 and 30-km horizontal grid spacing.

### **7.3.2 Simulation of the October - December 1997 Rainfall Season**

In this experiment category, we test the performance of the CCM3-RegCM2 nested system. The control (1988) run is based on ECMWF reanalysis and is assumed to be the most ideal model case, which compared well with the observations. Compared to the control model run (Figure 7.6a), the simulation for 1997 shows heavy rainfall over most parts of equatorial eastern Africa. During the control run (Figure 7.6a), the rainfall belt is confined to the western sector of the domain with rainfall amounts over 300 mm. Rainfall amounts of up to 100 mm are simulated over the eastern sectors of the domain. During the 1997 anomaly simulation, rainfall is well spread over the entire domain of study with amounts of 100 mm and more indicated (Figure 7.6b). Figure 7.6c shows the percentage difference between the 1997 and control run normalized by the control run. The figure indicates a complete shift of the rainfall belt from the western to the eastern sector of the domain. Trenberth (1998) indicated that these areas of the equatorial eastern Africa, which are usually semi-arid, were bounded by heavy rainfall episodes that resulted in destruction of the infrastructure, flooding, death and increase in diseases. Apart from being associated with a strong El Niño phenomenon of the decade, the year 1997 displayed unique heavy and prolonged rains over the region when compared to the previous El Niños. Similar conditions were observed in the region in 1961 (Anyamba 1984; Raverdin et al. 1986).

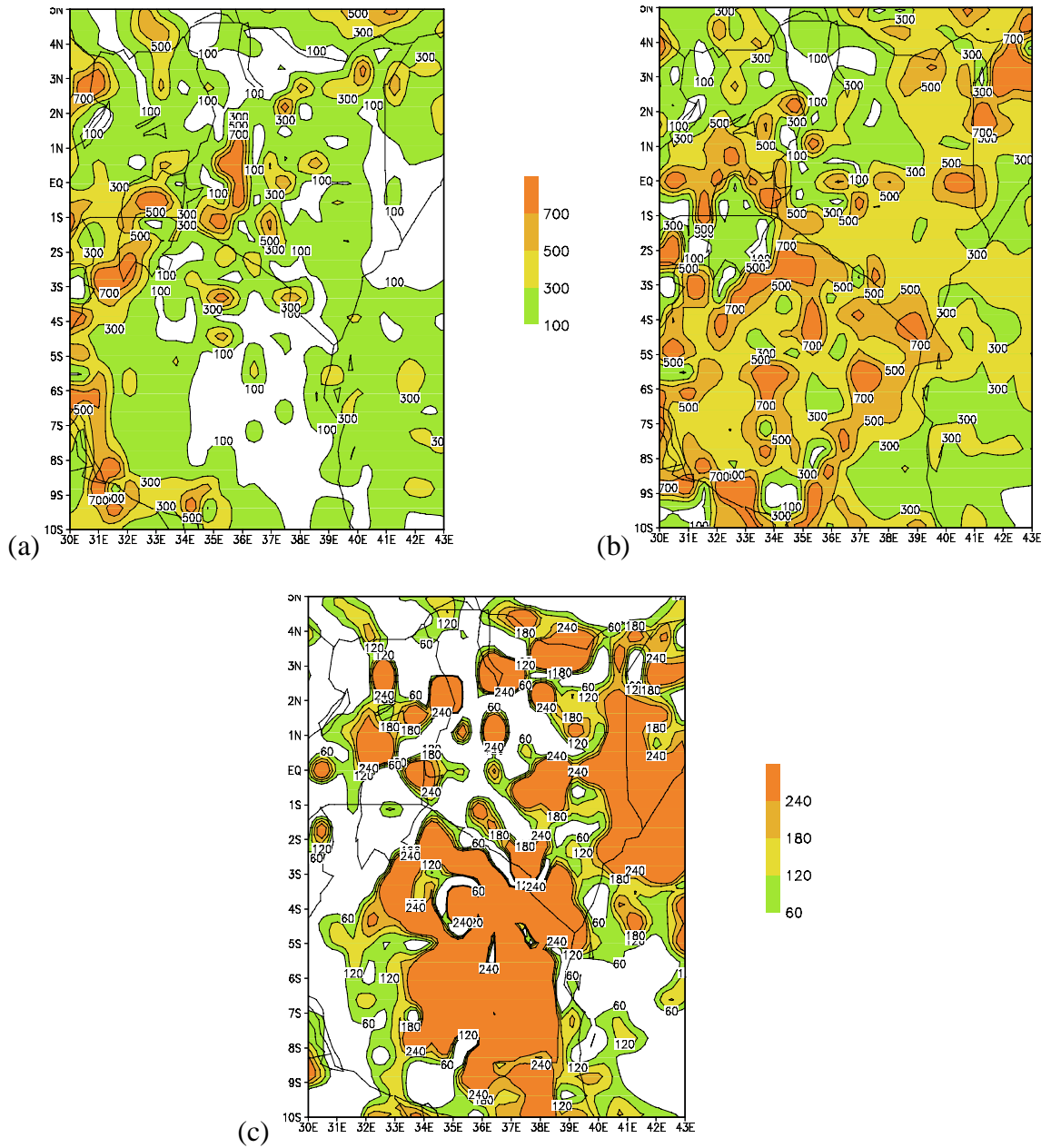


Figure 7.6: RegCM2 simulated rainfall for October-December. (a) Control run (1988), (b) simulation for 1997, and (c) percent normalized rainfall index for the 1997 minus control (normalized by the control run).

We postulate that the warm SST over the western Indian Ocean played a major role in determining the air-sea interactions and the resulting distribution of rainfall over equatorial eastern Africa during this year (1997). The usual global teleconnections manifested through the Walker circulation may have played a secondary role in the observed regional climate during this year. Webster et al. (1999) and Saji et al. (1999) have also examined evidence of unusual events in the tropical Indian Ocean that clearly point to the existence of a climate mode of interaction between the ocean and the atmosphere and rainfall distribution over eastern Africa (Anderson 1999). In chapter 3, and in Indeje and Semazzi (2000) we have proposed the possible link between rainfall over eastern Africa, the Indian Ocean dipole mode and the quasi-biennial oscillation in the equatorial lower stratospheric zonal wind.

#### ***7.3.2.1 Simulations of the Intraseasonal Rainfall Variability***

Several investigators have successfully applied various methods using observed rainfall to determine the rainfall events within the monsoon rainfall seasons over India (Asnani 1993) and East African seasonal rainfall (Jolliffe and Sarria-Dodd 1994; Okoola 1998). We adopt some of these previous methodologies in our analysis. Daily, 10-day (dekadal) cumulative frequencies of rainfall totals are used in this study to determine the onset/withdrawal of the rainfall season and determine the wet and dry episodes within the season over the climatological regions of equatorial eastern Africa. The purpose of this study is to determine whether the model is capable of simulating realistic in-season rainfall events, which are useful to the user community especially agricultural planning. Daily and expected onset and withdrawal of rains are important in determining the planting dates of agricultural crops.

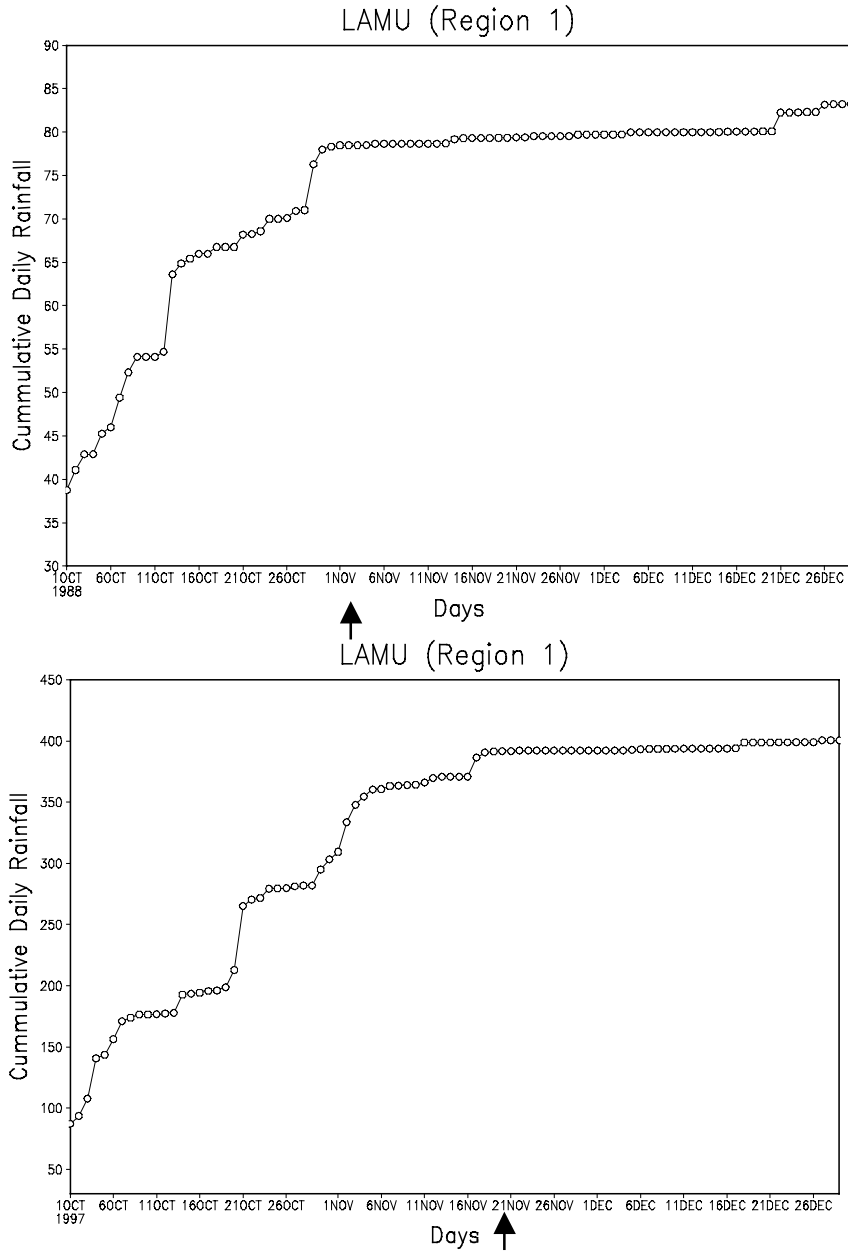


Figure 7.7: Daily evolution of model rainfall simulation for the control and 1997 anomaly run for some selected climatic regions of equatorial eastern Africa. The arrow indicates the approximate rainfall withdrawal dates.

Examples of cumulative mass curves for selected stations for the control and the 1997 simulation are represented in Figure 7.7. Over Lamu (the coastal region), there were strong

diurnal rainfall episodes during the season in 1997 of between 2 to 7 times as intense as that observed in the control run (1988). Similar conditions are simulated over the central and western Tanzania (Tabora) and the Eastern Highlands (Embu) of equatorial eastern Africa. Eastern Highlands are areas where heavy rainfall was observed that caused severe social economic impacts. Arua (northwestern part of the domain of study) depicts rainfall withdrawal much later during 1997 than in the control (1988). There were more frequent wet episodes in November compared to October in the control run. These results indicate an extended season over Arua during the 1997.

For Embu, rainfall withdrawal was observed around 1<sup>st</sup> December, but because of the heavy daily episodes realized in November, the amount of about 300 mm (~4 times that of the control run) was realized at the end of the rainfall season. There was however, an early rainfall withdrawal in 1997 than in the model control run. Nakuru (central Kenya) indicate withdrawal of rainfall around 16<sup>th</sup> November, with cumulative rainfall of about 750 mm in the control model simulation. In 1997, the rainfall withdrawal was realized around December 21<sup>st</sup> and had accumulated rainfall of about 600 mm. These results indicate a delayed rainfall withdrawal over Nakuru (Region 3) in the central Rift Valley. Over Tabora in central Tanzania, a late onset of rainfall is shown in 1997 that starts around 6<sup>th</sup> November. The late onset is followed by heavy daily rainfall episodes in the whole month of November and spilling-over to early December. During the control run, an early withdrawal of rainfall is shown at around 26<sup>th</sup> November. Similar conditions are shown over Arua in central and northern Uganda.

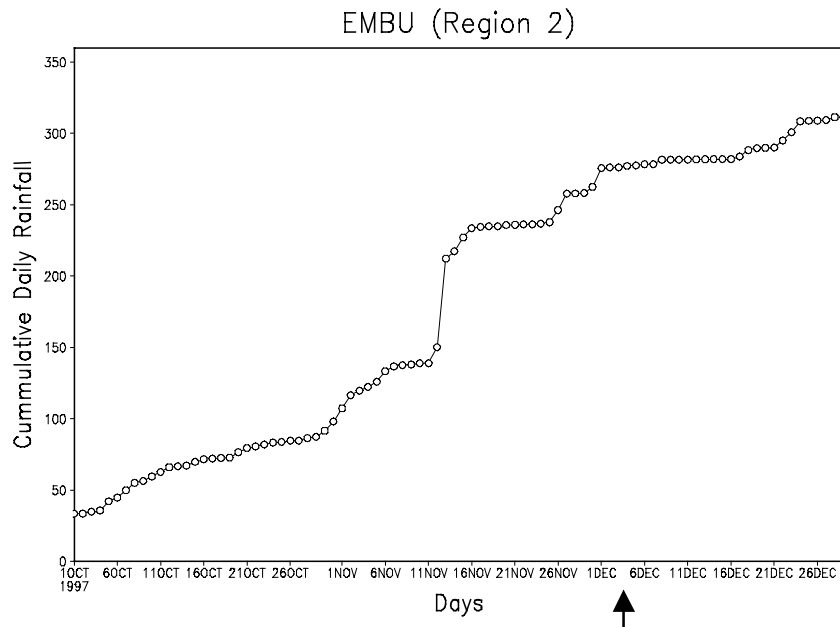
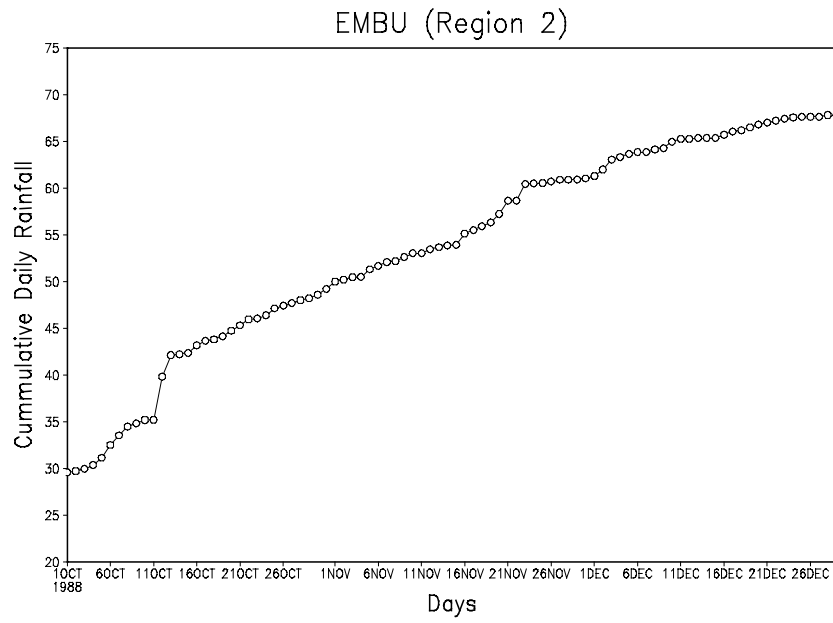


Figure 7.7 continued



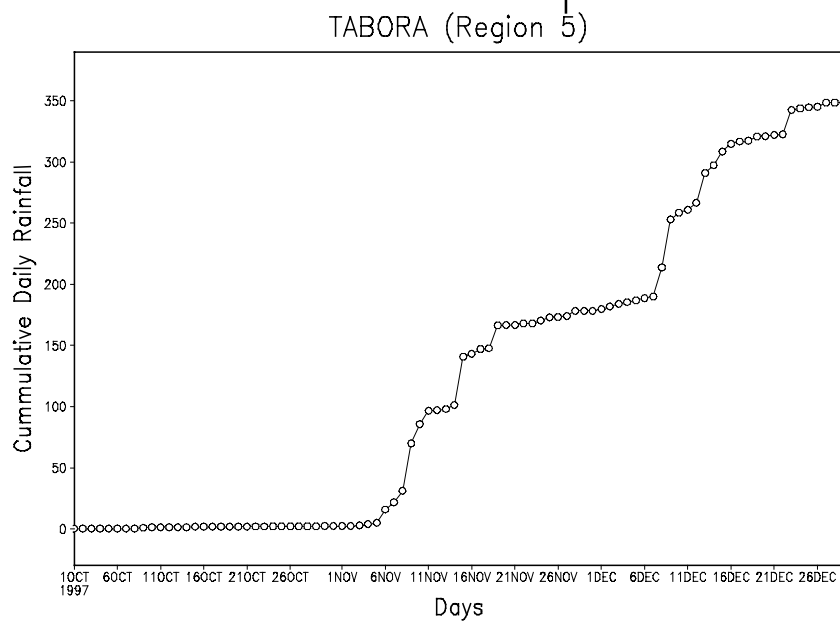
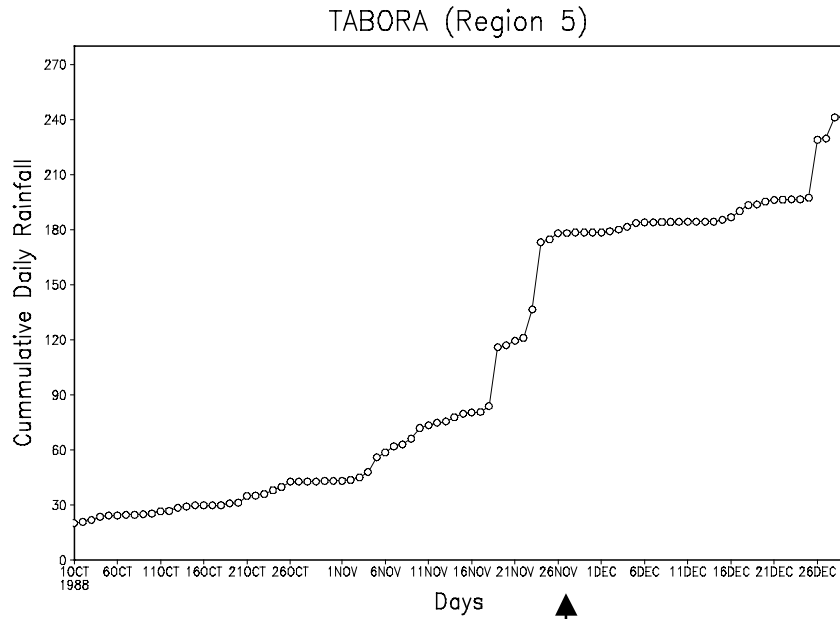


Figure 7.7continued

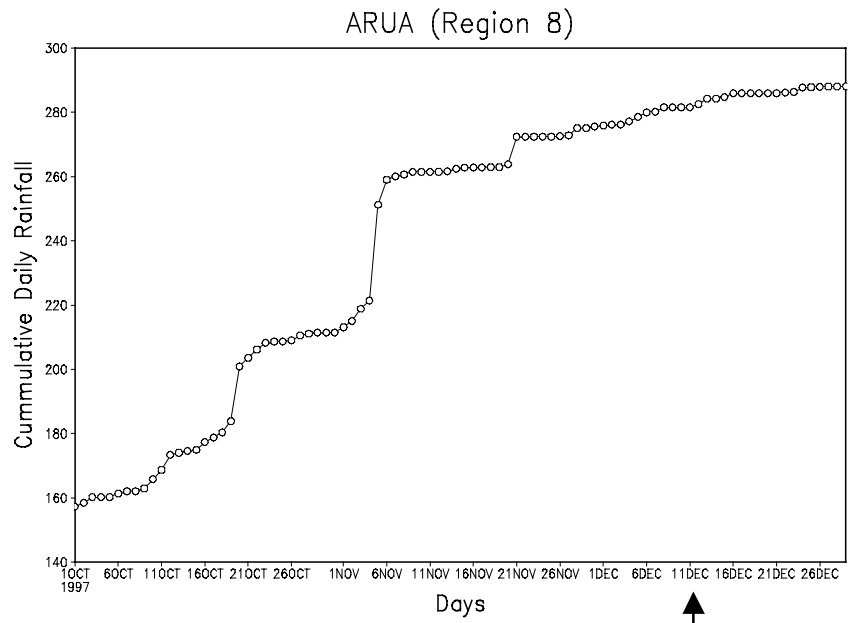
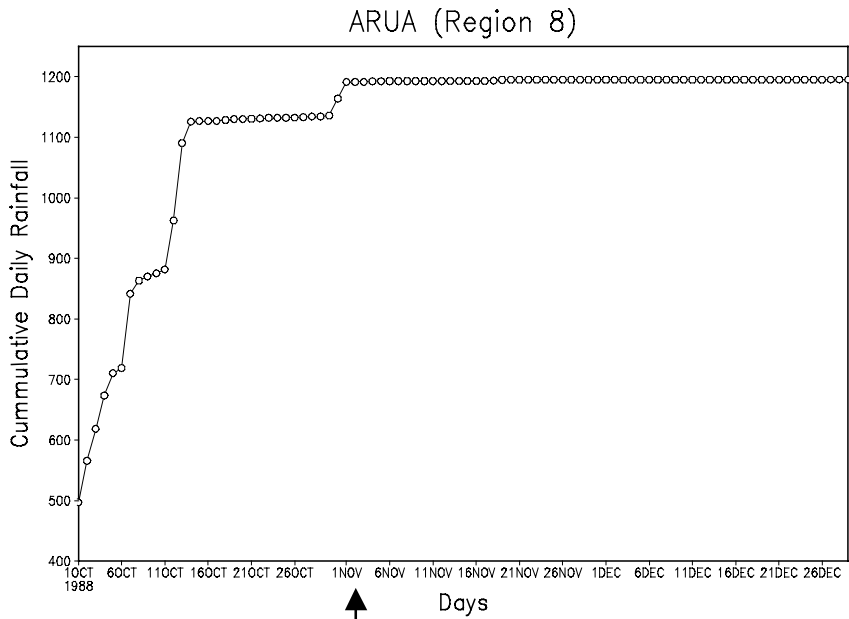


Figure 7.7 continued

The results obtained from the simulated cumulative rainfall indicate the ability of the model to reproduce the observed extreme climatic conditions over equatorial eastern

Africa during 1997. These results are an important attribute of the model that could be exploited in crop-farming management to stabilize crop yield. However more model experiments are required for other years to verify the model performance before being applied in predictive mode.

Figure 7.8 shows the observed and simulated dekadal rainfall for some selected stations. In region 3 (central Kenya), the simulated rainfall picks-up and recedes a dekad earlier than the observed rainfall. The correlation coefficient and rmse between the observed and the simulated dekadal rainfall is 0.54 and 40.36 mm respectively. The model captures the last rainfall peak in the 8<sup>th</sup> dekadal of October to December 1997. For region 5 (central Tanzania), the correlation coefficient and rmse between the observed and the simulated dekadal rainfall is 0.94 and 15.99 mm respectively. The model is capable of capturing the onset and the two peaks in the dekadal rainfall successfully. This indicates the ability of the model to faithfully reproduce the observed intraseasonal rainfall over central Tanzania. For region 8 (central Uganda), the simulated dekadal rainfall has a similar trend as the observed, but is slightly less in magnitude by 20-100 mm. The correlation coefficient and rmse between the observed and the simulated dekadal rainfall is 0.98 and 49.43 mm respectively. The model also captures the main peak in dekadal rainfall around the 4<sup>th</sup> dekad of October to December 1997.

The results obtained from the simulated evolution of the dekadal rainfall indicate the ability of the regional climate model in reproducing the intraseasonal climate variability

with skill. The model faithfully reproduces the observed rainfall trend and there is significantly high correlation and low rmse between the observed and simulated dekadal rainfall in most of the homogeneous climatic regions of the equatorial eastern African region. The model has large rmse over regions that have very steep orography like the western highlands (shown by Nakuru and Narok), and those neighboring Lake Victoria. This shows the ability of the regional climate model in simulation the regional climate with skill and could be employed for operational climate prediction over the region. More model simulations are however required for other anomalous and normal climatic years to fully validate the model, since the current validation is based on one year only.

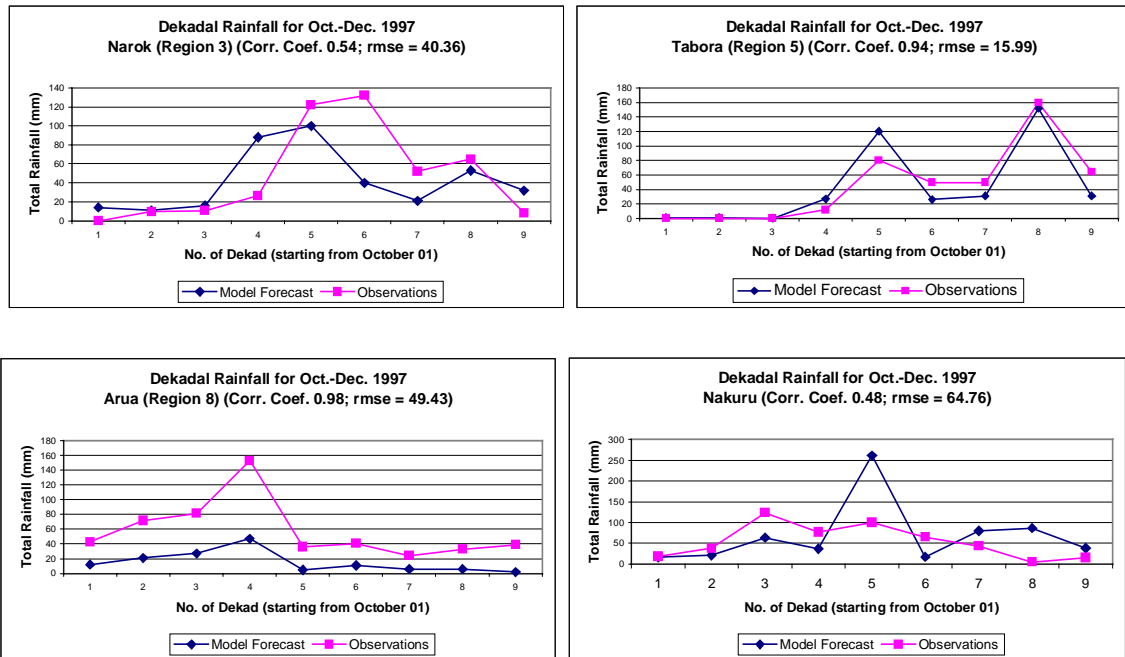


Figure 7.8: Model simulated and observed dekadal rainfall for some selected rainfall regions.

## Chapter 8

### 8 SUMMARY AND CONCLUSIONS

Statistical and numerical methods were employed in this study to investigate the short-term climate variability and predictability over equatorial eastern Africa. In chapter 2, we investigated the ENSO signals in the East African rainfall seasons. Results obtained in this diagnostic study showed large spatial and temporal variability in seasonal rainfall through the 30-years period (1961-1990). These results were consistent with earlier studies by Ogallo (1980), Beltrando (1990), Nyenzi (1992) and Nicholson (1996). Results obtained from the EOF analysis of the seasonal rainfall showed patterns that resemble the mean climatology, which is primarily dictated by the seasonal migration of the ITCZ as indicated in the first EOF mode. The interactions between the prevailing easterly flow and the meso-scale circulations that play a major role in the diurnal and intra-seasonal rainfall variability in the region were clearly discernible in the second dominant EOF rainfall. There was an indication of contributions, which may be associated with rainfall generating systems such as easterly waves, and the 30-60-wave oscillation, in the third EOF modes. The Principal Component time series for the EOF2 showed the years that were associated with floods/droughts during the study period, with 1961 having the highest amplitude of more than five standard deviations.

Iterative application of rotated EOF and simple correlation analyses yielded eight and nine homogeneous rainfall regions in equatorial eastern African region for the annual and seasonal rainfall respectively. Dyer (1977) used a similar approach for South Africa. The resulting homogeneous regions compare well with those obtained by earlier researchers (Nicholson et al. 1988; Ogallo 1989 among others) and are reasonable in spatial distribution.

The relationships between seasonal rainfall in equatorial eastern Africa and phases of ENSO were also identified. The results obtained from this investigation show, however, that not all areas/seasons of the region are wet/dry during the El Niño/post-ENSO (+1) years as previously claimed. Relatively wet conditions were observed during the March-May and October-December rainfall seasons of the El Niño years. Similar results were obtained during June-September of the post-ENSO (+1) years. Dry conditions dominate in June-September of the El Niño onset years and the two seasons (March-May, and October-December) of the post-ENSO (+1) years. The results also delineated areas that are prone to excess/deficit rainfall during the El Niño/post-ENSO (+1) years. Relatively wet conditions were observed during JJAS seasons of the La Niña onset years and dry conditions were dominant during the short- and long-rains season. Similar conditions were experienced during the post-La- Niña (+1) years. These results agree with the findings of Nicholson (1996) that there is a tendency for rainfall to be above average in most parts of East Africa during ENSO years and for rainfall deficits to occur during the following year, with positive rainfall anomalies occurring during the short rains of the ENSO year. Our

findings do not agree with her suggestion of negative anomalies during the long rains of the following year except in southern Tanzania.

Results obtained from this study have shown that ENSO plays a significant role in determining the monthly and seasonal rainfall patterns in the equatorial eastern African region. In some regions there are shifts in the onset/cessation of rainfall while in others there is a significant reduction in the seasonal rainfall peak during ENSO/post-ENSO (+1) years. For instance the June-July to August rainfall season over the central Rift Valley of Kenya (Region 3) is significantly diminished during the ENSO onset years. The suppression of this seasonal rainfall can have severe social economic impact especially on agriculture. The June-September rainfall maintains the different growing stages of crops especially wheat planted by both large-scale farmers and small-scale peasant farmers in the region. Advance knowledge of the expected seasonal rainfall performance in association with ENSO and other factors, and the fast dissemination of the climate information to the farmers, could be highly beneficial. These results show in detail the effects of ENSO in shaping the seasonal rainfall patterns over East Africa postulated by earlier researchers (Ropelewski and Halpert 1987; Ogallo 1989; Nicholson 1996 among others). This analysis could be performed in any region where rainfall is influenced by different phases of the ENSO cycle. The results obtained from this study have direct applications in operational seasonal rainfall monitoring and prediction for equatorial eastern Africa.

In chapter 3, we examined the coupled variability between the equatorial eastern African seasonal rainfall and the different QBO phases in the equatorial stratospheric zonal. The analyses were based on the application of the simple correlation and composite analyses. Both simultaneous and lag correlations were examined, in order to explore the optimum associations between equatorial stratospheric zonal winds and the seasonal rainfall. Results obtained from this study have revealed an important relationship between equatorial stratospheric quasi-biennial structure and the seasonal rainfall over the region, which raises the prospects for using the 30-mb zonal wind for prediction of equatorial eastern African seasonal rainfall. The main results can be summarized as follows: (a) a distinct seasonal cycle exists in the correlations, (b) boreal summer (June-August) is the season with the strongest relationships, (c) boreal winter (DJF) shows the weakest relationships, (d) in some seasons especially boreal summer, the lag correlations are strong enough to suggest the possibility of seasonal rainfall prediction, (e) the strongest correlations are found in western part of the region, (f) the correlations remain reasonably stable with time for several seasons, (g) the OND minus JJA trend of the equatorial zonal wind offers a useful index for seasonal climate monitoring of the long-rains over equatorial eastern Africa and, (h) there is high chances of above/below normal rainfall during the west/east phases of the QBO. The relationships failed during the years 1966, 1973 and 1983 when drought was experienced in the region that was modulated by strong and prolonged ENSO events. Similar observations have been made in the monsoon rainfall (Mukherjee et al. 1985) and in the South African rainfall (Mason and Tyson 1992). Visual inspection of the QBO-Index and the newly found Indian Ocean dipole mode index (DMI) indicated that the two

climate variables might be related significantly. Of the six extreme DMI events that were observed in 1961, 1967, 1972, 1982, 1994 and 1997, all except 1967 coincided with the easterly phase of the QBO-Index.

The study has further clarified the seasonal relationships, as well as proving general robustness of these relationships, and thus of their use in seasonal prediction. The apparent superior associations between the QBO-Index and seasonal rainfall after 1979 to date, means that the use of relatively short periods of recent data might provide better forecasts than the use of all available historic data. The underlying mechanisms responsible for the QBO/convection over western parts of equatorial eastern Africa have been proposed and explained in this study, and also some observational evidence has been presented, which may be useful for operational forecasting. The mechanisms that account for observed link between the ocean-atmosphere-coupled mode in the Indian Ocean (DMI) and the QBO/convection over parts of equatorial eastern Africa have been proposed. The high/low DMI phase is associated with easterly/westerly phases of the QBO-Index and low/high convective activities over the region.

This study has further indicated that about 36 percent of rainfall variability over the region during the long-rains is associated with the quasi-biennial oscillation in the lower equatorial stratospheric zonal winds. If the natural cyclical pattern of the QBO could be anticipated, the present finding may have some value in the general context of the long-range forecasting of the East African long-rains season. The results suggest that the

relative role of QBO and rainfall over eastern Africa is stronger in the time-lag sense than the simultaneous relationship. The present study has further demonstrated that the phase of the QBO prior to the season is a useful predictor index for the seasonal rainfall. This is particularly the case for the long-rains for which ENSO provides only limited skill in the predictability of the rains. This observation should be explored further in the search for more effective seasonal climate predictors over eastern Africa and the other regions of Africa.

In chapter 4, we investigated the climate over eastern Africa during the boreal winter season using the NCAR regional climate model (RegCM2). Specifically, the Turkana easterly low-level jet that lies between the Ethiopian highlands and the East African highlands was studied. The initial and lateral boundary conditions were obtained from the ECMWF reanalysis data. The control run was based on the October to December season of the year 1988. The model simulations in the control run were compared with the NCAR/NCEP reanalysis data to test the ability of the model in reproducing the observed climate patterns over the region. The model results of the Turkana easterly low-level jet were compared with the observations of the jet reported in Kinuthia and Asnani (1982) and Kinuthia (1992).

Results of the control run showed the ability of the model in reproducing the climate patterns over the eastern Africa. The simulated wind, temperature and humidity patterns compared well with the observations. The simulated patterns of the Turkana easterly low-

level jet compares well with its observed characteristics. Strong winds were simulated within the channel throughout the season with the wind speed decreasing in regions where the channel becomes wide. Two distinct jet streams, detached from each other, were simulated throughout the channel except at the middle of the channel where they combine into a single and elevated jet centered at about 700-hPa level. The level of maximum winds occurred in the layers 930-hPa and 650-hPa levels (~ 400 – 3200 m). Kinuthia (1992) reported the existence of maximum winds in the layer between 305 and 2438 m. Before and near the channel entrance and at the channel exit the levels of occurrence of maximum winds were almost the same. The levels of maximum winds slope down from the entrance to the middle region and then up again towards the channel exit. The direction of the mean wind backs to the east from surface to 800-hPa level where the flow is mainly easterly, turning to northeasterly aloft. The highest magnitude of mean maximum wind simulated in the channel was  $11 \text{ m s}^{-1}$  (~ 22 knots). Temperature, moisture and momentum flux convergence was dominant at the entrance and exit of the channel, with divergence of these fluxes indicated at the middle of the channel.

The dynamics of the Turkana channel could be explained in terms of the orographic channeling effects associated with the Bernoulli effect in barotropic flows. This study has verified this phenomenon by showing the dependence of the jet on the large-scale orography. Our results have also suggested the importance the large-scale monsoon flow and the depth of the channel in the development of the jet. The effect of the large-scale monsoon flow is to determine the wind speed in the jet cores whereas, the depth of the

channel is important in determining the vertical structure and location of the jet cores. Results obtained from this investigation further indicate that thermal and frictional forcing may play equal roles as that of the large-scale winds in the formation of the jet. The split in the jet over the middle of the channel is analyzed as a barotropic instability problem due to the divergence/convergence of momentum fluxes. Previous studies have shown similar phenomenon in the low-level jetstreams associated with barotropic flows (Thompson 1957; Wiin-Nielsen 1961; Krishnamurti et al. 1976). This study contributes to a better understanding of the dynamics and thermodynamics of the Turkana jet. Because of the general sparseness, paucity and ambiguity of most of the field data in the field programs, they do not usually provide mechanistic answers by themselves to many physical phenomena. Improved understandings in the dynamics of the atmospheric phenomena have therefore come from analytical, numerical and laboratory studies with the field data supplying confirmation of their applicability (Baines 1995).

The model results further show that the dry conditions observed over the Lake Turkana basin may be explained in terms of dominant downward vertical velocity, decrease in moisture flux convergence and increase in temperature flux divergence that inhibit active developments of meso-scale circulations and their interactions with large-scale flow over these areas. These results have also revealed the thermal and moisture structures across the Turkana channel that were not detected in the observational studies reported in Kinuthia (1992). Our model results indicate that the presence of the Turkana low-level jet is a significant climatic feature over the equatorial eastern African region as it plays the

role of the “skeletal” structure on which the anatomy of the regional climate of the northeastern Africa evolves. The regions of strong winds associated with the jet are important to the safety in the aviation industry. These regions may also provide alternative energy sources of wind energy since the observational studies have indicated that strong winds exist throughout the year in this valley. Climate dependent hydropower is the major source of energy in the equatorial eastern African region. If wind turbines were installed in areas in the valley with strong winds, then this could provide alternative energy resources. These resources could be used to alleviate the frequently experienced energy shortages that predominate during extremely dry seasons.

In chapter 5, we investigated the physical mechanisms responsible for the occurrences of floods and droughts over equatorial eastern Africa during the October-December rainy season using the NCAR RegCM2. Two contrasting years 1982 (El Niño) and 1987 (non-El Niño) that were associated with wet and dry episodes respectively were studied. The year 1988 that displayed near normal conditions was used in the control model simulations. The three anomalous years (1982, 1987 and 1988) used in this analyses were obtained from a time series of the normalized rainfall index for eastern Africa covering the 1961-1990.

The normalized rainfall time series indicate that on average the eastern African region received above normal rainfall in the 1960's and late 1970's. The year 1961 was wettest in the 30-year period as shown by other investigators (Anyamba 1984; Reverdin et al. 1986;

Indeje et al. 2000). Recent studies indicate that this 1961 anomalous year may be related to the climatic dipole mode index (DMI) over the Indian Ocean (Webster et al. 1999; Saji et al. 1999). Below normal rainfall was observed in late 1960's, early 1970's and 1980's. Near normal rainfall conditions occurred during the years 1962, 1965, 1984, 1988 and 1990. The climatic fluctuations over eastern Africa were explained in terms of the air-sea interactions over the Indian Ocean, as well as the latitudinal location and intensity of the large-scale Walker and Hadley circulations in the region.

Results obtained from the analysis of the horizontal wind structure indicated that wet years in eastern Africa are related to the deceleration of the mid-tropospheric easterlies into the region, enhancing the horizontal convergence within the ITCZ. Mid-tropospheric westerly and easterly wind flows from the Indian Ocean and the Congo forest respectively during wet El Niño years are relatively strong and converges into eastern Africa. The easterly flow into the region north of the equator is moist having traversed the Indian Ocean while the westerly anomaly south of the equator had its trajectory over the moist Congo forest. Orographic lifting of moist and strong easterly flow from the Indian Ocean promotes uplift over much of the region during wet spells and is a key mechanism for the occurrences of heavy rainfall over the eastern windward sides of the East African highlands and the Ethiopian Mountains during this season. Thus, the two mechanisms favorable for the precipitation enhancement namely moisture convergence and moisture advection are present during the wet years. The north-south wind shear shown on the 700-hPa level that

indicate the presence of a positive vorticity across the equator could be a unique feature for the wet years over eastern Africa.

During the dry year, strong mid-tropospheric westerly wind anomaly was simulated over much of the region. This westerly wind anomaly originated from about 10°S, 30°E and about 4°N, 28°E. The simulated acceleration of these westerlies away from eastern Africa could support enhanced horizontal divergence by linear acceleration. The anticyclonic circulations located over western parts of the region at 700-hPa enhancing the westerly wind anomaly over the region, could be a distinct feature for dry years over eastern Africa. The results further indicate that reduction in moisture advection from the Indian Ocean into the region is a feature of the dry years. The reduced moisture advection results in dry convection and reduces orographic precipitation leading to the dry conditions over eastern Africa. Increase in moisture flux divergence over areas that usually experience less seasonal rainfall like the northeastern Kenya, central Tanzania and southern Sudan could amplify the drought-like conditions in these areas. These results further indicated that during El Niño years, the interaction between the thermally-induced meso-scale circulations and large-scale flows is strong enough to sustain convection over the Lake Victoria basin and western sectors of eastern Africa through the release of latent heat, and is very weak during the non-El Niño year.

The simulated vertical cross sectional wind analyses show a correspondence between the anomalous wet year and the negative vertical shear of zonal wind. Negative wind shear

between westerlies/southerlies centered about 800-hPa level and the overlying easterlies/northerlies centered at about 200-hPa levels could be associated with active convection through enhanced overturning. These results agree with those obtained earlier by (Hills 1979) who indicated that divergence in upper levels (300- and 200-hPa) was present during the short-rains but convergence in long-rains over eastern Africa. This wind pattern accompanied by the diffluent wind anomalies observed in the low-levels for dry occurrences in November is indicative of the barotropic nature of rain-bearing mechanisms during the short rains. Vertical motion field suggests that the main convective zones associated with this east-west Walker circulation shifts eastwards to the East African region intensifying convection over the region during the wet El Niño year and these large-scale features are highly suppressed in the region during the dry non-El Niño years. The occurrences of deep convection simulated in the region during this season imply that these particular latent heat sources could impact the large-scale dynamics through the teleconnections.

The model reproduced the month-to-month tendency (increase or decrease) of the convective and non-convective rainfall for most parts of the region. The circulation differences discussed in section 6.4.3 were consistent with the buildup and subsequent precipitation of Indian Ocean water vapor over the eastern-highlands for the wet year, and more efficient eastward advection of moisture in the drought year. The simulated convective precipitation for both the wet and dry year were comparable in magnitude, which suggests that moisture advection contributes most in sustaining wet conditions over

eastern Africa than evaporation and moisture convergence during this season. Reason and Godred-Spenning (1998), also indicated that the major mechanism responsible for the modulation of rainfall over eastern Africa was related to the amount of moisture advected in the region by the easterly trades from the tropical South Indian Ocean rather than to the local evaporation. In the dry non-El Niño year, the eastward moisture advection deprives the western highlands of local moisture convergence resulting in dry convection and associated reduction in convective precipitation. The results obtained in this study gives an insight in the dynamics and thermodynamics associated with the wet and dry climates over equatorial eastern Africa during the short rains season. Understanding of these phenomena is necessary before attempting to predict the regional climate. The findings obtained from this study could be useful in the short and medium range climate guidance and forecasting in the region.

In chapter 6, we developed a scheme to explore the feasibility of short-term climate prediction of seasonal rainfall in the equatorial eastern Africa using a CCA model. The predictor variables included the July and December SST over the tropical Pacific and the predictand fields are the two October-December and March-May rainfall seasons of eastern Africa. EOF analysis was employed to condense the predictor and predictand data sets. The model was trained using the data for the period 1961-1990 and was then used to predict rainfall for the year 1997/98 seasons at three months lag.

The EOF analysis extracted fractions of variances that have physical significance. The first EOF mode extracts the El Niño/ La Niña SST pattern over the Pacific Ocean. In this mode, the largest variability of the SST anomaly over the tropical Pacific Ocean occurs over the eastern and central Pacific. The spatial and temporal patterns of the first CCA mode indicate the existing linear relationships between rainfall anomalies over eastern Africa and the SST anomalies over the eastern-central Pacific Ocean. The CCA prediction model, which has been constructed, exhibits high potential for predicting seasonal rainfall anomaly over many parts of the equatorial eastern Africa during the October-December season. The hindcast model for the March-May season was less stable indicating that this season is less predictable using the predictor field of the Pacific Ocean SST only. Inclusion of other predictors including the Atlantic and Indian Ocean SST, and the quasi-biennial variability in the equatorial lower stratosphere could improve the predictability of rainfall during this seasonal.

Dynamical as well as empirical approached could be used for the forecast task such as this. But because the dynamical and empirical methods often offer roughly the same skill levels we chose to use an empirical approach here for practical reasons which means less effort and expense (Barnston 1994). CCA has skill capability and its extensive set of diagnostics offers some insight into the physical bases of the relationships used to form the predictions (Barnston et al. 1996). The results obtained from CCA technique indicate the potential predictability of regional seasonal rainfall with some skill. The developed CCA model

could be applied in the operational short-medium range climate prediction over equatorial eastern Africa.

In chapter 7, we employed the RegCM2 to investigate the impact of horizontal grid spacing on the simulated regional climate and also to evaluate the model performance in reproducing the climate over equatorial eastern Africa in a predictive mode. The model-simulated results clearly showed that the nested model yields a large improvement in the simulation of regional climate details compared to a stand alone GCM. The model reproduced the location of rainfall belts and most of the local strong rainfall maxima correctly during the seasonal transition period. The simulated spatial and temporal variability of rainfall compared well with the available station observations. The model results showed considerable improvement in the simulated rainfall at a higher horizontal model grid spacing. Model simulations at 30-km horizontal spacing showed low model error of less than 25 % in the simulated rainfall over most of the homogeneous climatic regions of eastern Africa.

The results obtained from the simulated cumulative rainfall indicate the ability of the model in reproducing the observed extreme wet conditions over eastern Africa during 1997 season. The control (1988) run is based on ECMWF reanalysis and is assumed to be the most ideal model case, which compared well with the observations. Comparing the control (1988) model run based on ECMWF-RegCM2 and 1997 model forecast based (CCM3-RegCM2) on could be one of the worst possible scenarios since the ECMWF-

RegCM2 and the CCM3-RegCM2 may have inherent different day to day variability. But, in the absence of the RegCM2 model climatology and/or longer series in the CCM3 runs to force the RegCM2, this is the only best available option. This is more so since the control model run compares well with the observations. The RegCM2 model was also capable of reproducing the intraseasonal rainfall variability over the region. Daily cumulative rainfall showed the ability of the model in faithfully reproducing the expected onset, duration and withdrawal of the seasonal rainfall. Compared to the control run, the simulated rainfall for the 1997 season showed more frequent wet spells in November over most of the climatic regions of eastern Africa. These daily wet spells extended into December resulting in the observed severe flooding over the region. The model was also capable of reproducing the westerly shift in the rainfall belt during the 1997 season. More than 250% of the normalized rainfall amounts was simulated in many areas of the eastern lowlands of equatorial eastern Africa. This heavy rainfall was associated with severe social economic disasters in the region. Besides the ENSO teleconnections, we postulate that the air-sea interaction mechanisms over the western Indian Ocean contributed significantly to the 1997 anomalously wet conditions over equatorial eastern Africa. The model also reproduces the dekadal rainfall evolutions over homogeneous climatic regions with skill. The model results had reasonably low rmse and significant correlations between the observed and simulated dekadal rainfall. These results are an important attribute of the model that could be exploited in crop-farming management to stabilize crop yield. The overall results obtained from the numerical modeling study indicate the ability of the nested modeling approach as a powerful tool for improving regional climate simulations

and possible climate change scenarios. The downscaled climate information is much more valuable for policy makers than the simple area-average climate advisories based on contemporary GCMs.

## **9 SUGGESTED FUTURE WORK**

Here is a summary of the suggested future work, which will benefit more from the use of satellite-derived data and available station observations for model validations.

- (1) Our results show in detail the effects of ENSO in shaping the seasonal rainfall patterns over East Africa postulated by earlier researchers (Ropelewski and Halpert 1987; Ogallo 1989; Nicholson 1996 among others). Using a longer rainfall time series having more ENSO/rainfall composites may make the results more robust. Also, a higher frequency temporal analysis based on daily or five-day rainfall (pentads) that is useful in identifying the likely onset of seasonal rainfall and the planting dates is highly recommended.
- (2) We have shown that the relative role of QBO and rainfall over equatorial eastern Africa is stronger in the time-lag sense than the simultaneous relationship. The present study has further demonstrated that the phase of the QBO prior to the season is a useful predictor index for the seasonal rainfall. This is particularly the case for the long-rains for which ENSO provides only limited skill in the predictability of the rains. This observation should be explored further in the search for more effective seasonal climate predictors over eastern Africa and the other regions of Africa. The shown significant relationships could be used to

explore the possibility of incorporating QBO as an additional predictor in multi-linear prediction models for the MAM seasonal rainfall over the region. It would be worthwhile to investigate further the QBO in the stratospheric zonal winds, the regional rainfall and the DMI events over the Indian Ocean by adopting a dynamical modeling approach.

- (3) Our numerical modeling study contributes to a better understanding of the dynamics and thermodynamics of the Turkana jet. There are however some physical aspects important for the low-level jets that are not included in this study. Some of these factors include the air-sea interaction over the Indian Ocean that regulate the monsoon flow that ultimately affect the Turkana jet. The temperature difference between the eastern and western ends of the channel could be crucial in initiating the flow across the channel from east to west. In this study, we have only explained the thermal forcing as possible effects in the maintenance of the jet. Also detailed study of the surface fluxes of heat, moisture and momentum in the jet core is highly recommended including a detailed study of the diurnal variation of the jet since a detailed boundary layer dynamics is not present in our study. This limitation could be handled by using a finer model resolution of 30 km or higher with detailed boundary formulation. This study was done during the months when the easterly monsoon is not at its maximum. A similar study during the period June-August when the large-scale flow is strong would be recommended although our results indicate that the large-scale flow contributes to approximately a half in terms of the strength of the jet is concerned. Further mechanistic experiments are

required in order to understand the role of the primary lower boundary factors which determine the climate of equatorial eastern Africa. This would include investigating i) the role of orography of the rest of the region, ii) the role of the vegetation patterns, and iii) the role of the neighboring Indian and Atlantic SST.

- (4) Our investigation on the dynamics and physical mechanisms responsible for the ENSO/regional rainfall variability are based on only a single wet and dry year, i.e. 1982 and 1987. Although these years were selected from a 30-year climatology, (1961-1990) the results based on these two years might not necessarily reflect the general climatic conditions in the entire wet El Niño and dry non-El Niño years over the region. Similar experiments during the other anomalous years and the use of data from operational seasonal forecast GCMs are highly recommended.
- (5) The constructed CCA prediction model exhibits high potential for predicting seasonal rainfall anomaly over many parts of the equatorial eastern Africa during the October-December season. The hindcast model for the March-May season is less stable indicating that this season is less predictable using the predictor field of the Pacific Ocean SST only. Inclusion of other predictors including the Atlantic and Indian Ocean SST, and the quasi-biennial variability in the equatorial lower stratosphere could improve the predictability of rainfall during this seasonal. Also use of the Indian Ocean DMI (Saji et al. 1999) and rainfall over other regions of Africa as indicated in Semazzi et al. (1996) and Semazzi and Indeje (1999) may be additional predictor candidates.

- (6) We have demonstrated the ability of the RegCM2 in faithfully predicting the seasonal and intraseasonal climate variability with skill. Since only a case study of only one-year (1997) was carried out, we recommend the use of more years in order to establish the model climatology that would assist in performing more model statistics to further verify the performance and application of the model in a predictive mode. Once this has been established, the model can then be used in operational climate prediction over the equatorial eastern African region. The climate over the Lake Victoria basin and other large lakes over eastern Africa could be improved by using a coupled lake model, since in our experiments we used uncoupled 1-dimensional diffusion lake model. Recent studies have indicated that the use of ensemble projections from more than one model is superior to the forecasts from individual models. The suggestion is that the dynamical and empirical forecasts should be combined to get better predictions. These approaches need to be incorporated in the modeling studies over equatorial eastern Africa.

## 10 REFERENCES

- Acker, T. L., L. E. Buja, J. M. Rosinski, J. E. Truesdale, 1996: User's Guide to NCAR CCM3, NCAR Technical Note/TN-421+IA, Boulder, Colorado.
- Alapaty, K., Pleim, J. E., Raman, S., Niyogi, D. S., and D. W. Byun, 1996: Simulation of atmospheric boundary layer processes using local- and nonlocal-closure schemes. *J. Appl. Meteorol.* **36**, 214-233.
- Alusa, A. L., 1976: The occurrence and nature of hailstorms in Kericho, Kenya. *Proc. Of the 2nd IAMAP/WMO scientific conference on weather modification*, Boulder, Colorado, 2-6 August 1976, pp. 249-256.
- Anderson, D., 1999: Extremes in the Indian Ocean. *Nature.* **401**, 337-339.
- Anderson, D. L. T., 1976: The low-level jet as a western boundary current. *Mon. Wea. Rev.* **104**, 907-921.
- Anderson, T. W., 1963: Asymptotic theory for principal component analysis. *Ann. Math. Stat.* **34**, 122-148.
- Anthes, R. A., E. Y. Hsie, and Y. H. Kuo, 1987: Description of the Penn State/NCAR Mesoscale Model Version 4 (MM4). *NCAR Tech. Note*, NCAR/TN-282+STR.
- Anyamba, E. K., 1983: On the monthly mean lower tropospheric circulation and the anomalous circulation during the 1961/62 floods in East Africa. MSc. Thesis. University of Nairobi, Kenya, 240 pp.
- Anyamba, E. K., 1984: Some aspects of the origin of rainfall deficiency in East Africa. *Proc. of the WMO Regional Scientific Conference on GATE, WAMEX and Tropical Meteorology*, Dakar, Senegal, pp. 110-112.
- Anyamba, E. K., 1990: A diagnostic study of low frequency oscillations in tropical Out Going Longwave Radiation. Ph.D. Dissertation, University of Nairobi, Nairobi, Kenya, 190pp.
- Anyamba, E. K., 1992: Some properties of a 20-30 day oscillation in tropical convection. *J. African. Met. Soc.* **1**, 1-19.
- Anthes, R. A., E. Y. Hsie, and Y. H. Kuo, 1987: Description of the Penn State/NCAR Mesoscale Model Version 4 (MM4). *NCAR Tech. Note*, NCAR/TN-282+STR.
- Ardanuy, P., 1979: On the observed diurnal observation of the Somali jet. *Mon. Wea. Rev.* **107**, 1694-1700.

- Asnani, G. C., 1993: *Tropical Meteorology*. Published by Prof. G. C. Asnani, Pune, India.
- Asnani, G. C. and Kinuthia, J. H., 1979: *Diurnal variation of precipitation in East Africa*. E. Africa Met. Dept. Memo. 8, 58 pp.
- Atwoki, K., 1975: A factor analytic approach for the delimitation of the rainfall regions of Uganda. *East African Geogr. Rev.* **13**, 9-36.
- Ba, M. B., and S. E. Nicholson, 1998: Analysis of convective activity and its relationship to the rainfall over the Rift Valley lakes of East Africa during 1983-90 using the Meteosat Infrared Channel. *Journ. Appl. Met.* **37**, 1250-1264.
- Baines, P. G., 1995: *Topographic effects in stratified flows*. Published by the Press Syndicate of the University of Cambridge, Cambridge, 482 pp.
- Bannon, P. R., 1979a: On the dynamics of the East African jet I: Simulation of mean conditions for July. *J. Atmos. Sci.* **36**, 2139-2152.
- Bannon, P. R., 1979b: On the dynamics of the East African jet II: Jet transients. *J. Atmos. Sci.* **36**, 2153-2168.
- Barnett, T. P., and R. E. Davies, 1975: Eigenvector analysis and prediction of sea surface temperature fluctuation in the northern Pacific Ocean. *Proc. WMO/IAMAP Symposium on Long-term Climatic fluctuations*, Norwich, England, 439-450.
- Barnett, T. P., 1981: Statistical prediction of North American air temperatures from Pacific predictors. *Mon. Wea. Rev.* **109**, 1021-1041.
- Barnett, T. P., and R. W. Preisendorfer, 1987: Origins and levels of monthly and seasonal forecast skill for United States surface air temperatures determined by canonical correlation analysis. *Mon. Wea. Rev.*, **115**, 1825-1850.
- Barnett, T., 1990: A solar-ENSO relation: Fact or fiction. *Geophys. Res. Lett.* **16**, 803-806.
- Barnston, A. G. and H. M. van den Dool, 1993: A degeneracy in cross-validated skill in regression-based forecasts. *J. Climate*, **6**, 963-977.
- Barnston, A. G., 1994: Linear statistical short-term climate predictive skill in the Northern Hemisphere. *J. Climate*, **7**, 1513-1564.
- Barnston, A. G., and T. M. Smith, 1996: Specification and prediction of global surface temperature and precipitation from global SST using CCA. *J. Climate*, **9**, 2660-2697.

- Barnston, A. G., W. Thiao, and V. Kumar, 1996: Long-lead forecasts of seasonal precipitation in Africa using CCA. *Wea. and Forecasting*. **11**, 506-520.
- Barring, L., 1988: Regionalization of daily rainfall in Kenya by means of common factor analysis. *J. Climatol.* **8**, 371-389.
- Beltrando, G., 1990: Space-time variability in April and October-November over East Africa during the period 1932-1983. *J. Climatol.*, **10**, 691-702.
- Bjerknes, J., 1969: Atmospheric teleconnections from the equatorial Pacific. *Mon. Wea. Rev.* **97**, 163-172.
- Briegleb, B. P., 1992: Delta-Eddington approximation for solar radiation in the NCAR Community Climate Model. *J. Geophys. Res.* **97**, 7603-7612.
- Brier, G. W. and R. A. Allen, 1951: Forecast verification. In T. F. Malone, (ed), *Compendium of Meteorology*, American Meteorological Society, pp. 843-851.
- Brier, G. W., 1978: Quasi-Biennial Oscillation and Feedback Processes in the Atmosphere-Ocean-Earth System. *Mon. Wea. Rev.* **106**, 938-946.
- Brown, J., and K. Campana, 1978: An economical time-differencing system for numerical weather prediction. *Mon. Wea. Rev.* **106**, 1125-1136.
- Burpee, R.W., 1972: The origin and structure of easterly waves in the lower stratosphere of North Africa. *J. Atmos. Sci.* **29**, 77-90.
- Cadet, D. L. and Diehl B., 1985: Interannual variability of the surface field over Indian Ocean during recent decades. *Mon. Wea. Rev.* **113**, 1921-1935.
- Cane, M., S. E. Zebiak and S. C. Donald, 1986: Experimental forecasts for El Niño. *Nature*. **321**, 827-702.
- Cane, M., G. Eshel and R. Buckland, 1994: Forecasting Zimbabwean maize yield using eastern equatorial Pacific sea surface temperature. *Nature*. **370**, 204-205.
- Camberlin, P., 1995: June-September rainfall in north-eastern Africa and atmospheric signals over the tropics: A zonal perspective. *Inter. J. Climatol.* **15**, 773-783.
- Camberlin, P., and J. G. Wairoto, 1997: Intraseasonal wind anomalies related to wet and dry spells during the long and short rainy seasons in Kenya. *Theor. Appl. Climatol.* **58**, 57-69.
- Chen, Y., Chen, X. A. and Y. Zhang, 1994: A diagnostic study of the low-level jet during TAMEX IOP 5. *Mon. Wea. Rev.* **122**, 2257-2284.

- Chu, P. S., 1995: Hawaii rainfall anomalies and El Nino. *J. Climate*. **8**, 1697-1703.
- Cressman, G. P., 1979: An operational objective analysis system. *Mon. Wea. Rev.*; **87**, 367-381.
- D'Abreton, P. C. and P. D. Tyson, 1995: Divergent and non-divergent water vapor transport over southern Africa during wet and dry conditions. *Meteorol. Atmos. Phys.* **55**, 47-59.
- Datta, R. R., 1981: Certain aspects of monsoonal precipitation dynamics over Lake Victoria. In *Monsoon Dynamics*. J. Lighthill and R.P. Pearce, Eds. Cambridge University Press, 333-349.
- Davies, H. C., and R. E. Turner, 1977: Updating prediction models by dynamical relaxation: An examination of the unique. *Quart. Roy. Meteor. Soc.* **103**, 225-245.
- Davies, T. D., C. E. Vincent, and A. K. C. Beresford, 1985: July-August rainfall in west-central Kenya. *J. Climatol.* **5**, 17-33.
- Delsol, F., Miyakoda, K., and R. H. Clarke, 1971: Parameterized processes in the surface boundary layer of an atmospheric circulation model. *Quart. J. Roy. Meteor. Soc.* **97**, 181-208.
- Dickinson, R. E., A. Henderson-Sellers, and P. J. Kennedy, 1993: Biosphere-Atmosphere Transfer Scheme (BATS) version 1E as coupled to the NCAR Community Climate Model. *NCAR Tech. Note*. NCAR/TN-387+STR, 72 pp.
- Doswell, C. A., 1977: Obtaining meteorologically significant surface divergence fields through the filtering property of objective analysis. *Mon. Wea. Rev.* **105**, 885-892.
- Druyan, L. M. and K. D. Koster, 1989: Sources of Sahel precipitation for simulated drought and rainy seasons. *J. Climate*. **2**, 1438-1446.
- Dyer, T. G. J., 1977: The assignment of rainfall stations into homogeneous groups: An application of principal component analysis. *Quart. J. R. Met. Soc.* **101**, 1005-1013.
- Dyer, T. G. J., 1982: On the interannual variation in rainfall over the sub-continent of Southern Africa. *J. Climatol.* **2**, 47-64.
- Eliassen, A., 1949: The quasi-static equations of motion with pressure as independent variable. *Geofys. Publ.* **17**, No.3, 44 pp.
- Farmer, G., 1988: Seasonal forecasting of the Kenya Coast short-rains. *J. Climatol.*, **8**, 489-497.

- Findlater, J., 1966: Cross-equatorial jet streams at low-levels over Kenya. *Meteor. Mag.* **95**, 353-364.
- Findlater, J., 1977: Observational aspects of the low level cross-equatorial jet stream of the western Indian Ocean. *Pure Appl. Geophys.* **115**, 1251-1262.
- Fraedrich, K., and Muller, 1992: Climate anomalies in Europe associated with ENSO extremes. *Int. J. Climatol.* **12**, 25-31.
- Folland, C. K., J. A. Owen, M. N. Ward, and A. W. Colman, 1991: Prediction of seasonal rainfall in the Sahel region using empirical and dynamical methods. *J. Forecasting*, **10**, 21-56.
- Fritsch, J. M., and C. F. Chappell, 1980: Numerical prediction of the convectively driven mesoscale pressure systems. Part I: Convective parameterization. *J. Atmos. Sci.* **37**, 1722-1733.
- Funk, J. P. and Garnham, G. J., 1962: Australian ozone observations and a suggested 24-months cycle. *Tellus.* **14**, 378-382.
- Giorgi, F., and G. T. Bates, 1989: The climatological skill of a regional model over complex terrain. *Mon. Wea. Rev.* **117**, 2325-2347.
- Giorgi, F., and M. R. Marinucci, 1991: Validation of a regional atmospheric model over Europe: sensitivity of wintertime and summertime simulations to selected physics parameterizations and lower boundary conditions. *Quart. J. Roy. meteor. Soc.* **117**, 1171-1206.
- Giorgi, F., L. O. Mearns, 1991: Approaches to the simulation of regional climate change: A review. *Rev. Geophys.* **29**, 2, 191-216.
- Giorgi, F., M. R. Marinucci, and G. T. Bates, 1993a: Development of a second-generation regional climate model (RegCM2). Part I: Boundary-layer and radiative transfer processes. *Mon. Wea. Rev.* **121**, 2794-2813.
- Giorgi, F., M. R. Marinucci, and G. T. Bates, 1993b: Development of a second-generation regional climate model (RegCM2). Part II: Convective processes and assimilation of lateral boundary conditions. *Mon. Wea. Rev.* **121**, 2814-2832.
- Giorgi, F., and M. R. Marinucci, 1996: An investigation of the sensitivity of simulated precipitation to model resolution and its implications for climate studies. *Mon. Wea. Rev.* **124**, 148-166.
- Glantz, M., 1984: Floods, Fires, and Famines. It is El Niño to blame. *Oceanus.* **27**, 14-19.

- Graham, N. E., 1990: *Canonical correlation analysis*. WMO Review of Climate Diagnostics methods.
- Graham, N. E., 1995: Decadal-scale climate variability in the tropical and North Pacific during the 1970s and 1980s: Observations and model results. *Climate Dyn.*, **10**, 135-162.
- Grell, G. A., 1993: Prognostic evaluation of assumptions used by cumulus parameterizations. *Mon. Wea. Rev.* **121**, 764-787.
- Halpert, M. S. and C. F. Ropelewski, 1992: Surface temperature patterns associated with the Southern Oscillation. *J. Climate*. **5**, 577-593.
- Henderson-Sellers, A., and V. Gornitz, 1984: Possible climatic impacts of land cover transformations, with particular emphasis on tropical deforestation. *Clim. Change*. **6**, 231-258.
- Hasebe, F., 1980: A global analysis of the fluctuation of total ozone-II; Non-stationary annual oscillation, quasi-biennial oscillation and long-term variations in total ozone. *J. Met. Soc. Japan*. **58**, 104-117.
- Hastenrath, S., 1985: *Climate and circulation of the tropics*. D. Reidel Publishing Company, Dordrecht, Holland, 455 pp.
- Hastenrath, S., 1987: On the prediction of India monsoon rainfall anomalies. *J. Clim. Appl. Met.*, **26**, 847-857.
- Hastenrath, S., 1991: *Climate and circulation of the tropics*. D. Reidel Publishing Company, Dordrecht, Holland, 455 pp.
- Hastenrath, S., A. Nicklis, and L. Greischar, 1993: Atmospheric-hydrospheric mechanisms of climate anomalies in the western equatorial Indian Ocean. *J. Geophys. Res.* **98**, 20219-20235.
- Hills, R. C., 1979: The structure of the Inter-Tropical Convergence Zone in equatorial Africa and its relationship to East African rainfall. *J. Inst. Brit. Geogr.* **4-3**, 329-352.
- Holton, J. R., 1972: *An introduction to dynamic meteorology*. Academic Press, Inc., International Geophysical series, Vol. 48, 511 pp.
- Holton, J. R. and R. S. Lindzen, 1972: An updated theory for the quasi-biennial cycle of the tropical stratosphere. *J. Atmos. Sci.* **29**, 1076-1080.
- Holton, J. R. and H. C. Tan, 1980: The influence of equatorial quasi-biennial oscillation on the global circulation at 50 mb. *J. Atmos. Sci.* **37**, 2200-2208.

- Holtzlag, A. A. M., E. I. F. de Bruijn, and H. L. Pan, 1990: A high-resolution air mass transformation model for short-range weather forecasting. *Mon. Wea. Res.* **118**, 1561-1575.
- Hsie, E. Y., R. A. Anthes, and D. Keyser, 1984: Numerical simulation of frontogenesis in a moist atmosphere. *J. Atmos. Sci.*, **41**, 2581-2594.
- Huang, C. Y. and S. Raman, 1991: Numerical simulation of January 28 cold air outbreak during GALE. Part I: The model and sensitivity tests of turbulent closures. *Bound. Layer.* **55**, 381-407.
- Hutchinson, P., 1992: The Southern Oscillation and the prediction of 'Der' season rainfall in Somalia. *J. Climate.* **5**, 525-531.
- Indeje, M., 1994. Modification of Mesoscale Convergence over Kenya by changes in Roughness length. Preprints of the Sixth WMO Scientific Conference on Weather Modification, May-June 1994, Paestum, Italy, WMO/TD-No. 22b, pp. 421-424.
- Indeje, M., 1995: Pacific Ocean Sea-Surface Temperatures and East African Seasonal Rainfall. Preprints of the Second International Symposium on Assimilation of Observations in Meteorology and Oceanography, March 13-17, 1995, Tokyo, Japan., WMO/TD-NO. 651, Volume II, pp. 355-360.
- Indeje, M., and E. K. Anyamba, 1998: Sensitivity of mesoscale systems over Kenya to changes in roughness length', *J. African. Met. Soc.* **3**, 19-33.
- Indeje, M., F. H. M. Semazzi, and L. J. Ogallo, 2000: ENSO signals in East African rainfall and their prediction potentials. *Int. J. Climatol.* **20**, 19-46.
- Indeje, M., and F. H. M. Semazzi, 2000: Relationships between QBO in the lower equatorial stratospheric zonal winds and East African seasonal rainfall. *Meteorol. Atmos. Phys.* **73**, 227-244.
- Ininda, J. M., 1998: Simulation of the impact of sea surface temperature anomalies on the short rains over East Africa. *J. African. Met. Soc.*, **3**, 127-138.
- Intergovernmental Panel on Climate Change (IPCC) (1995) World Meteorological Office, United Nations Environmental Programme, Radiative Forcing of Climate Change. *The 1994 Report of the Scientific Assessment Working Group of IPCC. Summary for Policymakers.*
- Janowiak, J., 1988: An investigation of Interannual rainfall. *J. Climate.* **1**, 240-255.
- Johnson, D. H., and H. T. Morth, 1961: Forecasting research in East Africa, in *Tropical Meteorology in Africa.* edited by D. J. Bargman, pp. 56-137, Munitatalp, Nairobi, 1960.

- Jolliffe, I. T., and D. E. Sarria-Dodd, 1994: Early detection of the start of the wet season in tropical climates. *Int. J. Climatol.* **14**, 71-76.
- Jury, M. R., Mc Queen C., and K. Levey, 1994: SOI and QBO signals in the African region. *Theor. Appl. Climatol.* **50**, 103-115.
- Kalnay, K., M. Kanamitsu, R. Kistler, W. Collins, D. Deaven, L. Gandin, M. Iredell, S. Saha, G. White, J. Woollen, Y. Zhu, M. Chelliah, W. Ebisuzaki, W. Higgins, J. Janowiak, K. C. Mo, C. Ropelewski, J. Kerr, R. A., 1998: Models win big in forecasting El Niño. *Science.* **280**, 522-523.
- Kasahara, A., 1966: The dynamical influence of orography on the large-scale motion of the atmosphere. *J. Atmos. Sci.* **23**, 259-270.
- Kida, H., Koide, T., Sasaki, H. and M. Chiba, 1991: A new approach for coupling a limited area model to a GCM for regional climate simulations. *J. Meteor. Soc. Japan.* **69**, No. 6, 723-728.
- Kiehl, J. T., and B. P. Briegleb, 1993: The relative roles of surface aerosols and greenhouse gases in climate forcing. *Science.* **260**, 311-314.
- Kiehl, J. T., J. J., Hack, G. B., Bonan, B. A., Boville, D. L., Williamson, and P. J., Rasch, 1997: The National Center for Atmospheric Research Community Climate Model: CCM3. *J. Climate.* **11**, 1131-1150.
- Kiladis, G. N., and H. F. Diaz, 1989: Global climatic anomalies associated with extremes in the Southern Oscillation. *J. Climate.* **2**, 1069-1090.
- Kinuthia, J. H., and G. C. Asnani, 1982: A newly found jet in North Kenya (Turkana Channel). *Mon. Wea. Rev.* **110**, 1722-1728.
- Kinuthia, J. H., 1992: Horizontal and vertical structure of the Lake Turkana jet. *J. Appl. Meteorol.* **31**, 1248-1274.
- Koteswarran, P., 1958: The easterly jetstreams in the tropics. *Tellus.* **10**, 43-57.
- Kutzbach, J. E., 1967: Empirical eigenvectors of sea level pressure, surface temperature and precipitation complexes over north America. *J. Appl. Meteor.* **6**, 791-802.
- Kraiser, H. F., 1959: Computer program for varimax rotation in factor analysis. *Educ. Psychol. Meas.* **19**, 413-420.
- Krishnamurti, T. N., 1961: The subtropical jet-stream of winter. *J. Meteor.* **18**, 172-191.
- Krishnamurti, T. N., Molinari, J., and H. L. Pan, 1976: Numerical simulation of the Somali jet. *J. Atmos. Sci.* **33**, 2350-2362.

- Krishnamurti, T. N., Pasch, R. J., and P. Ardanuy, 1980: Prediction of African waves and specification of squall lines. *Tellus*. **32**, 215-231.
- Krishnamurti, T. N., and L. J. Ogallo, 1989: Recent African climate (1979-1984). Dept. of Meteorology, Florida State University, Tallahassee, FL. Report NO. FSU-89-13.
- Labitzke, K., and H. van Loon, 1988: Associations between the 11-year solar cycle, the QBO and the atmosphere. Part I: the troposphere and stratosphere in the northern hemisphere winter. *J. Atmos. Terr. Phys.* **50**, 197-206.
- Labitzke, K., and H. van Loon, 1990: Associations between the 11-year solar cycle, the QBO and the atmosphere: A summary of recent work. *Phil. Trans. R. Soc. Lond.* **A330**, 577-598.
- Lacis, A. A., D. J. Wuebbles, and J. A. Logman, 1990: Radiative forcing of climate by changes in the vertical distribution of ozone. *J. Geophys. Res.* **95**, 9971-9982.
- Landman, W. A. and S. J. Mason, 1999: Change in the association between Indian Ocean sea-surface temperatures and summer rainfall over South Africa and Namibia. *Int. J. Climatol.*, **19**, 1477-1492.
- Lau, K., and P. J. Sheu, 1988: Annual cycle, Quasi-Biennial Oscillation and Southern Oscillation in global precipitation. *J. Geophys. Res.* **93**, No. D9, 10975-10988.
- Laporte, N., S. J. Goetz, C. O. Justice, and M. Heinicke, 1998: A New Land Cover Map of central Africa derived from multi-resolution, multi-temporal satellite observations. *Int. J. Remote Sensing.* (**19**) 18, 3537-3350.
- Lindesay, J. A., 1988: Southern African rainfall, the Southern Oscillation and a Southern Hemisphere semi-annual cycle. *Int. J. Climatol.* **8**, 17-30.
- Liu, Y., F. Giorgi, and W. M. Washington, 1994: Simulation of summer monsoon climate over East Asia with an NCAR regional climate model. *Mon. Wea. Rev.* **122**, 2331-2348.
- Livezy, R. E., 1987: The evaluation of skill in climate predictions. In Radok, U. (ed.). *Towards understanding Climate Change*. Westview Press, Boulder and London, 200pp.
- Madala, R. V., 1981: Finite-Difference techniques for vectorized fluid dynamics calculations. Edited by D. L. Book, Springer Verlag, New York.
- Mason, S. J. and P. D. Tyson, 1992: The modulation of sea surface temperature and rainfall associations over southern Africa with Solar activity and Quasi-Biennial Oscillation. *J. Geophys. Res.* **97**, No. D5, 5847-5856.

- Mason, S. J., Lindsay, J. A., and P. D. Tyson, 1994: Simulating drought in the southern Africa using sea-surface temperature variations. *WaterSA*. 20, 15-22.
- Mason, S. J., 1998: Seasonal forecasting of South African rainfall using a non-linear discriminant analysis model. *Int. J. Climatol.*, **18**, 147-167.
- Matarira, C. H., and M. R. Jury, 1992: Contrasting meteorological structure of intraseasonal wet and dry spells in Zimbabwe. *Int. J. Climatol.* **12**, 165-176.
- Michaelsen, J., 1987: Cross-validation in statistical climate forecast models. *J. Clim. Appl. Meteorol.*, **26**, 1589-1600.
- Mukabana, J. R. and R. A. Pielke, 1996: Investigating the influence of synoptic-scale monsoonal winds and mesoscale circulations and diurnal weather patterns over Kenya using a mesoscale numerical model. *Mon. Wea. Rev.* **124**, 224-243.
- Mukherjee, B. K., K. Indira, R. S. Reddy and BH. V. Ramana Murty, 1979: High-level warming, winds and Indian summer monsoon. *Mon. Wea. Rev.* **107**, 1581-1588.
- Mukherjee, B. K., K. Indira, R. S. Reddy and BH. V. Ramana Murty, 1985: Quasi-biennial oscillation in stratospheric zonal winds and Indian summer monsoon. *Mon. Wea. Rev.* **113**, 1421-1424.
- Murakami, T., and W.L. Sumathipala, 1989: Westerly bursts during the 1982/83 ENSO. *J. Climate*. **2**, 71-85.
- Mutai, C. C., Ward, M. N. and Coleman, A. W., 1998: Towards the prediction of the East Africa short rains based on sea-surface temperature-atmosphere coupling. *Int. J. Climatol.* **18**, 975-997.
- Mylne, M. F., and P. R. Rowntree, 1992: Modeling the effects of albedo change associated with tropical deforestation. *Clim. Change*. **21**, 317-343.
- Nakamura, K., 1968: Equatorial westerlies over East Africa and their climatological significance. *Jpn. Prog. Climatol.* **20**, 9-27.
- Neave, H. R., 1978: *Statistical Tables*. George Allen & Unwin, London.
- Newell, R. E., 1979: Climate and the ocean. *Amer. Sci.* **67**, 405-416.
- Ngara, T. and G. C. Asnani, 1978: Five-day oscillation in the East African low-level jet. *Nature*. **272**, 708-709.
- Nicholls, N., 1978: Air-sea interaction and the Quasi-Biennial Oscillation. *Mon. Wea. Rev.*, **106**, 1505-1508.

- Nicholls, N., 1984: The stability of empirical long-range forecast techniques. A case study. *J. Clim. Appl. Met.*, **23**, 143-147.
- Nicholson, S. E., 1986: The nature of rainfall variability in Africa south of the equator. *J. Climatol.* **6**, 515-530.
- Nicholson, S. E. and Entekhabi, D., 1986: The quasi-periodic behavior of rainfall variability in Africa and its relationship to the Southern Oscillation. *Arch., Met. Geoph. Biocl. Ser. A*, **34**, 311.
- Nicholson, S. E., S. E. Kim, and Hoopingarner, 1988: Atlas of African rainfall and its variability. Department of Meteorology, Florida State University, Tallahassee, FL. 273pp.
- Nicholson, S. E. and B. S. Nyenzi, 1990: Temporal and spatial variability of SSTs in the tropical Atlantic and Indian Oceans. *Meteorol. Atmos. Phys.*, **42**, 1-17.
- Nicholson, S. E., 1996: A review of Climate Dynamics and Climate Variability in Eastern Africa. *The Limnology, Climatology and Paleoclimatology of the East African Lakes*. Gordon and Breach, New York, 57pp.
- Nyenzi, B. S., 1992: An analysis of Interannual variability of rainfall over East Africa. *J. African. Met. Soc.*, **1**, No. 1, 57-79.
- North G. R., T. L. Bell and R. F. Cahalan, 1982: Sampling errors in estimation of empirical orthogonal functions. *A. Meteorol. Soc.* **110**, 699-706.
- Ogallo, L. J. 1980: Rainfall variability in Africa. *Mon. Wea. Rev.* **107**, 1133-1139.
- Ogallo, L. J., 1982: Quasi-periodic patterns in the East African rainfall records. *Kenya J. Sci. and Techn.* **A3**, pp. 43-54.
- Ogallo, L. J., 1983: Quasi-periodic patterns in East African rainfall records. *Kenya J. Sci. and Techn.* **A3**, p. 43-54.
- Ogallo, L. J., 1988: Relationships between seasonal rainfall in East Africa and the Southern Oscillation. *Int. J. Climatol.* **8**, 31-43.
- Ogallo, L. J., Janowiak, J. E. and Halpert, M. S., 1988: Teleconnection between seasonal rainfall over East Africa and Global seas surface temperature anomalies. *J. Met. Soc. Jpn.* **66**, 807-822.
- Ogallo, L. J. 1989: The spatial and temporal patterns of the East African seasonal rainfall derived from principal component analysis. *Int. J. Climatol.* **9**, 145-167.

- Ogallo, L. J., R. E. Okoola and D. N. Wanjohi, 1994: Characteristics of Quasi-Biennial Oscillation over Kenya and their predictability potential for seasonal rainfall. *Mausam*, **45**, No. 1, 57-62.
- Okeyo A. E., 1986: The influence of Lake Victoria on the convective systems over the Kenya highlands. *Proc. International conference on short, medium range weather forecasting*. Tokyo, Japan, August 1986.
- Okoola, R. E., 1998: Spatial evolutions of the active patterns across the equatorial Eastern Africa region during northern hemisphere spring season using Outgoing Longwave Radiation records. *Meteorol. Atmos. Phy.* **66**, 51-63.
- Okoola, R. E., 1999: A diagnostic study of the eastern Africa monsoon circulation during the Northern Hemisphere spring season. *Int. J. Climatol.* **19**, 143-168.
- Overland, J. E. and R. W. Preisendorfer, 1982: A significance test for principal components applied to a cyclone climatology. *Mon. Wea. Rev.* **110**, 1-4.
- Owino, A., 1997: Dynamics of air flow through mountain gap. Ph.D. Thesis. University of Pune, India.
- Parker, D. E., C. K. Folland, and Ward M. N., 1988: Sea surface temperature anomaly patterns and prediction of seasonal rainfall in the Sahel region of Africa. In Gregory, S. (ed.). *Recent climatic change*, Bellhaven, London, pp. 166-178.
- Patwardhan, S. K., and G. C. Asnani, 1999: Meso-scale distribution of summer monsoon rainfall near the western Ghats (India). *Int. J. Climatol.* **20**, 575-581.
- Peixoto, J. P., and A. H. Oort, 1992: *Physics of Climate*. American Institute of Physics, NY. pp. 492-496.
- Philander, S. G. H., 1990: *El Nino, La Nina and the Southern Oscillation*. London: Academic Press, 293 pp.
- Phillips, J. G., Cane, M. A. and Rosenzweig, C., 1998: ENSO, seasonal rainfall patterns and simulated maize yield variability in Zimbabwe. *Agr. For. Meteorol.* **90**, 39-50.
- Phillips, J. G., and McIntyre, B., 1999: ENSO and interannual rainfall variability in Uganda: Implications for agricultural management. *Int. J. of Climatol.* (in press).
- Plumb, R. A., 1977: The interaction of two internal waves with the mean flow: Implications for the theory of the quasi-biennial oscillation. *J. Atmos. Sci.* **34**, 1847-1858.
- Plumb, R. A., J. R. Holton and Matsuno, T., 1984: *Quasi-biennial oscillation. Dynamics of the Middle Atmosphere*. Terra Scientific Publication Company. 217-251pp.

- Portmann, R. W., and S. Solomon, 1997: Radiative forcing of the Earth's climate system due to tropical tropospheric ozone. *J. Geophys. Res.* **102**, 9409-9417.
- Preisendorfer, R. W. and Mobley, C. D., 1984: Climate forecast verification, United States mainland, 1974-1983. *Mon. Wea. Rev.* **112**, 809-825.
- Reason, C. J. C., and C. R. Godfred-Spenning, 1998: SST variability in the south Indian Ocean and associated circulation and rainfall patterns over southern Africa. *Meteorol. Atmos. Phys.* **66**, 242-258.
- Reverdin, G., D. L. Cadet and Gutzler, D., 1986: Interannual displacements of convection and surface circulation over the equatorial Indian Ocean. *Quart. J. R. Met. Soc.*, **112**, 46-67.
- Ramachandran, G., K. V. Rao, and K. Krishna, 1980: An observational study of the boundary-layer winds in the exit region of a mountain gap. *J. Appl. Meteor.* **19**, 881-888.
- Rasmusson, E. M., Akhrin, P. A., Chen, W. Y. and J. B. Jalickee, 1981: Biennial variations in the surface temperature over the United States as revealed by singular value decomposition. *Mon. Wea. Rev.* **109**, pp. 587-598.
- Rasmusson, E. M. and R. D. Carpenter, 1983: Variation in the tropical sea surface temperatures and sea wind fields associated with the Southern Oscillation/El Niño. *Mon. Wea. Rev.* **110**, 354-384.
- Raverdin, G., D. L. Cadet, and D. Gutzler. 1986: Interannual displacements of convection and surface circulation over the equatorial Indian Ocean. *Quart. J. R. Met. Soc.* **112**, 43-67.
- Reynolds, R. W. and T. M. Smith, 1994: Improved global sea surface temperature analyses. *J. Climate.* **7**, 929-948.
- Richman, M. D., 1981: Obliquely rotated principal components. An improved meteorological map typing technique. *J. Appl. Met.* **20**, 1145-1159.
- Rocha, A., and I. T. Simmonds, 1997: Interannual variability of southeastern Africa summer rainfall. Part I: relationships with air-sea interaction processes. *Int. J. Climatol.* **17**, 235-266.
- Rodhe, H. and Virji, H., 1976: Trends and periodicities in East African rainfall. *Mon. Wea. Rev.* **104**, pp. 307-315.
- Ropelewski, C. F. and M. S. Halpert, 1987: Global and regional scale precipitation patterns associated with the El Niño/Southern Oscillation. *Mon. Wea. Rev.* **115**, 1606-1626.

- Ropelewski, C. F. and M. S. Halpert, 1989: Precipitation patterns associated with the high index phase of the Southern Oscillation. *J. Climate*. **2**, 268-284.
- Ropelewski, C. F., Halpert, M. S. and X. Wang, 1992: Observed tropospheric biennial variability and its relationship to the Southern Oscillation. *J. Climate*. **9**, 594-614.
- Rowell, D. P., C. K. Folland, K. Maskell, J. A. Owen, and M. N. Ward, 1994: Causes and predictability of Sahel rainfall variability. *Climate Research Technical Note No. 12*, Hadley Center, Bracknell, 15 pp.
- Saha, K. R., 1974: Zonal anomaly of sea-surface temperature in equatorial Indian Ocean and its possible effect upon monsoon circulation. *Tellus*. **22**, 403-409.
- Saji, N. H., B. N. Goswami, P. N. Vinayachandran, and T. Yamagata, 1999: A dipole mode in the tropical Indian Ocean. *Nature*. **401**, 360-363.
- Sarker, R. P., Sinha, K. C., and U. S. De, 1978: Dynamics of orographic rainfall. *Indian J. Met. Hydrol. Geophys.* **29**, 335-348.
- Schoeberl, M. R., 1978: Stratospheric warming. Observations and theory. *Res. Geophys. Space Phys.* **16**, 521-538.
- Semazzi, H. F. M., 1980a: Stationary barotropic flow induced by a mountain over a tropical belt. *Mon. Mea. Rev.* **108**, 922-930.
- Semazzi, H. F. M., 1980b: Numerical experiments on the orographic dynamic phenomenon over a tropical belt. *Arch. Met. Geoph. Biokl., Ser. A.*, **29**, 55-65.
- Semazzi, H. F. M., 1985: An investigation of the equatorial orographic dynamic mechanism. *J. Atmos. Sci.* **42**, 28-83.
- Semazzi, H. F. M., B. Burns, N. H. Lin and J. E. Schemm, 1996: A GCM study of the teleconnections between the continental climate of Africa and global sea-surface temperature anomalies. *J. Climate*, **9**, 2480-2497.
- Semazzi, H. F. M., and L. Sun, 1997: The role of orography in determining the Sahelian climate. *Intern. J. Climatol.* **17**, 581-596.
- Semazzi, F. H. M. and M. Indeje, 1999: Inter-seasonal variability of ENSO rainfall signal over Africa. *J. Afri. Meteorol. Soc.* **4**, 81-94.
- Shanko, D., and P. Camberlin, 1998: The effects of the southwest Indian Ocean tropical cyclones on the Ethiopian drought. *Int. J. Climatol.* **18**, 1373-1388.
- Shea, D. J., K. E. Trenberth, and R. W. Reynolds, 1992: A global monthly sea surface temperature climatology. *J. Climate*, **5**, 987-1001.

- Shukla, J., 1974: Effects of Arabian Sea-Surface Temperature Anomaly on Indian Summer Monsoon. A numerical study with the GFDL Model. *J. Atmos. Sci.* **32**, 503-511.
- Shukla, J and B. M. Misra. 1977: Relationships between Sea-Surface Temperature and windspeed over central Arabia and monsoon rainfall over India. *Mon. Wea. Rev.* **105**, 998-1002.
- Shukla, J., 1981: Dynamical predictability of monthly means. *J. Atmos. Sci.* **38**, 2547-2572.
- Shukla, J., C. Nobre, and P. J. Sellers, 1990: Amazon deforestation and climate change. *Science*. **247**, 1322-1325.
- Slingo, J. M., 1989: A GCM parameterization for the shortwave radiative property of the water clouds. *J. Atmos. Sci.* **46**, 1419-1427.
- Smith, I., 1994: Indian Ocean sea surface temperature patterns and Australian Winter rainfall. *Int. J. Climatol.* **14**, 287-305.
- Stull, B. S., 1988: *An introduction to boundary layer meteorology*. Kluwer Academic Publishers. Dordrecht, the Netherlands, 666 pp.
- Storch, H. V., and F. W. Zwiers, 1999: *Statistical analysis in climate research*. The Press Syndicate of the University of Cambridge, Cambridge, UK. 400pp.
- Sud, Y. C. and W. E. Smith, 1984: Ensemble formation of surface fluxes and improvement in evapotranspiration and cloud parameterization in a GCM. *Bound.-Layer Meteor.* **29**, 185-210.
- Sun, L., F. H. M. Semazzi, F. Giorgi, and L. J. Ogallo 1999a: Application of the NCAR Regional Climate Model to Eastern Africa. Part I: Simulations of Autumn Rains of 1988. *J. Geophys. Res.* **104**, No. D6, 6529-6548.
- Sun, L., F. H. M. Semazzi, F. Giorgi, and L. J. Ogallo 1999b: Application of the NCAR Regional Climate Model to Eastern Africa. Part II: Simulations of Interannual Variability. *J. Geophys. Res.* **104**, No. D6, 6549-6562.
- Thompson, P. D., 1957: A heuristic theory of large-scale turbulence and long period velocity variations in barotropic flow. *Tellus*. **9**, 69-91.
- Trenberth, K. E., 1974: A quasi-biennial standing wave in the southern hemisphere and interrelations with sea surface temperature. *Quart. J. Roy. Meteor. Soc.*, **101**, 55-74.
- Trenberth, E., 1992: Global analyses from ECMWF and Atlas of 1000 to 10 mb circulation statistics. NCAR Technical Note. NCAR/TN-373+STR. pp 191

- Trenberth, K. E. and J. W. Hurrell, 1994: Decadal ocean-atmosphere variations in the Pacific. *Climate Dyn.*, **9**, 303-319.
- Trenberth, K. E., 1997: The definition of El Niño. *Bull. Amer. Meteor. Soc.* **78**, 2771-2777.
- Trenberth, K. E., 1998: Forecasts of the development of the 1997-98 El Niño event. *Clivar Scientific Issues*. Based in part on presentations made at the Seventh session of the CLIVAR SSG in Santiago, Chile (April 1998).
- Vincent, C. E., T. D. Davies and A. K. C. Beresford, 1979: Recent changes in the level of Lake Naivasha, Kenya, as an indicator of equatorial westerlies over East Africa. *Climatic Chance*. **2**, 175-189.
- Wagner, R. G. and A. M. DA Silva, 1994: Surface conditions associated with the anomalous rainfall in the Guinea Coastal region. *Int. J. Climatol.* **14**, 179-199.
- Wallace, J. M., 1973: General circulation of the tropical lower stratosphere. *Res. Geophys. Space Phys.* **11**, 191-222.
- Wang, S., 1984: The El Niño events in 1860-1979. *Kexue Tongbao*. **30**, 728-932.
- Ward, M. N. and Folland C. K., 1991: Prediction of seasonal rainfall in the north Nordeste of Brazil using eigenvectors of sea-surface temperature. *Int. J. Climatol.*, **11**, 711-743.
- Ward, M. N., C. K. Folland, K. Maskell, A. W. Colman, D. P. Rowell, and K. P. Lane, 1993: Experimental seasonal forecasting of tropical rainfall at the UK Meteorological Office. In *Prediction of interannual climate variations*, volume **16**, pp. 197-216. NATO, Springer-Verlag.
- Webster, P. J., A. M. Moore, J. P. Loschnigg, and R. R. Leben, 1999: Coupled ocean-atmosphere dynamics of the Indian Ocean during 1997-98. *Nature*. **401**, 356-360.
- Weare, B. C., A. R. Navato and R. E. Newell, 1975: Empirical orthogonal analysis of Pacific sea surface temperatures. *Proc. WMO/IAMAP Symposium on Long-term Climatic fluctuations*, Norwich, England, pp. 167-174.
- Wiin-Nielsen, A., 1961: On short and long term variations in quasi-barotropic flow. *Mon. Wea. Rev.* **89**, 461-476.
- Wilby R. L., and T. M. L. Wigley, 2000: Precipitation predictors for downscaling: Observed and general circulation model relationships. *Int. J. Climatol.*, **20**, 641-661.
- Wilks, D. S., 1995: *Statistical methods in the atmospheric sciences*. Academic Press, San Diego, 467 pp.

- Xue, Y. and J. Shukla, 1997: Model simulation of the influence of Global SST anomalies on Sahel rainfall. *Mon. Wea. Rev.* **126**, 2782-2792.
- Xue, M. and A.J. Thorpe, 1990: A mesoscale numerical model using the nonhydrostatic pressure-based sigma-coordinate equations: Model experiments with dry mountain flow. *Mon. Wea. Rev.* **119**, 1168-1185.
- Zhang, D. -L., and R A. Anthes, 1982: A high-resolution model of the planetary boundary layer-sensitivity tests and comparisons with SESAME-79 data. *J. Appl. Meteor.* **21**,1594-1609.
- Zhang, H., A. Henderson-sellers, and K. Mcguffie, 1996a: Impacts of tropical deforestation. Part I: Process analysis of local climatic change. *J. Climate.* **9**, 1497-1517.
- Zhang, H., A. Henderson-sellers, and K. Mcguffie, 1996b: Impacts of tropical deforestation. Part II: The role of large-scale dynamics. *J. Climate.* **9**, 2498-2521.

# **APPENDIX A**

## **ABSTRACTS OF SELECTED PUBLICATIONS**

Abstracts of selected publications are as follows.

## **ENSO SIGNALS IN EAST AFRICAN RAINFALL SEASONS**

Matayo Indeje, Fredrick H. M. Semazzi, and Laban J. Ogallo  
International Journal of Climatology, vol. 20, 19-46, (2000)

The evolutions of ENSO modes in the seasonal rainfall patterns over East Africa are examined in this study. The study covers the period 1961-1990. Both Rotated Empirical Orthogonal Function (EOF) and simple correlation analyses were used to delineate a network of 136 stations over East Africa into homogeneous rainfall regions in order to derive rainfall indices. Time series generated from the delineated regions were later used in the rainfall/ENSO analyses. Such analyses involved the development of composite rainfall map patterns for El Niño and post-ENSO (+1) years in order to investigate the associations between seasonal evolution of El Niño/Southern Oscillation (ENSO) signals and the space-time evolution of rainfall anomalies over the region.

Analyses based on both EOF and simple correlation techniques yielded eight homogeneous rainfall regions over East Africa. The results showed unique seasonal evolution patterns in rainfall during the different phases of the ENSO cycles. East African rainfall performance characteristics were stratified to identify distinct rainfall anomaly patterns associated with ENSO and post-ENSO (+1) years. These can be applied in conjunction with skillful long lead (up to 12 months) ENSO prediction to provide guidance on likely patterns of seasonal rainfall anomalies over the region. Such information can be crucial for early warning of socio-economic disasters associated with extreme rainfall anomalies over East Africa.

# **Relationships between QBO in the lower Equatorial Stratospheric Zonal Winds and East African Seasonal Rainfall**

Matayo Indeje and Fredrick H. M. Semazzi

Journal of Meteorology and Atmospheric Physics, vol. 23, 227-244, (2000).

Teleconnections between the seasonal rainfall anomalies of March through May ("long-rains") over eastern Africa (Uganda, Kenya and Tanzania) and the lower equatorial stratospheric (30-mb) zonal winds for the 32-year period 1964-1995 are examined using statistical methods. The analysis is based on the application of the simple correlation method and QBO/rainfall composite analysis. A statistical study of spatial correlation patterns is made in an effort to understand the climatic associations between the equatorial stratospheric zonal wind and regional rainfall at the interannual scale. The aim of this analysis is to establish whether this global signal can be employed as predictor variable in the long-range forecasts. The study is part of an ongoing investigation, which aims at designing a comprehensive and objective, multi-variate-forecast system of seasonal rainfall over eastern Africa. The correlation parameters include simultaneous (zero lag), and the non-zero lag correlations. The statistical significance of the correlation coefficient [r] is tested based on the Monte Carlo t-statistical method, and the standard correlation tables.

Our results indicate significant positive simultaneous and non-zero lag correlations between rainfall over parts of East Africa and lower equatorial stratospheric zonal wind during the months of March-May and June-August. Significantly high correlations are concentrated over the western regions of eastern Africa with peak values of (+0.8) observed over these areas. These associations have been observed to be more prominent during lag than in the simultaneous correlations. Strong month to month lag coherence is observed after June prior to the onset of the March to May seasonal rainfall and persists for more than 4 months. Correlation indices for the eight homogeneous rainfall regions over eastern Africa which are derived from our Empirical Orthogonal Function/Cluster analysis shows a clear annual cycle with significant relationships between QBO and seasonal rainfall occurring during boreal summer (June-August). The season with the weakest relationship is December-February. It is however, noted that although the coherence between QBO-Index and rainfall during the long-rains is significantly high, there are some wet/dry years for which the relationship between the long rains and the lower equatorial zonal wind are not significant (for example in 1966, 1973 and 1983). These years have been associated with strong and prolonged ENSO events. Preliminary comparison of the QBO-Index and the newly found Indian Ocean dipole mode index (DMI) indicates that the two climate variables may be significantly related. Of the six high dipole mode events in the Indian Ocean that were observed in 1961, 1967, 1972, 1982, 1994 and 1997, all except 1967 coincided with the easterly phase of the QBO-Index and below normal rainfall over western highlands of eastern Africa. Contingency analyses indicate 60 percent likelihood for the occurrence of above normal rainfall during the

westerly phase of the QBO and 63 percent likelihood of below normal rainfall during the east phase of the QBO. Our correlation analysis results indicate that about 36 percent of the variability of the long-rains season over eastern Africa are associated with the QBO-Index. Our results further show that the tendency of the lower equatorial stratospheric zonal wind prior to the season is a good indicator of the performance of the long rains of eastern Africa. A positive OND minus JJA QBO trend is a good indicator for the non-occurrence of drought over eastern Africa. Similarly, a negative trend is a good indicator for the non-occurrence of high rainfall over the region. The identified characteristics and domain of influence of the QBO signal in different regions of East Africa suggests that this global oscillator may offer useful input to objective multi-variate rainfall prediction models for eastern Africa.

# **Mechanistic Model Simulations of the East African Climate using NCAR Regional Climate Model: Influence of large-scale Orography on the Turkana Low-level Jet**

Matayo Indeje, Fredrick H. M. Semazzi, Lian Xie, and Laban J. Ogallo  
Journal of Climate, (2000). (Accepted)

The climate over eastern Africa is simulated during the boreal winter season using the NCAR regional climate model (RegCM). More specifically, we simulate the Turkana easterly low-level jet that lies between the Ethiopian and the East African highlands. The role of the large-scale orography and two other factors (the large-scale monsoonal flow and the Turkana channel depth) are investigated in order to understand the kinematics and thermodynamics of this jet.

The simulated patterns of the Turkana easterly low-level jet compares well with its observed characteristics. Two distinct jet streams, detached from each other, are indicated throughout the channel except at the middle of the channel where they combine into a single and high-level jet centered at about 700-hPa level. The level of maximum winds ( $\sim 11 \text{ m s}^{-1}$ ) occurs in the layers 930-hPa and 650-hPa levels. Temperature, moisture and momentum flux convergence is dominant at the entrance and exit of the channel, with divergence of these fluxes indicated at the middle of the channel. The dynamics within the Turkana channel can be explained in terms of the orographic channeling effects associated with the Bernoulli effect in barotropic flows. Our results show that orography, the large-scale monsoon flow and the depth of the channel are crucial in the simulation of the jet. Of the three forcing mechanisms, orography is the most dominant factor in the development and maintenance of the jet. The effect of the large-scale monsoon flow is to determine the wind speed and direction in the jet cores whereas, the depth of the channel is important in determining the vertical structure and location of the jet cores. Our results have further indicated that thermal and frictional forcings may be playing equivalent roles as that of the large-scale winds in the formation of the jet. The split in the jet cores over the middle of the channel is analyzed as a barotropic instability problem due to the divergence/convergence of momentum fluxes.

The model results further show that the dry conditions observed over the Lake Turkana basin may be explained in terms of dominant downward vertical velocity, decrease in moisture flux convergence and increase in temperature flux divergence that inhibit active developments of meso-scale circulations and their interactions with large-scale flow over these areas. The presence of the Turkana low-level jet has been found to be a significant climatic feature over the East African region. The identified regions of strong winds associated with the jet are important to the safety in the aviation industry. These regions may also provide alternative renewable energy resources in the form of wind energy.